TRƯỜNG ĐẠI HỌC QUY NHƠN
QUY NHON UNIVERSITY

TẠP CHÍ KHOA HỌC
TRƯỜNG ĐẠI HỌC QUY NHƠN

QUY NHON UNIVERSITY
JOURNAL OF SCIENCE

KHOA HỌC TỰ NHIÊN VÀ KỸ THUẬT
NATURAL SCIENCES AND ENGINEERING

18 (1)
2024

FEBRUARY 2024

QUY NHON UNIVERSITY
JOURNAL OF SCIENCE
VOLUME 18, ISSUE 1, FEBRUARY 2024
ISSN: 1859-0357 E-ISSN: 2815-6242

CONTENTS

TẠP CHÍ KHOA HỌC
TRƯỜNG ĐẠI HỌC QUY NHƠN

Dung dịch nano bạc, các phương pháp điều chế, những đặc tính và khả năng ứng dụng

Nguyễn Đức Hùng*

Viện Hóa học và Vật liệu, Viện Khoa học Công nghệ Quân sự, Việt Nam

Ngày nhận bài: 28/09/2023; Ngày sửa bài: 23/10/2023;
Ngày nhận đăng: 08/11/2023; Ngày xuất bản: 28/02/2024

TÓM TẮT

Sự phát triển của vật liệu qua các thời kỳ: đồ đá, đồng, sắt, cao phân tử và hiện nay là vật liệu nano. Với các kích thước cực nhỏ, diện tích bề mặt rất lớn và hiệu ứng lượng tử vật liệu nano mang lại nhiều đặc tính vượt trội và ứng dụng đặc biệt. Vật liệu nano bạc (AgNPs) vừa mở rộng và bổ sung những đặc tính mới của Ag nên phạm vi ứng dụng cũng phát triển hơn, đặc biệt trong lĩnh vực môi trường, y học và bảo vệ sức khỏe con người. AgNPs được điều chế từ kim loại "trên xuống" hoặc từ ion "dưới lên" bằng các phương pháp vật lý, hóa học, hóa lý, sinh học hoặc kết hợp hỗn hợp. Sản phẩm AgNPs là dung dịch thật hệ keo có những đặc tính phụ thuộc vào các phương pháp điều chế, song những đặc tính cơ bản như cộng hưởng bề mặt plasmonic của hạt nano bạc bằng UV-Vis, hình dạng, kích thước và cấu trúc hạt bằng TEM, SEM, AFM, FTIR, XPS, XRD, phân bố cỡ hạt bằng Laser Scattering Particle Size Distribution Analyzer và Zeta Phoremeter Instrumentation. Nồng độ nano bạc được xác định bằng AAS, ICP-MS, ICP-OES. Tùy thuộc vào mục đích sử dụng vào lĩnh vực: xúc tác, quang điện, vi điện tử, môi trường, y dược, sức khỏe,... còn xác định thêm các phương pháp xác định các tính chất tương ứng. Do AgNPs có nhiều đặc tính đặc biệt nhất là lĩnh vực diệt nhiều vi khuẩn bảo vệ môi trường và sức khỏe con người nên chiến lược nghiên cứu phát triển AgNPs được đặc biệt chú ý tại nhiều quốc gia trên thế giới.

Từ khóa: *AgNPs, các phương pháp điều chế, những đặc tính, khả năng ứng dụng.*

**Tác giả liên hệ chính.*
Email: nguyenduchung1946@gmail.com

QUY NHON UNIVERSITY
JOURNAL OF SCIENCE

Silver nano solution: manufacturing methods, characteristics and applicability

Nguyen Duc Hung*

Institute for Chemistry and Materials, Academy of Military Science and Technology, Vietnam

Received: 28/09/2023; Revised: 23/10/2023;
Accepted: 08/11/2023; Published: 28/02/2024

ABSTRACT

The development of human society is associated with the development of materials through the ages of stone, copper, iron, polymers and now nano materials. With extremely small sizes, very large surface areas and quantum effects of nanomaterials, nano materials offer many outstanding properties and opens up many special applications. Silver nanoparticles (AgNPs) have both the properties of metallic silver while expanding and adding new properties, so the application scope is also more developed, especially in the fields of environment, medicine and human health protection. Silver nano is prepared according to the principle of "top-down" from metal or "bottom-up" from ion by physical, chemical, physicochemical or biological techniques or a mixture of combinations. The obtained silver nano product is a true colloidal solution whose properties are very dependent on the preparation methods, but the basic properties are the nature of the plasmonic surface resonance of silver nanoparticles by UV-Vis, particle shape, size and structure by TEM, SEM, AFM, FTIR, XPS, XRD, nanoparticle and colloidal size distribution by Laser Scattering Particle Size Distribution Analyzer and Zeta Phoremeter Instrumentation. The concentration of nano silver is usually determined by methods such as AAS, ICP-MS, ICP-OES. Depending on the intended use in the fields of catalysis, photovoltaic, microelectronics, environment, medicine, health, etc., methods to determine the corresponding properties are also applied. AgNPs has many special characteristics, the most prominent of which is in the field of killing many bacteria and viruses to protect the environment and human health, so the AgNPs development research strategy is specially noticed in many countries in the worlds.

Keywords: *AgNPs, methods, characteristics, applicability.*

1. INTRODUCTION

Metallic silver was discovered thousands of years BC and has become a very precious metal used as currency in feudal society in many countries as well as jewelry and household items.[1] With properties as good conductor of electricity, heat, light sensitivity and antiseptic, silver has been used in the fields of electricity, electronics, film and medicine since very early. Since the development of nanomaterials with effects on subatomic small size, large area and quantum,[2,3] silver nanoparticles (AgPNs) have also been focused on researching innovations such as:[4,5] electrical properties,[6] electronic,[7] catalytic,[8] and especially antibacterial.[9-11] Because AgNPs have many applications in science, technology and life, especially with very good antibacterial ability,[12-14] many research and manufacturing methods such as physics,[15-17] biology,[18-20]

**Corresponding author.*
Email: nguyenduchung1946@gmail.com

https://doi.org/10.52111/qnjs.2024.18101

chemistry,[21-23] and electrochemistry[24-27] have focused their research, including new method to create high purity or local green raw matrials are available and cheap.

2. MANUFACTURING METHODS

2.1. Physical methods

2.1.1. The "top - down" approach

Fabrication of AgNPs by physical method follows the “top-down” principle with bulk metallic silver using a large amount of heat to separate the silver into vapor and then condense it like PVD,[28,29] or granular and then dispersed. such as laser cutting[30,31] or electric arc.[32,33] Figure 1 shows the principle of laser method (a)[30] and arc discharge (b)[33] along with corresponding TEM images of the obtained AgNPs particle size and shape and size.

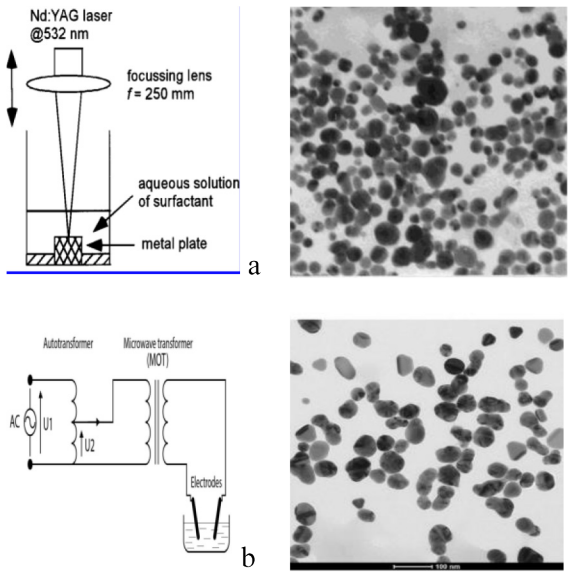

Figure 1. Schematic diagram and TEM image of AgNPs, a) Laser method,[30] b) arc discharge method.[33]

The AgNPs solution obtained by the above methods has a time-dependent light to dark yellow color and has a characteristic UV-Vis spectrum from 400 to 404 nm. Figure 1 shows that the shape of the nanoparticles is not uniform, so the particle size distribution spectrum is wide from 10 to 300 nm and the average is 46.8 to 48.9 nm. The zeta potential values from -20.4 to -22.31 mV show that AgNPs colloidal solutions can be prepared by physical methods without the need for stable stabilizers. Although the production of AgNPs by the above physical methods does not use chemicals, it has high purity, but the equipment is complicated, uses a lot of energy, the concentration is not high and the quantity obtained is not large. Therefore, the cost is high and the field of use is limited.

2.1.2. The "bottom - up" approach

Physical methods can implement the principle of preparing AgNPs from the “bottom-up” by beams: gamma,[34-37] electrons,[38] or microwave[39] activating components in solution to reduce Ag^+ of $AgNO_3$ salts into AgNPs.

According to the author group Bui Duy Du,[40] the energy of gamma rays can affect the components of the medium such as water to form strong reactive agents including strong reducing agents such as H- radical with potential value - 2, 3 V:

$$H_2O \xrightarrow{\gamma-\text{radiation}} e^-_{aq},\ H^\bullet,\ OH^\bullet,\ H_2O_2,\ H_2,\ H_3O^+, \ldots s \quad (1)$$

$$Ag^+ + H^\cdot \rightarrow Ag^0 + H^+ \quad (2)$$

$$nAg^0 \rightarrow AgNPs \quad (3)$$

Although the obtained AgNPs have the best shape and small size, the fabrication process must use different stabilizers[34-37,40,41] and the maximum value of the UV-Vis spectrum ranges from 405.5 to 41.8 nm. With the advantage of using available equipment, the process of technology is not complicated and can prepare a large amount of AgNPs solution, so the cost will be more reasonable, but the resulting solution still has a large amount of NO_3^- ions, as well as other stabilizers and by-products, the field of application is only suitable for environmental remediation.

2.2. Chemical methods

2.2.1. Reducing agents

The chemical method of preparing AgNPs solution is to follow the principle from the “bottom-up” to create nanoparticles from the Ag^+ ions of silver salts by reducing the

reduction process.[42] The commonly used silver salts are $AgNO_3$ and the reducing agents that have been used very different such as glucose ($C_6H_{12}O_6$),[43,44] sacarose ($C_{12}H_{22}O_{11}$),[45] hydrazine (N_2H_4),[46-48] ethylene glycol ($C_2H_6O_2$), ethanol (C_2H_5OH), aniline ($C_6H_5NH_2$),[49] sodium citrat ($Na_3C_6H_5O_7$),[46,50-53] hydrogen (H_2),[52] sodium borhydird ($NaBH_4$).[53-57]

Table 1. Reducing and reactions to create AgNPs.

Reducing agent	Reaction equation	Size, nm	Ref
$C_6H_{12}O_6$	$C_6H_{12}O_6+2Ag^+ + 2OH^- \rightarrow 2Ag^0+C_6H_{12}O_7+H_2O$ (4)	20.80 sphere	44
N_2H_4	$4AgNO_3+N_2H_4+4NaOH \rightarrow 4Ag^0+N_2+4NaNO_3 + 4H_2O$ (5)		48
N_2H_4	$4AgNO_3 + N_2H_4 \rightarrow 4Ag^0+N_2+ 4HNO_3$ (6)	8-50 sphere	46
RCHO	$2AgNO_3+RCHO+2NaOH \rightarrow 2Ag^0+ RCOOH+ 2NaNO_3 +H_2O$ (7)	10-250	49
$C_6H_5NH_2$	$C_6H_5NH_2+AgNO_3\rightarrow Ag^0+ C_6H_5NH_2NO_3$ (8)	10-30	49
$C_6H_5O_7Na_3$	$4AgNO_3+C_6H_5O_7Na_3+ 2H_2O \rightarrow 4Ag^0+C_6H_8O_7+ 3NaNO_3+ HNO_3 +O_2$ (9)		50
$NaBH_4$	$AgNO_3 + NaBH_4 \rightarrow Ag^0 + 1/2H_2 +1/2B_2H_6 + NaNO_3$ (10)	10-80	54-57
$NaBH_4$	$AgNO_3 + NaBH_4 + 3H_2O \rightarrow Ag^0+7/2H_2 + B(OH)_3 + NaNO_3$ (11)	30-40	58

Table 1 presents the reaction equation to form AgNPs with a number of different reducers. To ensure the reduction process is completely done, the reducing agent usually has many times compared to silver salt. From the reactions in Table 1 it can be seen that in addition to the spherical silver nanoparticles after the reaction, there are ions of silver salt such as NO_3^-, Na^+, the products of reducing agents and stabilizers are added. Removing these Na^+ and NO_3^- ions to obtain pure AgNPs is very dificult and expensive and also changes the properties of AgNPs. Therefore, products containing ions are only applied in areas that do not require high purity of AgNPs.

Table 1 also shows that nanoparticles are obtained as a wide area, so it is necessary to use stabilizers to control the size of nanoparticles as desired. From Table 1, the reducing reaction mechanism according to different authors[54-58] is also different. It means that the substances in AgNPs solution after the reaction will also vary, for example, $NaBH_4$ reduction reaction (10) creating B_2H_6[54-57] gas will escape from the solution and if the reaction (11) quantity H_2 gas from the solution is 3.5 times higher than (10).[58]

2.2.2. Stabilizers

The process of creating a silver nano colloidal solution with reducing agents that always exists in the system with ions and reducing agents, so silver colloids can be formed according to the equation:

$$2Ag^+ + 2OH^- \rightarrow Ag_2O + H_2O \quad (12)$$

$$Ag_2O + R\text{-}CHO \rightarrow 2Ag^0 + R\text{-}COOH \quad (13)$$

$$nAg^+ + nNaBH_4 \rightarrow nAg^0(BH_4^-)_x + nNa^+ \quad (14)$$

and simulated as shown in Figure 2.[44,54]

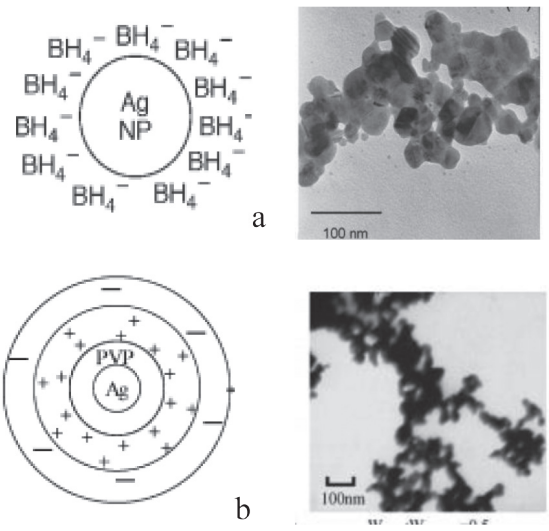

Figure 2. AgNPS colloidal seeds and stamp images made up of $AgNO_3$ chemical reduction with reducing agents: a) $NaBH_4$,[44] b) R-HO with PVP.[54]

In order to control the size and shape of AgNPs in the colloidal solution, it is not

https://doi.org/10.52111/qnjs.2024.18101

formed into a large particles, stabilizers are high molecular compounds or surfactants added to the chemical reaction.[59-61] Stabilizers often have functional groups, dissolve well in the reaction environment, good compatibility or high biological activity, non-toxic and biodegradable ability.[62] Table 2 is about presentation of some stabilizera often used for chemical manufactoring of AgNPs such as: chitosan,[62-67] PVA,[68,69] PVP,[51,59,70] ...

Table 2. Stabilizers often used in the process of chemical manufactoring of AgNPs.

Stabilizers	Chemical formula	M_{ever}, g/mol	Ref.
Chitosan poly β(1,4)D-glucosamine cation	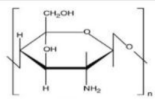	3,800-20,000	66
PVP polyvinyl-pyrrolindone	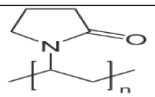 $(C_6H_9NO)n$	40,000	59
PVA poly vinyl alcohol	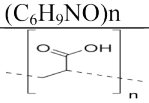 $(C_2H_4O)n$	85.000	
PAA polyarcrylic acid	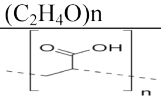 $(C_3H_3NaO_2)n$	15,000	
PAH poly allylamine hydrochloride	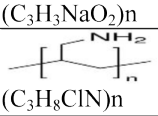 $(C_3H_8ClN)n$	15,000	
CMC carboxymethyl cellulose	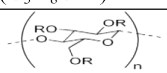 $C_{28}H_{30}Na_8O_{27})n$	90,000	
NaDDBS Surfactnts (anion)	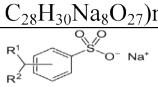 $C_{18}H_{29}SO\,Na$	348	
SDS Surfactants (anion)	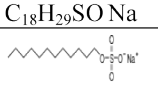 $C_{12}H_{25}SO_4Na$	288	
TW80 Surfactants (neutral)	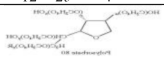 $C_6H_{124}O_{26}$	1,310	
CTAB Surfactans (cation)	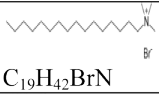 $C_{19}H_{42}BrN$	365	
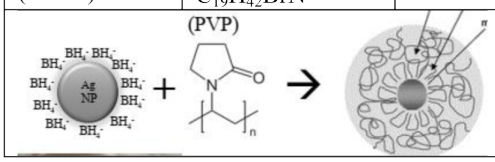			

From Table 2, stabilizers can be found with electrical charge groups of straight or cyclic circuits, that can orient the adsorption on the AgNPs core to form a micell or reverse micell with the corresponding charge to combat flocculation of the colloidal system[71,72] so that the stabilizers with the appropriate nature and concentration will control the size and shape of the AgNPs colloid as well as the characteristics of AgNPs as desired.

2.2.3. Silver nanocomposite

Fabrication of silver nanocomposite with chemical reducing processes will diversify AgNPs carried materials for applications in life. Composite materials carried AgPNs are usually studied as polymers PP, PET, Nylon, PC, ABS,[73,74] PU,[75] PE,[76] ceramic, pottery,[77-79] glass,[80] fabric, fiber,[81-83] paint.[84-85] Common manufacturing methods are dispersed AgNPs made by chemical methods in materials, but can also be made *in-situ* from $AgNO_3$ with reducing agents in the material during the processing ceramics, fabric or polymers.[86-88]

2.3. Biological method

2.3.1. Microorganism

The biology method uses bacterial microorganisms, yeast, mushrooms, molds as $AgNO_3$ silver-deducted agents into metal silver and AgNPs[89-91,119] microorganisms using silver salts as nutrients to survive and develop as described in Figure 3.

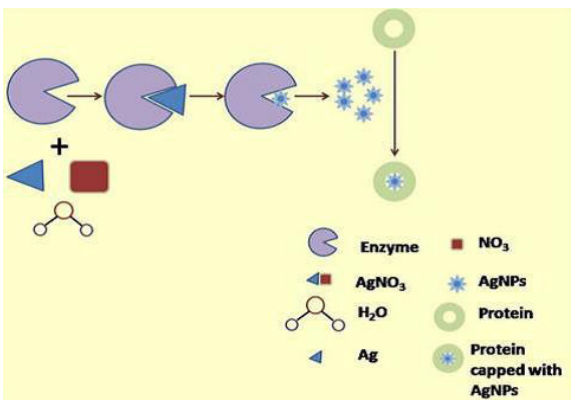

Figure 3. Microorganisms use Ag^+ as a nutrient and reduce it to AgNPs.[91,119]

From Figure 3 it can be seen that the protein can act as a stabilizer to control the size of AgNPs. There are many types of microorganisms studied and used to make AgNPs from $AgNO_3$ which are presented in Table 3.

The results from Table 3 show that microorganisms can reduce $AgNO_3$ salts to AgNPs with characteristic UV-Vis wavelengths from 380 to 460 nm and average particle sizes less than 100 nm. The special thing is that AgNPs products are stabilized with stable proteins for more than 6 months, so there is no need for stabilizers. However, the ions of $AgNO_3$ salt are still present in the reaction product, so the purity of AgNPs is not enough for application in the field of medicine.

Table 3. Particle size, characteristic UV-Vis spectra and references of some typical microorganisms using AgNPs preparation.

Microorganism	Size/UV, nm	Ref.
Enterobacteria	52.5 / 420-430	92
Rhodopseudomonas palustris	5-20 / 420-460	93
Rhodobacter Sphaeroides	9.56 / 420	94
vibrio alginolyticus	75 / 420	95, 96
Halococcus salifodinae BK6	50.3 / 380-440	97
Bacillus	42-94 / 450	98
Euplotes focardii	20-70 / 420	99
Haloferax	27.7 / 458	100
Verticillium (fungus)	25 / 420	101
Aspergillus fumigatus	5-25 / 420	102
Penicilium	5-25 / 430	103

2.3.2. Extraction solution – green chemistry

Humans develop in association with the plant environment and often use many types of plants for food or medicine, so using plants in the preparation of AgNPs is also a method with many advantages in terms of extremely rich raw materials, environmentally friendly and low cost. Therefore, the method of preparing AgNPs by plant extracts has been studied all over the world such as USA,[104] China,[105] India,[106] Germany,[107] Africa[108] and Vietnam.[109] Water extracted from parts of plants such as leaves,[110] roots,[111] bark,[112] tubers,[113] flowers,[114] fruits[115] can all be used to prepare AgNPs. Table 4 presents extracts of some plants used to prepare AgNPs. Using plant water extract as $AgNO_3$ reducing agent to prepare AgNPs does not need to use more stabilizers, but the product is still available with NO_3^- ions and reducing products, so it also limits the application field.

Table 4. Extracts of some plants used to prepare $AgNO_3$.

The plants	Science name	Part	Ref.
Geraniums	*pelargonium graveolens*	Flower	104
Cordyceps	*Cordyceps militaris*	Total	105
Mud	*Brillantaisia patula, Crossopteryx febrifuga and Senna siamea*	Tree and leaves	108
Soybean	*soymida febrifuga*	Total	110
Carrot	*D. carota*	Tubers	111
Dill	*Syzygium cumini*	Total	112
Turmeric	*Curcuma Longa*	Tubers	113
Hibiscus	*Hibiscus Rosa*	Flower	114
Papaya	*Papaya*	Fruit	115
Basil	*Ocimum santum*	Total	117
Ginger	*Zingiber oficinale*	Total	123
Tea	*Camellia sinensis*	Leaf	125
Sinus	*Azadirachta indica*	Leaf	124

https://doi.org/10.52111/qnjs.2024.18101

Sesame oil (castor oil)	*Jatropha curcas*	Total	126
Euphorbiaceae	*Acalypha Indica*	Total	135
Mint	*Mentha piperita*	Total	122
Chrysanthemum	*Stevia rebaudiana*	Total	134
Amaranthaceae	*Chenopodium album*	Total	120
Fabaceae	*Casia fistula*	Total	133
Terminalia	*Terminallia chebula*	Leaf	118
Cinnamon, Camphor	*Cinnamomum camphora zeylanicum*	Bark	121
Garlic	*Allium sativum*	Total	127
Curry patta	*Murraya koenigii*	Leaf	132
Lemon basil	*Coleus amboinicus*	Total	131
Alfalfa	*Medicago sativa*	Total	130
Oranges, Lemons	*Citrus sinensis*	Total	128
Lemongrass	*Lemon grass*	Total	119
Bình bát	*Coccinia grandis*	Leaf	129
Combretaceae	*Terminalia catappa*	Leaf	128
Aloe vera	*Aloe vera*	Leaf	116
Lime tree	*Robustra*	Leaf	109

From Table 4, it can be seen that plants from all continents of the world are food sources and spices such as oranges, lemons, papayas, sesame, basil to pharmaceuticals such as cinnamon, garlic, lemongrass, and cordyceps as well as wood-bearing trees such as neem tree, etc., which can be extracted using water containing $AgNO_3$ desalting agents into AgNPs. Common reducing agents in plant extracts are flavonoids, terpenoids, polyphenols, alkaloids, glucose which are compounds having carbonyl and hydroxyl groups or amine groups.[136]

2.4. Electrochemical method

2.4.1. Role of electrolyte

The electrochemical method in the field of Physical chemistry can perform a top-down process by oxidizing the metal silver anode in the electrolyte into Ag+ ions with electrode potential value +0.799 V:[137]

$$Ag \rightarrow Ag^+ + e \quad (15)$$

Simultaneously combined with the cathode reaction to reduce silver ions from the electrolyte to form silver nanoparticles, performing the bottom-up process: [138-142]

$$Ag^+ + e \rightarrow Ag^0 \quad (16)$$

$$nAg^0 \rightarrow AgNPs \quad (17)$$

It is also possible to perform the preparation of AgNPs by simply reducing the reaction on the cathode (16) with $AgNO_3$ salt dissolved in the electrolyte solution and an inert anode such as Pt.[143,144] To control the size of AgNPs obtained at the cathode, it is possible to use electrochemical parameters such as voltage, current density, conductivity as well as supporting measures such as pulses, ultrasound or will even produce strong gas release on the electrode at a higher voltage than conventional water electrolysis. With the usual electrochemical method, the electrolyte or anion NO_3^- of $AgNO_3$ still exists in AgNPs products, so it also limits the application field.

2.4.2. Role of applied voltage

Electrode reactions can occur in a non-electrolyte medium such as double distilled water with very low conductivity but the voltage must be sufficiently high[138,139,141] or very high.[145-149] There are two typical electrode arrangements in the electrochemical reactor when using high voltage (Figure 4).

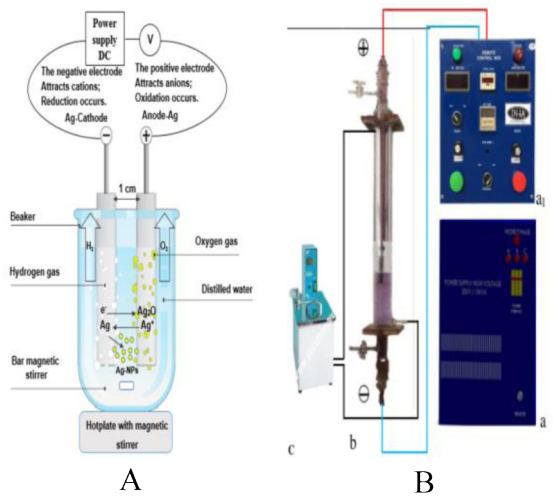

Figure 4. a) the cathode is parallel to the anode,[140] b) the bottom cathode is far from the upper anode146.[148]

With high DC voltage the potential drop across the electrodes will still be greater than the decomposition potential of water as well as the equilibrium electrode potential of Ag and the electrochemical oxidation on the anode to form Ag^+ ions as the reaction (15) as well as water is electrochemically decomposed to form O_2:

$$2H_2O - 4e \rightarrow O_2 + 4H^+ \qquad (18)$$

At the same time on the cathode, the water will also be decomposed to form H_2 gas that escapes strongly towards the anode as shown in Figure 4b:

$$2H_2O + 4e \rightarrow H_2 + 2OH^- \qquad (19)$$

Due to the strong escaping gas covering the cathode surface, the amount of Ag^+ ions generated from the anode moves slowly due to poor conductivity, so it is difficult to reach the cathode to carry out the reaction (16). Therefore, the process of reducing Ag^+ to Ag^0 and then to AgNPs according to (17) will be carried out with new H_2 atoms generated from the cathode and dispersed into the solution:

$$2Ag^+ + H_2 \rightarrow 2Ag^0 \qquad (20)$$

Figure 5 shows the process of generating AgNPs by H_2 generated from the cathode by electrochemical reaction from high voltage. Figure 5a shows that the color of distilled water is transparent, but after 3 minutes of reaction, H_2 gas escaping from the cathode turned white (b), and after 15 minutes of reaction, AgNPs formed turned dark color from the cathode side (c) and after 30 min the color of AgNPs occupied the entire reaction vessel (d).

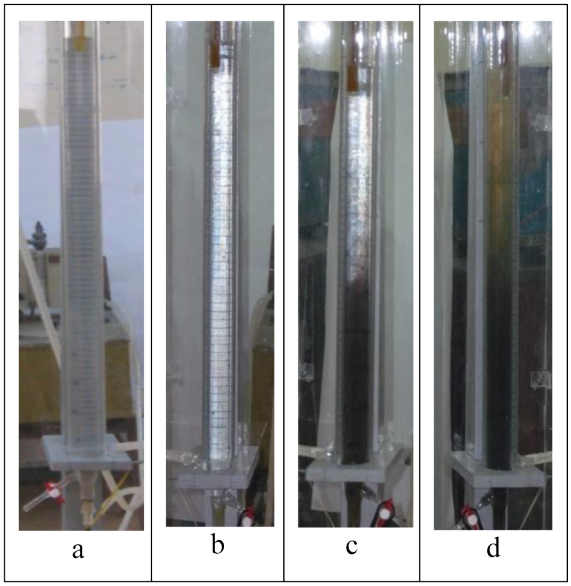

Figure 5. AgNPs generation process by high voltage electrochemical reaction.

With the method of electrochemical manufactoring AgNPs by high voltage DC in distilled water with Ag electrode, the obtained product still has a spherical shape, size smaller than 100 nm with UV-Vis spectrum at about 420 nm and the ability to kill all kinds of bacteria very good. However, the zeta potential is opposite in sign to the chemical method and has a high value, so there is practically no need to use a stabilizer. The conductivity of colloidal solutions is very small because there are no ions of the reactants, so the high purity is suitable for applications where only AgNPs are required.

2.5. Plasma method

Plasma is the fourth state of matter, the ionized state is changed from a gaseous state when further energized.[150] Unlike high-temperature plasma which produces a fully ionized state with only electrons and ions, low-temperature plasma ionization process only partially contains not only electrons, ions but also atoms, neutral

https://doi.org/10.52111/qnjs.2024.18101

molecules and radicals and is being applied in many fields of science, technology and life.[151] The cold plasma state is also used for the preparation of AgNPs by the reduction of $AgNO_3$ by free electrons or hydrogen atoms generated by plasma according to the reaction (16) or (20).[152-154] Figure 6 shows the plasma generation methods for the preparation of AgNPs.[152,153,155]

From Figure 6 it is shown that the gaseous medium can be used either by air on the surface (Figure 6A,b) or by blowing air between the two electrodes (Figure 6a and b) or by the ARC arc generating steam (Figure 6c).

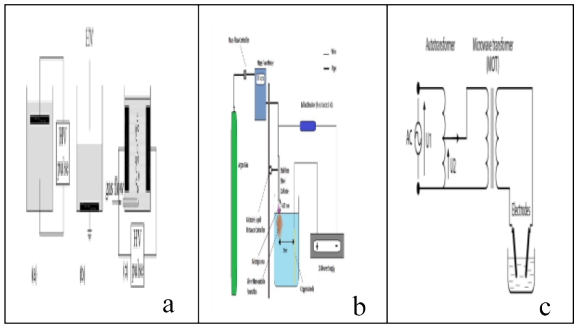

Figure 6. Principle of plasma generation for the preparation of AgNPs.

The plasma generation process uses electrodes and electrochemical reactions to create a gaseous environment when the electrodes are arranged as shown in Figures 4b and Figures 5 or Figure 6a, so the plasma method can also be considered as an electrochemical method with high voltage. In the plasma state, the water will be decomposed on the electrodes to create a large amount of gas that does not obey Faraday's electrochemical theorem as well as ionization reactions to create atoms, molecules and radicals:[152]

On the cathode: $2H_2O \rightarrow 2H_2 + O_2$ (21)

On the anode: $4H_2O \rightarrow O_2 + 3H_2 + H_2O_2$ (22)

$H_2O + e \rightarrow H^{\bullet} + OH^{\bullet}$ (23)

$H^{\bullet} + H^{\bullet} \rightarrow 2H$ (24)

$OH^{\bullet} + OH^{\bullet} \rightarrow 2H_2O + 2O$ (25)

$OH^{\bullet} + OH^{\bullet} \rightarrow H_2O_2$ (26)

$OH^{\bullet} + H_2O_2 \rightarrow HO_2^{\bullet} + H_2O$ (27)

$H_2O + e \rightarrow H_2O^{\bullet}$ (28)

$H_2O^{\bullet} + H_2O \rightarrow H_2O + H^{\bullet} + OH^{\bullet}$ (29)

$H_2O^{\bullet} + H_2O \rightarrow H_2 + O^{\bullet} + H_2O$ (30)

$H_2O^{\bullet} + H_2O \rightarrow 2H^{\bullet} + O^{\bullet} + H_2O$ (31)

UV rays in the presence of plasma also contribute to the radical reaction:

$H_2O_2 + hv \rightarrow 2OH^{\bullet}$ (32)

The reactants generated from the plasma medium can participate in the formation of AgNPs in addition to the reactions (16) and (20):

$2Ag^+ + 2OH^- \rightarrow Ag_2O + H_2O$ (33)

$2Ag^+ + O_2 \rightarrow Ag_2O_2$ (34)

$Ag_2O + H_2 \rightarrow 2Ag^0 + H_2O$ (35)

$Ag_2O + H_2O_2 \rightarrow 2Ag^0 + H_2O + O_2$ (36)

$Ag_2O + H_2O_2 \rightarrow Ag_2O_2 + H_2O$ (37)

$Ag_2O_2 + 2H_2 \rightarrow 2Ag^0 + 2H_2O$ (38)

Figure 7 presents the process of generating AgNPs by high-voltage DC with the contribution of electrochemical plasma, showing that after the time of gas generation from the electrochemical reaction (Figure 7a), an anodic electrochemical plasma will appear after 15 minutes (Figure 7b) and the light yellow AgNPs color appearing from the anode towards the cathode gradually darkens over time of 23, 26, 35 min, respectively with Figures 7c, 7d and 7e.

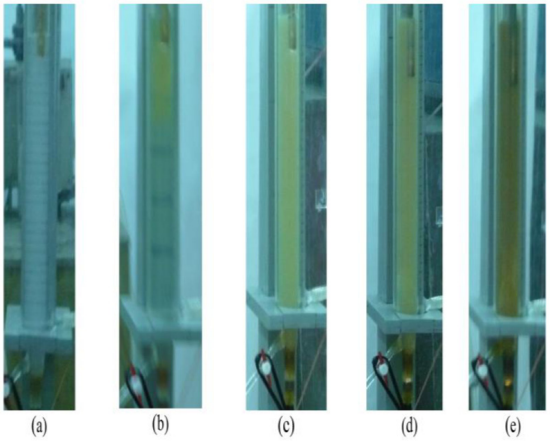

Figure 7. The process of generating AgNPs by high voltage DC with the contribution of electrochemical plasma.

The process of creating Ag_2O and Ag_2O_2 intermediates besides Ag^0 due to the presence of O_2, OH^-, $OH^•$, H_2O_2 agents, etc. in the electrochemical plasma environment has created a yellow color before turning black.[156] By Ronghen, EDX and XPS spectra also demonstrated the presence of O in AgNPs accounting for 5.77 ÷ 9.6% and also increased the bactericidal efficiency of AgNPs.[157-160] Similar to the method of preparing AgNPs by High voltage DC, electrochemical plasma contribution will create the ability to increase the speed, product concentration as well as the ability to kill bacteria, although there is a small amount of Ag_2O or Ag_2O_2, but it does not affect the purity of the product.

3. CHARACTERISTICS OF NANOSILVER

3.1. Silver nanoparticles

The characteristics of shape and size of AgNPs were determined by imaging methods by electron microscopy SEM, TEM, FE-TEM. Particle size distribution was determined by statistical particle counting software from SEM or by Laser Scattering Particle Size Distribution Analyzer. Figure 8 presents TEM images of AgNPs shape and size (a) as well as particle size distribution from TEM (b) and laser determination (c). Figure 8 shows that AgNPs prepared by different methods all have near-spherical shape but different sizes in the nanometer region with Gaussian distribution as determined by laser method.[154,158,161]

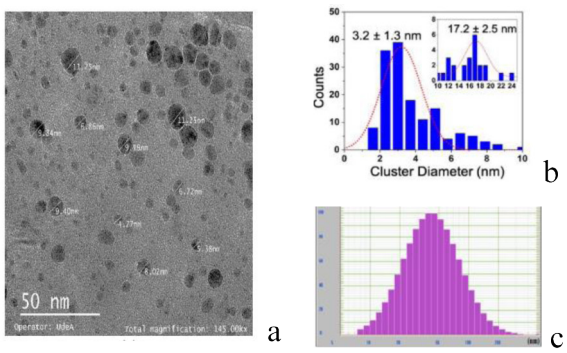

Figure 8. (a) TEM image of AgNPs, (b) particle size distribution counted from TEM image and (c) laser particle size distribution analysis.[154,158,161]

X-Ray,[162] XRD,[153] XPS[142,152] methods are also used to further investigate the properties of AgNPs particles in terms of phase, ratio of elements or ions: $Ag/Ag^+/O$, contributing to a better understanding of state of AgNPs in solution.

3.1.1. Color

Figure 9 presents AgNPs products prepared by different methods such as: a) chemical,[54] or b) plasma.[155]

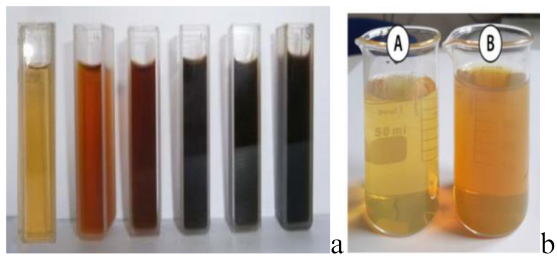

Figure 9. Color of AgNPs colloid a) chemically prepared,[54] b) by plasma at different times and concentrations.[155]

The AgNPs products obtained are all true solutions in the state of a transparent colloidal system with color from light yellow to brown or black depending on the concentration and preparation time, while the colorless solution will have no AgNPs.[163]

3.1.2. UV-Vis and zeta potential

The AgNPs colloidal solution has the important properties of UV-Vis plasmon spectrum and zeta potential. Figure 10 shows the UV-Vis spectrum,[164] zeta potential and colloidal particle distribution.[155]

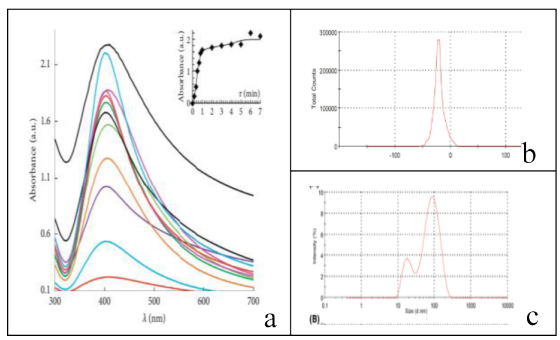

Figure 10. UV-Vis spectrum (a), zeta potential (b) and colloidal particle size distribution and (c) of AgNPs colloidal solution.

https://doi.org/10.52111/qnjs.2024.18101

From Figure 10a, the UV-Vis spectrum can be found of the AgNPs colloidal solution that has a range of 400 nm and increases the height when the concentration or reaction time increases and the location is moved when the acacia grain nature is essentially affected. Figure 10b shows that the Zeta value is about -22.31 mV, proving that the surface of the AgNPs colloidal particles is positive and Figure 10c shows that the colloidal particles size is distributed from 20 to 90 nm. Therefore, Zeta is the diffusion layer, the surface of the colloidal particles should be dependent on the environment and charge of the AgNPs particles surface with values that change from yin and yang, but the absolute value is greater than 20 mV, the colloidal system will be durable over time. Table 5 presents the zeta value of AgNPs colloidal solutions with different stabilizers.[60,66,139,159]

Table 5. The zeta value of some stabilizers.

Stabilizer	Chemical formula	mW, g/mol	ζ, mV
NaDDBS	$C_{18}H_{29}SO_3Na$	348	5 ÷ -30
SDS	$C_{12}H_{25}SO_4Na$	288	-2 ÷ -20
TW80	$C_{64}H_{12}4O_{26}$	1310	4 ÷ -15
CTAB	$C_{19}H_{42}BrN$	365	20 ÷ -30
PVP	$(C_6H_9NO)n$	40000	0 ÷ -25
PAA	$(C_3H_3NaO_2)n$	14000	5 ÷ - 25
PAH	$(C_3H_8ClN)n$	15000	5 ÷ 20
CMC	$(C_{28}H_{30}Na_8O_{27})$	90000	0 ÷ -10
Chitosan	$(C_6H_{11}NO_4)n$	20000	50 ÷ 70
PP SH[165]	*Entada spiralis*	Chiết	-80,7
PPĐH[139]	DC 25 kV	Ag	-(27 ÷ 39)
PPPL[159]	ARC discharge	Ag	-(40 ÷ 70)

Table 5 shows that the value of zeta is very dependent on the nature of stabilization of chemical structure, weight, electronegativity,[66,67] as well as depending on the modulation method and composition of ions that exist in glue solution.

3.1.3. Conductivity and pH

Because Ag^0 or AgNPs silver particles are dispersed in water environments, it is impossible to conduct electronic conduct as metal as well as ionic forms like electrolyte solution. However, while using $AgNO_3$ in the methods as well as reducing the ionic amount of: NO_3^- as well as the reducing agent: Na^+ or the products of the reducing agent will create the conductivity of the AgNPs solution. Moreover, AgNPs colloidal seeds adsorb ion and create charge.

Table 6. Electrical conductivity (χ, mS/cm) and pH of AgNPs solution are prepared by chemical and electrochemical methods.

Chem	*c*, ppm	RO	100	200	300	500
	χ, mS/cm	0,01	0,27	0,36	0,46	0,58
	pH	6,9	4,6	4,9	4,4	4,5
Electr	*c*, ppm	NC	109	185	285	411
	χ, mS/cm	0,003	0,08	0,07	0,07	0,07
	pH	6,9	6,64	5,63	5,78	5,79

Table 6 also shows that with the methods using of $AgNO_3$, conductivity levels increases when the concentration increases, but the methods of electrochemical or plasma use the silver electrode, the conductivity is small and has almost no change, even when the synthesis time as well as when the concentration increases.[166]

3.1.4. Concentration of AgNPS

Determining the concentration of AgNPs is not as simple as determining the concentration of soluble substances because it is difficult to separate between silver nano and ionic. With AgNPs synthesis methods by using $AgNO_3$ often think that the process of reaction completely and the AgNPs concentration is also considered as $AgNO_3$ concentration. The AAS method transfers AgNPs to Ag^+ so it cannot be determined by the nano form. With the methods of using Ag metal, it is possible to determine by soluble silver weight ($c_{\Delta m}$) with the assumption that silver is

soluble for formation of AgNPs.[167] It can also determine the amount of AgNPs by adjectives The amount of electricity according to the law of Faraday ($c_{Far.}$), but besides the dissolving process, there are other electrochemical processes, so the concentration of Faraday's law is usually larger than the amount of soluble metal ($c_{Far.} > c_{\Delta m}$).[139] The AAS method can also be used to determine the AgNPs concentration of the electrochemical and plasma modulation methods, but it cannot be separated from Ag^+. The UV-Vis spectroscopic method for the determination of AgNPs alone would be the most accurate, but standard curve construction is not feasible because standard solutions are difficult to obtain.

3.2. Antibacterial ability

3.2.1. Traditional

Since BC, silver's bactericidal properties have been used for prevention and treatment of diseases such as: acupuncture needles, containers for liquids and drinking water for the prevention and treatment of infections. Former feudal dynasties in many countries around the world used spoons, knives, bowls and plates in eating and drinking to kill pathogens to ensure life safety. Silver has also been used for a long time in dentistry, to treat neurological diseases, eye diseases, to treat wounds, and to disinfect drinking water systems. During the World Wars, colloidal silver was used to fight gastrointestinal diseases and infections. From the late 19th century to the present, colloidal silver has been used quite widely in the form of oral and injectable drugs to treat arthritis, bronchitis, respiratory, lung, influenza as well as gastrointestinal diseases, stomach ulcers or Disinfection of purulent-necrotic burn wounds, dermatosis, boils or even syphilis, mastitis, meningoencephalitis, vestibular,...[168]

3.2.2. Outstanding antibacterial properties

Elemental silver has outstanding bactericidal ability because Ag^+ ions exist in the form of salt.[163] In the form of AgNPs, with extremely large contact area, it is easy to provide Ag^+, so the bactericidal efficiency is improved many times. Although there is still no consensus, the bactericidal mechanism of Ag^+ aligned with 3 possibilities: (1) Destruction of the function of the cell wall; (2) Destruction of respiratory function due to inactivation of -SH group in O_2 transporter; (3) Destruction of DNA function by dimerization of pyridine interferes with DNA replication of bacterial cells. In addition, atomic oxygen is produced from the reaction:

$$2Ag^+ + O^{2-} \rightarrow 2Ag^0 + O^0 \qquad (39)$$

It also inhibits the growth of bacteria. Furthermore, the plasmons of AgNPs are susceptible to thermogenesis and destruction of bacteria. Because of many different ways to kill bacteria, the bactericidal ability of AgNPs cannot be greasy or resistant like current antibiotics.

3.2.3. Antibacterials

Unlike antibiotics that are only suitable for bacteria, AgNPs can kill up to 650 types of bacteria, gram negative and positive as well as viruses and fungi, mold.[168-170] Recent studies have shown AgNPs have remarkable anti-inflammatory and antiviral potential, even against viruses such as HIV[171,172] or Sars corona,[173,174] Monkeypox,[175] Hepatitis B,[176] Syncytial,[177] Herpes,[178] Tacaribe,[179] West Nile, Hanta, Nipah, Hendra, Chikugunya, as well as viruses of avian origin and pig.[173,180]

3.2.4. Toxicity

The toxicity of silver and silver ions has been of concern for a long time due to the phenomenon of blue skin when the amount of silver accumulates and has not been eliminated in time.[180] With its small size, it is dispersed in gaseous and liquid environments and solids when used, AgNPs also easily penetrate into the body and accumulate in cells through the respiratory tract,[181] esophagus or skin contact.[182] Therefore, the toxicity of AgNPs is also very noticeable.[183,184] Although AgNPs are not as toxic as ions, AgNPs still generate ions[185] from AgNPs and accumulate in organs such as lungs,[186] liver, and spleen[187] and cause harmful effects depending on the time and concentration of exposure[188] as well as the size. and the shape of AgNPs.[189]

https://doi.org/10.52111/qnjs.2024.18101

4. APPLICATIONS

4.1. In chemistry

Silver metal as well as silvernano are applied due to its properties such as absorption and optical control, bactericidal, electrical and thermal conductivity, and especially as a catalyst for some reactions as well as as a sensor in analysis in chemistry.[190]

4.1.1. Catalysis

The reduction of oxygen of epoxides to alkenes catalyzed by AgNPs can be 99% as efficient as using Au or AuNPs.[191] AgNPs are used as catalysts for the reduction reactions of nitro aromatic compound,[192] carbonyl as well as oxidation of alcohols, silanes, olefins, alkylation of amines and arenes as well as ring-opening or closing reactions and a variety of value reactions.[193] AgNPs are used as homogeneous or heterogeneous catalysts to synthesize many special chemical compounds with high efficiency such as:[194] pyrimido 96%, triazole 98%, pyrano 96%, isoxazole 93%, quinoline 88%, tetrazole 93%, benzopyranopyrimidine 95%, bivalent amine 92% , etc.

4.1.2. Analysis

With advantages in size, shape and surface, silver nanomaterials also play an important role in determining and controlling electrical, optical, physical and especially chemical properties. With the GC electrode combined with AgNPs, it is possible to have excellent electrocatalytic activation as a sensor for determining H_2O_2 in water with a concentration of 0.92 µM.[195] With different techniques, it is possible to fabricate the mounted electrode. AgNPs for performing cyclic voltammetry CV, differential voltammetry DPV, linear sweep voltammetry LSV, square wave voltammetry SWV analyzes with up to the limit of ppb detection of various organic compounds.[196] Especially, it has advantages in detecting chemical contamination in the state of the environment, so the number of publications by 2022 has been increasing rapidly.[197]

4.2. In environmental treatment

The excellent bactericidal ability of AgNPs has been applied to environmental treatment mainly in three directions as surface disinfection, water disinfection and air sterilization.[198]

4.2.1. Contact surface

Contact with material surfaces is the most frequent activity, so the antibacterial properties of AgNPs are also studied for applications in construction materials, fabrics or plastic tools. Interior paints with additive AgNPs 0.1 ÷ 0.5 ppm have good antibacterial effect.[199] Glass surface coated with AgNPs not only has bactericidal value but also has plasmon effect to increase absorption capacity energy.[200] Plastic coated with AgNPs has many useful applications in medical transmission materials, in food packaging and preservation,[201-203] as well as export tropical fruits.[204-206] Fabric fibers surface coated with AgNPs with the amount of 180 mg/kg have a bactericidal effect of 99.28%, even after 30 washing cycles it is still 98.77%.[207]

4.2.2. Water treatment

Water is necessary for the life of all things. Humans use water for all living activities as well as production, so they need clean water, but it is easy to pollute water sources with different wastes.[208] AgNPs with special chemical and biological properties should be noticed. It is intended for use in environmental treatment systems including water.[209] The European Union alone uses up to 20.5 tons of AgNPs to treat wastewater each year.[210] Effects of AgNPs in water treatment not only in the ability to kill bacteria but also in the chemical reaction ability[211] as well as sensor application to control water pollution.[212] In aquaculture, seafood AgNPs have also been used in water treatment to reduce pollution, infection as well as prevention of network diseases so as to have high economic efficiency.[213-215]

4.2.3. Air handling

The excellent bactericidal effect of AgNPs has also been studied for application to air

https://doi.org/10.52111/qnjs.2024.18101

purification. By depositing AgNPs into a porous quartz tube fitted with an air purifier with a capacity of 250 m^3/h, it is possible to both process organic compounds up to 91.6% butanol, 80% acetone, and 70.1%, diethyl ether and 43% benzene as well as 99% bacteria and fungi and installed for E Hanoi hospital.[216] The air conditioning system combined with AgNPs to improved heat transfer ability saved energy on average 36 - 58%.[217] However, when using AgNPs to treat air pollution, great care must be taken to limit the dispersion of AgNPs into the air so as not to cause inflammation of the respiratory system.[218] Therefore, the concentration of AgNPs to spray in the air should also be kept to a low level and avoid long exposure times.[219]

4.3. In nanomedicine

AgNPs are widely used in many biomedical applications, known as nanomedicine including diagnostics, therapeutics, drug manufacturing, medical device coating, and personal healthcare. With increasing applications in medicine, a better understanding of the mechanisms is becoming necessary.[220]

4.3.1. Disinfectant

Because the hospital environment needs to be clean, the special antibacterial ability of AgNPs is noticed as a disinfectant agent for the environment as well as tools. The MBC concentration of AgNPs for hospital bacterial strains such as S. Aureus or P. Aeruginosa in the operating room after 20 minutes is 100 µg/mL and after 24 hours it is 12.5 µg/mL.[221] Fluid pathways or medical instruments are also tested for emergency disinfection with AgNPs.[201] Even the air in hospital rooms can be treated with contamination by bacteria as well as organic substances with AgNPs.[215]

4.3.2. Diagnose

Silver nanoparticles are used in imaging diagnosis and treatment of dental and oral cancers, acting as a carrier to disperse to targets along with chemotherapy agents and as radiation and phototherapy enhancers. It is valuable for studying inflammation, tumors, immune responses, and the effects of stem cell therapy, in which contrast agents are conjugated or surface-modified and bioconjugated to particles. nano. Silver has an important role in imaging systems with plasmonic properties that should produce a clearer image.[222,223] Due to the reaction of AgPs with oxygen (ROS) of cancer cells, AgNPs have the effect of controlling and destroying DNA, contributing to the formation of nano cancer diagnosis and treatment in nano medicine.[224,225]

4.3.3. Healing

The advantage of AgNPs is that they can kill many types of bacteria[171-180] and are not resistant to drugs like antibiotics,[226] so special attention is paid to exploiting them to treat diseases. Disinfecting all types of open wounds[227] especially in the treatment of burns[228] or teeth and mouth[229] with AgNPs not only heals the wound quickly but also leaves almost no scars after healing. With infectious diseases such as HIV, hepatitis, SARC, and chickenpox, injections with a concentration of 20 ppm of 10 nm AgNPs have achieved good curative effects.[230] Because cancer is currently an incurable disease, AgNPs have also been researched and applied and found that cancer cells have been inhibited by AgNPs from proliferating as well as angiogenesis due to the destruction of living and proliferation conditions.[231] Furthermore, AgNPS particles have the ability to absorb heat, so they can use energy from the laser source to kill cancer cells.[232]

5. CONCLUSION

Silver nano is prepared by chemical, physical, biological and physicochemical methods. Raw materials for the preparation process are $AgNO_3$ salt and reducing chemicals such as $NaBH_4$, citrate salt, plant water as well as reducing microorganisms, or activating rays that create reducing properties of the solution such as γ. It is also possible to use Ag to disperse by laser or dissolve the anode into ions and then reduce it to form AgNPs. The appropriate purity for different practical applications of AgNPs products

https://doi.org/10.52111/qnjs.2024.18101

depends on the method and materials used. Pure AgNPs solution is prepared by high-voltage electrochemical method or electrochemical plasma method because it only uses Ag and distilled water.

The basic characteristic of AgNPS is that the nanoparticle has a nearly spherical shape, the size is in the nanometer range and the UV-Vis spectrum is in the range of 420 nm with the height depending on the concentration and the pH value depending on the size. The zeta potential has an absolute value of ≥ 20 mV, which characterizes the stability of the silver nano colloid solution, then the negative or positive value depends on the method and the composition of ions in the solution. Pure AgNPs colloidal solution has a very small electrical conductivity, but the conductivity value will increase depending on the concentration of reducing agent ions or reaction products in the solution. A very important characteristic of AgNPs is the ability to kill microorganisms from positive and negative bacteria, viruses to fungus by destroying cell membranes, affecting -SH groups as well as destroying functions microbial DNA.

AgNPs are applied in chemical fields as catalysts and analytical sensors. In the environment, AgNPs are applied to treat bacterial infections as well as air and water pollution. In medicine, AgNPS is given special attention in research and application to treat environmental infections, medical tools and equipment; diagnose and heal many diseases, including dangerous diseases such as, burn, HIV, SARC and cancer.

REFERENCES

1. C. R. Hammond. *Handbook of chemistry and physics (81st edition)*, CRC Press, Boca Raton, Florida, 2000.
2. K. E. Drexler. *Nanosystems: molecular machinery, manufacturing, and computation*, John Wiley & Sons, New York, 1992.
3. H. Goesmann, C. Feldmann. Nanoparticulate functional materials, *Angewandte Chemie – International Edition*, **2010**, *49*, 1362-1395.
4. S. Chernousova, M. Epple. Silver as antibacterial agent: ion, nanoparticle, and metal, *Angewandte Chemie - International Edition,* **2013**, *52*(6), 1636-1653.
5. B. C. Jiménez, M. E. Johnson, A. R. M. Bustos, K. E. Murphy, M. R. Winchester, J. R. V. Baudrit. Silver nanoparticles: technological advances, societal impacts, and metrological challenges, *Frontiers in Chemistry*, **2017**, *5*, 1-26.
6. N. Matsuhisa, M. Kaltenbrunner, T. Yokota, H. Jinno, K. Kuribara, T. Sekitani, T. Someya. Printable elastic conductors with a high conductivity for electronic textile applications, *Nature Communication*, **2015**, *6*, 7461.
7. D. Chen, X. Qiao, X. Qiu, J. Chen. Synthesis and electrical properties of uniform silver nanoparticles for electronic applications, *Journal of Material Science*, **2009**, *44*(4), 1076-1081.
8. X. Y. Dong, Z. W. Gao, K. F. Yang, W. Q. Zhang, L. W. Xu. Nanosilver as a new generation of silver catalysts in organic transformations for efficient synthesis of fine chemicals, *Catalysis Science & Technology*, **2015**, *5*, 2554-2574.
9. J. W. Alexander. History of the medical use of silver, *Surgical Infection (Larchmt)*, **2009**, *10*(3), 289-292.
10. S. Eckhardt, P. S. Brunetto, J. Gagnon, M. Priebe, B. Giese, K. M. Fromm. Nanobio silver: its interactions with peptides and bacteria, and its uses in medicine, *Chemical Reviews*, **2013**, *113*(7), 4708-4754.
11. S. B. N. Krishna, P. Govender, J. K. Adam. Biomedical applications and toxicity of nanosilver: a review, *Medical Technology SA*, **2015**, *29*(2), 13-29.
12. H. D. Beyene, A. A. Werkneh, H. K. Bezabh, T. G. Ambaye. Synthesis paradigm and applications of silver nanoparticles (AgNPs): a review, *Sustainable Materials and Technologies*, **2017**, *13*, 18-23.

13. J. V. Baudrit, S. M. Gamboa, E. R. Rojas, V. V. Martínez. Synthesis and characterization of silver nanoparticle and their application as an antibacterial agent, *International Journal of Biosensors & Bioelectronics,* **2019**, *5*(5), 166-173.

14. L. Xu, Y. Y. Wang, J. Huang, C. Y. Chen, Z. X. Wang, H. Xie. Silver nanoparticles: synthesis, medical applications and biosafety, *Theranostics*, **2020**, *10*(20), 8996-9031.

15. F. Mafuné, J. Y. Kohno, Y. Takeda, T. Kondow, H. Sawabe. Structure and stability of silver nanoparticles in aqueous solution produced by laser ablation, *The Journal of Physical Chemistry B*, **2000**, *104*(35), 8333-8337.

16. M. Tsuji, M. Hashimoto, Y. Nishizawa, M. Kubokawa, T. Tsuji. Microwave-assisted synthesis of metallic nanostructures in solution, *Chemistry-A European Journal*, **2004**, *11*(2), 440-452.

17. K. Shameli, M. B. Ahmad, W. M. Z. W. Yunus, N.A.Ibrahim,Y.Gharayebi,S.Sedaghat.Synthesis of silver/montmorillonite nanocomposites using γ-irradiation, *International Journal of Nanomedicine*, **2010**, *5*, 1067-1077.

18. M. Behravan, A. H. Panahi, A. Naghizadeh, M. Ziaee, R. Mahdavi, A. Mirzapour. Facile green synthesis of silver nanoparticles using Berberis vulgaris leaf and root aqueous extract and its antibacterial activity*, International Journal of Biological Macromolecules,* **2019**, *124*, 148-154.

19. L. T. Hai, L. T. T. Uyen. Biosynthesis of silver nanoparticles from silver nitrat solution using aqueus extrat of lemongrass leaves, *UED Journal of Social Sciences, Humanities & Education*, **2017**, *7*(5), 5-9.

20. T. Sowmyya, G. V. Lakshmi. Green synthesis and characterization of silver nanoparticles using Soymida febrifuga aqueous leaf extract, *World Journal of Pharmacy and Pharmaceutical Sciences*, **2015**, *5*(1), 786-805.

21. K. Shameli, M. B. Ahmad, M. Zargar, W. M. Z. W. Yunus, N. A. Ibrahim, P. Shabanzadeh, M. G. Moghaddam. Synthesis and characterization of silver/montmorillonite/chitosan bionanocomposi es by chemical reduction method and their antibacterial activity, *International Journal of Nanomedicine*, **2011**, *6*, 271-284.

22. N. H. Chau, L. A. Bang, N. Q. Buu, T. T. N. Dung, H. T. Ha, D. V. Quang. Some results in manufacture of nanosilver and investigation of its application for disinfection, *Advances in Natural Sciences*, **2008**, *9*(2), 241-248.

23. M. A. Awad, A. Hendi, K. M. Ortashi, R. A Alotaibi, M. S. Sharafeldin. Characterization of silver nanoparticles prepared by wet chemical method and their antibacterial and cytotoxicity activities, *Tropical Journal of Pharmaceutical Research*, **2016**, *15*(4), 679-685.

24. G. R. Nasretdinova, R. R. Fazleeva, R. K. Mukhitova, I. R. Nizameev, M. K. Kadirov, A. Y. Ziganshina, V. V. Yanilkin. Electrochemical synthesis of silver nanoparticles in solution, *Electrochemistry Communications*, **2015**, *50*, 69-72.

25. N. D. Hung, N. M. Thuy, M. V. Phuoc, N. Nhi. Preparation of nanosilver colloidal solution by anodic dissolution under high DC voltage, *Electrochemistry*, **2013**, *81*(6), 454-459.

26. L. B. Naranjo, M. Vazquez, D. M. Benjumea, G. Cirob. Electrochemical synthesis of silver nanoparticles and their potential use as antimicrobial agent: a case study on escherichia coli, *Portugaliae Electrochimica Acta*, **2012**, *30*(2), 135-144.

27. N. D. Hung, V. N. Nam, L. V. Trung, T. T. N. Dung. Electrochemical preparation of nano silver by combining high DC voltage with anodic plasma, *Vietnam Journal of Science and Technology*, **2019**, *57*(2), 186-198.

28. U. Backman. *Studies on nanoparticle synthesis via gas-to-particle conversion*, VTT Publications, Helsinki, Finland, 2005.

29. X. F. Zhang, Z. G. Liu, W. Shen, S. Gurunathan. Silver nanoparticles: synthesis, characterization, properties, applications, and therapeutic approaches, *International Journal of Molecular Science*, **2016**, *17*(9), 1534.

30. F. Mafuné, J. Y. Kohno, Y. Takeda, T. Kondow. Formation and size control of silver nanoparticles by laser ablation in aqueous

solution, *The Journal of Physical Chemistry B*, **2000**, *104*, 9111-9117.

31. A. Pyatenko, K. Shimokawa, M. Yamaguchi, O. Nishimura, M. Suzuki. Synthesis of silver nanoparticles by laser ablation in pure water, *Applied Physical A: Materials Science and Processing*, **2004**, *79,* 803-806.

32. D. C. Tien, C. Y. Liao, J. C. Huang, K. H. Tseng, J. K. Lung, T. T. Tsung, W. S. Kao, T. H. Tsai, T. W. Cheng, B. S. Yu, H. M. Lin, L. Stobinski. Novel technique for preparing a nano-silver water suspension by the arc-discharge method, *Reviews on Advanced Marterials Science*, **2008**, *18*(8), 752-758.

33. J. Jabłońska, K. Jankowski, M. Tomasik, D. Cykalewicz, P. Uznański, S. Całuch, M. Szybowicz, J. Zakrzewska, P. Mazurek. Preparation of silver nanoparticles in a high voltage AC arc in water, *SN Applied Sciences*, **2021**, *3*(244), 04177.

34. P. Chen, L. Song, Y. Liu, Y. E. Fang. Synthesis of silver nanoparticles by γ-ray irradiation in acetic water solution containing chitosan, *Radiation Physics and Chemistry,* **2007**, *76*(7), 1165-1168.

35. D. V. Phu, B. D. Du, N. N. Duy, N. T. Anh, N. T. K. Lan, V. T. K. Lang, N. Q. Hien. The effect of pH and molecular weight of chitisan on silver nanoparticles synthesized by gama-irradiation, *Vietnam Journal of Science and Technology*, **2009**, *47*(6), 47-52.

36. D. Long, W. Guozhong, S. Chen. Preparation of oligochitosan stabilized silver nanoparticles by gamma irradiation, *Radiation Physics Chemistry*, **2007**, *76*(7), 1126-1131.

37. H. S. Shin, H. J. Yang, S. B. Kim, M. S. Lee. Mechanism of growth of colloidal silver nanoparticles stabilized by polyvinyl pyrrolidone in γ-irradiated silver nitrate solution, *Journal of Colloid and Interface Science*, **2004**, *274*(1), 89-94.

38. O. Dial, C. C. Cheng, A. Scherer. Fabrication of high-density nanostructures by electron beam lithography, *Journal of Vacuum Science & Technoly B: Microelectronics and Nanometer Structures*, **1998**, *16*(6), 3887-3890.

39. H. Jiang, K. S. Moon, Z. Zhang, S. Pothukuchi, C. P. Wong. Variable frequency microwave synthesis of silver nanoparticles, *Journal of Nanoparticle Research*, **2006**, *8*(1), 117-124.

40. B. D. Du, D. V. Phu, N. N. Duy, N. T. K. Lan, V. T. K. Lang, N. V. K. Thanh, N. T. P. Phong, N. Q. Hien. Preparation of colloidal silver nanoparticles in poly(N-vinylpyrrolidone) by γ-irradiation, *Journal of Experimental Nanoscience*, **2008**, *3*(3), 207-213.

41. N. T. Man, L. Hai, L. H. Tu, T. T. Hong, N. D. Hang, P. T. L. Ha, T. T. Thuy, T. T. Tam, N. T. H. Phong, L. X. Cuong. Preparation of silver nanoparticles by gamma irradiation method using chitosan as stabilizer, *Nuclear Science and Technology*, **2014**, *4*(3), 43-46.

42. A. Salleh, R. Naomi, N. D. Utami, A. W. Mohammad, E. Mahmoudi, N. Mustafa, M. B. Fauzi. The potential of silver nanoparticles for antiviral and antibacterial applications: a mechanism of action, *Nanomaterials*, **2020**, *10*, 1566-1586.

43. T. R. Sertbakan, E. K. A. Shakarchi, S. S. Mala. The preparation of nano silver by chemical reduction method, *Journal of Modern Physics*, **2022**, *13*, 81-88.

44. H. Wang, X. Qiao, J. Chen, S. Ding. Preparation of nanoparticles by chemical reduction method, *Colloids and Surfaces A: Physicochemical and Engineering Aspects*, **2005**, *256*(2-3), 111-115.

45. N. T. Huong, N. V. Hung. Preparation of silver nano colloidal solution by reducing sucrose, *Journal of Military Science and Technology Research*, **2011**, *10*(15), 86-91.

46. M. G. Guzmán, J. Dille, S. Godet. Synthesis of silvernanoparticles by chemical reduction method and their antibacterial activity, *International Journal of Chemical and Biomolencular Engineering*, **2009**, *2*(3), 104-111.

47. V. V. Tatarchuk, A. P. Sergievskaya, T. M. Korda, I. A. Druzhinina, V. I. Zaikovsky. Kinetic factors in the synthesis of silver nanoparticles by reduction of Ag^+ with hydrazine in reverse micelles of triton N-42, *Chemistry of Materials*, **2013**, *25*(18), 3570-3579.

48. N. Q. Hien, N. T. A. Trinh, D. V. Phu, N. N. Duy, L. A. Quoc. Synthesis of silver nanoparticles doped in the zeolite framework by chemical reduction method, *Journal of Science and Technology*, **2015**, *53*(3), 348-354.

49. S. M. Landage, A. I. Wasif, P. Dhuppe. Syntheis of nanosilver using chemical reduction method, *International Journal of Advanced Research in Engineering and Applied Sciences*, **2014**, *3*(5), 14-22.

50. G. Suriati, M. Mariatti, A. Azizan. Synthesis of silver nanoparticles by chemical reduction method: efect of reducing agent and surfactant concentration, *International Journal of Automotive and Mechanical Engineering*, **2014**, *10*(1), 1920-1927.

51. A. Shenava. Synthesis of silver nanoparticles by chemical reduction method and their antifungal activity, *International Research Journal of Pharmacy,* **2013**, *4*(10), 111-113.

52. G. Krishna, S. C. Maringanti. Synthesis of silver nanoparticles by chemical and biological methods and their antimicrobial properties, *Jounal of Experimental Nanoscience,* **2016**, *11*(9), 714-721.

53. C. Q. Quiroz, N. Acevedo, J. Z. Giraldo, L. E. Botero, J. Quintero, D. Z. Triviño, J. Saldarriaga, V. Z. Pérez. Optimization of silver nanoparticle synthesis by chemical reduction and evaluation of its antimicrobial and toxic activity, *Biomaterials Research*, **2019**, *23*(27), 1-15.

54. S. D. Solomon, M. Bahadory, A. V. Jeyarajasingam, S. A. Rutkowsky, C. Boritz. Synthesis and study of silvernanoparticles, *Journal of Chemical Education,* **2007**, *84*(2), 322-325.

55. K. Mavani, M. Shah. Synthesis of silver nanoparticles by using sodium borohydride as a reducing agent, *International Journal of Engineering Research & Technology*, **2013**, *2*(3), 1-5.

56. B. Zeytuncua, M. H. Morcali. Fabrication and characterization of antibacterial polyurethane acrylate-based materials, *Materials Research*, **2015**, *18*(4), 867-872.

57. V. X. Hoa, D. T. T. Tra, P. T. T. Ha, D. K. Trinh, N. X. Huong, D. V. Son. Synthesis and study of silver nanoparticles for antibacterial activity against escherichia coli and staphylococcus aureus, *Advances in Natural Sciences: Nanoscience and Nanotechnology,* **2018**, *9*(2), 025019.

58. K. C. Song, S. M. Lee, T. S. Park, B. S. Lee. Preparation of colloidal silver nanoparticles by chemical reduction method, *Korean Journal of Chemical Engineering*, **2009**, *26*(1), 153-155.

59. F. Fischer, S. Bauer. Polyvinylpyrrolidon, ein tausendsassa in der chemie, *Chemie in Unserer Zeit*, **2009**, *43*(6), 376-383.

60. E. Bae, H. J. Park, J. Park, J. Yoon, Y. Kim, K. Choi, J. Yi. Effect of chemical stabilizers in silver nanoparticle suspension on nanotoxicity, *Bulletin of the Korean Chemical Society,* **2011**, *32*(2), 613-619.

61. D. Amir, R. R. Nasaruddin, N. S. Engliman, S. Sulaiman, M. S. Mastuli. Effect of stabilizers in the synthesis of silver nanoparticles and methylene blue oxidation, *IOP Conference Series: Materials Science and Engineering*, **2021**, *1192*, 012031.

62. K. Shameli, M. B. Ahmad, M. Zargar, W. M. Z. W. Yunus, N. A. Ibrahim, P. Shabanzadeh, M. G. Moghaddam. Synthesis and characterization of silver/montmorillonite/chitosan bionanocomposites by chemical reduction method and their antibacterial activity, *International Journal of Nanomedicine*, **2011**, *6*, 271-284.

63. M. A. Hettiarachchi, P. A. S. R. Wickramarachchi. Synthesis of chitosan stabilized silver nanoparticles using gama ray irradiation and characterization, *Journal of Science of the University of Kelaniya*, **2012**, *6*, 65-75.

64. J. V. Baudrit, R. A. Meza, F. S. Jiménez. Synthesis of silver nanoparticles using chitosan as a coating agent by sonochemical method, *Avances en Química*, **2014**, *9*(3), 125-129.

65. R. Kalaivani, M. Maruthupandy, T. Muneeswaran, A. H. Beevi, M. Anand, C. M. Ramakritinan, A. K. Kumaraguru. Synthesis of

https://doi.org/10.52111/qnjs.2024.18101

chitosan mediated silver nanoparticles (AgNPs) for potential antimicrobial application, *Frontiers in Laboratory Medicine*, **2018**, *2*(1), 30-35.

66. L. O. Cinteza, C. Scomoroscenco, S. N. Voicu, C. L. Nistor, S. G. Nitu, B. Trica, M. L. Jecu, C. Petcu. Chitosan-stabilized Ag nanoparticles with superior biocompatibility and their synergistic antibacterial effect in mixtures with essential oils, *Nanomaterials*, **2018**, *8*(10), 826-832.

67. L. Q. Luan, N. H. P. Uyen, P. H. Giang. Study on the antifungal effect of silver nano particlechitosan prepared by irradiation method on phytophthora capsica causing the blight disease on pepper plant, *Academia Journal of Biology*, **2014**, *36*(1), 152-157.

68. M. J. Schnepf, M. Mayer, C. Kuttner, M. Tebbe, D. Wolf, M. Dulle, T. Altantzis, P. Formanek, S. Forster, S. Bals, T. A. F. Konig, A. Fery. Nanorattles with tailored electric field enhancement, *Nanoscale*, **2017**, *9*(27), 9376-9385.

69. H. Kaczmarek, M. Metzler, K. W. Drzymalska. Effect of stabilizer type on the physicochemical properties of poly(acrylic acid)/silver nanocomposites for biomedical applications, *Polymer Bulletin*, **2016**, *73*(10), 2927-2945.

70. J. J. Richards, A. D. Scherbarth, N. J. Wagner, P. D. Butler, Mixed ionic/electronic conducting surface layers adsorbed on colloidal silica for flow battery applications, *ACS Applied Materials & Interfaces*, **2016**, *8*(36), 24089-24096.

71. K. Shiomori, T. Honbu, Y. Kawano, R. Kuboi, I. Komasawa. Formation and structure control of reverse micelles by the addition of alkyl amines and their applications for extraction processes of proteins, *Studies in Surface Science and Catalysis*, **2001**, *132*, 141-144.

72. B. S. Gangadharappa, M. Dammalli, S. Rajashekarappa, K. Murthy, G. B. Siddaiah. Reverse micelles as a bioseparation tool for enzymes, *Journal of Proteins and Proteomics*, **2017**, *8*(2), 105-120.

73. L. J. Hua, C. G. Bac. Method for the preparation of silvernanoparticles-polymer composite, Patent Cooperation Treaty (PCT), World Intellectual Property Organization (WIPO), WO2005085339A1, 2005.

74. H. N. T. Luan, H. C. Cuong, H. T. C. Nhan, L. Q. Vinh, L. V. Hieu. Synthesis and study on mechanical properties of the polypropylene/TiO_2-nano Ag composite for antibacterial application, *Science & Technology Development*, **2015**, *18*(T1), 70-80.

75. H. A. Son, V. T. Phong, T. A. Tuan. Study and preparation of antiseptic filter film based on polyurethane/nanosilver composite for water treatment, *Journal of Analytical Sciences,* **2007**, *12*(4), 3-8.

76. J. Deng, Q. M. Ding, W. Li, J. H. Wang, D. M. Liu, X. X. Zeng, X. Y. Liu, L. Ma, Y. Deng, W. Su, B. Ye. Preparation of nano-silver-containing polyethylene composite film and ag ion migration into food-simulants, *Journal of Nanoscience and Nanotechnology*, **2020**, *20*(3), 1613-1621.

77. L. Yaohui, H. Liu, Z. Wang, S. Liu, L. Hao, Y. Sang, D. Liu, J. Wang, R. I. Boughton. Silver nanoparticle-decorated porous ceramic composite for water treatment, *Journal of Membrane Science*, **2009**, *331*(1-2), 50-56.

78. M. Kumar, G. Pugazhenthi, D. Vasanth. Synthesis of zirconia-ceramic composite membrane employing a low-cost precursor and evaluation its performance for separation of microbially produced silver nanoparticles, *Journal of Environmental Chemical Engineering*, **2022**, *10*(3), 107569.

79. N. D. Hung, N. T. T. Ha, T. T. N. Dung. Manufacturing of porous nanosilver-covered ceramic for waste water treatment in Thi Nai lagoon - Binh Dinh province, *Quy Nhon University Journal of Science*, **2016**, *10*(4), 139-145.

80. N. D. Hung, N. T. Linh, T. T. N. Dung. Study on fabrication of antibacterial surface with nano silver for glass, ceramic, *Hanoi National University Journal of Science,* **2016**, *32*(4), 53-57.

81. R. M. E. Shishtawy, A. M. Asiri, N. A. M. Abdelwahed, M. M. A. Otaibi. In situ production of silver nanoparticle on cotton fabric and its antimicrobial evaluation, *Cellulose*, **2011**, *18*(1), 75-82.

82. S. Erdoğan. Textile finishing with chitosan and silver nanoparticles against Escherichia coli ATCC 8739, *Trakya University Journal of Natural Sciences*, **2020**, *21*(1), 21-32.

83. Y. N. Gao, Y. Wang, T. N. Yue, Y. X. Weng, M. Wang. Multifunctional cotton non-woven fabrics coated with silver nanoparticles and polymers for antibacterials, superhydrophobic and high performance microwave shielding, *Journal of Colloid and Interface Science*, **2021**, *582*, 112-123.

84. J. Weber, L. Henssler, L. Zeman, C. Pfeifer, V. Alt, M. Nerlich, M. Huber, T. Herbst, M. Koller, W. S. Brachert, M. Kerschbaum, T. Holzmann. Nanosilver/DCOIT-containing surface coating efectively and constantly reduces microbial load in emergency room surfaces, *Journal of Hospital Infection*, **2023**, *135*, 90-97.

85. H. Zhang, J. Cui, J. Zhu, Y. Shao, H. Zhang. Fabrication of nano-silver–silver ion composite antibacterial agents for green powder coatings, *Coatings*, **2023**, *13*(3), 575.

86. T. T. N. Dung, N. H. Chau. Manufacturing silver nano - porous ceramic membrane for disifection of drinking water by in-situ reduction method, *Vietnam Journal of Science and Technology*, **2015**, *53*(6), 715-722.

87. M. S. Khalilabad, M. E. Yazdanshenas, A. Etemadifar. Fabricating multifunctional silver nanoparticles-coated cotton fabric, *Arabian Journal of Chemistry*, **2013**, *10*, S2355-S2362.

88. K. M. F. Hasan, P. G. Horváth, Z. Kóczán, M. Bak, T. Alpár. Colorful and facile in situ nanosilver coating on sisal/cotton interwoven fabrics mediated from European larch heartwood, *Scientific Reports*, **2021**, *11*(1), 22397.

89. D. Mandal, M. E. Bolander, D. Mukhopadhyay, G. Sarkar, P. Mukherjee. The use of microorganisms for the formation of metal nanoparticles and their application, *Applied Microbiology Biotechnology*, **2006**, *69*(5), 485-492.

90. A. B. Moghaddam, F. Namvar, M. Moniri, P. M. Tahir, S. Azizi, R. Mohamad. Nanoparticles biosynthesized by fungi and yeast: a review of their preparation, properties, and medical applications, *Molecules*, **2015**, *20*(9), 16540-16565.

91. N. T. Khan, M. J. Khan. Mycofabricated silver nanoparticles: an overview of biological organisms responsible for its synthesis, *Biochemistry & Molecular Biology Journal*, **2017**, *3*(1), 1-5.

92. A. R. Shahverdi, S. Minaeian, H. R. Shahverdi, H. Jamalifar, A. A. Nohi. Rapid synthesis of silver nanoparticles using culture supernatans of enterobacteria: a novel biological approarch, *Process Biochemistry*, **2007**, *42*(5), 919-923.

93. C. C. Jing, B. H. Juan. Biosynthesis of silver nanoparticles using the phototrophic bacteria rhodopseudomonas palustris and its antimicrobial activity against escherichia coli and staphylococcus aureus, *Microbiology China*, **2010**, *37*(12), 1798-1804.

94. H. J. Bai, B. S. Yang, C. J. Chai, G. E. Yang, W. L. Jia, Z. B. Yi. Green synthesis of silver nanoparticles using rhodobacter sphaeroides, *World Journal of Microbiology Biotechnology*, **2011**, *27*(11), 2723-2728.

95. S. Rajeshkumar, C. Malarkodi, K. Paulkumar, M. Vanaja, G. Gnanajobitha, G. Annadurai. Intracellular and extracellular biosynthesis of silver nanoparticles by using marine bacteria vibrio alginolyticus, *Nanoscience and Nanotechnology: An International Journal*, **2013**, *3*(1), 21-25.

96. S. Rajeshkumar, C. Malarkodi, V. Sivakumar, K. Paulkumar, M. Vanaja. Biosynthesis of silver nanoparticles by using marine bacteria vibrio alginolyticus, *International Research Journal of Pharmaceutical and Biosciences,* **2014**, *1*(1), 19-23.

97. P. Srivastava1, J. M. Braganca, S. R. Ramanan, M. Kowshik. Green synthesis of silver nanoparticles by haloarchaeon halococcus salifodinae BK6, *Advanced Materials Research*, **2014**, *938,* 236-241.

98. V. L. Das, R. Thomas, R. T. Varghese, E. V. Soniya, J. Mathew, E. K. Radhakrishnan. Extracellular synthesis of silver nanoparticles by the Bacillus strain CS 11 isolated from industrialized area, *3 Biotech*, **2014**, *4*, 121-126.

99. M. S. John, J. A. Nagoth, K. P. Ramasamy, A. Mancini, G. Giuli, A. Natalello, P. Ballarini, C. Miceli, S. Pucciarelli. Synthesis of bioactive silver nanoparticles by a pseudomonas strain associated with the antarctic psychrophilic protozoon euplotes focardii, *Marine Drugs*, **2020**, *18*(1), 38.

100. H. M. Tag, A. A. Saddiq, M. Alkinani, N. Hagagy. Biosynthesis of silver nanoparticles using haloferax sp. nrs1: image analysis, characterization, in vitro thrombolysis and cytotoxicity, *AMB Express*, **2021***, 11*, 75.

101. P. Mukherjee, A. Ahmad, D. Mandal, S. Senapati, S. R. Sainkar. Fungus-mediated synthesis of silver nanoparticles and their immobilization in the mycelial matrix: a novel biological approach to nanoparticle synthesis, *Nano Letters*, **2001**, *1*(10), 515-519.

102. K. C. Bhainsa, S. F. D. Souza. Extracellular biosynthesis of silver nanoparticles using the fungus aspergillus fumigatus, *Colloids and Surfaces B: Biointerfaces*, **2006**, *47*(2), 160-164.

103. K. Kathiresan, S. Manivannan, M. A. Nabeel, B. Dhivya. Studies on silver nanoparticles synthesized by a marine fungus penicillum fellutanum isolated from coastal mangrove sediment, *Colloids and Surface B: Biointerfaces*, **2009**, *71*(1), 133-137.

104. M. Pandian, R. Marimuthu, G. Natesan, R. E. Rajagopa, J. S. Justin, A. J. A. H. Mohideen. Development of biogenic silver nano particle from pelargonium graveolens leaf extract and their antibacterial activity, *American Journal of Nano Research and Applications*, **2013**, *1*(2), 57-64.

105. L. Wang, C. C. Liu, Y. Y. Wang, H. Xu, H. Su, X. Cheng. Antibacterial activities of the novel silver nanoparticles biosynthesized using cordyceps militaris extract, *Current Applied Physics*, **2016**, *16*(9), 969-973.

106. M. Zargar, A. A. Hamid, F. A. Bakar, M. N. Shamsudin, K. Shameli, F. Jahanshiri, F. Farahani. Green synthesis and antibacterial effect of silver nanoparticles using vitex negundo L., *Molecules*, **2011**, *16*(8), 6667-6676.

107. M. Kowshik, S. Ashtaputre, S. Kharrazi, W. Vogel, J. Urban, S. K. Kulkarni, K. M. Paknikar. Extracellular synthesis of silver nanoparticles by a silver-tolerant yeast strain MKY3, *Nanotechnology,* **2003**, *14*(1), 95-100.

108. E. K. Kambate, C. I. Nkanga, B. P. I. Mutonkole, A. M. Bapolisi, D. O. Tassa, J. M. I. Liesse, R. W. M. Krause, P. B. Memvaga. Green synthesis of antimicrobial silver nanoparticles using aqueous leaf extracts from three Congolese plant species (brillantaisia patula, crossopteryx febrifuga and senna siamea), *Heliyon*, **2020**, *6*(8), 4493.

109. L. T. K. Anh, L. D. Vuong, V. V. Q. Bao, N. T. P. Nga, N. H. Thinh, N. T. Q. Anh, P. T. T. Hien. Synthesis of silver-nanoparticles with aqueous extract of robusta plant leaves as reducing agent, *Hue University Journal of Science: Natural Science*, **2022**, *131*(1A), 119-126.

110. T. Sowmyya, G. V. Lakshmi. Green synthesis and characterization of antimicrobial and catalytic silver nanoparticles using soymida febrifuga aqueous leaf axtract, *World Journal Pharmacy and Pharmaceutical Science*, **2016**, *5*(1), 786-805.

111. M. Umadevi, S. Shalini, M. R. Bindhu. Synthesis of silver nanoparticle using D. carota extract, *Advances in Natural Science: Nanoscience and Nanotechnology*, **2012**, *3*(2), 025008.

112. R. Prasad, V. S. Swamy. Antibacterial activity of silver nanoparticles synthesized by bark extract of syzygium cumini, *Journal of Nanoparticles*, **2013**, *2013*, 431218.

113. K. Shameli, M. B. Ahmad, A. Zamanian, P. Sangpour, P. Shabanzadeh, Y. Abdollahi, M. Zargar. Green biosynthesis of silver nanoparticles using Curcuma longa tuber powder, *International Journal of Nanomedicine*, **2012**, *7*, 5603-5610.

114. A. Reveendran, S. Varghese, K. Viswanathan. Green synthesis of silver nano particle using

hibiscus rosa sinensis, *IOSR Journal of Applied Physics*, **2016**, *8*(3), 35-38.

115. D. Jain, H. K. Daima, S. Kachhwaha, S. L. Kothar. Synthesis of plant-mediated silver nanoparticles using papaya fruit extract and evaluation of their anti microbial activities, *Digest Journal of Nanomaterials and Biostructures*, **2009**, *4*(3), 557-563.

116. Y. Zhang, X. Cheng, Y. Zhang, X. Xue, Y. Fu. Biosynthesis of silver nanoparticles at room temperature using aqueous aloe leaf extract and antibacterial properties, *Colloids Surfaces A: Physicochemical and Engineering Aspects*, **2013**, *423*(2), 63-68.

117. L. T. Hai, N. T. L. Anh. Biosynthesis of silver nanoparticles from $AgNO_3$ solution using aqueous extract of ocimum basilicum L. leaf as the reducing agent, *GSC Advanced Research and Reviews*, **2023**, *14*(1), 151-158.

118. L. T. Hai. Biosynthesis, characterization and photocatalytic activity of copper/copper oxide nanoparticles produced using aqueous extract of lemongrass leaf, *Composite Materials*, **2019**, *3*(1), 30-35.

119. C. Ankit, M. M. Sharma, A. Singh. Green nanoparticle synthesis and their applications, *International Journal of Pharmacognosy*, **2015**, *2*(3), 110-115.

120. A. D. Dwivedi, K. Gopal. Biosynthesis of silver and gold nanoparticles using chenopodium album leaf extract, *Colloids Surfaces A: Physicochemical and Engineering Aspects*, **2010**, *369*(1-3), 27-33.

121. J. Huang, Q. Li, D. Sun, Y. Lu, Y. Su, X. Yang, H. Wang, Y. Wang, W. Shao, N. He. Biosynthesis of silver and gold nanoparticles by novel sundried Cinnamomum camphora leaf, *Nanotechnology*, **2007**, *18*(10), 105104.

122. M. S. Shirazi, M. M. Farimani, A. Foroumadi, K. Ghanemi, M. Benaglia, P. Makvandi. Bioengineered synthesis of phytochemical-adorned green silver oxide (Ag_2O) nanoparticles via mentha pulegium and ficus carica extracts with high antioxidant, antibacterial, and antifungal activities, *Scientific Reports*, **2022**, *12*, 21509.

123. M. Mohammadi, S. A. Shahisaraee, A. Tavajjohi, N. Pournoori, S. Muhammadnejad, S. R. Mohammadi, R. Poursalehi, H. H. Delavari. Green synthesis of silver nanoparticles using zingiber officinale and thymus vulgaris extracts: characterisation, cell cytotoxicity, and its antifungal activity against candida albicans in comparison to fluconazole, *IET Nanobiotechnology*, **2019**, *13*(2), 114-119.

124. S. A. Kumari, A. K. Patlolla, P. Madhusudhanachary. Biosynthesis of silver nanoparticles using azadirachta indica and their antioxidant and anticancer effects in cell lines, *Micromachines: Basel,* **2022**, *13*(9), 1416.

125. Y. Y. Loo, B. W. Chieng, M. Nishibuchi, S. Radu. Synthesis of silver nanoparticles by using tea leaf extract from camellia sinensis, *International Journal of Nanomedicine*, **2012**, *7*, 4263-4267.

126. H. Bar, D. K. Bhui, G. P. Sahoo, P. Sarkar, S. P. De, A. Misra. Green synthesis of silver nanoparticles using latex of jatropha curcas, *Colloids and Surfaces A Physicochemical and Engineering Aspects*, **2009**, *339*(1-3), 134-139.

127. M. Abbas, T. Hussain, J. Iqbal, A. U. Rehman, M. A. Zaman, K. Jilani, N. Masood, S. H. A. Mijalli, M. Iqbal, A. Nazir. Synthesis of silver nanoparticle from allium sativum as an eco-benign agent for biological applications, *Polish Journal Environmental Studies*, **2022**, *31*(1), 533-538.

128. J. Yaday, P. Chauhan. Green synthesis of silver nanoparticles using citrus x sinensis (orange) fruit extract and assessment of their catalytic reduction, *Materialstoday: Proceedings*, **2022**, *62*(10), 6177-6181.

129. Y. H. Momim, V. C. Yeligar. Synthesis of coccina grandis (L.) voigt extract's silver nanoparticles and it's *in vitro* antidiabetic activity, *Journal of Applied Pharmaceutical Science*, **2021**, *11*(8), 110815.

130. K. Song, D. Zhao, H. Sun, J. Gao, S. Li, T. Hu, X. He. Green nanopriming: responses of alfalfa (medicago sativa L.) seedlings to alfalfa extracts capped and light-induced silver nanoparticles, *BMC Plant Biology*, **2022**, *22*(323), 1-16.

https://doi.org/10.52111/qnjs.2024.18101

131. S. Vadivel, S. Suja. Green synthesis of silver nanoparticles using coleus amboinicus lour, antioxidant activity and invitro cytoxicity against Ehrlich's Ascite carcinoma, *Journal of Pharmacy Research*, **2012**, *5*(2), 1268-1272.

132. N. K. Sajeshkumar, P. J. Vazhacharickal, J. J. Mathew, A. Sebastin. Synthesis of silver nano particles from cury leaf (muraya koenigii) extract and its antibacterial activity, *CIBTech Journal of Pharmaceutical Sciences*, **2015**, *4*(2), 15-25.

133. Y. K. Mohanta, S. K. Panda, K. Biswas, A. Tamang, J. Bandyopadhyay, D. De, D. Mohanta, A. K. Bastia. Biogenic synthesis of silver nanoparticles from cassia fistula (Linn.): in vitro assessment of their antioxidant, antimicrobial and cytotoxic activities, *IET Nanobiotechnology*, **2016**, *10*(6), 438-444.

134. M. Timotina , A. Aghajanyan , R. Schubert, K. Trchounian , L. Gabrielyan. Biosynthesis of silver nanoparticles using extracts of stevia rebaudiana and evaluation of antibacterial activity, *World Journal of Microbiology Biotechnology*, **2022**, *38*(11), 196.

135. C. Krishnaraj, E. G. Jagan, S. Rajasekar, P. Selvakumar, P. T. Kalaichelvan, N. Mohan. Synthesis of silver nanoparticles using acalypha indica leaf extracts and its antibacterial activity against water borne pathogens, *Colloids and Surfaces B: Biointerfaces*, **2010**, *76*(1), 50-56.

136. M. Rai, C. Posten. *Green biosynthesis of nanoparticles: mechanisms and applications*, CABI Digital Library, Wallingford, Oxfordshire, 2013.

137. N. D. Hung. Electrochemical technology and metal protection, *Journal of Science and Technology*, **2012**, *50*(6), 767-779.

138. R. A. Khaydarov, R. Khaydarov, O. Gapurova, Y. Estrin, T. Scheper. Electrochemical method for the synthesis of silver nanoparticles, *Journal of Nanoparticle Research*, **2009**, *11*(5), 1193-1200.

139. N. D. Hung, M. V. Phuoc, N. M. Thuy. Manufactoring of nano silver solution using electrochemical technology, *Vietnam Journal of Chemistry*, **2012**, *50*(2), 261-263.

140. M. J. Haider, M. S. Mahdi. Synthesis of silver nanoparticles by electrochemical method, *Engineering and Technolgy Journal*, **2015**, *33B*(7), 1361-1373.

141. H. A. P. Sierra, G. P. Rodríguez, G. C. Bedoya. Silver colloidal nanoparticles by electrochemistry: temporal evaluation and surface plasmon resonance, *Journal of Physics: Conference Series*, **2021**, *2046*, 012064.

142. C. Gasbarri, M. Ronci, A. Aceto, R. Vasani, G. Iezzi, T. Florio, F. Barbieri, G. Angelini, L. Scotti. Structure and properties of electrochemically synthesized silver nanoparticles in aqueous solution by high-resolution techniques, *Molecules*, **2021**, *26*(17), 5155.

143. N. D. Hung, N. C. Phuc. Bactericidal activity of electrochemically precipitated nanosilver and Ag/Al_2O_3 nanocomposites, *Vietnam Journal of Chemistry*, **2010**, *48*(4), 409-412.

144. M. V. Roldán, N. Pellegri, O. D. Sanctis. Electrochemical method for Ag-PEG nanoparticles synthesis, *Journal of Nanoparticles*, **2013**, *2013,* 524150.

145. T. Q. Tuan, P. V. Hao, L. M. Quynh, N. H. Luong, N. H. Hai. Preparation and properties of silver nanoparticles by heat-combined electrochemical method, *VNU Journal of Science: Mathematics-Physics*, **2015**, *31*(2), 36-44.

146. N. D. Hung, T. V. Cong, H. N. Trang. Synthesis of bimetallic Cu-Ag nanoparticles prepared by DC high voltage electrochemical method, *Vietnam Journal of Chemistry*, **2019**, *57*(5), 609-614.

147. M. V. Phuoc, N. M. Thuy, N. D. Hung. Energy balance in the process of creating silver nanoparticles by high voltage electrochemical technology, *Vietnam Journal of Chemistry*, **2014**, *52*(6B), 183-186.

148. N. M. Thuy, N. D. Hung, M. V. Phuoc, N. N. Tru. Characterization of particles size distribution for nano silver solution prepared by high DC voltage electrochemical technique, *Vietnam Journal of Chemistry*, **2014**, *52*(5), 543-547.

149. N. M. Thuy, N. D. Hung, N. T. N. Tinh, N. N. Tru. Silver nano solution produced

by electrochemical method high voltage: bactericidal ability and application in medicine-pharmaceutical, *Vietnam Journal of Chemistry*, **2012**, *50*(5A), 134-138.

150. D. A. F. Kamenetski. *Plasma, the fourth state of matter*, Plenum Press, New York, 1972.

151. P. K. Chu, X. Lu. *Low temperature plasma technology, methods and application*, CRC Press-Taylor&Francis Group, Boca Raton, 2013.

152. M. Er. *Synthesis of silver nanoparticles using a plasma-liquid process*, PhD thesis, Université Sorbonne Paris, 2020.

153. U. Shuaib, T. Hussain, R. Ahmad, M. Zakaullah, F. E. Mubarik, S. T. Muntaha, S. Ashraf. Plasma-liquid synthesis of silver nanoparticles and their antibacterial and antifungal applications, *Materials Research Express*, **2020**, *7*(3), 035015.

154. V. S. Santosh, K. Kondeti, U. Gangal, S. Yatom, P. J. Bruggeman. Ag^+ reduction and silver nanoparticle synthesis at the plasma–liquid interface by an RF driven atmospheric pressure plasma jet: mechanisms and the effect of surfactant, *Journal of Vacuum Science & Technology A*, **2017**, *35*(6), 1-12.

155. J. Jabłońska, K. Jankowski, M. Tomasik, D. Cykalewicz, P. Uznański, S. Całuch, M. Szybowicz, J. Zakrzewska, P. Mazurek. Preparation of silver nanoparticles in a high voltage AC arc in water, *SN Applied Sciences*, **2021**, *3*(2), 244.

156. N. D. Hung, V. V. Nam, L. V. Trung, T. T. N. Dung. Electrochemical preparation of nanosilver by combining high DC voltage with anodic plasma, *Vietnam Journal of Science and Technology*, **2019**, *57*(2), 186-198.

157. X. Wang, H. F. Wu, Q. Kuang, R. B. Huang, Z. X. Xie, L. S. Zheng. Shape-dependent antibacterial activities of Ag_2O polyhedral particles, *Langmuir*, **2010**, *26*(4), 2774-2778.

158. N. M. Thuy. *Research on electrochemical anodic dissolution at positive electrode (anode) for manufactoring of silver nanoparticles using high voltage*, PhD thesis, Military Academy of Science and Technology, Hanoi, 2010.

159. C. Gasbarri, M. Ronci, A. Aceto, R. Vasani, G. Iezzi, T. Florio, F. Barbieri, G. Angelini, L. Scotti. Structure and properties of electrochemically synthesized silver nanoparticles in aqueous solution by high-resolution techniques, *Molecules*, **2021**, *26*, 5155.

160. A. Y. Vasilkov, R. I. Dovnar, S. M. Smotryn, N. N. Iaskevich, A. V. Naumkin. Plasmon resonance of silver nanoparticles as a method of increasing their antibacterial action, *Antibiotics,* **2018**, *7*(3), 1-18.

161. Y. Niu, E. Omurzak, R. Cai, D. Syrgakbekkkyzy, Z. Z. kubanalievich, A. Satyvaldiev, R. E. Palmer. Eco-frendly synthesis of silver nanoparticles using pulsed plasma in liquid of surfactants, *Surfaces*, **2022**, *5*(1), 202-208.

162. M. Skiba, A. Pivovarov, A. Makarova, V. Vorobyova. Plasma-chemical synthesis of silver nanoparticles in the presence of citrate, *Chemistry Journal of Moldova,* **2018***, 13*(1), 7-14.

163. S. Iravani, H. Korbekandi, S. V. Mirmohammadi, B. Zolfaghari. Synthesis of silver nanoparticles: chemical, physical and biological methods, *Research in Pharmaceutical Sciences*, **2014**, *9*(6), 385-406.

164. M. I. Skiba, V. I. Vorobyova, I. V. Kossogina. Preparation of silver nanoparticles in a plassma-liquid system in presence of PVA: antimicrobial, catalytic, and sensing properties, *Journal of Chemistry*, **2020**, *2020*, 5380950.

165. W. K. A. W. M. Khalir, K. Shameli, S. D. Jazayeri, N. A. Othman, N. W. C. Jusoh, N. M. Hassan. Biosynthesized silver nanoparticles bay aqueous stem extract of entada spriralis and screening of their biomedical activity, *Frontiers in Chemistry*, **2020**, *8*(620), 1-15.

166. N. D. Hung, M. V. Phuoc, N. M. Thuy. The electrical conductivity of nano silver solution, *Journal of Military Science and Technology Research*, **2012**, *17*(2), 96-111.

167. N. D. Hung, L. V. Hung, N. M. Thuy. Using of UV-Vis for metallic nanosilver solution preparated by anodic dissolution with untral-high voltage, *Journal of Military Science and Technology Research,* **2012***, 19*(6), 94-99.

https://doi.org/10.52111/qnjs.2024.18101

168. L. Ge, Q. Li, M. Wang, J. Ouyang, X. Li, M. M. Q Xing. Nanosilver particles in medical application: synthesis, performance, and toxicity, *International Journal of Nanomedicine*, **2014**, *9*, 2399-2407.

169. G. Pedersen. *A fighting chance: how to win the war against virus and bacteria with silver*, Self-Published, New York, 2011.

170. G. Pedersen. *A new fighting chance: silver solution: a quantum leap in silver technology*: *how molecular structuring safely destroys bacteria, viruses and yeast*, CreateSpace Publishing, New York, 2014.

171. R. W. Y. Sun, R. Chen, N. P. Y. Chung, C. M. Ho, C. L. S. Lin, C. M. Che. Silver nanoparticles fabricated in Hepes buffer exhibit cytoprotective activities toward HIV-1 infected cells, *Chemical Communication,* **2005**, *28*(40), 5059-5061.

172. H. H. Lara, L. I. Turrent, E. N. G. Treviño, C. R. Padilla. PVP-coated silver nanoparticles block the transmission of cell-free and cell-associated HIV-1 in human cervical culture, *Journal of Nanobiotechnology,* **2010**, *8*, 15-25.

173. S. Galdiero, A. Falanga, M. Vitiello, M. Cantisani, V. Marra, M. Galdiero. Silver nanoparticles as potential antiviral agents, *Molecules*, **2011**, *16*(10), 8894-8918.

174. Z. A. Ratan, F. R. Mashrur, A. P. Chhoan, S. M. Shahriar, M. F. Haidere, N. J. Runa, S. Kim, D. H. Kweon, H. Hosseinzadeh, J. Y. Cho. Silver nanoparticles as potential antiviral agents, *Pharmaceutics*, **2021**, *13*(12), 2034.

175. J. V. Rogers, C. V. Parkinson, Y. W. Choi, J. L. Speshock, S. M. Hussain. A preliminary assessment of silver nanoparticles inhibition of monkeypox virus plaque formation, *Nanoscale Research Letters,* **2008**, *3*, 129-133.

176. L. Lu, R. W. Y. Sun, R. Chen, C. M. Hui, C. M. Ho, J. M. Luk, G. K. K. Lau, C. M. Che. Silver nanoparticles inhibit hepatitis B virus replication, *Antiviral Therapy,* **2008**, *13*, 253-262.

177. L. Sun, A. Singh, K. Vig, S. R. Pillai, S. R. Sing. Silver nanoparticles inhibit replication of respiratory syncytial virus, *Journal of Biomedical Nanotechnology,* **2008**, *4*(2), 149-158.

178. D. B. Pinto, S. Shukla, N. Perkas, A. Gedanken, R. Sarid. Inhibition of herpes simplex virus type 1 infection by silver nanoparticles capped with mercaptoethane sulfonate, *Bioconjugate Chemistry,* **2009**, *20*(8), 1497-1502.

179. J. L. Speshock, R. C. Murdock, L. K. B. Stolle, A. M. Schrand, S. M. Hussain. Interaction of silver nanoparticles with tacaribe virus, *Journal of Nanobiotechnology,* **2010**, *8(19)*, 19-27.

180. C. T. T. Huyen, N. T. T. Binh, T. N. Duong, N. T. Hai. Nanosilver and prospects of medicinal applications, *VNU Journal of Science: Natural Sciences and Technology*, **2014**, *30*(2), 23-32.

181. N. Hadrup, A. K. Sharma, K. Loeschner, N. R. Jacobsen. Pulmonary toxicity of silver vapours, nanoparticles and fine dusts: a review, *Regulatory Toxicology and Pharmacology,* **2020**, *115*, 104690.

182. Y. S. Kim, J. S. Kim, H. S. Cho, D. S. Rha, J. M. Kim, J. D. Park, B. S. Choi, R. Lim, H. K. Chang, Y. H. Chung, I. H. Kwon, J. Jeong, B. S. Han, I. J. Yu. Twenty-eight-day oral toxicity, genotoxicity, and genderrelated tissue distribution of silver nanoparticles in Sprague-Dawley rats, *Inhalation Toxicology,* **2008**, *20*(6), 575-583.

183. P. Mathur, S. Jha, S. Ramteke, N. K. Jain. Pharmaceutical Aspects of silver nanoparticles, *Artificial Cells, Nanomedicine, and Biotechnology,* **2018**, *46*, 115-126.

184. N. R. Panyala, E. M. P. Méndez, J. Havel. Silver or silver nanoparticles: a hazardous threat to the environment and human health? *Journal of Applied Biomedicine,* **2008**, *6*(3), 117-129.

185. S. Kittler, C. Greulich, J. Diendorf, M. Koller, M. Epple. Toxicity of silver nanoparticles increases during storage because of slow dissolution under release of silver ions, *Chemistry of Materials,* **2010**, *22*(16), 4548-4554.

186. L. V. Stebounova, A. A. Dodd, J. S. Kim, H. Park, P. T. O'Shaughnessy, V. H. Grassian, P. S. Thorne. Nanosilver induces minimal lung toxicity or inflammation in a subacute murine inhalation model, *Particle and Fibre Toxicology,* **2011**, *8*(5), 5-17.

187. T. Zhang, L. Wang, Q. Chen, C. Chen. Cytotoxic potential of silver nanoparticles, *Yonsei Medical Journal*, **2014**, *55*(2), 283-291.

188. E. M. Luther, Y. Koehler, J. Diendorf, M. Epple, R. Dringen. Accumulation of silver nanoparticles by cultured primary brain astrocytes, *Nanotechnology*, **2011**, *22*, 375101.

189. W. Liu, Y. Wu, C. Wang, H. C. Li, T. Wang, C. Y. Liao, L. Cui, Q. F. Zhou, B. Yan, G. B. Jiang. Impact of silver nanoparticles on human cells: effect of particle size, *Nanotoxicology,* **2010**, *4*(3), 319-330.

190. S. Barcikowski, P. Wagener, N. Bärsch. Ligandenfreie laser-generierte nano-partikel für biomedizin und katalyse, *BioPhotinik*, **2013**, *2*, 34-37.

191. T. Mitsudome, A. Noujima, Y. Mikami, T. Mizugaki, K. Jitsukawa, K. Kaneda. Supported gold and silver nanoparticles for catalytic deoxygenation of epoxides into alkenes, *Angewandte Chemie,* **2010**, *49*(32)*,* 5677-5680.

192. P. Saha, M. Mahiuddin, A. B. M. N. Islam, B. Ochiai. Biogenic synthesis and catalytic efficacy of silver nanoparticles based on peel extracts of citrus macroptera fruit, *ACS Omega*, **2021**, *6*(28), 18260-18268.

193. X. Y. Dong, Z. W. Gao, K. F. Yang, W. Q. Zhanga, L. W. Xu. Nanosilver as a new generation of silver catalysts in organic transformations for efficient synthesis of fine chemicals, *Catalysis Science Technology,* **2015**, *5*, 2554-2574.

194. L. S. Ardakani, A. Surendar, L. Thangavelu, T. Mandal. Silver nanoparticles (AgNPs) as catalyst in chemical reactions, *Synthetic Communications,* **2021**, *51*(10), 1-21.

195. V. K. Shukla, R. S. Yadav, P. Yadav, A. C. Pandey. Green synthesis of nanosilver as a sensor for detection of hydrogen peroxide in water, *Journal of Hazardous Materials*, **2012**, *213-214*, 161-166.

196. M. Zahran, Z. Khalifa, M. A. H. Zahrana, M. A. Azzema. Recent advances in silver nanoparticle-based electrochemical sensors for determining organic pollutants in water: a review, *Materials Advances*, **2021**, *2*(22), 7350.

197. I. Ivanišević. The role of silver nanoparticles in electrochemical sensors for aquatic environmental analysis, *Sensors*, **2023**, *23*(7), 3692.

198. I. Shah, R. Adnan, W. S. W. Ngah, N. Mohamed. A review of the use of silver nanoparticles in environment, *International Journal of Chemistry*, **2014**, *35*(1), 1459-1471.

199. L. T. N. Hoa, T. Q. Minh, H. T. Kha, V. N. An. Synthesis and evaluation of the antibacterial activity of silver nanoparticles in indoor waterborne architectural coating, *Can Tho University Journal of Science*, **2021**, *57*(3A), 10-22.

200. B. Barman, H. Dhasmana, A. Verma, A. Kumar, D. N. Singh, V. K. Jain. Fabrication of silver nanoparticles on glass substrate using low-temperature rapid thermal annealing, *Energy & Envoronment*, **2018**, *29*(3), 358-371.

201. D. Roe, B. Karandikar, N. B. Savage, B. Gibbins, J. B. Roullet. Antimicrobial surface functionalization of plastic catheters by silver nanoparticles, *Journal of Antimicrobial Chemotherapy*, **2008**, *61*(4), 869-876.

202. A. Sadeghnejad, A. Aroujalian, A. Raisi, S. Fazel. Antibacterial nano silver coating on the surface of polyethylene films using corona discharge, *Surface & Coatings Technology*, **2014**, *245*, 1-8.

203. C. Lambré, J. M. B. Baviera, C. Bolognesi, A. Chesson, P. S. Cocconcelli, R. Crebelli, D. M. Gott, K. Grob, E. Lampi, M. Mengelers, A. Mortensen, I. L. Steffensen, C. Tlustos, H. V. Loveren, L. Vernis, H. Zorn, L. Castle, E. D. Consiglio, R. Franz, N. Hellwig, S. Merkel, M. R. Milana, E. Barthélémy, G. Rivière. Safety assessment of the substance silver nanoparticles for use in food contact materials, *EFSA Journal*, **2021,** *19*(8), 06790.

204. L. H. Tien. *Research on the preparation of chitosan - nano silver applied in post-harvest preservation of fruits*, PhD thesis, Hanoi University of Science and Technology, 2019.

205. N. B. Trung. *Research on synthesis of nano-silver-chitosan combination products for post-harvest preservation of dragon fruit*, PhD thesis, University of Danang, 2016.

https://doi.org/10.52111/qnjs.2024.18101

206. N. H. D. Tuan. *Research on fabrication of chitosan - nano silver film and initial experiment in preserving Hoa Loc mango*, PhD thesis, Can Tho University, 2014.

207. H. Chen, G. Zhang, W. Zhang, W. Gao. Silver nanoparticles deposited on a cotton fabric surface via an in situ method using reactive hyperbranched polymers and their anibachterial properties, *RSC Advances*, **2023**, *13*(17), 11450-11456.

208. M. F. Chaplin. Water: its importance to life, *Biochemistry and Molecular Biology Education*, **2001**, *29*(2), 54-59.

209. S. S. Ratpukdi, M. Fürhacker. Review: issues of silver nanoparticles in engineered environmental treatment systems, *Water, Air & Soil Pollution*, **2014**, *225*, 1939.

210. C. Forstner, T. G. Orton, P. Wang, P. M. Kopittke, P. G. Dennis. Wastewater treatment processing of silver nanoparticles strongly influences their effects on soil microbial diversity, *Environmental Science & Technology*, **2020**, *54*(21), 13538-13547.

211. G. Palani, H. Trilaksana, R. M. Sujatha, K. Kannan, S. Rajendran, K. Korniejenko, M. Nykiel, M. Uthayakumar. Silver nanoparticles for waste water management, *Molecules*, **2023**, *28*(8), 3520.

212. A. Fiorati, A. Bellingeri, C. Punta, I. Corsi, I. Venditti. Silver nanoparticles for water pollution monitoring and treatments: ecosafety challenge and cellulose-based hybrids solution, *Polymers,* **2020**, *12*(8), 1635.

213. N. T. Kien, T. T. T. Huong, N. H. Chau, D. D. Kim, D. T. Thuy. Size effect of copper nanoparticals on microcystis aeruginosa, *Vietnam Journal of Biotechnology*, **2018**, *16*(2), 361-367.

214. P. H. Lam, M. T. Le, D. M. T. Dang, T. C. Duc Doan, N. P. C. Tu, C. M. Dang. Safe concentration of silver nanoparticles in solution for white leg shrimp (litopeaneus vannamei) farming, *Biological and Chemical Research*, **2020**, *7*, 35-45.

215. L. C. Jiménez, A. R. A. Sánchez, C. H. M. Ruíz. Silver nanoparticles (AgNPs) as antimicrobials in marine shrimp farming: a review, *Aquaculture Reports*, **2020,** *18*, 100512.

216. T. S. Le, T. H. Dao, D. C. Nguyen, H. C. Nguyen, I. L. Balikhin. Air purification equipment combining a filter coated by silver nanoparticles with a nano-TiO_2 photocatalyst for use in hospitals, *Advances in Natural Sciences: Nanoscience and Nanotechnology*, **2015**, *6*, 015016.

217. R. Parameshwaran, S. Kalaiselvam. Energy conservative air conditioning system using silver nano-based PCM thermal storage for modern buildings, *Energy and Buildings*, **2014**, *69*, 202-212.

218. M. E. Quadros, L. C. Marr. Environmental and human health risks of aerosolized silver nanoparticles, *Journal of the Air Waste Management Association*, **2010**, *60*(7), 770-781.

219. E. Jankowska, J. Lukaszewska. Potential exposure to silver nanoparticles during spraying preparation for air-conditioning cleaning, *Medycyna Pracy*, **2013**, *64*(1), 57-67.

220. L. Ge, Q. Li, M. Wang, J. Ouyang, X. Li, M. M. Q Xing. Nanosilver particles in medical applications: synthesis, performance, and toxicity, *International Journal of Nanomedicine*, **2014**, *9*, 2399-2407.

221. T. D. Binh, T. T. Loan. Initial results of study on silver nanoparticles concentration applicated in hospital infection, *Journal of Medicine and Pharmacy - Hue University of Medicine and Pharmacy*, **2021**, *9*, 26-30.

222. S. Johaley, F. Karjodkar, P. Kaustubh, Sansare, S. Sharma, M. Saalim. Silver nanoparticles: new diagnostic and therapeutic approach in treatment of oral diseases, *European Journal of Pharmaceutical and Medical Research*, **2018**, *5*(6), 239-244.

223. E. A. A. Neel, L. Bozec, R. A. Perez, H. W. Kim, J. C. Knowles. Nanotechnology in dentistry: prevention, diagnosis, and therapy, *International Journal of Nanomedicine*, **2015**, *10*, 6371-6394.

224. P. Takáč, R. Michalková, M. Čižmáriková, Z. Bedlovičová, L. Balážová, G. Takáčová. The role of silver nanoparticles in the diagnosis and treatment of cancer: are there any perspectives for the future?, *Life*, **2023**, *13*, 466.

225. P. Mathur, S. Jha, S. Ramteke, N. K. Jain. Pharmaceutical aspects of silver nanoparticles, *Artificial Cells, Nanomedicine, and Biotechnology*, **2018**, *46*, 115-126.

226. V. L. Li. *Advancing silver nanostructures towards antibacterial applications*, PhD thesis, RMIT University, 2014.

227. X. Chen, H. J. Schluesener. Nanosilver: a nanoproduct in medical application, *Toxicology Letters*, **2008**, *176*, 1-12.

228. M. Konop, T. Damps, A. Misicka, L. Rudnick. Certain aspects of silver and silver nanoparticles in wound care: a minireview, *Journal of Nanomaterials*, **2016**, *2016,* 7614753.

229. F. Paladini, M. Pollini. Antimicrobial silver nanoparticles for wound healing application: progress and future trends, *Materials: Basel,* **2019**, *12*(16), 2540.

230. R. Pangestika, R. Ernawati, Suwarno. *Antiviral activity efect of silver nanoparticles (AgNPs) solution against the growth of infectious bursal disease virus on embryonated chickken eggs with elesa test*, The Veteribary Medicine International Conference, VMIC 2017, East Java, Indonesia, 2017.

231. E. O. Mikhailova. Silver nanoparticles: mechanism of action and probable bio-application, *Journal of Functional Biomaterials*, **2020**, *11*(4), 84.

232. R. R. Koyale, I. L. Patel, S. D. Pingale. Detection of cholera toxin using lactose-decorated silver nanoparticles, *Science and Technology*, **2018**, *4*(2), 902-906.

https://doi.org/10.52111/qnjs.2024.18101

TẠP CHÍ KHOA HỌC
TRƯỜNG ĐẠI HỌC QUY NHƠN

Tối ưu hóa các ước lượng trạng thái mũ cho hệ rời rạc dương với trễ thời gian và nhiễu

Nguyễn Thị Na[1], Lê Nguyễn Anh Thi[1], Lê Nguyễn Anh Thư[1], Đỗ Hữu Tuấn[1], Tô Gia Bảo[1], Trần Ngọc Nguyên[2,*]

[1]*Khoa Sư phạm, Trường Đại học Quy Nhơn, Việt Nam*
[2]*Khoa Toán và Thống kê, Trường Đại học Quy Nhơn, Việt Nam*

Ngày nhận bài: 21/07/2023; Ngày sửa bài: 02/10/2023;
Ngày nhận đăng: 23/10/2023; Ngày xuất bản: 28/02/2024

TÓM TẮT

Trong bài báo này, chúng tôi xem xét đến bài toán ước lượng trạng thái mũ cho hệ dương rời rạc với trễ thời gian và nhiễu. Bằng việc sử dụng một phép đổi trạng thái, chúng tôi chuyển hệ dương rời rạc với trễ thời gian và nhiễu về một hệ tương ứng không còn nhiễu. Bằng cách sử dụng các kỹ thuật tối ưu hóa, chúng tôi đưa ra các ước lượng trạng thái cho hệ nhận được (không có nhiễu), từ đó chúng tôi cũng thu được chặn trạng thái mũ cho hệ ban đầu. Một số ví dụ số đưa ra để minh họa cho các kết quả lý thuyết đạt được.

Từ khóa: *Hệ rời rạc dương, trễ thời gian, nhiễu, ước lượng trạng thái mũ, tối ưu hóa.*

**Tác giả liên hệ chính.*
Email: tranngocnguyen@qnu.edu.vn

https://doi.org/10.52111/qnjs.2024.18102

QUY NHON UNIVERSITY
JOURNAL OF SCIENCE

Optimization of exponential state estimates for positive discrete-time systems with delays and disturbances

Nguyen Thi Na[1], Le Nguyen Anh Thi[1], Le Nguyen Anh Thu[1]
Do Huu Tuan[1], To Gia Bao[1], Tran Ngoc Nguyen[2,*]

[1] *Faculty of Education, Quy Nhon University, Vietnam*
[2]*Department of Mathematics and Statistics, Quy Nhon University, Vietnam*

Received: 21/07/2023; Revised: 02/10/2023;
Accepted: 23/10/2023; Revised: 28/02/2024;

ABSTRACT

In this paper, we consider the problem of exponential state estimate for positive discrete-time system with time delays and disturbances. By using a state transformation, we reformulate a positive discrete-time system with time delays and disturbances to system without disturbances. By using optimization techniques, we derive the optimal exponential state estimate for the obtained systems (no noise), from which we also obtain the exponential state estimate for the original system. Some numerical examples are given to illustate the obtained theoretical results.

Keywords: *Positive discrete-time system, time delays, disturbances, exponential state estimate, optimization.*

1. INTRODUCTION

Positive systems are dynamical systems in which the state vectors are always belong to the nonnegative orthant providing that the initial value functions are nonnegative. This kind of systems has attracted a lot of attention in the mathematics community. Due to the positivity requirement, it is much more complicated and difficult to study on positive systems than on general systems. On one hand, similar to general systems, the time delay appears in the positive system and it can affect the stability of the system. On the other hand, different from general systems with time delays in which the quadratic Lyapunov-Krasovskii functional is used, the co-positive Lyapunov-Krasovskii functional is applied to study the stability and the performance of positive time-delay systems. In the research,[1] for the first time, the stability of linear positive systems with constant delays was considered by using the co-positive Lyapunov-Krasovskii functional. This result is extended to linear positive systems with time-varying delays in the research.[2] The L_1-gain and L_∞-gain are first mentioned by Briat[3] where the input-output gain is represented by linear inequalities. The Lyapunov-Krasovskii functional method is also a useful tool to study the problem of α-exponential stability for positive systems with bounded time-varying delays.[4,5]

*Corresponding author.
Email: tranngocnguyen@qnu.edu.vn

https://doi.org/10.52111/qnjs.2024.18102

Another approach to study positive systems is based on the comparison principle. There are many developments of this approach have been introduced in the literature, see, e.g:[6,7]

In practical time-delay systems, disturbance is a factor which appears very often and cannot be avoided. State estimate for time-delay systems with bounded disturbances is one of the key problems in control theory. For positive systems, the main approach for solving this problem is based on the property of Metzler/Hurwitz/Schur matrices.[5,8–11] For discrete-time systems,[4,12,13] consider the problem of state estimate for positive discrete-time systems with delays without disturbances. More specifically,[4,13] combined the co-positive Lyapunov-Krasovskii functional method with the solution comparison principle to address the exponential state estimate for positive systems with time-varying delays. In the research,[12] authors combined the solution comparison princple with the expontial state transformation. By using positive time-delay systems to bound from above switching sytems,[14] derived bounds for state vectors of switching systems with delays and disturbances. The state estimating problem for positive discrete-time systems with delays and bounded disturbances has been studied in.[11,15,16] In particular, the disturbances considered in[16] are assumed to be bounded from above and below by some known vectors. In,[17] the state bounding problem for positive singular systems with time-varying delay and bounded disturbances is addressed. However, it should be noted that these above state estimates have not yet been optimized.

Motivated by the above observation, in this paper, we consider the optimization problem of state estimates for positive discrete-time systems with delays and bounded disturbances. This work can be considered as a counterpart of[18] in which the continuous case was studied. Firstly, a state transformation is used to reformulate the problem of finding the optimized exponential state estimate for a positive discrete time-delay system with bounded disturbances into the problem of finding the optimized exponential state estimate for the positive discrete time-delay system without disturbance. Then, we apply an optimization scheme to the method proposed in[11] to obtain a better exponential componentwise estimate for the state vector of the transformed positive time-delay system (without disturbance). Consequently, we receive a more accurate exponential componentwise state estimate for the considered perturbed positive time-delay system.

2. NOTATION AND PRELIMINARIES

Notation: $\mathbb{N}$, $\mathbb{R}^n$ and $\mathbb{R}^n_{0,+}$ are respectively the set of nonnegative integers, the n-dimensional vector space and the nonnegative orthant in $\mathbb{R}^n$; $e = [1\ 1\ \cdots\ 1]^\top \in \mathbb{R}^n$; for two vectors $x = [x_1\ x_2\ \cdots\ x_n]^\top$, $y = [y_1\ y_2\ \cdots\ y_n]^\top$ in $\mathbb{R}^n$, two $n \times n$-matrices $A = [a_{ij}]$, $B = [b_{ij}]$, $x \prec y$ ($x \preceq y$) means that $x_i < y_i$ ($x_i \leq y_i$), $\forall i = 1, \cdots, n$ and $A \prec B$ ($A \preceq B$) means that $a_{ij} < b_{ij}$ ($a_{ij} \leq b_{ij}$), $\forall i, j = 1, \cdots, n$; A is a nonnegative matrix if $0 \preceq A$; $x \succeq y$ ($A \succeq B$) means that $y \preceq x$ ($B \preceq A$); $\rho(A) = \max\{|\lambda| : \lambda \in \sigma(A)\}$ is the spectral radius of A; I_n is the identity matrix of size n. The maximum, minimum of a finite set of vectors (of matrices) are understood componentwise.

Consider the following positive discrete-time system with time-varying delays and bounded disturbances

$$x(t+1) = A_0 x(t) + A_1 x(t - h_1(t)) + \omega(t),\ t \in \mathbb{N}, \quad (1)$$

$$x(s) = \varphi(s),\ s \in \{-h, -h+1, \ldots, 0\}, \quad (2)$$

where $x(t)$ is the state vector; $h_1(t) \in \{0, 1, \ldots, h\}$ is the time-varying delay; h is a known positive integer; A_0 and A_1 are two known nonnegative matrices; $\omega(t) \in \mathbb{R}^n_{0,+}$ is the vector of disturbance; $\varphi(s) \in \mathbb{R}^n_{0,+}$, $s \in \{-h, -h+1, \ldots, 0\}$, is the initial value function. Both $\omega(\cdot)$ and $\varphi(\cdot)$ are unknown but assumed to be bounded by some time-varying functions, i.e.

$$0 \preceq \omega(t) \preceq \bar{\omega}(t),\ t \in \mathbb{N}, \quad (3)$$

$$0 \preceq \varphi(s) \preceq \bar{\varphi}(s),\ s \in \{-h, -h+1, \ldots, 0\}, \quad (4)$$

where $\bar{\omega}(t)$, $\bar{\varphi}(s)$ are two known time-varying functions. Let denote by $x(t, \varphi, \omega)$ the unique solution of

(1) with respect to the initial value function $\varphi(s)$ and the vector of disturbance $\omega(t)$.

The aim of this paper is to find the smallest possible exponential estimate with a predefined decay rate $\lambda > 1$ of the solution $x(t, \varphi, \omega)$. More specifically, we tend to find the two smallest possible vectors β_l and β_r such that

$$x(t, \varphi, \omega) \preceq \beta_l + \beta_r \lambda^{-t}, \forall t \in \mathbb{N}. \quad (5)$$

Remark 2.1. Since $\bar{\omega}(t)$ is a known function, with a predefined decay rate λ, it can be found two nonnegative constant vectors $\bar{\omega}_l$ and $\bar{\omega}_r$ such that

$$\bar{\omega}(t) \preceq \bar{\omega}_l + \bar{\omega}_r \lambda^{-t} := \tilde{\omega}(t),\ t \in \mathbb{N}. \quad (6)$$

In this paper, we will assume the existence of $\bar{\omega}_l$ and $\bar{\omega}_r$ satisfying (6).

Remark 2.2. For each positive scalar $\lambda > 0$, let us define the matrix

$$M_\lambda := \lambda A_0 + \lambda^{h+1} A_1. \quad (7)$$

As in,[4,11] to guarantee the existence of exponential state estimate for system (5), it must be assumed that M_λ is a nonnegative and a Schur matrix, i.e. $\rho(M_\lambda) < 1$.

An exponential state estimate under the form (5) for system (1) is obtained via a solution comparison with the following system

$$y(t+1) = A_0 y(t) + A_1 y(t - h_1(t)) + d(t), t \in \mathbb{N}, \quad (8)$$

where $d(t)$ is a vector of disturbance which will be defined later.

The next lemma give us some useful facts related to systems (1) and (8) which will be needed in next parts of the paper.

Lemma 2.3. (i) Systems (1) and (8) are nonnegative;

(ii) With two initial value functions $0 \preceq \varphi_l(s) \preceq \varphi_r(s),\ s \in \{-h, \dots, 0\}$, and two vectors of disturbance $0 \preceq \omega_l(t) \preceq \omega_r(t),\ t \in \mathbb{N}$, we then have

$$x(t, \varphi_l, \omega_l) \preceq x(t, \varphi_r, \omega_l),$$
$$x(t, \varphi_r, \omega_l) \preceq x(t, \varphi_r, \omega_r),$$
$$x(t, \varphi_r, \omega_r) \preceq y(t, \varphi_r, \omega_r),$$
$$y(t, \varphi_l, \omega_l) \preceq y(t, \varphi_l, \omega_r).$$

Proof. The proof of this lemma can be conducted similarly as in.[5] □

3. EXPONENTIAL STATE ESTIMATE FOR POSITIVE DISCRETE-TIME SYSTEMS WITH DELAYS (WITHOUT DISTURBANCE)

Let us consider the following positive discrete-time system (without disturbance)

$$z(t+1) = A_0 z(t) + A_1 z(t - h_1(t)),\ t \in \mathbb{N}, \quad (9)$$
$$z(s) = \phi(s), s \in \{-h, -h+1, \dots, 0\}, \quad (10)$$

where the initial value function $\phi(\cdot)$ is unknown but assumed to be upper bounded by a known time-varying function $\bar{\phi}(\cdot)$, i.e.,

$$0 \preceq \phi(s) \preceq \bar{\phi}(s),\ s \in \{-h, -h+1, \dots, 0\}. \quad (11)$$

In this section, under the assumption that $\rho(M_\lambda) < 1$, we present a method to obtain a λ-exponential state estimate for the solution $z(t, \phi)$ of the system (9). By Lemma 2.3, one has

$$z(t, \phi) \preceq z(t, \bar{\phi}), t \in \mathbb{N}. \quad (12)$$

As in,[11] if there exist a vector $p \succ 0$, a number $\delta \in (0, 1)$ such that

$$(A_0 + A_1) p \prec \delta p \quad (13)$$

and a nonnegative scalar γ such that

$$\bar{\phi}(s) \preceq \gamma p \lambda^{-s}, s \in \{-h, -h+1, \dots, 0\}, \quad (14)$$

where $\lambda = \delta^{\frac{-1}{h+1}}$, we then have

$$z(t, \bar{\phi}) \preceq \gamma p \lambda^{-t}, t \in \mathbb{N}. \quad (15)$$

It should be noted that condition (13) is equivalent to $\rho(M_\lambda) < 1$ where M_λ is defined in (7). Combining two inequalities (12) and (15), we get

$$z(t, \phi) \preceq \gamma p \lambda^{-t}, t \in \mathbb{N}. \quad (16)$$

A vector $(p, \gamma) \in \mathbb{R}^n_+ \times \mathbb{R}_{0,+}$ satisfying the condition $(M_\lambda - I)\, p \prec 0$ and (14) can be found as below

https://doi.org/10.52111/qnjs.2024.18102

$$p = \left(I - \lambda A_0^\top - \lambda^{h+1} A_1^\top\right)^{-1} e, \tag{17}$$

$$\gamma = \max\left\{\max_{s=-h,\ldots,0} \frac{\|\bar{\phi}(s)\|_\infty}{p_1}, \ldots, \max_{s=-h,\ldots,0} \frac{\|\bar{\phi}(s)\|_\infty}{p_n}\right\}. \tag{18}$$

It can be seen that the factor vector (p, γ) of the exponential state estimate (16) has not been optimized. From this inequality, for each $i \in \{1, \ldots, n\}$, the exponential estimate of the i-th element of the state vector $z(t, \phi)$ can be obtained as below

$$z_i(t, \phi) \preceq \gamma p_i \lambda^{-t}, t \in \mathbb{N}. \tag{19}$$

For each $i \in \{1, \ldots, n\}$, our aim is to find a vector $(p, \gamma) \in \mathbb{R}_+^n \times \mathbb{R}_{0,+}$ such that the coefficient γp_i in (19) is minimized.

For simplicity, let us consider the case $i = 1$. Since the function $\bar{\phi}(s)$ is given, for each $i \in \{1, \ldots, n\}$, we can define the number

$$a_i := \max_{s \in \{-h, -h+1, \ldots, 0\}} \frac{\|\bar{\phi}_i(s)\|_\infty}{\lambda^{-s}}. \tag{20}$$

Let $a = [a_1, a_2, \ldots, a_n]$. Then, condition (14) is equivalent to $\gamma p \succeq a$.
Let

$$\Omega := \left\{(p, \gamma) \in \mathbb{R}_+^n \times \mathbb{R}_{0,+} \;\middle|\; \begin{array}{l} (M_\lambda - I)\, p \prec 0, \\ \gamma p \succeq a \end{array}\right\},$$

and $f(p, \gamma) := \gamma p_1$.
The smallest factor γp_1 of the exponential estimate of the first element in (19) is the optimal value of the following optimization problem:

$$\min f(p, \gamma) = \gamma p_1 \text{ such that } (p, \gamma) \in \Omega. \quad (\mathbf{OP}_1)$$

It should be noted that ($\mathbf{OP}_1$) is a nonconvex optimization problem. Hence, this problem is quite difficult to be solved. However, ($\mathbf{OP}_1$) can be reformulated under the form of the following linear programming:

$$\min g(u) = u_1 \text{ such that } u \in \Lambda, \quad (\mathbf{LP}_1)$$

where

$$\Lambda := \left\{u \in \mathbb{R}_+^n | \, (M_\lambda - I)\, u \prec 0, u \succeq a\right\}. \tag{21}$$

It can be seen that the two problems ($\mathbf{OP}_1$) and ($\mathbf{LP}_1$) have the same optimal value.

Similarly, for each $i \in \{2, 3, \ldots, n\}$, by solving linear programming problems

$$\min g(u) = u_i \text{ such that } u \in \Lambda, \quad (\mathbf{LP}_i)$$

where Λ is defined in (21), we find the smallest factor u_i^*, of the i-th element of the exponential state estimate $z_i(t, \phi)$ under the form (19). Combine the above procedures, we receive the minimized vector $u_r = [u_1^*, u_2^*, \ldots, u_n^*]^\top$ of the following exponential state estimate of the system (9)

$$z(t, \phi) \preceq u_r \lambda^{-t}, t \in \mathbb{N}. \tag{22}$$

From the above development, the main result of this section is summarized in the following theorem.

Theorem 3.1. Assume that $\rho(M_\lambda) < 1$ and $0 \preceq \phi(s) \preceq \bar{\phi}(s)$. The solution $z(t, \phi)$ of the system (9) has an exponential state estimate under the form

$$z(t, \phi) \preceq u_r \lambda^{-t}, \; t \in \mathbb{N} \tag{23}$$

where $u_r = [u_1^*, u_2^*, \ldots, u_n^*]^\top$ is the optimal factor vector and $u_i^*, i = 1, \ldots, n$, is the optimal value of the problem ($\mathbf{LP}_i$).

4. EXPONENTIAL STATE ESTIMATE FOR POSITIVE DISCRETE-TIME SYSTEMS WITH DELAYS AND BOUNDED DISTURBANCES

In this section, we will establish an exponential state estimate for the positive discrete-time system with time-varying delays and bounded disturbances system (1). Choose $\lambda > 1$ such that $\rho(M_\lambda) < 1$. Let us define two nonnegative vectors

$$q_l := (I - M_1)^{-1} \overline{\omega}_l, \tag{24}$$

$$q_r := (I - M_\lambda)^{-1} \overline{\omega}_r. \tag{25}$$

Let

$$\psi(s) := \max\left\{\bar{\varphi}(s), \; q_l + q_r \lambda^{-s+1}\right\}, \tag{26}$$

$$\phi(s) := \psi(s) - q_l - q_r \lambda^{-s+1}, \tag{27}$$

$$d(t) := \bar{\omega}_l + \bar{\omega}_r \lambda^{-t} + \lambda^{-t}(\lambda^{h+1} A_1 - \lambda^{h_1(t)+1} A_1) q_r. \tag{28}$$

Then, by comparing with conditions (3), (4), (6), and noting that $h_1(t) \le h$, $A_1 \succeq 0$, it can be verified that $\varphi(s) \preceq \bar{\varphi}(s) \preceq \psi(s),\ 0 \preceq \phi(s)$ và $\omega(t) \preceq \tilde{\omega}(t) \preceq d(t)$. From Lemma 2.3, one has

$$x(t,\varphi,\omega) \preceq x(t,\psi,\omega) \preceq y(t,\psi,\tilde{\omega}) \preceq y(t,\psi,d). \tag{29}$$

From the above inequalites, we just need to find an exponential state estimate for the solution $y(t,\psi,d)$ of the system (8).

Set

$$z(t) := y(t) - q_l - q_r\lambda^{-t+1},\ t \ge -h. \tag{30}$$

From (8), we then have

$$\begin{aligned}
&z(t+1)\\
&= y(t+1) - q_l - q_r\lambda^{-t}\\
&= A_0y(t) + A_1y\left(t-h_1(t)\right) + d(t)\\
&\quad - q_l - q_r\lambda^{-t}\\
&= A_0\left(z(t) + q_l + q_r\lambda^{-t+1}\right)\\
&\quad + A_1\left(z\left(t-h_1(t)\right) + q_l + q_r\lambda^{-t+h_1(t)+1}\right)\\
&\quad + d(t) - q_l - q_r\lambda^{-t}\\
&= A_0z(t) + A_1z\left(t-h_1(t)\right) + (A_0+A_1-I)q_l\\
&\quad + \lambda^{-t}(\lambda A_0 + \lambda^{h+1}A_1 - I)q_r\\
&\quad - \lambda^{-t}\left(\lambda^{h+1}A_1 - \lambda^{h_1(t)+1}A_1\right)q_r + d(t)\\
&= A_0z(t) + A_1z\left(t-h_1(t)\right)\\
&\quad + (M_1 - I)(I-M_1)^{-1}\bar{\omega_l}\\
&\quad + \lambda^{-t}(M_\lambda - I)(I-M_\lambda)^{-1}\bar{\omega_r}\\
&\quad - \lambda^{-t}\left(\lambda^{h+1}A_1 - \lambda^{h_1(t)+1}A_1\right)q_r + d(t)\\
&= A_0z(t) + A_1z\left(t-h_1(t)\right) - \bar{\omega_l} - \bar{\omega_r}\lambda^{-t}\\
&\quad - \lambda^{-t}\left(\lambda^{h+1}A_1 - \lambda^{h_1(t)+1}A_1\right)q_r + d(t)\\
&= A_0z(t) + A_1z\left(t-h_1(t)\right).
\end{aligned}$$

This means that we obtain the positive discrete-time system with delay and without disturbance. We then deduce from (30) that

$$y(t,\psi,d) = z(t,\phi) + q_l + q_r\lambda^{-t+1}, \tag{31}$$

where, $\phi(\cdot)$ is defined in (27). Combine inequalites (29) and (31), one gets

$$x(t,\varphi,\omega) \preceq z(t,\phi) + q_l + q_r\lambda^{-t+1}. \tag{32}$$

From (22) and (32), we have

$$\begin{aligned}
x(t,\varphi,\omega) &\preceq u_r\lambda^{-t} + q_l + q_r\lambda^{-t+1}\\
&= q_l + (u_r + \lambda q_r)\lambda^{-t}.
\end{aligned}$$

From this, we obtain an exponential state estimate (5) for system (1) with factor vectors defined by

$$\beta_l := q_l,\ \beta_r := u_r + \lambda q_r, \tag{33}$$

where the vector u_r is found as in Theorem 3.1. The main result of this section is summarized in the following theorem.

Theorem 4.1. *Assume that* $\rho(M_\lambda) < 1$, (3) *and* (4) *hold. The solution* $x(t,\varphi,\omega)$ *is estimated via the formula* (5) *where the vectors* β_l, β_r *are found by* (33).

5. NUMERICAL EXAMPLES

In this section, we present two numerical examples to illustrate the results obtained in Theorems 3.1 and 4.1.

Example 5.1. Consider the following time-delay system

$$\begin{aligned}
x(t+1) &= A_0x(t) + A_1x(t-h_1(t)) \quad t \in \mathbb{N},\\
x(s) &= \phi(s), \quad s = -2,-1,0,
\end{aligned} \tag{34}$$

where, $x(t) \in \mathbb{R}^3, h_1(t) \in \{0,1,2\}$, A_0 and A_1 are two nonnegative matrices with coefficients

$$A_0 = \begin{bmatrix} 0.21 & 0.21 & 0.12\\ 0.04 & 0.12 & 0.14\\ 0.12 & 0.05 & 0.26 \end{bmatrix},$$

$$A_1 = \begin{bmatrix} 0.32 & 0.01 & 0.18\\ 0.03 & 0.12 & 0.02\\ 0.04 & 0.01 & 0.21 \end{bmatrix},$$

the initial value function $\phi(\cdot)$ is unknown and satisfies $|\phi(s)| \preceq \bar{\phi}(s)$ where

$$\bar{\phi}(-2) = \begin{bmatrix} 2 & 3 & 0.5 \end{bmatrix}^\top,$$

$$\bar{\phi}(-1) = \begin{bmatrix} 3.1 & 2.4 & 3.2 \end{bmatrix}^\top,$$

$$\bar{\phi}(0) = \begin{bmatrix} 0.3 & 0.5 & 0.1 \end{bmatrix}^\top.$$

https://doi.org/10.52111/qnjs.2024.18102

By using Remark 4 in the ressearch,[4] we deduce that the range of the decay rate λ is $[1, 1.1375]$.

Let us consider the case $\lambda = 1.1$. By applying Theorem 3.1, we receive the following table.

Methods	$\lambda = 1.10$		
	u_1	u_2	u_3
Our new method	4.9163	2.4793	2.9091
Method in [11]	9.6567	3.2000	5.6305

The above table shows that with the decay rate $\lambda = 1.10$, the elements of the factor vectors obtained by our new method is smaller than the ones obtained by.[11]

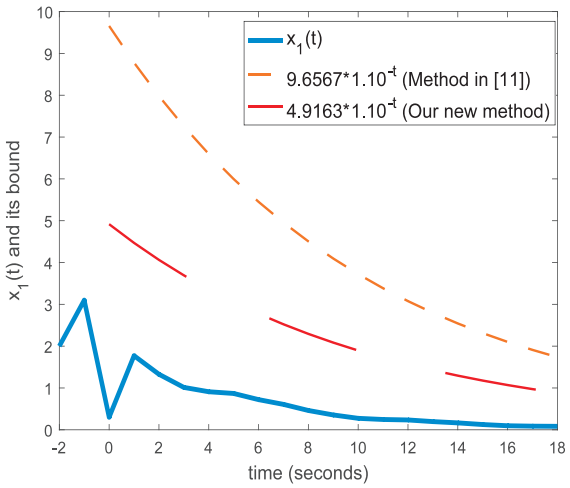

Figure 1. $x_1(t)$ and its bounds.

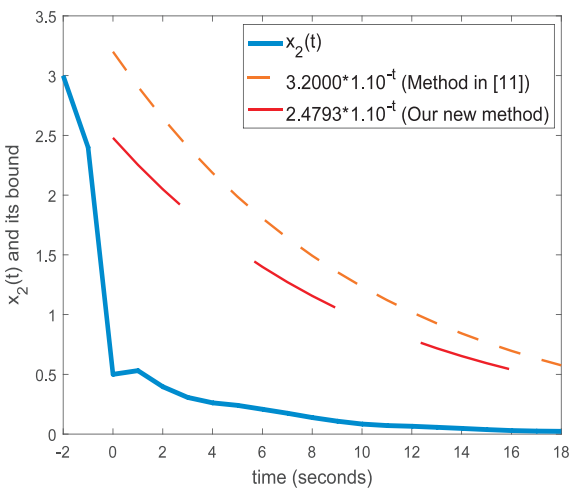

Figure 2. $x_2(t)$ and its bounds.

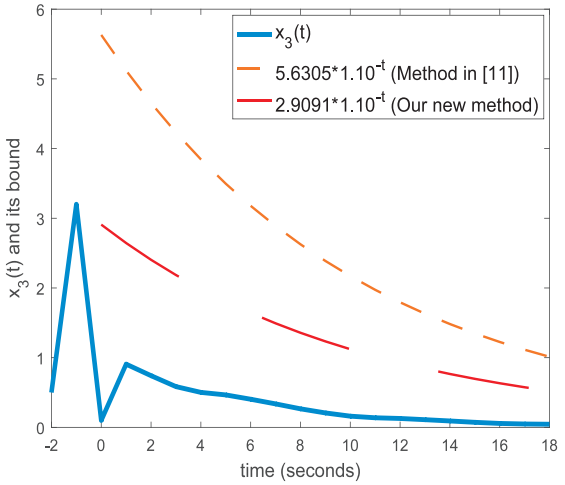

Figure 3. $x_3(t)$ and its bounds.

For visual illustration, let us choose $h_1(t) = 1 + \sin t$. Figures 1-3 give us the trajectories of state vector $x(t, \varphi, \omega)$ and its bounds. It can be seen that our new method provides more accurate estimates for the state vector of the system (34).

Example 5.2. Consider the following positive discrete-time system with delays and disturbances

$$\begin{aligned} x(t+1) &= A_0 x(t) + A_1 x(t - h_1(t)) + \omega(t) \quad t \in \mathrm{N}, \\ x(s) &= \varphi(s), \quad s = -2, -1, 0, \end{aligned} \tag{35}$$

where, $x(t) \in \mathbb{R}^3, h_1(t) \in \{0, 1, 2\}$, A_0 are A_1 non-negative matrices with

$$A_0 = \begin{bmatrix} 0.21 & 0.21 & 0.12 \\ 0.04 & 0.12 & 0.14 \\ 0.12 & 0.05 & 0.26 \end{bmatrix},$$

$$A_1 = \begin{bmatrix} 0.32 & 0.01 & 0.18 \\ 0.03 & 0.12 & 0.02 \\ 0.04 & 0.01 & 0.21 \end{bmatrix},$$

$\omega(t) \in \mathbb{R}^n_{0,+}$ is the vector of disturbance satisfying $0 \preceq \omega(t) \preceq \bar{\omega}(t), t \in \mathbb{N}$; the initial value function $\varphi(s)$, $s = -2, -1, 0$, satisfying condition $|\varphi(s)| \preceq \bar{\varphi}(s)$ with

$$\bar{\varphi}(s) = \begin{bmatrix} 13 \\ 8 \\ 10.2 \end{bmatrix}, \bar{\omega}(t) = \begin{bmatrix} 0.6 \\ 1 \\ 0.7 \end{bmatrix} + \begin{bmatrix} 0.2 \\ 0.3 \\ 0.5 \end{bmatrix} \lambda^{-t}.$$

By using Remark 4 in,[4] we find that the range of decay rate is $[1, 1.1375]$.

Let us consider the case $\lambda = 1.1$. By applying the development in Section 4, we find that

$$\beta_l = \begin{bmatrix} 4.1627 & 2.2965 & 2.8374 \end{bmatrix}^\top,$$
$$\beta_r = \begin{bmatrix} 13.0887 & 5.7035 & 7.7428 \end{bmatrix}^\top.$$

This gives us the exponential state estimate for the positive discrete-time system with delays and disturbances (35).

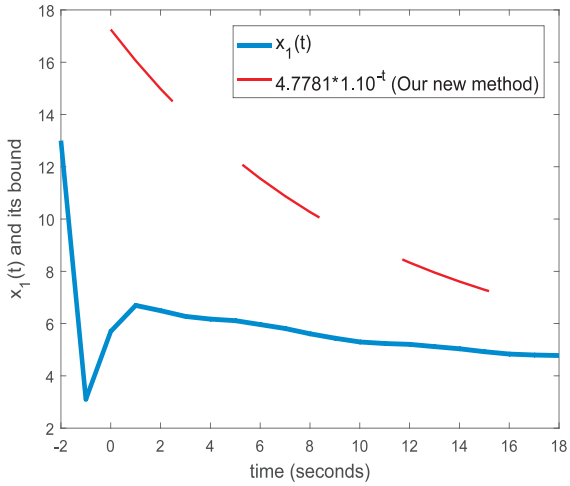

Figure 4. $x_1(t)$ and its bounds.

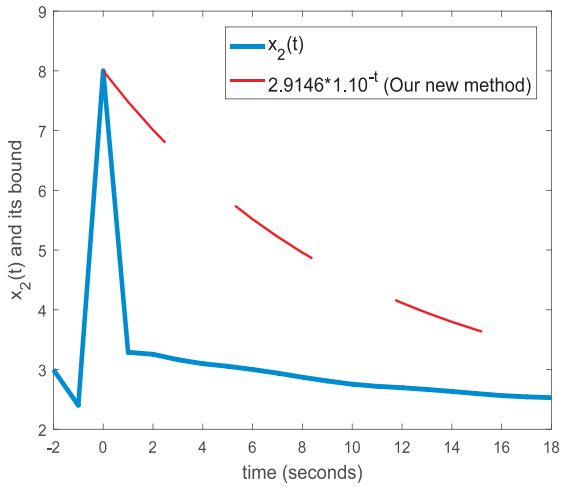

Figure 5. $x_2(t)$ and its bound.

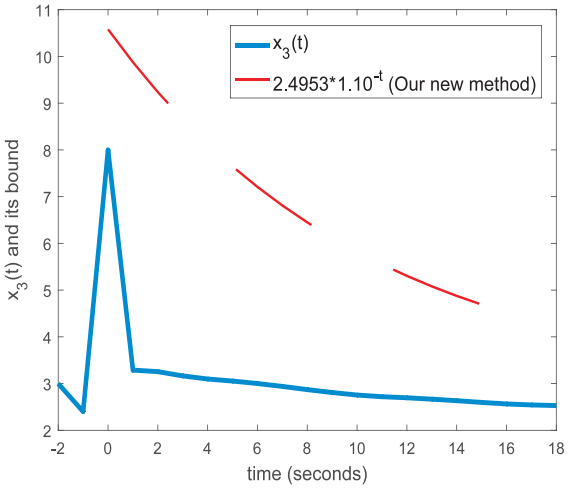

Figure 6. $x_3(t)$ and its bound.

For visual illustration, let us choose $h_1(t) = 1 + \sin t$. Figures 4-6 give us the trajectories of state vector $x(t, \varphi, \omega)$ and its bound obtained by our new method.

6. CONCLUSION

In this paper, we have considered the problem of exponential state estimate for positive discrete-time systems with delays and disturbances. A state transformation is used to transform positive discrete-time systems with delays and disturbances to systems without disturbance. By applying an optimization techique, we have found the smallest possible exponential state estimate for the transfromed systems from which the estimates for the considered systems are derived. The approach in this paper can be used to study some other classes of positive systems comprising disturbances.

Acknowledgment

The authors would like to thank the anonymous referees for his/her careful reading and insightful comments. This research is conducted within the framework of science and technology projects at institutional level of Quy Nhon University under the project code T2023.791.01.

REFERENCES

1. W. M. Haddad, V. Chellaboina. Stability theory for nonnegative and compartmental dynamical systems with time delay, *Systems & Control Letters*, **2004**, *51*(5), 355–361.

2. M. A. Rami. *Stability analysis and synthesis for linear positive systems with time-varying delays*, Springer, Berlin Heidelberg, 2009.

3. C. Briat. Robust stability and stabilization of uncertain linear positive systems via integral linear constraints: L_1-gain and L_∞-gain characterization, *International Journal of Robust and Nonlinear Control*, **2013**, *23*(17), 1932–1954.

4. P. T. Nam, P. N. Pathirana, H. Trinh. Partial state bounding with a pre-specified time of non-linear discrete systems with time-varying delays, *IET Control Theory & Applications*, **2016**, *10*(13), 1496–1502.

5. P. T. Nam, H. Trinh, P. N. Pathirana. Minimization of State bounding for perturbed positive systems with delays, *SIAM Journal on Control and Optimization*, **2018**, *56*(3), 1739–1755.

6. X. Liu, W. Yu, L. Wang. Stability analysis of positive systems with bounded time-varying delays, *IEEE Transactions on Circuits and Systems II: Express Briefs*, **2009**, *56*(7), 600–604.

7. P. T. Nam, T. H. Luu. State bounding for positive coupled differential-difference equations with bounded disturbances, *IET Control Theory & Applications*, **2019**, *13*(11), 1728–1735.

8. L. V. Hien, H. M. Trinh. A new approach to state bounding for linear time-varying systems with delay and bounded disturbances, *Automatica*, **2014**, *50*(6), 1735–1738.

9. P. Nam, P. Pathirana, H. Trinh. Reachable set bounding for nonlinear perturbed time-delay systems: the smallest bound, *Applied Mathematics Letters*, **2015**, *43*, 68–71.

10. P. H. A. Ngoc. Stability of positive differential systems with delay, *IEEE Transactions on Automatic Control*, **2013**, *58*(1), 203–209.

11. P. H. A. Ngoc, L. T. Hieu. New criteria for exponential stability of nonlinear difference systems with time-varying delay, *International Journal of Control*, **2013**, *86*(9), 1646–1651.

12. C. Tinh, P. Nam, T. Nguyen, H. Trinh. Exponential estimate with a time-varying factor for positive discrete-time systems with time-delays, *Applied Mathematics Letters*, **2021**, *119*, 107194.

13. S. Zhu, M. Meng, C. Zhang. Exponential stability for positive systems with bounded time-varying delays and static output feedback stabilization, *Journal of the Franklin Institute*, **2013**, *350*(3), 617–636.

14. H. Haimovich, M. Seron. Bounds and invariant sets for a class of discrete-time switching systems with perturbations, *International Journal of Control*, **2014**, *87*(2), 371–383.

15. L. Xu, S. S. Ge. Exponential ultimate boundedness of nonlinear stochastic difference systems with time-varying delays, *International Journal of Control*, **2015**, *88*(5), 983–989.

16. P. T. Nam, H. M. Trinh, P. N. Pathirana. Componentwise ultimate bounds for positive discrete time-delay systems perturbed by interval disturbances, *Automatica*, **2016**, *72*, 153–157.

17. N. H. Sau, M. V. Thuan. State bounding for positive singular discrete-time systems with time-varying delay and bounded disturbances, *IET Control Theory & Applications*, **2019**, *13*, 2571–2582.

18. C. T. Tinh, D. L. Thuy, P. T. Nam, H. M. Trinh. Componentwise state bounding of positive time-delay systems with disturbances bounded by a time-varying function, *International Journal of Control*, **2023**, *96*(2), 332–338.

TẠP CHÍ KHOA HỌC
TRƯỜNG ĐẠI HỌC QUY NHƠN

Tổng hợp xanh vật liệu khung kim loại - hữu cơ Cu_3BTC_2 loại bỏ methylene blue trong môi trường nước

Nguyễn Thị Thu Hương[1], Nguyễn Văn Bằng[2], Nguyễn Thị Lan Anh[2], Trịnh Dương Vương[3], Nguyễn Mạnh Tiến[4], Đỗ Bình Minh[1], Lã Đức Dương[2], Nguyễn Thị Hoài Phương[2,*]

[1]Viện Công nghệ mới, Viện Hàn lâm Khoa học và Công nghệ Việt Nam, Việt Nam
[2]Phân viện Hóa - Môi trường, Trung tâm Nhiệt đới Việt - Nga, Việt Nam
[3]Trường Sĩ quan Không quân, Việt Nam
[4]Viện Kỹ thuật Phòng không - Không quân, Việt Nam

Ngày nhận bài: 10/09/2023; Ngày sửa bài: 14/12/2023;
Ngày nhận đăng: 17/01/2024; Ngày xuất bản: 28/02/2024

TÓM TẮT

Nghiên cứu này trình bày kết quả nghiên cứu tổng hợp, mô tả đặc trưng và khả năng hấp phụ của vật liệu khung cơ kim trên cơ sở Cu(II) và phối tử hữu cơ 1,3,5-benzene tricarboxylate (Cu-BTC). Cu-BTC được tổng hợp bằng phương pháp vi sóng đơn giản và được đo FTIR, SEM, XRD để kiểm tra đặc tính liên kết, hình thái, cấu trúc tinh thể. Cu-BTC được sử dụng làm chất hấp phụ để loại bỏ thuốc nhuộm họ azo như methylene blue (MB) trong nước. Các nghiên cứu về ảnh hưởng của pH, nồng độ, thời gian hấp phụ cho thấy loại bỏ MB theo mô hình hấp phụ đẳng nhiệt Freundlich và mô hình động học biểu kiến bậc hai. Do đó, cơ chế hấp phụ MB đa lớp trên bề mặt Cu-BTC không đồng nhất và chịu ảnh hưởng của lực hút tĩnh điện. Những đặc trưng này cho thấy Cu-BTC là vật liệu hứa hẹn trong việc loại bỏ MB ra khỏi nước thải định hướng ứng dụng tiềm năng trong xử lý môi trường.

Từ khóa: *Hóa học xanh, vật liệu khung kim loại - hữu cơ, kỹ thuật vi sóng, methylene blue, xử lý môi trường.*

**Tác giả liên hệ chính.*
Email: hoaiphuong1978@gmail.com

QUY NHON UNIVERSITY
JOURNAL OF SCIENCE

Green synthesis of metal-organic framework material Cu_3BTC_2 removes methylene blue from aqueous media

Thu Huong Nguyen Thi[1], Van Bang Nguyen[2], Lan Anh Nguyen Thi[2], Duong Vuong Trinh[3], Manh Tien Nguyen[4], Binh Minh Do[1], Duc Duong La[2], Hoai Phuong Nguyen Thi[2,*]

[1]Institute of New Technology, Vietnam Academy of Science and Technology, Vietnam
[2]Department of Chemistry and Environment, Joint Vietnam-Russia Tropical Science and Technology Research Center, Vietnam
[3]Air Force Officer School, Vietnam
[4]Institute of Technology Air Defense - Air Force, Vietnam

Received: 10/09/2023; Revised: 14/12/2023;
Accepted: 17/01/2024; Published: 28/02/2024

ABSTRACT

This study presents the results of the synthesis, characterization, and adsorption capacity of organometallic framework materials based on Cu(II) and the organic ligand 1,3,5-benzene tricarboxylate (Cu-BTC). Cu-BTC was synthesized by simple microwave method, and FTIR, SEM, and XRD were measured to check the bonding, morphology, and crystal structure properties. Cu-BTC is an adsorbent to remove azo dyes such as methylene blue (MB) from water. Studies on the effects of pH, concentration, and adsorption time showed that MB was removed according to the Freundlich isotherm adsorption model and the apparent second-order kinetic model. Therefore, the multilayer MB adsorption mechanism on the Cu-BTC surface is heterogeneous and influenced by electrostatic attraction. These characteristics show that Cu-BTC is a promising material for removing MB from wastewater with potential applications in environmental treatment.

Keywords: *Green chemistry, metal-organic frameworks, microwave method, methylene blue, environment treatment.*

1. INTRODUCTION

Textile industry wastewater has severe impacts on living organisms. It must be treated to a certain extent before being released into the environment. Dyeing process wastewater contains non-biodegradable and high-toxic pigments,[1] which have been found to damage the balance[2-4] and integrity of ecological systems[5,6] and have carcinogenic effects on long-term exposure.[7-9] Therefore, wastewater treatment in the textile dyeing industry has become a concern on a global scale.[10,11] In this context, researchers have proposed metal-organic frameworks (MOFs) as one of the effective methods to remove dye wastewater.[12-14] MOF exhibits high adsorption capacity in dye removal with tunable pore diameter and surface morphology compared with other conventional adsorbent materials such as activated carbon,[15,16] carbon nanotubes,[17] zeolites,[18] etc. In addition, the metal-organic

**Corresponding author.*
Email: hoaiphuong1978@gmail.com

https://doi.org/10.52111/qnjs.2024.18103

framework material also has a significant photocatalytic activity for treating different dye types.[19-21] These studies also evaluated the effectiveness of these MOFs in the process of dye removal from wastewater. Metal-organic frameworks based on copper (II) have also been synthesized, modified, combined, doped, hybridized... and evaluated for their ability to remove dyes in water environments.[22,23]

Many studies have applied different synthesis methods to fabricate copper-based metal-organic frameworks. Solvothermal, one-step in situ growth, and pre-grinding methods have all been studied to synthesize this material.[24,25] Synthesis of MOFs has also been of interest to meet green chemistry requirements where selection of synthesis elements has been based on reduced energy input, safe reaction solvents (such as water and supercritical solvents), continuous manufacturing method, and performance design of MOFs through theoretical predictions.[26,27] In this study, copper-based metal-organic framework (Cu-BTC) was synthesized green by microwave method using water/ethanol mixed solvent mixture. Cu-BTC was also evaluated for its ability to remove dyes in water through pure adsorption and simultaneous catalytic-adsorption mechanisms.

2. EXPERIMENTAL

2.1. Chemicals, equipment and tools

Copper (II) chloride dihydrate ($CuCl_2.2H_2O$ 99%) was purchased from Xilong Chemical Co., Ltd., Guangdong, China. 1,3,5-benzene tricarboxylic acid (H_3BTC 98%) is imported from Shanghai Macklin Biochemical Co., Ltd., Shanghai, China. Methylene blue ($C_{16}H_{18}ClN_3S$, MB ≥ 85%) was gotten from Merck, Germany. Ethanol solution (C_2H_5OH 96%), Sodium hydroxide (NaOH > 96%), and Hydrochloric acid (HCl > 35%) were bought from Duc Giang Chemical, Vietnam. Double distilled water is made in the laboratory.

The equipment used in the experiment includes an Electrolux microwave oven (50 Hz, 1050 W), drying cabinet, and Ultrasonic Cleaner Ultrasonic Cleaner JP-060S made in China; Centrifuge Hettich Universal 320 from Germany.

2.2. Material synthesis

The material was synthesized from $CuCl_2$: Weigh 1.7g of $CuCl_2.2H_2O$ into a 250 mL beaker, then add 100 mL distilled water, add 2.8g H_3BTC acid, and stir well. Put the glass cup in the microwave (reaction conditions are 45 min, 80^{o}C). Next, filter and wash the precipitate with ethanol and distilled water 5 times using an ultrasonic cleaner, and then centrifuge at 7,000 rpm for 10 min with a centrifuge to obtain a very blue solid product. Then, the solid product is dried at 120 ^{o}C for 2 hours in a drying oven. Store the synthetic material in a tightly closed plastic container and use it for the following experiments.

2.3. Techniques and methods

Characterizations. The functional groups present in the material were determined using the FTIR infrared spectroscopy technique in the 400-4000 cm^{-1} wavelength range. The material's morphology was observed using scanning electron microscopy techniques with magnification capabilities up to 100,000 times. The crystal structure of the Cu-BTC framework material in powder form was analyzed through an X-ray diffraction analyzer-D8-Advance. At 1.54Å in a copper X-ray tube (Cu-Kα), the device is operated at 44 mA and 40 kV voltage. The scanning speed is 0.2^o/min to measure materials in the range (2θ) from 10^o to 70^o.

Methylene blue adsorption. The MB solution (1 g/L) was diluted with distilled water twice to prepare the required MB solution concentrations (10, 20, 30, 40, and 50 mg/L). Methylene blue (MB) was used as a dye to study the adsorption capacity of the synthesized Cu-BTC organometallic framework. The pH of the MB solution was normalized with 1M NaOH solution and 1M HCl solution. Conducting experiments on the influence of pH on the MB adsorption process. 10 mg of Cu-BTC

was added to each test tube containing 20 mL of MB solution. Each glass test tube with MB solution pH of 3, 5, 7, 9, and 11, respectively, was sealed with a rubber stopper, put into a closed light-blocking cabinet, and a light cabinet to study the effect of light. Then, the test tubes were thoroughly mixed by ultrasonic washing for 15 minutes, shaking with a shaker at 200 rpm at room temperature to filter the solution, and finally, photometrically. UV-Vis spectrum at maximum absorption wavelength to determine MB concentration based on the linear equation from the MB standard curve. Experiments to investigate the effect of pH on dye handling were carried out under the same conditions. Sample dilution was performed with double distilled water if the MB solution concentration value exceeded the maximum adsorption limit of the graph containing the MB calibration curve. Investigation of the kinetics of the adsorption process by influencing factors of pH, adsorption time, and initial MB solution concentration with the same amount of Cu-BTC adsorbent at equilibrium time was studied the same as above. The maximum wavelength of the MB solution is determined to be 662 nm. The equation can determine the concentration of MB solution at time t (unit is mg/L) to be

C = (Abs -0.0216)/0.1587 (R^2 = 0.9985),

where A is the light absorption intensity.

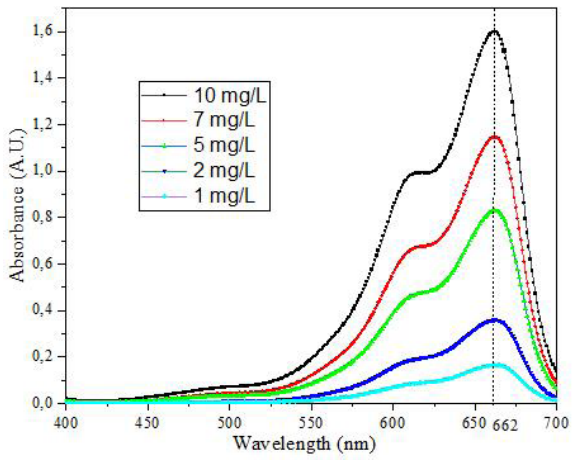

Figure 1. UV-Vis spectra of the MB standard sample at 400 to 700 nm wavelengths.

The MB removal efficiency of the material is calculated according to the equation:

$$H = \frac{C_0 - C_t}{C_0} \times 100\%$$

The adsorption capacity was calculated according to the formula:

$$q_t = \frac{V \times (C_0 - C_t)}{m}$$

Where C_o and C_t are the initial concentration of MB solution and at time t (mg/L), respectively; V is the volume of MB solution used (L), and m is the mass of Cu-BTC (g).

Isothermal and kinetics of MB adsorption. Langmuir, Freundlich, and Temkin adsorption models are used to describe the adsorption equilibrium as follows:

Langmuir model: $\frac{C_e}{q_e} = \frac{1}{K_L q_m} + \frac{C_e}{q_m}$

Freundlich model: $\ln q_e = \ln K_F + \frac{1}{n} \ln C_e$

Temkin model: $q_e = B_T \ln K_T + B_T \ln C_e$

$$B_T = \frac{RT}{b_T}$$

In which q_e is the equilibrium adsorption capacity (mg/g), q_m is the maximum adsorption capacity (mg/g), K_L is the Langmuir constant (L/mg), K_F is the Freundlich [(mg/g)(L/mg)$^{1/n}$], and K_T is the Temkin constant (L/g); C_e is the equilibrium concentration of adsorbent (mg/L); n is Freundlich's linear constant, b_T is related to the adsorption heat, R is the universal gas constant and T is the temperature. The Langmuir adsorption model assumes that all adsorption sites have the same affinity and reach a maximum value for the adsorbent and adsorbate after forming a monolayer on a uniform adsorbent surface at a specific temperature and no interactions between the adsorbed molecules. In contrast to the Langmuir model, the Freundlich model assumes that the adsorption surface energy is heterogeneous. The n value represents

https://doi.org/10.52111/qnjs.2024.18103

the deviation from the linearity, the heterogeneity of the adsorption site. If n is between 1 and 10, then the adsorption is favorable. The larger n is, the higher the heterogeneity of the adsorption site. The Temkin is a chemical adsorption model based on the interaction between positive and negative charges.

To elucidate the adsorption kinetic process of MB on Cu-BTC, three apparent kinetic models, namely first-order, second-order, and intra-particle diffusion, are considered to explain the experimental data:

First-order apparent kinetic model:

$$\ln(q_e - q_t) = \ln(q_e) - k_1 t$$

Second-order apparent kinetic model:

$$\frac{t}{q_t} = \frac{1}{k_2 q_e^2} + \frac{t}{q_e}$$

Particle diffusion model: $q_t = k_i t^{1/2} + C$

In which q_e, q_t is the adsorption capacity at equilibrium time and at time t on the material (mg/g), respectively; k_1 is the first-order apparent adsorption rate constant (min^{-1}), k_2 is the second-order apparent adsorption rate constant (g/mg.min); C is the blocking coefficient in the particle and k_i is the diffusion rate constant in the particle ($mg/g.min^{1/2}$).

3. RESULTS AND DISCUSSION

3.1. Characterization

The FTIR spectra of the H_3BTC sample and the Cu-BTC organometallic framework material (Figure 2) contain characteristic peaks at ~1640, ~1447, and ~1370 cm^{-1}. FTIR spectrum of Cu-BTC using KBr in the 400 - 1700 cm^{-1} range. The peaks at ~1640, ~1447, and ~1370 cm^{-1} characteristically bond the carboxylate group -COO- in Cu-BTC, indicating the formation of Cu-BTC organometallic framework material.[28,29] The broad bands at 3346 cm^{-1} are believed to be OH bonds and water adsorbed on the Cu-BTC surface. In addition, no peak was observed in the 1680 - 1750 cm^{-1} range, which shows no free H_3BTC ligand in the Cu-BTC material.[28] The range 1500 - 1400 cm^{-1} represents the C=C bond in the aromatic ring.[28] The FTIR shows the carbonyl group in H_3BTC peaks at 1721 cm^{-1}.[29] The -CO-C bond in Cu-BTC is demonstrated by the appearance of the peak at about 1109 cm^{-1}. The 827 - 1153 cm^{-1} range belonged to the OC=O and CO bond of 1,4 benzene dicarboxylic acid. At 487 cm^{-1} and 728 cm^{-1}, it is assigned the CH bond of the benzene ring and the Cu-O bond form between the carboxylic groups of H_3BTC and Cu(II), respectively.[30,31]

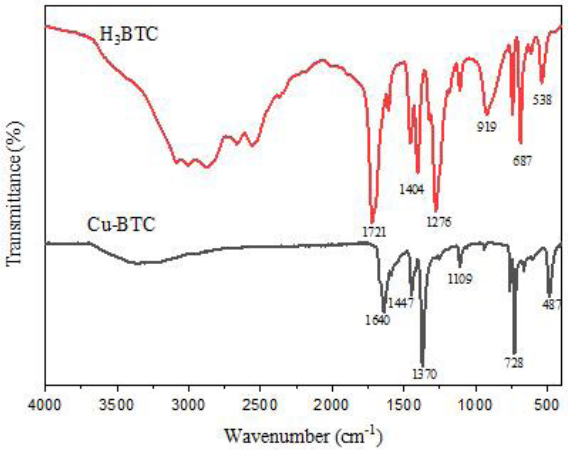

Figure 2. FTIR spectrum of H_3BTC and Cu-BTC.

SEM image of Cu-BTC material in Figure 3. Cu-BTC crystal particles have an octahedral shape. Cu-BTC morphology is consistent with other reported SEM images.[28,32,33] Some particles that do not have a characteristic morphology in the SEM images are fused particles of Cu-BTC crystals.

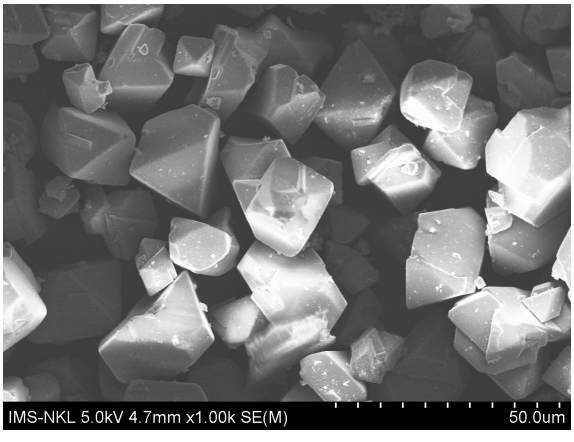

Figure 3. SEM images of Cu-BTC.

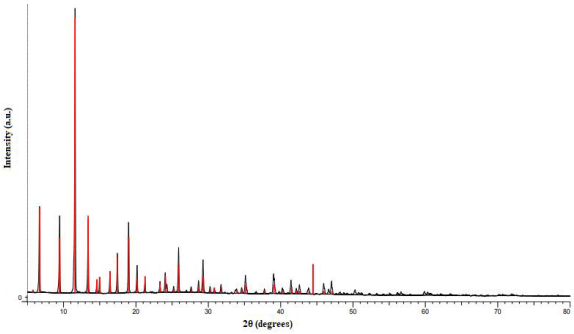

Figure 4. XRD patterns of Cu-BTC.

X-ray diffraction (XRD) analysis examined the crystal structure of the powdered Cu-BTC in Figure 4. The characteristic peaks are found in the Cu-BTC crystalline in the range up to 2θ, namely 11.6°, 13.5°, 14.9°, and 16.6° corresponding to the crystal faces (222), (400), (420), (422) and is consistent with the published study,[28,32,34-37] which shows that metal-organic frameworks are successfully fabricated. The peak with the highest intensity at 2θ = 11.59° is related to the high degree of crystallinity of the material.[30] XRD and SEM spectrum results show the successful fabrication of Cu-BTC.

3.2. Effect of pH on the adsorption of methylene blue

The adsorption capacity of the MB solution is significantly influenced by its pH level.[38] Figure 5 and Table 1 show that the optimal pH for methylene blue adsorption onto Cu-BTC is pH ~ 7. The results are similar to previous studies.[30-39]

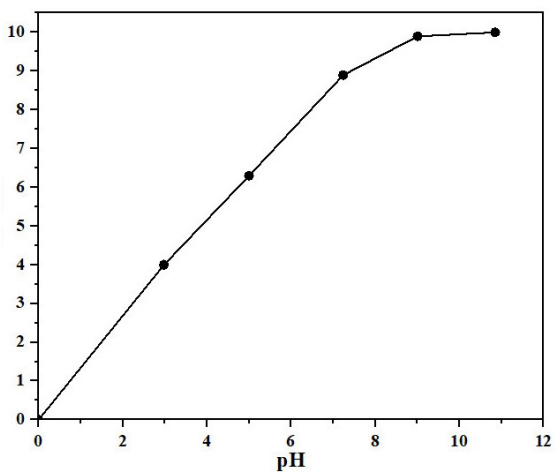

Figure 5. Effect of pH on the adsorption capacity of MB. Experimental conditions include 25°C, 0.011g Cu-BTC.

The adsorption capacity of MB increases when the pH rises from 4 to 7. However, the adsorption capacity remained almost constant with an increase in pH from 7 to 11. The point of zero charge of pH (pH_{PZC}) for Cu-BTC material was found to be 4.[40] When pH < 4, the surface of the adsorbent turns positively charged, and the adsorption process of methylene blue onto Cu-BTC is difficult. When pH ≥ 4, the surface of the adsorbent turns negatively charged, and this process is easy. When 4 ≤ pH < 7, H^+ ions compete with dye cations through electrostatic attraction, causing a decrease in adsorption. It is possible that a low pH might not be suitable for adsorption of MB. When pH increases, the MB solution containing Cl^- binds to Cu-BTC material quickly and reacts with NaOH to form NaCl and MB-S+ OH. The mass of NaCl can change the adsorption of MB-S+ OH on the surface of Cu-BTC material. While pH ~ 7, the hydrolysis process to release MB molecules is negligible.

Table 1. Effect of pH on removal of MB after 30 minutes of Cu-BTC in adsorption processes.

pH	C_t (mg/L)	H (%)	q_t (mg/g)
2.98	7.83	21.7	4.0
5.00	6.56	34.4	6.3
7.24	5.11	48.9	8.9
9.01	4.54	54.6	9.9
10.85	4.48	55.2	10.0

Note: Experimental conditions include 25°C, 0.011g Cu-BTC, and 20 mL of 10 mg/L MB solution.

3.3. Isothermal and Kinetics of MB adsorption

The ability and mechanism of MB dye adsorption of Cu-BTC were investigated and predicted through adsorption experiments. The isotherm of the adsorption process explains the reaction mechanism between MB molecules and Cu-BTC, helping to optimize the factors affecting the adsorption process. Kinetic models were studied to better explain the reaction mechanism by analyzing adsorption capacity over time.

https://doi.org/10.52111/qnjs.2024.18103

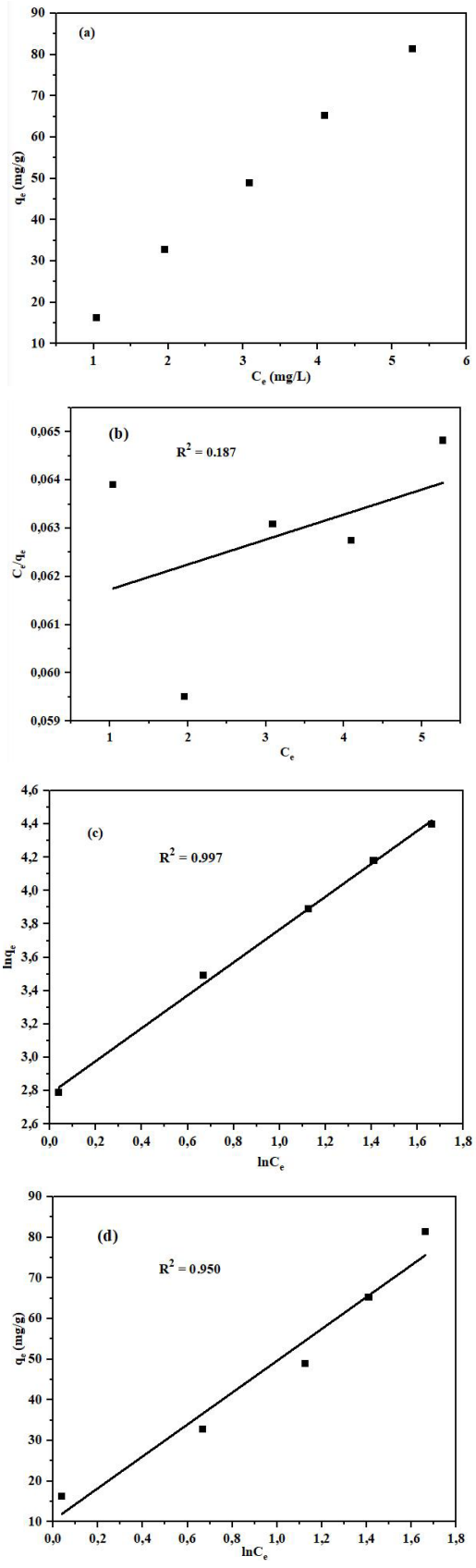

Figure 6. The adsorption isotherm of MB on Cu-BTC (a), (b) Langmuir adsorption model, (c) Freundlich adsorption model, (d) Temkin adsorption model.

Figure 6 shows the isotherm modeling results of MB onto Cu-BTC, and the model parameters of the three isotherms are summarized in Table 2. The Freundlich isotherm model fits the concentration quite well. Test (correlation coefficient R^2 = 0.9968). The Temkin model (R^2 = 0.9503) fits reasonably well. The value n = 1.01 for the Freundlich isotherm model demonstrates the suitability of this model with experimental data. The results show the adsorption mechanism on heterogeneous surfaces, heterogeneous surfaces, and multilayer adsorption, which is also consistent with the characteristics of the synthesized materials. However, the maximum adsorption capacity of the material calculated according to the Langmuir model reached 1929.5 mg/g, higher than the absorption capacity of other materials, such as nano Fe_3O_4 (161.8 mg/g), tannic acid/graphene nanocomposite (200 mg/g).[28] Due to its high adsorption capacity and simple synthesis process, Cu-BTC is considered one of the essential materials for MB removal.

Table 2. Parameter values of Langmuir, Freundlich, and Temkin adsorption isotherm equations of MB on Cu-BTC.

Isotherms	Parameters	Value
Langmuir	q_m (mg/g)	1,929.5
	K_L (L/mg)	0.0085
	R^2	0.187
Freundlich	K_F [(mg/g)(L/mg)$^{1/n}$]	16.139
	n	1.01
	R^2	0.997
Temkin	K_T (L/g)	1.30
	b_T (J/mol)	63.15
	R^2	0.950

Initial concentration and adsorption time are essential parameters for the adsorption capacity of MB on Cu-BTC. As shown in Table 3, at the same initial concentration, the adsorption capacity of MB on the Cu-BTC organometallic

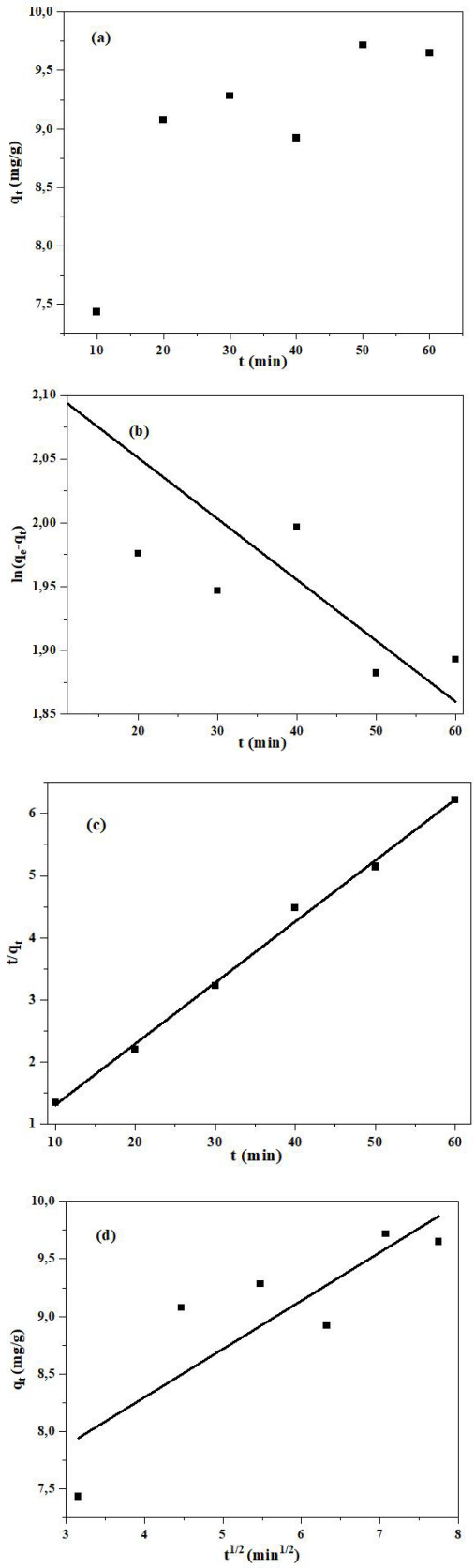

Figure 7. Effect of time on adsorption capacity (a), model of apparent first-order (b), apparent second-order (c), intra-particle diffusion (d) for MB adsorption on Cu-BTC.

framework material increased as the adsorption time increased. Similarly, in Figure 7a, at five different initial concentrations of MB of 10, 20, 30, 40, and 50 mg/L, the adsorption capacity of MB on the Cu-BTC organometallic framework material increased when The initial concentration of MB increased. That shows that the adsorption efficiency depends on the adsorption time and initial concentration of MB.

Table 3. Effect of time on MB adsorption of Cu-BTC in the adsorption process.

Time (min)	C_t (mg/L)	H (%)
10	5.91	40.9
20	5.01	49.9
30	4.89	51.1
40	5.09	49.1
50	4.65	53.5
60	4.69	53.1

Note: Experimental conditions are pH = 7.24; 25 ^oC, 0.011 g Cu-BTC; 20 mL of MB solution, initial concentration of MB is 10 mg/L.

The three models are shown in Figure 7, and their kinetic parameters are presented in Table 4.

Note: Experimental conditions are pH = 7.24; 25 ^oC, 0.011g Cu-BTC; 20 mL of MB solution, the initial concentrations of MB are 10, 20, 30, 40, and 50 mg/L, respectively.

Table 4. Parameters of the apparent kinetic equation of MB adsorption onto Cu-BTC with an initial 10 mg/L concentration.

Kinetic model	Parameter	Value
First-order apparent model	k_1 (min^{-1})	-8.10^{-5}
	$q_{e,cal}$ (mg/g)	8.55
	$q_{e,exp}$ (mg/g)	16.29
	R^2	0.5957
Second-order apparent model	k_2 (g/mg.min)	0.0296
	$q_{e,cal}$ (mg/g)	10.16
	$q_{e,exp}$ (mg/g)	16.29
	R^2	0.9948
Intraparticle diffusion model	k_i (mg/g.$min^{1/2}$)	0.42075
	C (mg/g)	6.61
	R^2	0.6692

https://doi.org/10.52111/qnjs.2024.18103

From Table 4, it can be seen that the correlation coefficient R^2 of the apparent quadratic model ($R^2 = 0.9948$) is more significant than that of the clear first-order model ($R^2 = 0.5957$), and the model experimental diffusion pattern ($R^2 = 0.6692$). In addition, the equilibrium adsorption capacity value calculated according to the apparent quadratic kinetic equation ($q_{e,cal}$) is much closer to the experimentally calculated adsorption capacity value ($q_{e,exp}$) than the value The adsorption capacity value was calculated according to the apparent first-order kinetic equation. These results indicate that the apparent first-order model does not describe the adsorption process. From that, the apparent second-order kinetic model describes the MB adsorption process for the entire adsorption time. However, the apparent first- and second-order models could not determine the diffusion mechanism of MB adsorption on Cu-BTC MOFs, so the intra-particle diffusion model was used to determine the diffusion mechanism. Table 4 shows that the correlation coefficient model R^2 of the particle diffusion kinetics model ($R^2 = 0.6692$) is lower than that of the apparent quadratic model. The adsorption process is related to the diffusion of particles. Dispersed in the particles, it is not the only factor affecting adsorption. Therefore, the adsorption process occurs in an apparent second-order pattern and is controlled by other factors such as pH.

4. CONCLUSION

This study used a simple microwave method to synthesize Cu-BTC organometallic framework material to remove MB in water. The synthesized Cu-BTC MOFs have octahedral morphology. Studies on the effects of pH, concentration, and adsorption time showed that MB was removed according to the Freundlich isotherm adsorption model and the apparent second-order kinetic model. Therefore, the multilayer MB adsorption mechanism on the surface of Cu-BTC MOFs is not uniform and is influenced by electrostatic attraction. These characteristics show that Cu-BTC MOFs are ideal for further research on MB removal from wastewater and potential applications in environmental research.

Acknowledgment

This research is conducted and funded by the Department of Inorganic Materials, Institute of Chemistry and Materials.

REFERENCES

1. V. Z. Sönmez, N. Sivri. Change of acute toxicity of dyestuff wastewaters, *Polish Journal of Environmental Studies*, **2020**, *29*(1), 491-498.
2. P. O. Oladoye, T. O. Ajiboye, E. O. Omotola, O. Oyewola. Methylene blue dye: toxicity and potential technologies for elimination from (waste) water, *Results in Engineering*, **2022**, *16*(6), 100678.
3. T. Tomar, N. Kahandawala, J. Kaur, L. Thounaojam, I. Choudhary, S. Bera. Bioremediation of synthetic dyes from wastewater by using microbial nanocomposites: an emerging field for water pollution management, *Biocatalysis and Agricultural Biotechnology*, **2023**, *51*, 102767.
4. P. O. Oladoye, O. M. Bamigboye, O. D. Ogunbiyi, M. T. Akano. Toxicity and decontamination strategies of Congo red dye, *Groundwater for Sustainable Development*, **2022**, *19*(1), 100844.
5. M. Andriamanantena, F. F. Razafimbelo, B. Raonizafinimanana, D. Cardon, P. Danthu, J. Lebeau, T. Petit, Y. Caro. Alternative sources of red dyes with high stability and antimicrobial properties: towards an ecological and sustainable approach for five plant species from Madagascar, *Journal of Cleaner Production*, **2021**, *303*, 126979.
6. W. U. Khan, S. Ahmed, Y. Dhoble, S. Madhav. A critical review of hazardous waste generation from textile industries and associated ecological impacts, *Journal of the Indian Chemical Society*, **2023**, *100*(1), 100829.
7. P. S. Preethi, S. Vickram, R. Das, N. M. Hariharan, M. Rameshpathy, R. Subbaiya, N. Karmegam, W. Kim, M. Govarthanan. Bioprospecting of novel peroxidase from streptomyces coelicolor strain

SPR7 for carcinogenic azo dyes decolorization, *Chemosphere*, **2023**, *310*, 136836.

8. S. A. Bhat, F. Zafar, A. U. Mirza, P. Singh, A. H. Mondal, N. Nishat. Nanovertenergie: bactericidal polymer nanocomposite beads for carcinogenic dye removal from aqueous solution, *Journal of Molecular Structure*, **2023**, *1284*, 135232.
9. M. M. Haque, M. A. Haque, M. K. Mosharaf, A. Rahman, M. S. Islam, K. Nahar, A. H. Molla. Enhanced biofilm-mediated degradation of carcinogenic and mutagenic azo dye by novel bacteria isolated from tannery wastewater, *Journal of Environmental Chemical Engineering*, **2023**, *11*(5), 110731.
10. S. Samsami, M. Mohamadizaniani, M. H. Sarrafzadeh, E. R. Rene, M. Firoozbahr. Recent advances in the treatment of dye-containing wastewater from textile industries: overview and perspectives, *Process Safety and Environmental Protection*, **2020**, *143*(10), 138-163.
11. S. K. Selvi, M. Eswaramurthi. Treatment of textile dyeing wastewater using a low-cost adsorbent, *Materials Today: Proceedings*, **2023** (in press).
12. S. Sağlam, F. N. Türk, H. Arslanoğlu. Use and applications of metal-organic frameworks (MOF) in dye adsorption, *Journal of Environmental Chemical Engineering*, **2023**, *11*(5), 110568.
13. I. Salahshoori, M. N. Jorabchi, S. Ghasemi, M. Golriz, S. Wohlrab, H. A. Khonakdar, Advancements in wastewater treatment: a computational analysis of adsorption characteristics of cationic dyes pollutants on amide functionalized-MOF nanostructure MIL-53 (Al) surfaces, *Separation and Purification Technology*, **2023**, *319*, 124081.
14. Y. Zhao, H. Zhou, M. Song, Z. Xu, Z. Sun, Q. Xu, Y. Chen, X. Liao. Interface engineering of Ti-MOFs: adsorption of anionic, cationic and neutral dyes in wastewater, *Journal of Molecular Structure*, **2023**, *1283*, 135268.
15. A. Vakili, A. A. Zinatizadeh, Z. Rahimi, S. Zinadini, P. Mohammadi, S. Azizi, A. Karami, M. Abdulgader. The impact of activation temperature and time on the characteristics and performance of agricultural waste-based activated carbons for removing dye and residual COD from wastewater, *Journal of Cleaner Production*, **2023**, *382*, 134899.
16. N. Kumar, A. Pandey, Rosy, Y. C. Sharma. A review on sustainable mesoporous activated carbon as adsorbent for efficient removal of hazardous dyes from industrial wastewater, *Journal of Water Process Engineering*, **2023**, *54*, 104054.
17. D. D. Hu, Y. D. Li, Y. Weng, H. Q. Peng, J. B. Zeng. Mussel inspired stable underwater superoleophobic cotton fabric combined with carbon nanotubes for efficient oil/water separation and dye adsorption, *Applied Surface Science*, **2023**, *631*, 157566.
18. M. Mahamud, A. M. Taddesse, Y. Bogale, Z. Bezu. Zeolite supported $CdS/TiO_2/CeO_2$ composite: synthesis, characterization and photocatalytic activity for methylene blue dye degradation, *Materials Research Bulletin*, **2023**, *161*, 112176.
19. X. Y. Lu, M. L. Zhang, Y. X. Ren, J. J. Wang, X. G. Yang. Design of Co-MOF nanosheets for efficient adsorption and photocatalytic degradation of organic dyes, *Journal of Molecular Structure*, **2023**, *1288*, 135796.
20. D. Mukherjee, B. V. Bruggen, B. Mandal. Advancements in visible light responsive MOF composites for photocatalytic decontamination of textile wastewater: a review, *Chemosphere*, **2022**, *295*, 133835.
21. V. Singh, S. Gautam, S. Kaur, N. Kajal, M. Kaur, R. Gupta. Highly functionalized photo-activated metal–organic frameworks for dye degradation: recent advancements, *Materials Today Communications*, **2023**, *34*, 105180.
22. A. H. Shah, Z. U. Abideen, S. Maqsood, F. Rashid, R. Ullah, A. U. Rehman, M. Dildar, M. Ahmad, K. Ullah, M. N. Rafi, F. Teng. Porous Cu-based metal organic framework (Cu-MOF) for highly selective adsorption of organic pollutants, *Journal of Solid State Chemistry*, **2023**, *322*, 123935.
23. X. Yang, J. Zhao, C. P. Artur, J. Su, H. Wang. Encapsulated laccase in bimetallic Cu/Zn ZIFs as stable and reusable biocatalyst for decolorization of dye wastewater, *International Journal of Biological Macromolecules*, **2023**, *233*, 123410.

https://doi.org/10.52111/qnjs.2024.18103

24. M. Shahbakhsh, H. Saravani, M. Dusek, M. Poupon. Study of the one-step in situ growth synthesis of Cu-Pic coordination polymer and Cu-BTC MOF and their performances for detection of 4-Nitrophenol, *Microchemical Journal*, **2023**, *189*, 108557.

25. Y. P. Yu, M. M. Pan, M. Jiang, X. Yu, L. Xu. Facile synthesis of self-assembled three-dimensional flower-like Cu-MOF and its pyrolytic derivative Cu-N-C450 for diverse applications, *Journal of Environmental Chemical Engineering*, **2023**, *11*(2), 109400.

26. N. Faaizatunnisa, R. Ediati, H. Fansuri, H. Juwono, S. Suprapto, A. R. P. Hidayat, L. L. Zulfa. Facile green synthesis of core–shell magnetic MOF composites (Fe_3O_4@SiO_2@ HKUST-1) for enhanced adsorption capacity of methylene blue, *Nano-Structures & Nano-Objects*, **2023**, *34*, 100968.

27. N. Rabiee, M. Atarod, M. Tavakolizadeh, S. Asgari, M. Rezaei, O. Akhavan, A. Pourjavadi, M. Jouyandeh, E. C. Lima, A. H. Mashhadzadeh, A. Ehsani, S. Ahmadi, M. R. Saeb. Green metal-organic frameworks (MOFs) for biomedical applications, *Microporous and Mesoporous Materials*, **2022**, *335*, 111670.

28. Y. Liu, P. Ghimire, M. Jaroniec. Copper benzene-1,3,5-tricarboxylate (Cu-BTC) metal-organic framework (MOF) and porous carbon composites as efficient carbon dioxide adsorbents, *Journal of Colloid and Interface Science*, **2019**, *535*, 122-132.

29. D. Qian, C. Lei, G. P. Hao, W. C. Li, A. H. Lu. Synthesis of hierarchical porous carbon monoliths with incorporated metal–organic frameworks for enhancing volumetric based CO_2 capture capability, *ACS Applied Materials & Interfaces*, **2012**, *4*(11), 6125-6132.

30. R. Kaur, A. Kaur, A. Umar, W. A. Anderson, S. K. Kansal. Metal-organic framework (MOF) porous octahedral nanocrystals of Cu-BTC: synthesis, properties, and enhanced adsorption properties, *Materials Research Bulletin*, **2019**, *109*, 124-133.

31. M. S. Hosseini, S. Zeinali, M. H. Sheikhi. Fabrication of capacitive sensor based on Cu-BTC (MOF-199) nanoporous film for detection of ethanol and methanol vapors, *Sensors and Actuators B: Chemical*, **2016**, *230*, 9-16.

32. G. Latha, N. Devarajan, P. Suresh. Framework copper-catalyzed oxidative synthesis of quinazolinones: a benign approach using $Cu_3(BTC)_2$ MOF as an efficient and reusable catalyst, *ChemistrySelect*, **2020**, *5*(32), 10041-10047.

33. C. Y. Chuah, T. H. Bae. Incorporation of Cu_3BTC_2 nanocrystals to increase the permeability of polymeric membranes in O_2/N_2 separation, *BMC Chemical Engineering*, **2019**, *1*(1), 1-9.

34. J. R. Mason, J. N. Weyrich, H. Yang. Mechanistic study of porosity formation in liquid-assisted mechanochemical synthesis of metal-organic framework $Cu_3(BTC)_2$ for adsorption-based applications, *Sustainability*, **2022**, *14*(15), 9150.

35. E. Irandoost, H. Farsi, A. Farrokhi. Effects of water content on electrochemical capacitive behavior of nanostructured $Cu_3(BTC)_2$ MOF prepared in aqueous solution, *Electrochimica Acta*, **2021**, *368*, 137616.

36. X. T. Lu, Y. F. Pu, L. Li, N. Zhao, F. Wang, F. K. Xiao. Preparation of metal-organic frameworks $Cu_3(BTC)_2$ with amino-functionalization for CO_2 adsorption, *Journal of Fuel Chemistry and Technology*, **2019**, *47*(3), 338-343.

37. J. Xiao, Y. Zhang, T. C. Zhang, Y. Wang, S. Yuan. Cu_3BTC_2 MOF-impregnated boron-doped biochar derived from orange peels for enhanced NH_3 capture, *Applied Surface Science*, **2023**, *635*, 157735.

38. B. H. Hameed, A. A. Ahmad. Batch adsorption of methylene blue from aqueous solution by garlic peel, an agricultural waste biomass, *Journal of Hazardous Materials*, **2009**, *164*(2-3), 870-875.

39. M. C. Ncibi, B. Mahjoub, M. Seffen. Kinetic and equilibrium studies of methylene blue biosorption by posidonia oceanica (L.) fibres, *Journal of Hazardous Materials*, **2007**, *139*(2), 280-285.

40. W. Y. Siew, N. H. H. A. Bakar, M. A. Bakar, A. Z. Abidin. Influence of various Cu/Fe ratios on the surface properties of green synthesized Cu-Fe-BTC and its relation to methylene blue adsorption, *Journal of Hazardous Materials*, **2021**, *416*, 125846.

TẠP CHÍ KHOA HỌC
TRƯỜNG ĐẠI HỌC QUY NHƠN

Thành phần hóa học của cây lăn tăn

Phạm Thị Khánh Linh[1], Hồ Thị Thùy Vân[1], Nguyễn Kim Phi Phụng[1], Phạm Nguyễn Kim Tuyến[2], Đinh Văn Phúc[3], Huỳnh Bùi Linh Chi[4,*]

[1]Trường Đại học Khoa học Tự nhiên, Đại học Quốc gia Thành phố Hồ Chí Minh, Việt Nam
[2]Trường Đại học Sài Gòn, Việt Nam
[3]Trường Đại học Nguyễn Tất Thành, Việt Nam
[4]Trường Đại học Đồng Nai, Việt Nam

Ngày nhận bài: 20/09/2023; Ngày sửa bài: 06/11/2023;
Ngày nhận đăng: 08/11/2023; Ngày xuất bản: 28/02/2024

TÓM TẮT

Chi *Pilea* là chi lớn nhất của họ Urticaceae, bao gồm hơn 600 loài. *Pilea* được mô tả lần đầu tiên bởi nhóm tác giả Lindley năm 1821 và Weddell năm 1869 và có thể dễ dàng phân biệt với các chi khác trong họ Urticaceae bằng sự kết hợp của các lá mọc đối, các lá kèm trong cuống lá có dây chằng ở mỗi nách lá. Dựa vào hình thái rìa lá, 159 loài của chi *Pilea* đã được định danh và phân thành 3 nhóm: Integrifoliae, Heterophyllae và Dentatae. Killip vào năm 1936 chia *Pilea* thành 12 nhóm chủ yếu dựa trên nghiên cứu của Weddell vào năm 1856, 1869. Hầu hết các loài là các loại thảo mộc nhỏ, nhiều trong số đó là thực vật biểu sinh. Từ cao chloroform và cao acetone của cây Lăn tăn (*Pilea microphylla*) đã phân lập được bảy hợp chất tinh khiết, bao gồm ergosterol (**1**), *β*-sitosterol (**2**), daucosterol **(3)**, isoarborinyl acetate **(4)**, 2′,4′-dihydroxy-6′-methoxy-3′,5′-dimethylchalcone **(5)**, 3,5,7-trihydroxy-8-methoxyflavone **(6)** và kaempferol **(7)**. Cấu trúc hóa học của các hợp chất được xác định dựa trên các phương pháp hóa lý hiện đại như phổ HR-ESI-MS, 1D và 2D-NMR và so sánh với tài liệu tham khảo. Tất cả bảy hợp chất này lần đầu tiên được cô lập từ chi *Pilea*.

Từ khóa: *Pilea microphylla (L.), urticaceae, steroid, triterpenoid, flavonoid.*

**Tác giả liên hệ chính.*
Email: huynhbuilinhchi@gmail.com

QUY NHON UNIVERSITY
JOURNAL OF SCIENCE

Chemical constituents of *Pilea microphylla* (L.)

Pham Thi Khanh Linh[1], Ho Thi Thuy Van[1], Nguyen Kim Phi Phung[1], Pham Nguyen Kim Tuyen[2], Dinh Van Phuc[3], Huynh Bui Linh Chi[4,*]

[1]University of Science, Vietnam National University Ho Chi Minh City, Vietnam
[2]Sai Gon University, Vietnam
[3]Nguyen Tat Thanh University, Vietnam
[4]Dong Nai University, Vietnam

Received: 20/09/2023; Revised: 06/11/2023;
Accepted: 08/11/2023; Published: 28/02/2024

ABSTRACT

Pilea, the largest genus of the Urticaceae, included over 600 species. This genus, first described by Lindley in 1821 and Weddell in 1869, is easily distinguished from other Neotropical Urticaceae by the combination of opposite leaves and ligulate intrapetiolar stipules in each leaf axil. Based on the isomorphy and margin morphology of the leaf 159 species were recognized and classified into three groups: Integrifoliae, Heterophyllae, and Dentatae. Killip in 1936 subdivided *Pilea* into 12 groups largely based on Weddell's studies in 1856, 1869. Most of the species are small herbs, many of which are facultatively epiphytic or epipetric. Phytochemical investigations of the chloroform and acetone extracts of the whole plant *Pilea microphylla* led to the isolation of seven pure compounds, including ergosterol (**1**), *β*-sitosterol (**2**), daucosterol (**3**), isoarborinyl acetate (**4**), 2′,4′-dihydroxy-6′-methoxy-3′,5′-dimethylchalcone (**5**), 3,5,7-trihydroxy-8-methoxyflavone (**6**), and kaempferol (**7**). Their chemical structures were elucidated by extensive HR-ESI-MS, 1D and 2D-NMR spectroscopic data analysis, and comparison with previously published ones. Seven compounds were reported for the first time from *Pilea* genus.

Keywords: *Pilea microphylla (L.), urticaceae, steroids, triterpenoid, flavonoid.*

1. INTRODUCTION

Pilea microphylla, a succulent herb or small shrub growing in heavy shade, does not produce fruit. This species can spread entirely depending on vegetative reproduction. According to Pacific Island Ecosystems at Risk in 2010, *P. microphylla* is considered as a problematic weed affecting the tropical and subtropical environments worldwide.[1,2] Zou *et al*[3] reported the presence of some flavonoid glycosides in *P. microphylla,* quercetin 3-*O*-rutinoside, 3-*O*-caffeoylquinic acid, luteolin 7-*O*-glucoside, apigenin 7-*O*-rutinoside, apigenin 7-*O*-*β*-D-glucopyranoside and quercetin.[3] Chahardehi *et al*[4] showed that some extracts of this plant possessed antioxidant and antimicrobial activities. This paper would like to present some secondary metabolites of this species.

2. MATERIALS AND METHODS

2.1. General experimental procedures

The HR–ESI–MS was recorded on an HR–ESI–MS MicrOTOF–Q mass spectrometer. The

**Corresponding author.*
Email: huynhbuilinhchi@gmail.com

https://doi.org/10.52111/qnjs.2024.18104

^{1}H-NMR (500 MHz) and ^{13}C-NMR (125 MHz) spectra were recorded on a Bruker Avance 500 spectrometer. Chemical shifts are expressed in ppm using a residual solvent signal as an internal reference ($CDCl_3$ δ_H 7.26, δ_C 77.2). Thin-layer chromatography (TLC) was carried out on precoated silica gel 60 F_{254} or silica gel 60 RP–18 F254S (Merck) and the isolated compounds were visualized by spraying with vanillin (contains H_2SO_4) ethanol solution (for TLC stain) followed by heating. Gravity column chromatography was performed on silica gel 60 (0.040 mm ÷ 0.063 mm, Himedia).

2.2. Plant material

Pilea microphylla (L.) was collected in August 2018, at Bien Hoa city, Dong Nai province, Vietnam. The scientific name was authenticated by PhD. Dang Van Son, Institute of Tropical Biology, Southern Vietnam.

2.3. Extraction and isolation

The fresh whole plant (47.0 kg) was cleaned under running tap water, then air-dried and ground. The dried powder (3.1 kg) was macerated with methanol at room temperature. After filtration, the methanol solution was exhaustively evaporated at the reduced pressure yielding a dark-green residue (483.7g). The methanol residue was subjected to silica gel solid phase extraction and eluted consecutively with *n*-hexane, chloroform, acetone, ethyl acetate. After evaporated at the reduced pressure of these extracted solutions, five extracts were obtained, including *n*-hexane (25.5g), chloroform (40.7g), ethyl acetate (36.9g), acetone (71.9g), and the remaining methanol residue (189.1g).

The chloroform extract (40.7g) was applied to silica gel column chromatography eluted with *n*-hexane: chloroform (stepwise, 9:1 to 0:10) to afford thirteen fractions (**C1** ÷ **C13**). The fraction **C5**(126.3mg)wasselectedforfurtherfractionation by silica gel column chromatography, eluting with *n*-hexane: chloroform (stepwise, 10:0 to 0:10) to obtain compound **4** (20 mg). Fraction **C11** (4,850.4 mg) was applied on silica gel column chromatography eluting with *n*-hexane: ethyl acetate (stepwise, 9.8:0.2 to 5:5) to obtain compound **2** (15 mg). Fraction **C12** (3,664.5 mg) was selected for further fractionation by silica gel column chromatography using an isocratic mobile phase consisting of *n*-hexane: ethyl acetate (10:0 to 0:10) to obtain compound **1** (7.5 mg).

The acetone extract (7.5 g) was applied to silica gel column chromatography, eluted with solvent systems of *n*-hexane: ethyl acetate (10:0 to 0:10), then ethyl acetate: methanol (7:3 to 0:10) to afford eight fractions (**A1** ÷ **A8**). The fraction **A2** (168.2 mg) was applied on silica gel column chromatography using *n*-hexane: ethyl acetate (8:2), then *n*-hexane: chloroform (8:2) and finally by *n*-hexane: acetone (9:1) to obtain compound **5** (5.0 mg). The fraction **A5** (1150 mg) was applied on silica gel column chromatography using *n*-hexane: ethyl acetate (6:4 to 0:10) then methanol 100% to obtain four subfractions (**A5.1** ÷ **A5.4**). The **A5.1** (39.1 mg) was applied to a silica gel column chromatography using *n*-hexane: chloroform (5:5 to 0:10), then *n*-hexane: acetone (9:1) to obtain compound **6** (5.3 mg). The same procedure was applied to **A5.2** (222.6 mg), using *n*-hexane: chloroform (5:5 to 0:10), then chloroform: methanol (9:1) to obtain compound **7** (9.3 mg). Fraction **A7** (408.5 mg) was applied on silica gel column chromatography using chloroform: methanol (stepwise, 9:1 to 0:10) to obtain compound **3** (15 mg).

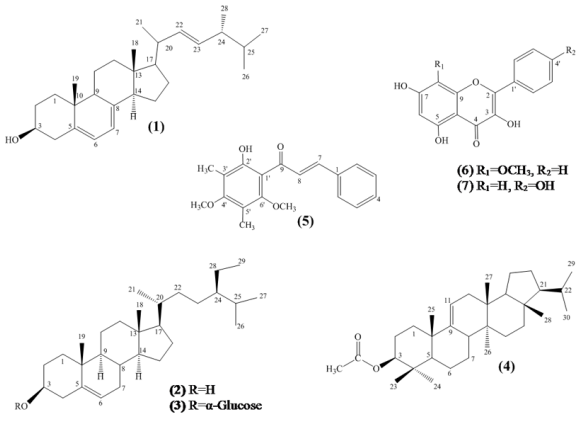

Figure 1. Structures of isolated compounds **1** ÷ **7**.

3. RESULTS

By using efficient separation techniques, the chemical investigation of the chloroform and acetone extracts of the whole plant of *Pilea microphylla* led to the isolation of seven compounds. Their chemical structures were elucidated by 1D and 2D NMR and HR-ESI-MS analysis. They were three steroids, ergosterol **(1)**, *β*-sitosterol **(2)**, and daucosterol (**3)**, one triterpenoid, isoarborinyl acetate **(4)** and three flavonoids, 2′,4′-dihydroxy-6′-methoxy-3′,5′-dimethylchalcone **(5)**, 3,5,7-trihydroxy-8-methoxyflavone **(6)**, and kaempferol **(7)**.

Ergosterol **(1)**: Colorless crystals. HR-ESI-MS (positive mode) *m/z* 397.3483 $[M+H]^+$ (calcd. for $C_{28}H_{44}O$+H, 397.3473). The ^{1}H and ^{13}C-NMR ($CDCl_3$) see Table 1.

β-Sitosterol (**2**): White powder. ^{1}H-NMR data ($CDCl_3$) (*J* in Hertz): δ_H 3.55 (1H, *ddd,* 15.8, 11.0, 4.6, H-3), 5.38 (*d*, 5.2, H-6), 1.03 (3H, *s*, H-18), 0.70 (3H, *s*, H-19), 0.95 (3H, *d*, 6.6, H-21), 0.88 (3H, *d*, 7.5, H-26), 0.84 (3H, *d*, 6.5, H-27), 0.85 (3H, *t*, 7.0, H-29). The ^{13}C-NMR ($CDCl_3$): δ_C 37.3 (C-1), 31.7 (C-2), 71.8 (C-3), 42.3 (C-4, C-13), 140.8 (C-5), 121.7 (C-6), 31.9 (C-7, C-8), 50.2 (C-9), 36.1 (C-10, C-20), 21.1 (C-11), 39.8 (C-12), 56.8 (C-14), 26.2 (C-15), 28.2 (C-16), 56.1 (C-17), 11.9 (C-18), 18.8 (C-19, C-21), 34.0 (C-22), 24.3 (C-23), 45.9 (C-24), 29.2 (C-25), 19.4 (C-26), 19.8 (C-27), 23.1 (C-28), 12.0 (C-29).

Daucosterol (**3**): White crystal, HR-ESI-MS (positive mode) *m/z* 577.4498 $[M+H]^+$ (calcd. for $C_{35}H_{60}O_6$ + H, 577.4428). ^{1}H-NMR data ($CDCl_3$) (*J* in Hertz): δ_H 4.24 (*m,* H-3), 5.33 (*m*, H-6), 0.63 (3H, *s*, H-18), 0.91 (3H, *s*, H-19), 0.96 (3H, *d*, 6.4, H-21), 0.83 (3H, *d*, 6.8, H-26), 0.87 (3H, *d*, 7.4, H-27), 0.85 (3H, *m*, H-29), 5.01 (1H, *d*, 7.7, H-1′), 4.02 (1H, *t*, 8.1, H-2′), 3.89-3.96 (1H, *m*, H3′, 4′),) 4.24 (1H, *m*, H-5′), 4.37 (1H, *dd*, 11.7, 5.3, H-6′a), 4.52 (1H, *dd*, 11.8, 2.5, H-6′b). The ^{13}C-NMR ($CDCl_3$): δ_C 37.5 (C-1), 30.8 (C-2), 79.1 (C-3), 39.9 (C-4), 141.5 (C-5), 122.4 (C-6), 32.6 (C-7), 32.7 (C-8), 51.0 (C-9), 38.0 (C-10), 21.8 (C-11), 40.5 (C-12), 43.0 (C-13), 57.4 (C-14), 25.0 (C-15), 29.1 (C-16), 56.8 (C-17), 12.5 (C-18), 20.0 (C-19), 36.9 (C-20), 19.6 (C-21), 34.8 (C-22), 27.0 (C-23), 46.6 (C-24), 30.0 (C-25), 19.8 (C-26), 20.5 (C-27), 24.0 (C-28), 12.7 (C-29), 103.1 (C-1'), 75.9 (C-2'), 79.0 (C-3'), 72.3 (C-4'), 78.7 (C-5'), 63.4 (C-6').

Isoarborinyl acetate (**4**): Colorless crystal, HR-ESI-MS (positive mode) *m/z* 469.4044 $[M+H]^+$ (calcd. for $C_{32}H_{53}O_2$+H, 469.4048). The ^{1}H and ^{13}C-NMR ($CDCl_3$) see Table 1.

2′,4′-Dihydroxy-6′-methoxy-3′,5′-dimethylchalcone (**5**): Pale yellow crystal, HR-ESI-MS (positive mode) *m/z* 299.1291 $[M+H]^+$ (calcd. for $C_{18}H_{18}O_4$+H, 299.1283). The ^{1}H and ^{13}C-NMR ($CDCl_3$) see Table 2.

3,5,7-Trihydroxy-8-methoxyflavone (**6)**: White powder, HR-ESI-MS (positive mode) *m/z* 301.0706 $[M+H]^+$ (calcd. for $C_{16}H_{12}O_6$+H, 301.0712). The ^{1}H and ^{13}C-NMR ($CDCl_3$) see Table 2.

Kaempferol **(7)**: Yellow amorphous powder, HR-ESI-MS (positive mode) *m/z* 287.0515 $[M+H]^+$ (calcd. for $C_{15}H_{10}O_6$+H, 287.0555). The ^{1}H and ^{13}C-NMR ($CDCl_3$) see Table 2.

4. DISCUSSION

The chemical structures of seven isolated compounds were elucidated based on the analysis of HR-MS, 1D and 2D NMR spectroscopic spectra as well as the comparison of their data with those in the literature. The common compounds in plants such as *β*-sitosterol[5] and daucosterol,[6,7] after comparison of the data with the ones in the literature, their NMR ones were presented in the Part 2- Material and Methods, without discussion on their chemical elucidation.

Compound **1** was isolated as colorless crystals. Its molecular formula was determined as $C_{28}H_{44}O$ through its molecular ion peak at *m/z* 397.3483 $[M+H]^+$ (calcd. for $C_{28}H_{44}O$+H, 397.3473). The ^{1}H-NMR data exhibited signals

https://doi.org/10.52111/qnjs.2024.18104

for six methyl groups δ_H 0.63 (*s*, H-19), 0.83 (*d*, *J* = 7.6 Hz, H-26), 0.83 (*d*, *J* = 6.8 Hz, H-27), 0.92 (*d*, *J* = 6.9 Hz, H-28), 0.95 (*s*, H-18), and 1.04 (*d*, *J* = 6.7 Hz, H-21), signals δ_H 5.57 (*dd*, *J* = 5.8, 2.6 Hz) and 5.38 (*dd, J* = 5.6, 2.8 Hz) diagnostic for olefin hydrogens H-6 and H-7, besides multiplet in δ_H 3.63 (H-3) indicate the presence of hydrogen linked to carbinolic carbon. Double bonds were observed at signal δ_H 5.19 (*m*) and 5.21 (*m*) relative to H-22 and H-23. The ^{13}C-NMR spectra revealed C28-sterol ergostane skeleton, including signals of six methyl carbons, seven methylene carbons, eleven methine carbons (four olefinic carbons, one oxygenated methine carbon), and four quaternary carbons (two olefinic carbons) (*Table 1*). The good compatibility of its NMR and HR-ESI-MS data with those in the literature proposed that compound **1** was ergosterol.[8]

The molecular formula of compound **2** was determined as $C_{29}H_{50}O$. The ^{1}H-NMR spectrum of **2** showed the presence of two methyl singlet protons at δ_H 1.03 (*s*, H-18), and 0.70 (*s*, H-19), three methyl doublet protons at δ_H 0.95 (*d*, *J* = 6.5 Hz, H-21), 0.88 (*d*, *J* = 7.5 Hz, H-26), and 0.84 (*d*, *J* = 6.5, H-27) and methyl triplet protons at δ_H 0.85 (3H, *t*, 7.0, H-29) together with one olefinic proton at δ_H 5.38 (*d*, *J* = 5.2 Hz, H-6) which suggested the sterol structure. In addition, the spectrum of compound **2** showed the presence of twenty nine carbons, including six methyl carbons δ_C 11.9 (C-18), δ_C 12.0 (s, C-29), δ_C 18.8 (C-19), δ_C 19.0 (C-21), δ_C 19.4 (C-26), and δ_C 19.8 (C-27), eleven methylene carbons δ_C 21.1– 42.3, nine methine carbons δ_C 29.2 – 71.8 [one oxynated methine carbon δ_C 71.8 (C-3), one olefinic carbon δ_C 121.7 (C-6)], and three methine carbon δ_C 36.1 (C-10), δ_C 42.3 (C-13), δ_C 140.8 (C-5). Based on the above evidence and the comparison of NMR spectral data with those reported for phytosterols, compound **2** was a plant sterol, *β*-sitosterol.[9]

Compound **3** was isolated as a white crystal. It was quickly identified as daucosterol because it possessed similar NMR data to compound **2**. The similarity in the NMR data just with the replacement of hydroxyl proton of carbon C-3 (δ_H 4.24). It was replaced by glucopyranose (δ_H 3.89 – 5.01). Its molecular formula $C_{35}H_{60}O_6$ was determined through the pseudomolecular ion peak at *m/z* 577.4498 $[M+H]^+$ (calcd. for $C_{35}H_{60}O_6$+H, 577.4428). Consequently, the structure of compound **3** was daucosterol.[10,11]

Compound **4** was obtained as colorless powder. Mass spectra exhibited a pseudo-molecular ion peak at *m/z* 469.4044 (calcd for $C_{32}H_{53}O_2^+$, 469.4067), which corresponded with $C_{32}H_{52}O_2$. The ^{1}H- and ^{13}C-NMR data of **4** disclosed 32 carbon signals including one acetyl ester group (δ_H 2.04, 3H, *s*; δ_C 21.3, 171.0, 3–$COCH_3$), one oxymethine (δ_H 4.47, *dd*, 11.7, 4.1 Hz; δ_C 80.9, C-3); one olefinic methine (δ_H 5.22, *d*, 6.2 Hz; δ_C 114.6, C-11); one olefinic quartenary carbon (δ_C 148.5, C-9); six quaternary methyls {(δ_H 0.85, 3H, *s*; δ_C 28.2, C-23); (0.87, 3H, *s*; 16.8, C-24); (1.04, 3H, *s*; 22.2, C-25); (0.79, 3H, *s*; 17.0, C-26); (0.75, 3H, *s*; 15.3, C-27); (0.74, 3H, *s*; 14.0, C-28)}; two tertiary methyls {(δ_H 0.88, 3H, *d*, 6.5 Hz; δ_C 22.1, C-29) and (0.82, 3H, *d*, 6.5 Hz; δ_C 23.0, C-30)} and 9 methylenes, 5 methines and 5 quarternary carbons in the high field zone. The presence of 32 signals on ^{13}C-NMR and the correlations observed on 1D and 2D spectra led to identification of compound **4** as isoarborinyl acetate, a hopane triterpene.[5]

Compound **5** was isolated as a pale yellow powder. The combination of analysis of ^{1}H- and ^{13}C-NMR data revealed that **5** contained a mono-substituted benzene ring {(δ_H 7.65, 2H, *dd*, 7.6, 2.0 Hz, H-2, H-6), (7.41, 3H, *m*, H-3, H-4, H-5); δ_C 135.6 (C1), 128.6 (C-2), 129.1 (C-3), 130.3 (C-4), 129.1 (C-5), 128.6 (C-6)}; a hexa-substituted benzene one {δ_C 109.3 (C1′), 162.2 (C-2′), 106.7 (C-3′), 159.3 (C-4′), 109.0 (C-5′), 159.1 (C-6′)}; one conjugated ketone carbon (δ_C 193.5), two *E*-configuration olefinic

https://doi.org/10.52111/qnjs.2024.18104

carbons {(δ_H 7.84, 1H, *d*, 15.7 Hz, δ_C 143.0, C-7) and (7.98, 1H, *d*, 15.7 Hz, δ_C 127.0, C-8)}; one methoxy group (δ_H 3.66, 3H, *s;* δ_C 62.5, 6′–OCH_3) and two methyl groups {(δ_H 2.13, 3H, *s*; δ_C 7.7, 3′–CH_3) and (2.16, 3H, *s*; δ_C 8.4, 5′–CH_3). The positions of these substituents were supported by keys of HMBC correlation (Figure 2). The molecular formular of **5** was determined as $C_{18}H_{18}O_4$ proved by the pseudomolecular ion peak at *m/z* 299.1291 $[M+H]^+$ (calcd. for $C_{18}H_{18}O_4$+H, 299.1283) in the HR-ESI-MS spectrum. Therefore, **5** was 2′,4′-dihydroxy-6′-methoxy-3′,5′-dimethylchalcone.[6,7]

Compound **6** was isolated as white powder. Its molecular formula was determined as $C_{16}H_{12}O_6$ through its pseudomolecular ion peak at *m/z* 301.0706 $[M+H]^+$ (calcd. for $C_{16}H_{12}O_6$+H, 301.0712) in the HR-ESI-MS spectrum. The combination of analysis of HR-MS, ^{1}H- and ^{13}C-NMR data revealed that **6** was a flavonoid with a mono-substituted B ring {(δ_H 8.23, 2H, *m*, H-2′, H-6′), 7.50–7.55 (3H, *m*, H-3′, H-4′, H-5′); δ_C 130.9 (C-1′), 127.7 (C-2′), 128.9 (C-3′), 130.5 (C-4′), 128.9 (C-5′), 127.7 (C-6′)}; a penta-substituted A ring {(δ_H 6.46, *s*, H-6); δ_C 155.6 (C-5), 98.4 (C-6), 156.8 (C-7), 127.1 (C-8), 148.2 (C-9), 103.8 (C-10)}; three carbons of the C ring {δ_C 145.1 (C-2), 136.7 (C-3), 175.8 (C-4)}, and a methoxy group (δ_H 4.05, 3H, *s;* δ_C 62.1, 8–OCH_3). The positions of these substituents were supported by keys of HMBC correlation (*Figure 2*). The comparison of these data with those of 3,5,7-trihydroxy-8-methoxyflavone showed the similarity.[9] Therefore, the chemical structure of **6** was elucidated as shown.[12]

Compound **7** was obtained as a yellow amorphous powder. Its molecular formula was determined as $C_{15}H_{10}O_6$ through its pseudomolecular ion peak at *m/z* 287.0515 $[M+H]^+$ (calcd. for $C_{15}H_{10}O_6$+H, 287.0555). The combinated analysis of HR-MS, 1D and 2D-NMR data (*Tables 2 and Figure 2*) as well as the comparison of its data with the ones in the literature[10] showed that compound **7** was kaempferol.[13]

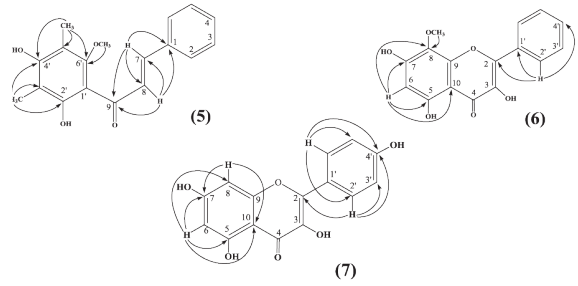

Figure 2. Keys HMBC correlation of **5** ÷ **7**.

5. CONCLUSION

From the chloroform and acetone extracts of the *Pilea microphylla* (L.), collected at Bien Hoa city, Dong Nai province, Vietnam, using various chromatographic methods, seven compounds were isolated. They were ergosterol **(1)**, *β*-sitosterol **(2)**, daucosterol **(3)**, isoarborinyl acetate **(4)**, 2′,4′-dihydroxy-6′-methoxy-3′,5′-dimethylchalcone **(5)**, 3,5,7-trihydroxy-8-methoxyflavone **(6)** and kaempferol **(7)**. Although these compounds were already known in other species, this is the first time they were reported in *Pilea microphylla.*

REFERENCES

1. L. Gaglioti, S. Romaniuc, A. K. Monro. Pilea brasiliensis: a new species of pilea (urticaceae) from Central Brazil, *Phytotaxa*, **2016**, *26*(1), 17-20.

2. F. Scafidi, F. M. Raimondo. First record of pilea microphylla (urticaceae) in Sicily, *Flora Mediterranea*, **2018**, *28*, 79-84.

3. Y. Zhou, H. C. Ren, R. D. Qin, Q. Y. Zhang, H. Liang. Phenolic compounds isolated from pilea microphylla prevent radiation-induced cellular DNA damage, *Acta Pharmaceutica Sinica B*, **2011**, *1*(4), 226-235.

4. A. M. Chahardehi, D. Ibrahim, S. F. Sulaiman. Antioxidant, antimicrobial activity and toxicity test of pilea microphylla, International Journal of Microbiology, **2010**, 826830.

5. A. K. Chakravarty, K. Masuda, H. Suzuki, H. Ageta. Unambiguous assignment of ^{13}C

chemical shifts of some hopane and migrated hopane derivatives by 2D NMR, *Tetrahedron*, **1994**, *50*(9), 2865-2876.

6. V. Choommongkol, K. Punturee, P. Klumphu, P. Rattanaburi, P. Meepowpan, P. Suttiarporn. Microwave-assisted extraction of anticancer flavonoid, 2',4'-dihydroxy-6'-methoxy-3',5'-dimethyl chalcone (DMC), rich extract from syzygium nervosum fruits, *Molecules*, **2022**, *27*(4), 1397.

7. E. C. Amor, I. M. Villasenor, A. Yasin, M. Iqbal Choudhary. Prolyl endopeptidase inhibitors from syzygium samarangense (blume) Merr. & L. M. Perry, *Zeitschrift fur Naturforschung - Section C Journal of Biosciences*, **2004**, *59c*, 86-92.

8. T. R. Alexandre, M. L. Lima, M. K. Galuppo, J. T. Mesquita, M. A. Nascimento, A. L. Santos, P. Sartorelli, D. C. Pimenta, A. G. Tempone. Ergosterol isolated from the basidiomycete *Pleurotus salmoneostramineus* affects *Trypanosoma cruzi* plasma membrane and mitochondria, *Journal of Venomous Animals and Toxins Including Tropical Diseases*, **2017**, *23*, 30.

9. V. S. P. Chaturvedula, I. Prakash. Isolation of stigmasterol and β-Sitosterol from the dichloromethane extract of rubus suavissimus, *Chaturvedula and Prakash*, **2012**, *1*(9), 239-242.

10. L. Angelika, W. Ingrid, G. Sabine, K. Christa, M. Pavel, P. Armin, R. Gottfried, J. Johann, D. W. Taylor. Phenolic and terpenoid compounds from chione venosa (SW.) URBAN var. venosa (Bois Bande), *Phytochemistry*, **2005**, *66*(19), 2381-2387.

11. S. Mouffok, H. Haba, C. Lavaud, C. Long, M. Benkhaled. Chemical constituents of centaurea omphalotricha Coss. & Durieu ex Batt. & Trab., *Records of Natural Products*, **2012**, *6*(3), 292-295.

12. A. S. Sufian, K. Ramasamy, N. Ahmat, Z. A. Zakaria, M. Izwan, M. Yusof. Isolation and identification of antibacterial and cytotoxic compounds from the leaves of muntingia calabura L., *Journal of Ethnopharmacology*, **2013**, *146*, 198-204.

13. L. S. Aisyah, Y. F. Yun, T. Herlina, E. Julaeha, A. Zainuddin, I. Nurfarida, A. T. Hidayat, U. Supratman, Y. Shiono. Flavonoid compounds from the leaves of kalanchoe prolifera and their cytotoxic activity against P-388 murine leukimia cells, *Natural Product Sciences*, **2017**, *23*(2), 139-145.

APPENDIX

Table 1. ^{13}C and ^{1}H NMR data for compound **1** and compound **4** (125 MHz and 500 MHz).

No.	1		4	
	δ_H, J	δ_C	δ_H, J	δ_C
1		38.5		35.7
2		32.2		24.2
3	3.63 (1H, *m*)	70.6	4.47 (1H, *dd*, 11.7, 4.1)	80.9
4		41.0		38.0
5		139.9		52.4
6	5.57 (1H, *dd*, 5.8, 2.6)	119.7		21.3
7	5.38 (1H, *dt*, 5.6, 2.8)	116.4		26.6
8		141.5		40.9
9		46.4		148.5
10		37.2		39.5
11		21.3	5.22 (1H, *d*, 6.2)	114.6
12		39.2		36.1
13		43.0		36.8
14		54.7		38.2
15		23.2		29.7
16		28.4		35.9
17		55.9		42.9
18	0.95 (3H, *s*)	12.2		52.1
19	0.63 (3H, *s*)	16.4		20.2
20		40.6		28.2
21	1.04 (3H, *d*, 6.7)	21.3		59.6
22	5.17 (1H, *dd*, 15.3, 7.7)	135.7		30.8
23	5.23 (1H, *dd*, 15.3, 7.1)	132.1	0.85 (3H, *s*)	28.2
24		43.0	0.87 (3H, *s*)	16.8
25		33.2	1.04 (3H, *s*)	22.2
26	0.84 (3H, *d*, 7.0)	19.8	0.79 (3H, *s*)	17.0
27	0.82 (3H, *d*, 6.5)	20.1	0.75 (3H, *s*)	15.3
28	0.92 (3H, d, 6.9)	17.7	0.74 (3H, *s*)	14.0
29			0.88 (3H, *d,* 5.0)	22.1
30			0.82 (3H, *d*, 6.5)	23.0
$H_3\underline{C}$-CO			2.04 (3H, *s*)	21.3
H_3C-$\underline{C}O$				171.0

https://doi.org/10.52111/qnjs.2024.18104

Table 2. ^{13}C and ^{1}H NMR data for compound **5-7** (125 MHz and 500 MHz).

No.	5		6		7	
	δ_H, J	δ_C	δ_H, J	δ_C	δ_H, J	δ_C
1		135.6				
2	7.65 (*dd*, 7.6, 2.0)	128.6		145.1		148.1
3	7.41 (*m*)	129.1		136.7		137.2
4	7.41 (*m*)	130.2		175.8		177.4
5	7.41 (*m*)	129.1		155.6		162.5
6	7.65 (*dd*, 7.6, 2.0)	128.6	6.46 (*s*)	98.4	6.18 (*d*, 2.1)	99.3
7	7.84 (*d*, 15.7)	143.0		156.8		165.6
8	7.98 (*d*, 15.7)	127.0		127.1	6.40 (*d*, 2.1)	94.5
9		193.5		148.2		158.3
10				103.8		104.6
1′		109.3		130.9		123.8
2′		162.2	8.23 (1H, *dd*, 8.2, 1.3)	127.7	8.09 (*d*, 8.9)	130.7
3′		106.7	7.54 (*m*)	128.9	6.91 (*d*, 8.9)	116.3
4′		159.3	7.50 (*m*)	130.5		160.5
5′		109.0	7.55 (*m*)	128.9	6.91 (*d*, 8.9)	116.3
6′		159.1	8.23 (1H, *dd*, 8.2, 1.3)	127.7	8.09 (*d*, 8.9)	130.7
2′-OH	13.58 (*s*)	-				
3′-Me	2.16 (*s*)	8.4				
5′-Me	2.13 (*s*)	7.7				
6′-OMe	3.66 (*s*)	62.5				
8-OMe			4.05 (*s*)	62.1		

TẠP CHÍ KHOA HỌC
TRƯỜNG ĐẠI HỌC QUY NHƠN

Tăng cường khả năng ứng dụng chất nền carbon từ vỏ chuối kết hợp với g-C_3N_4 làm chất quang xúc tác xử lý môi trường

Phan Thị Thùy Trang[1,*], Trương Thanh Tâm[1], Mai Thị Tường Vy[2], Nguyễn Thị Lan[1,*]

[1]Khoa Khoa học Tự nhiên, Trường Đại học Quy Nhơn, Việt Nam
[2]Phòng hành chính - Tổng hợp, Trường Đại học Quy Nhơn, Việt Nam

Ngày nhận bài: 28/09/2023; Ngày sửa bài: 14/11/2023;
Ngày nhận đăng: 01/12/2023; Ngày xuất bản: 28/02/2024

TÓM TẮT

Chất xúc tác quang carbon/g-C_3N_4 (BC/CN) được tổng hợp thành công bằng phương pháp nung đơn giản từ tiền chất carbon (tổng hợp từ vỏ chuối) và urea. Hoạt tính quang xúc tác và độ bền của vật liệu BC/CN được đánh giá qua sự phân hủy dung dịch RhB dưới vùng ánh sáng khả kiến. Ảnh hưởng của hàm lượng carbon trong composite trên hoạt tính xúc tác đã được khảo sát. Kết quả cho thấy hiệu suất quang xúc tác của composite BC/CN cao hơn g-C_3N_4 (CN) tinh khiết và so với các vật liệu composite ở các tỷ lệ khác. Điều này cho thấy vật liệu BC/CN-150 có độ bền quang xúc tác dưới vùng ánh sáng khả kiến. Kết quả này sẽ cung cấp cái nhìn mới về việc điều chế các chất xúc tác quang có hiệu quả cao trên nền g-C_3N_4.

Từ khóa: *Carbon, g-C_3N_4, chất xúc tác quang, rhodamine B, vỏ chuối.*

**Tác giả liên hệ chính.*
Email: phanthithuytrang@qnu.edu.vn; nguyenthilan@qnu.edu.vn

QUY NHON UNIVERSITY
JOURNAL OF SCIENCE

Enhance the applicability of carbon substrates from banana peels combined with g-C_3N_4 as a photocatalyst for environmental treatment

Phan Thi Thuy Trang[1,*], Truong Thanh Tam[1], Mai Thi Tuong Vy[2], Nguyen Thi Lan[1,*]

[1]Faculty of Natural Sciences, Quy Nhon University, Vietnam
[2]Administrative - General Office, Quy Nhon University, Vietnam

Received: 28/09/2023; Revised: 14/11/2023;
Accepted: 01/12/2023; Published: 28/02/2024

ABSTRACT

Carbon/g-C_3N_4 photocatalyst (BC/CN) was successfully prepared by a simple calcination method from carbon precursor (synthesized from waste banana peels) and urea. The activity and stability of BC/CN were evaluated by rhodamine B (RhB) degradation under visible light. The influence of carbon content in the composite on catalytic activity was studied. The results show that the photocatalytic efficiency of the BC/CN composite is higher than that of the g-C_3N_4 (CN) pristine and the rate constant of the BC/CN-150 sample is higher than the other samples. This shows that BC/CN-150 material has photocatalytic stability under the visible light region. This process will provide new insight into preparing highly efficient g-C_3N_4-based photocatalysts.

Keywords: *Carbon, g-C_3N_4, photocatalyst, rhodamine B, banana peels.*

1. INTRODUCTION

Photocatalysis, with many outstanding advantages, has become a subject of extensive research by scientists for application in treating toxic organic compounds in water. Recently, graphitic carbon nitride (g-C_3N_4) has exhibited great potential to be applied in visible light photocatalysis.[1] This material has many advantages, such as having a narrow bandgap energy (about 2.7 eV), high surface area, and unique morphology. However, g-C_3N_4 has a high photogenerated electron-hole pair recombination rate, which reduces the photocatalytic efficiency of the material. Many methods have been proposed to adjust the morphological structure and surface chemical state of g-C_3N_4 to improve the photocatalytic efficiency of the material. One of the most used methods is to combine with other materials to create composites such as MoS_2,[2] WO_3,[3] and SnS_2.[4]

Carbon materials with sp^2 hybridized π bonds can suppress photogenerated electron-hole recombination and improve the utilization of visible light when combined with other photocatalysts.[5] Specifically, the research group of Ong et al.[6] synthesized reduced graphene oxide (rGO)/g-C_3N_4 material through electrical interaction. With the excellent electrical conductivity and high electron storage capacity of graphene, photogenerated electrons transfer

**Corresponding author.*
Email: phanthithuytrang@qnu.edu.vn; nguyenthilan@qnu.edu.vn

https://doi.org/10.52111/qnjs.2024.18105

from g-C_3N_4 to rGO through an osmosis mechanism to improve the efficiency of CO_2 reduction into CH_4 by photocatalysis. Gu and his colleagues[7] synthesized rGO/g-C_3N_4 material by microwave method from GO and melamine precursors. The results showed that the existence of rGO did not disrupt the structure of g-C_3N_4. The rate of decomposition of rhodamine B is 2.86 times that of g-C_3N_4 under visible light; this may be due to the more effective photogenerated electron-hole separation of the composite due to the synergistic effect of rGO and g-C_3N_4.

Therefore, carbon is an ideal material to manufacture carbon/g-C_3N_4 composites for use as photocatalysts. Besides, the surface of activated carbon is a lot of carboxyl, phenolic hydroxyl, carbonyl, lactone, and amide groups, which can chemically react with polymers to form composites. Furthermore, activated carbon synthesized from by-product biomass materials has partly helped reduce environmental pollution. Making effective use of banana peels is also beneficial for reducing resource waste.

In this study, banana peels waste was used as a biological pretreatment agent to produce activated carbon through calcination. Then, the carbon/g-C_3N_4 composite was obtained by calcination from the carbon and g-C_3N_4 precursors. Various characterizations were conducted to clarify the structure and morphology of the synthesized material. Then, an efficient, economical, and environmentally friendly photocatalytic method is used to remove rhodamine B in wastewater.

2. EXPERIMENTAL SECTION

2.1. Material synthesis

Chemicals: All chemicals for materials synthesis include banana peel, urea, KOH 20%, HCl 2 M, C_2H_5OH, H_2O_2, and rhodamine B (China).

Materials synthesis: Banana peels were washed with deionized water to remove dirt and cut into small pieces while still fresh. Then, it was dried in a vacuum environment for 24 hours at 110 ^oC. The dry shell was finely ground and calcined in an Argon gas at 800 ^oC for 5 hours, and the heating rate is 5 ^oC/min. Then, the obtained product is further treated with KOH 20% solution at 70 ^oC for 2 hours and HCl 2 M solution at 60 ^oC for 15 hours. The obtained product is filtered, washed, and dried in a vacuum environment at 110 ^oC for 12 hours. Next, the product is calcined in air at 300 ^oC for 3 hours. After calcination, the product is filtered, washed with HCl 2 M solution and water, and dried to obtain the product activated carbon from banana peel, denoted BC.

The mixture of urea (20 g) with BC (0.1 g) was dispersed into 50 ml of water and alcohol solution and stirred continuously at a temperature of 60 ^oC until completely dry. Grind the solid amount finely and calcine in the Argon gas at 550 ^oC for 1 hour. The solid was filtered, washed, and dried at 80 ^oC for 12 hours to obtain the C/g-C_3N_4 composite (symbolized as BC/CN). For comparison, the material g-C_3N_4 was also synthesized similarly to the above conditions but without the presence of activated carbon (symbolized as CN).

2.2. Material characterization

X-ray diffraction spectra of the samples were measured on a Bruker D2 Advance diffractometer with a Cu X-ray tube with wavelength λ (CuKα) = 1.5406 Å, power 40 kV, current 40 mA. Scanning angle from 10 to 80^o. Infrared spectra were recorded on an IRAffinity-1S spectrometer (Shimadzu) with wavenumbers ranging from 400 to 4000 cm^{-1}. The composition of the element was determined by EDS spectroscopy. UV-Vis-DRS spectra of material samples were determined on a Jasco-V770 machine with wavelengths from 200 - 800 nm. TEM images were measured on a JEOL JEM-2100F.

2.3. Photocatalytic properties

The photocatalytic activity of the material was determined through the decomposition reaction of RhB in aqueous solution under visible light. Add 50 mg of catalyst into 100 mL of RhB solution with a concentration of 10 mg/L and

stir in the dark for 1 hour to achieve adsorption-desorption equilibrium. Then, proceed with the photocatalytic process with a 30W LED lamp. Every 10 minutes, take 5 mL of the solution and centrifuge, removing the solid part. The concentration of RhB in the solution was determined on a UV-Vis meter (CE-2011) at a wavelength of 553 nm.

3. RESULTS AND DISCUSSION

3.1. Material characteristics

Characteristic results of the crystal structure of materials BC, CN, and BC/CN-x (x=100, 150, and 200) were investigated by X-ray diffraction spectrum, and the results are shown in Figure 1.

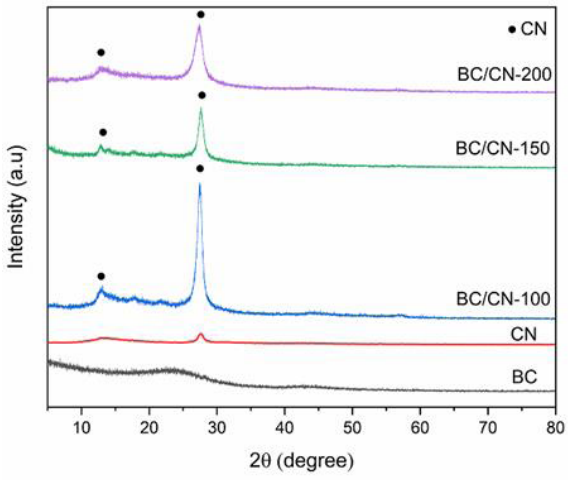

Figure 1. XRD patterns of BC, CN, and BC/CN-x (x = 100; 150; 200).

The results in Figure 1 show that the BC sample has a raised area in the value range 2θ = 20-30°, which is characteristic of the amorphous structure of activated carbon.[8] The CN sample has a diffraction peak at 2θ = 13.2° and 27.5° due to the layered structure of g-C_3N_4 with alternating stacking of conjugated aromatic units similar to the structure of graphite.[9] In the BC/CN-x composite, all the peaks of g-C_3N_4 appeared, but no peaks of the BC sample were seen. This may be due to the overlap of carbon layers between g-C_3N_4 crystals by composite formation.

The chemical bond characteristics of the samples were characterized by FT-IR spectroscopy. The results are shown in Figure 2.

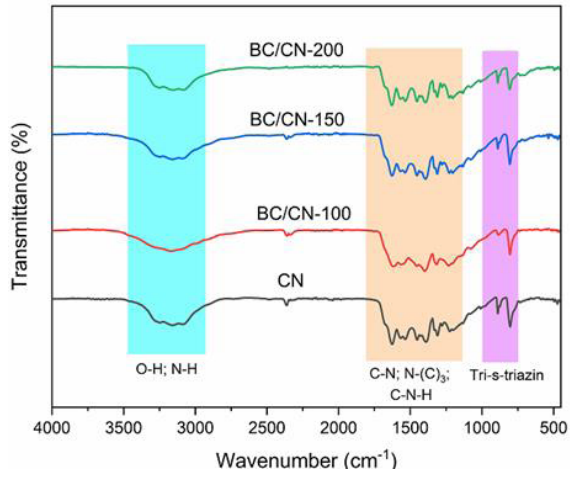

Figure 2. FT-IR spectra of CN and BC/CN-x (x = 100; 150; 200).

For the CN sample, the intensity band at 809.6 cm^{-1} shows the typical characteristic structure of tri-s-triazine.[10] Bands at 1635.1, 1570.8, and 1418.3 cm^{-1} are assigned to the aromatic C-N vibration. The bands at 1324.6 and 1254.9 cm^{-1} are assigned to the stretching vibrations of the bonded blocks of fully condensed N-(C)3 and partially condensed C-N-H, respectively.[11] Absorbance in the range of 3200 – 3400 cm^{-1} is related to residual N-H groups and O-H bands.[12] Thereby, it is seen that there is no obvious change between the CN and the BC/CN-x, which shows that the presence of amorphous carbon does not change the structure of g-C_3N_4.

The structures of BC, CN, and BC/CN composite are characterized by TEM images shown in Figure 3.

The TEM image of the BC sample (Figure 3a) shows a complex structure with defective graphene layers. The CN material (Figure 3b) has a morphology similar to a 2D nanosheet with a thin layer structure. However, compared to the 2D layered sheets of CN, the BC/CN (Figure 3c) shows stacked layers. This can be amorphous carbon materials grown on CN to form composites with surfaces in close contact with each other by heat treatment. The EDX spectrum of the composite shows the full elemental compositions of C and N (Figure 3d).

https://doi.org/10.52111/qnjs.2024.18105

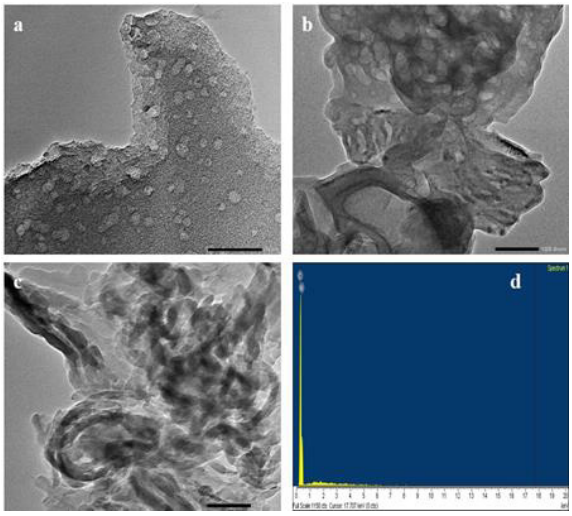

Figure 3. TEM image of BC (a), CN (b), BC/CN-150 (c), and EDX of BC/CN-150 (d).

To determine the photoelectric properties of CN and BC/CN-x composite, UV-Vis diffuse reflectance spectra were performed in Figure 4.

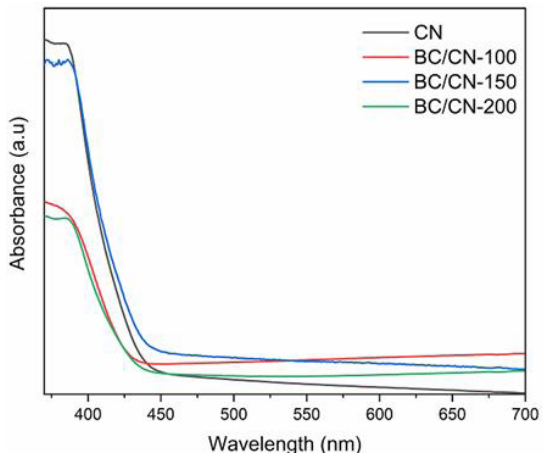

Figure 4. UV-vis diffuse reflectance spectra of CN; BC and BC/CN-x composite.

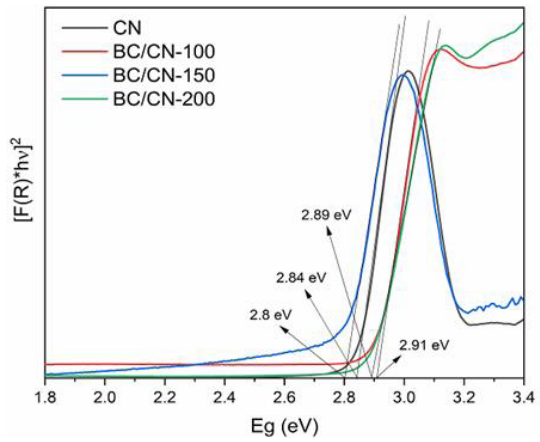

Figure 5. Band gap energy of CN and BC/CN-x composite.

The results show that the composite, after combining with amorphous carbon has a higher absorption intensity over the wavelength range investigated. This is clearly shown in Figure 5 about the band gap of the material. In which the band gap of BC/CN-150 sample (Eg=2.8 eV) has a smaller value than the two other samples BC/CN-100 (Eg=2.89 eV); BC/CN-200 (Eg=2.91 eV) and CN pure (Eg=2.84 eV).

3.2. Photocatalytic properties of materials

BC, CN, and BC/CN-x composites were investigated for their photocatalytic activity in decomposing RhB under visible light. The results are shown in Figure 6. Before evaluating the photocatalytic efficiency, the samples were adsorbed in the dark for 60 minutes to reach the adsorption-desorption balance.

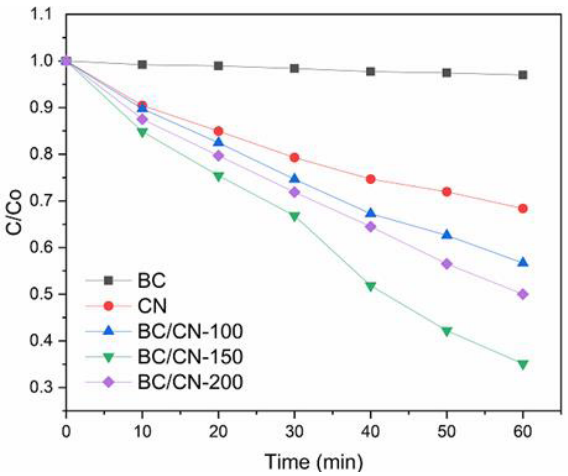

Figure 6. RhB decomposition under visible light of materials (reaction conditions = 10 mg. L^{-1} of RhB dye; 50 mg of catalyst weight; irradiation is LED light).

Figure 6 shows CN, BC/CN-100, BC/CN-150, and BC/CN-200 have an efficiency of 32%, 43.3%, 65%, and 50%, respectively. This shows that composite has higher photocatalytic efficiency than simple materials. This may be because BC material acts as an agent that increases the electrical conductivity and photo-adsorption capacity in the visible light region of the composite, demonstrated through the UV-Vis DRS spectrum (Figure 4) and Eg value (Figure 5). The laws of photocatalytic kinetics of materials all comply with the Langmuir-Hinshelwood model (Figure 7).

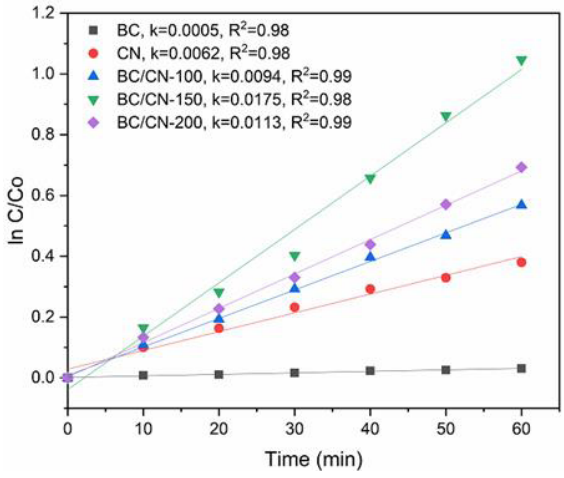

Figure 7. Kinetic fitting plot using the pseudo-first-order model of BC, CN, and BC/CN-x composite (reaction conditions = 10 mg. L^{-1} of RhB dye; 50 mg of catalyst weight; irradation is LED light).

4. CONCLUSION

BC/CN-x composite with different ratios were successfully synthesized via a simple reduction heating method in an Argon atmosphere from urea and carbon precursors. In particular, carbon materials are synthesized from waste biomass raw materials of banana peels. The photocatalytic activity of the composite material BC/CN-150 (H = 65%) is much higher than that of the g-C_3N_4 single (H = 32%) for the decomposition of RhB after 60 minutes of reaction under the visible light region. Therefore, this shows that the presence of carbon significantly improves the photocatalytic efficiency of the materials. This is a promising new research direction in utilizing waste as materials for wastewater treatment and minimizing environmental pollution.

REFERENCES

1. S. Kumaravel, C. Chandrasatheesh, G. Palanisamy, J. Lee, I. Hasan, S. Kumaravel, B. Avula, U. D. Pongiya, K. Balu. Highly efficient solar-light-active Ag-decorated g-C_3N_4 composite photocatalysts for the degradation of methyl orange dye, *Micromachines*, **2023**, *14*, 1454-1467.

2. T. H. Ha, N. T. M. Duyen, N. V. Phuc, N. T. Lan, P. T. T. Trang, H. Q. Dat, L. H. Hoang, K. J. Sung, V. Vien. One-pot synthesis of S-scheme MoS_2/g-C_3N_4 heterojunction as effective visible light photocatalyst, *Scientific Reports*, **2021**, *11*(1), 14787-14799.

3. J. Meng, J. Pei, Z. He, S. Wu, Q. Lin, X. Wei, J. Li, Z. Zhang. Facile synthesis of g-C_3N_4 nanosheets loaded with WO_3 nanoparticles with enhanced photocatalytic performance under visible light irradiation, *RSC Advances,* **2017**, *7*(39), 24097-24104.

4. N. T. T. Huong, T. H. Ha, N. P. Hung, N. V. Phuc, L. Q. Dai, N. T. Lan, P. T. T. Trang, V. Vien. A facile synthesis of SnS_2/g-C_3N_4 S-scheme heterojunction photocatalyst with enhanced photocatalytic performance, *Journal of Science: Advanced Materials and Devices*, **2022**, *7*(2), 100402-100410.

5. Q. Xu, B. Cheng, J. Yu, G. Liu. Making co-condensed amorphous carbon/g-C_3N_4 composites with improved visible-light photocatalytic H_2-production performance using Pt as cocatalyst, *Carbon*, **2017**, *118*, 241-249.

6. W. J. Ong, L. L. Tan, S. P. Chai, S. T. Yong, A. R. Mohamed. Surface charge modification via protonation of graphitic carbon nitride (g-C_3N_4) for electrostatic self-assembly construction of 2D/2D reduced graphene oxide (rGO)/g-C_3N_4 nanostructures toward enhanced photocatalytic reduction of carbon dioxide to methane, *Nano Energy,* **2015**, *13*, 757-770.

7. Y. Gu, Y. Yu, J. Zou, T. Shen, Q. Xu, X. Yue, J. Meng, J. Wang. The ultra-rapid synthesis of rGO/g-C_3N_4 composite via microwave heating with enhanced photocatalytic performance, *Materials Letters*, **2018**, *232*, 107-109.

8. T. V. Thuan, B. T. P. Quynh, T. D. Nguyen, V. T. T. Ho, L. G. Bach. Response surface methodology approach for optimization of Cu^{2+}, Ni^{2+} and Pb^{2+} adsorption using KOH-activated carbon from banana peel, *Surfaces and Interfaces,* **2017**, *6,* 209-217.

9. M. R. Islam, A. K. Chakraborty, M. A. Gafur, M. A. Rahman, M. H. Rahman. Easy preparation of recycle thermally stable visible-light-active graphitic-C_3N_4/TiO_2 nanocomposite photocatalyst for efficient decomposition

of hazardous organic industrial pollutions in aqueous medium, *Research on Chemical Intermediates*, **2019**, *45*, 1753-1773.

10. J. Liu, T. Zhang, Z. Wang, G. Dawson, W. Chen. Simple pyrolysis of urea into graphitic carbon nitride with recyclable adsorption and photocatalytic activity, *Journal of Materials Chemistry,* **2011**, *21*(38), 14398-14401.
11. X. Du, G. Zou, Z. Wang, X. Wang. A scalable chemical route to soluble acidified graphitic carbon nitride: an ideal precursor for isolated ultrathin g-C_3N_4 nanosheets, *Nanoscale,* **2015**, *7*(19), 8701-8706.
12. X. She, L. Liu, H. Ji, Z. Mo, Y. Li, L. Huang, D. Du, H. Xu, H. Li. Template-free synthesis of 2D porous ultrathin nonmetal-doped g-C_3N_4 nanosheets with highly efficient photocatalytic H_2 evolution from water under visible light, *Applied Catalysis B: Environment and Energy*, **2016**, *187*, 144-153.

TẠP CHÍ KHOA HỌC
TRƯỜNG ĐẠI HỌC QUY NHƠN

Xác định chủng virus khảm thuốc lá và virus khảm dưa chuột trên giống Địa hoàng 19 (*Rehmannia glutinosa* varieties 19) bằng kỹ thuật Enzyme Linked Immunosorbent Assay

Hà Thị Tâm Tiến, Phạm Thanh Loan*

Viện Nghiên cứu Ứng dụng và Phát triển, Trường Đại học Hùng Vương, Phú Thọ, Việt Nam

Ngày nhận bài: 18/10/2023; Ngày sửa bài: 03/01/2024;
Ngày nhận đăng: 17/01/2024; Ngày xuất bản: 28/02/2024

TÓM TẮT

Virus khảm thuốc lá (Tobacco Mosaic Virus - TMV) và virus khảm dưa chuột (Cucumber Mosaic Virus - CMV) thường gây bệnh hại trên cây Địa hoàng. Nghiên cứu xác định chủng virus TMV và CMV bằng kỹ thuật Enzyme-Linked Immunosorbent Assay (ELISA) trên các cây mẹ được lấy mẫu để nhân giống, nhằm loại bỏ tác nhân gây bệnh hại ngay từ giai đoạn vào mẫu ban đầu. Kết quả cho thấy các mẫu thân, rễ củ, chồi cấp một và cây *in vitro* giống Địa hoàng 19 (*Rehmannia glutinosa* variety 19) đều không bị nhiễm hai chủng virus TMV và CMV. Đây là nguồn vật liệu khởi đầu phục vụ nhân giống cây sạch bệnh tạo nguồn giống cây Địa hoàng 19 *in vitro* đảm bảo chất lượng tốt.

Từ khóa: *Địa hoàng 19, kỹ thuật ELISA, virus khảm dưa chuột, virus khảm thuốc lá.*

**Tác giả liên hệ chính.*
Email: Loandhhv@gmail.com

QUY NHON UNIVERSITY
JOURNAL OF SCIENCE

Detection of tobacco mosaic virus and cucumber mosaic virus on *Rehmannia glutinosa* variety 19 by Enzyme-Linked Immunosorbent Assay

Thi Tam Tien Ha, Thanh Loan Pham*

Institute of Applied Research and Development, Hung Vuong University, Phu Tho, Vietnam

Received: 18/10/2023; Revised: 03/01/2024;
Accepted: 17/01/2024; Published: 28/02/2024

ABSTRACT

Tobacco Mosaic Virus **(**TMV) and Cucumber Mosaic Virus (CMV) are common pathogens of *Rehmannia glutinosa* Libosch. The study conducted experiments to detect TMV and CMV viruses by Enzyme-Linked Immunosorbent Assay (ELISA) on the mother plants sampled for propagation to eliminate pathogens from the initial sampling stage. The detection results of the stem, tuberous roots, primary shoots, and *in vitro* seedlings of *Rehmannia glutinosa* variety 19 (RG19) showed that the samples were not infected with two types of TMV and CMV viruses. This is the starting material for propagating disease-free seedlings to create a highly qualified source of ***in vitro*** RG19 for crops.

Keywords: *Rehmannia glutinosa variety 19, ELISA, cucumber mosaic virus, tobacco mosaic virus.*

1. INTRODUCTION

Rehmannia glutinosa Libosch (RG) root contains iridoid glucoside compounds, phenylpropanoids, polysaccharides, and phenolic acids,[1] which are widely used in traditional Chinese medicines possessing anti-anemia, antipyretic, anti-inflammatory activities and the effect on lowering blood sugar, anti-aging,[2] and strengthening the immune system.[3] During the RG cultivation using tuberous roots, asexual propagation materials have been practiced through many successive propagation seasons; however, there was a problem of decreasing crop yield and productivity, which led to the degradation of the variety, causing smaller tuber diameter and more extended tuber length output and quality decline. Wang *et al*.[4] identified the Tobacco Mosaic Virus **(**TMV) and the Cucumber Mosaic Virus (CMV) that are common pathogens on RG grown in Henan province, Shandong province, China, and confirmed that they are the cause of the decline in RG varieties. According to Teng *et al*.,[5] TMV and CMV have caused severe damage to RG crops due to their effects on sprout degradation, leading to yield and quality decline. Some other authors have determined the cause of diseases on RG from TMV and CMV viruses. Matsumoto *et al*.[6] detected 27% of RG plants infected with TMV in the first year, 31% in the second year, and up to 63% in the third year, grown in Fukuoka, Japan by ELISA. The damage also reduced the verbascoside content in the tubers each year (verbascoside content reached 0.021% in the first year and only 0.016%

**Corresponding author.*
Email: Loandhhv@gmail.com

https://doi.org/10.52111/qnjs.2024.18106

in the third year). Zhang *et al*.[7] detected the virus that infected RG in Henan province, China by ELISA and gene sequencing. The results showed that TMV is the primary virus infecting RG. Sequencing Gene CP of TMV isolated from RG showed that samples' nucleotide and amino acid sequences were 86.5% and 94.3% with strain TMV U1, respectively, and up to 79.3% and 95.0% against other TMV strains. It was named the Rehmannia Mosaic Virus strain (ReMV) and belongs to the genus Tobamovirus. Liao *et al*.[8] isolated a ReMV strain from the plants grown in Taiwan and Henan province by Chen *et al*.,[9] China. Wardani *et al*.[10] also isolated the harmful ReMV strain on Tobacco plants in Yogyakarta, Indonesia.

In order to control harmful viruses on RG, Teng *et al*.[5] created two varieties of RG, including LBA1 and LBA2, that are resistant to infection by TMV and CMV viruses by genetic engineering. In addition, plants propagated by *in vitro* seedlings can also control diseases caused by viruses by using growth tips as explants or strictly controlling mother plants, using disease-free mother plants as a source of breeding materials. Therefore, we conducted the study to detect TMV and CMV viruses on *Rehmannia glutinosa* variety 19 (RG19) to select disease-free plants as a source of *in vitro* propagation.

2. RESEARCH METHODS

2.1. Research materials

RG19 was provided by Hung Vuong University and accepted for circulation according to notice No. 909/TB-TT-CLT dated July 31, 2020, of the Department of Crop Production, Ministry of Agriculture and Rural Development, Vietnam. Samples of five-month-old RG19 were collected at three locations: Dan Quyen commune, Tam Nong district, Phu Tho province, Vietnam; Bach Luu commune, Song Lo district, Vinh Phuc province, Vietnam; and Trung Yen commune, Son Duong district, Tuyen Quang province, Vietnam. Primary *in vitro* shoot samples and *in vitro* seedlings were provided by the Center for Environmental Biotechnology, Hung Vuong University - Phu Tho, Vietnam.

Laboratory chemicals: PathoScreen® Kit to detect TMV and CMV viruses purchased from Agdia-USA. Laboratory equipment: Biotek ELISA system, sample crusher Tissue Lyser II, thermal printer, sample storage refrigerator, micropipettes.

2.2. Research duration and location

The study was conducted from February 2021 to December 2022 at the Department of Molecular Pathology, Vietnam Institute of Agricultural Genetics and Center for Biotechnology - Environment, Hung Vuong University.

2.3. Research methods

2.3.1. Sampling method

Selection of mother plants: Only well-grown plants were selected: five plants/collection site × three collection sites (one collection site/province × three provinces). Each plant was tested for viruses both from stem and tuberous roots. Thirty samples were collected due to each sampled plant was separated into stem and tuberous root parts for virus testing.

Selection of primary shoots: Using the tuberous roots of the selected mother plants, proceeded to *in vitro* samples. After twenty days, the shoots from the tuber roots were identified as primary shoots. Thirty primary shoots were selected from thirty tuber slices for virus testing.

Selection of *in vitro* samples for rooting: Randomly selected one plant pot-1 from thirty pots of rooting plants in the laboratory for virus testing.

2.3.2. ELISA test method

The ELISA test was conducted according to the instructions of the PathoScreen® Kit as follows:

Sample fixation: Crush the test samples in GEB-coated buffer at a ratio of 1:10 and centrifuge at 10,000 rpm for five minutes to collect the supernatant, which was then added to three microplates (100 µl/well) for each

test sample. The positive and negative control samples were added into separate wells with the same volume in three replicates.

Sample incubation: Pack the sample tray tightly into the box and incubate at 2°C - 8°C for 12 hours.

The first sample washing: Samples were washed with PBST buffer seven times, 100 µl/time after incubation.

Immobilization of antibody-binding enzyme: Add 100 µl/well of alkaline phosphatase enzyme into each test sample tube and incubate for 2 hours at room temperature.

The second sample wash: After enzyme incubation, the samples were washed with PBST buffer eight times, 100 µl/time.

Addition of PNP substrate: PNP substrate concentration 1 mg/ml was added to the wells, 100 µl/well, then incubated for sixty minutes in the dark at room temperature. PNP will be hydrolyzed to nitrophenol phosphate under the catalysis of alkaline phosphate enzyme. Nitrophenol phosphate is a yellow substance that can be detected by the eye or by an ELISA reader. Reactive coloration and colorimetric test results were evaluated using an ELISA Biotek machine, determining the OD value at 450 nm.

Statistical data analysis: The collected data were analyzed using the IRRISTAT 5.0 program. The treatments' means were compared using the Least Significant Difference (LSD) test at the 0.05 level.

3. RESULTS AND DISCUSSION

3.1. Testing of TMV and CMV virus on stem and root samples of RG19

Stem and tuberous root test samples from healthy and well-developed RG19 seedlings were used for TMV and CMV assays, and the results can be seen in Table 1. Table 1 data showed that thirty samples of stem and roots in the experimental wells were colorless, which indicates the negative test results. In the TMV test, the OD values for all thirty samples ranged from 0.047 to 0.074, while the negative control value was 0.067. In the CMV test, the OD values for all thirty samples ranged from 0.050 to 0.061, while the negative control value was 0.056. The positive control is stable, and the colorimetric results of the three wells are all yellow for positive test results. The OD value for TMV was 1.820, which is significantly twenty-four times higher than the negative reactions. Similarly, the OD value for CMV was 2.908, which is significantly forty-seven times higher than that of negative reactions. Thus, all thirty samples of stem and root tubers of RG19 were not infected with two types of TMV and CMV. The tuberous roots of these plants are used as material in the samples for *in vitro* propagation.

Table 1. Detection of TMV and CMV virus on the stem and root of RG19.

No.	Sample ID	TMV Virus			CMV Virus		
		Color	OD value	Result	Color	OD value	Result
1	PT - R1	Nil	$0.049^{a} \pm 0.002$	-	Nil	$0.050^{a} \pm 0.005$	-
2	PT - R2	Nil	$0.061^{a} \pm 0.003$	-	Nil	$0.053^{a} \pm 0.006$	-
3	PT - R3	Nil	$0.050^{a} \pm 0.004$	-	Nil	$0.052^{a} \pm 0.000$	-
4	PT - R4	Nil	$0.047^{a} \pm 0.002$	-	Nil	$0.050^{a} \pm 0.004$	-
5	PT - R5	Nil	$0.051^{a} \pm 0.004$	-	Nil	$0.056^{a} \pm 0.002$	-
6	PT - T1	Nil	$0.059^{a} \pm 0.009$	-	Nil	$0.055^{a} \pm 0.003$	-
7	PT - T2	Nil	$0.054^{a} \pm 0.004$	-	Nil	$0.056^{a} \pm 0.002$	-
8	PT - T3	Nil	$0.059^{a} \pm 0.002$	-	Nil	$0.057^{a} \pm 0.005$	-
9	PT - T4	Nil	$0.052^{a} \pm 0.005$	-	Nil	$0.053^{a} \pm 0.002$	-

https://doi.org/10.52111/qnjs.2024.18106

10	PT - T5	Nil	$0.057^{a} \pm 0.008$	-	Nil	$0.050^{a} \pm 0.002$	-
11	VP - R1	Nil	$0.059^{a} \pm 0.001$	-	Nil	$0.061^{a} \pm 0.001$	-
12	VP - R2	Nil	$0.068^{a} \pm 0.004$	-	Nil	$0.059^{a} \pm 0.002$	-
13	VP - R3	Nil	$0.059^{a} \pm 0.001$	-	Nil	$0.060^{a} \pm 0.007$	-
14	VP - R4	Nil	$0.055^{a} \pm 0.004$	-	Nil	$0.053^{a} \pm 0.001$	-
15	VP - R5	Nil	$0.073^{a} \pm 0.003$	-	Nil	$0.059^{a} \pm 0.008$	-
16	VP - T1	Nil	$0.058^{a} \pm 0.006$	-	Nil	$0.060^{a} \pm 0.002$	-
17	VP - T2	Nil	$0.066^{a} \pm 0.003$	-	Nil	$0.060^{a} \pm 0.003$	-
18	VP - T3	Nil	$0.064^{a} \pm 0.003$	-	Nil	$0.061^{a} \pm 0.005$	-
19	VP - T4	Nil	$0.050^{a} \pm 0.004$	-	Nil	$0.054^{a} \pm 0.003$	-
20	VP - T5	Nil	$0.063^{a} \pm 0.005$	-	Nil	$0.056^{a} \pm 0.006$	-
21	TQ - R1	Nil	$0.059^{a} \pm 0.007$	-	Nil	$0.056^{a} \pm 0.006$	-
22	TQ - R2	Nil	$0.056^{a} \pm 0.006$	-	Nil	$0.058^{a} \pm 0.007$	-
23	TQ - R3	Nil	$0.057^{a} \pm 0.003$	-	Nil	$0.054^{a} \pm 0.002$	-
24	TQ - R4	Nil	$0.064^{a} \pm 0.004$	-	Nil	$0.060^{a} \pm 0.005$	-
25	TQ - R5	Nil	$0.066^{a} \pm 0.004$	-	Nil	$0.060^{a} \pm 0.002$	-
26	TQ - T1	Nil	$0.066^{a} \pm 0.007$	-	Nil	$0.058^{a} \pm 0.002$	-
27	TQ - T2	Nil	$0.063^{a} \pm 0.008$	-	Nil	$0.059^{a} \pm 0.009$	-
28	TQ - T3	Nil	$0.063^{a} \pm 0.008$	-	Nil	$0.056^{a} \pm 0.004$	-
29	TQ - T4	Nil	$0.074^{a} \pm 0.004$	-	Nil	$0.060^{a} \pm 0.004$	-
30	TQ - T5	Nil	$0.069^{a} \pm 0.004$	-	Nil	$0.053^{a} \pm 0.007$	-
31	PC (+)	Yellow	$1.820^{b} \pm 0.128$	+	Yellow	$2.908^{b} \pm 0.033$	+
32	NC (-)	Nil	$0.067^{a} \pm 0.014$	-	Nil	$0.056^{a} \pm 0.008$	-
$LSD_{0.5}$			*0.038*			*0.012*	

Note: Positive (+), Negative (-), Phu Tho (PT), Vinh Phuc (VP), Tuyen Quang (TQ), negative control (NC-), positive control (PC+), Root (R), Trunk (T)

Different letters (a, b) in the same column represent significant differences $p < 0.05$.

3.2. Detection of TMV and CMV virus on primary shoots of RG19

After twenty days in the root sample of RG19, the tuber root slices began to sprout to produce primary shoots. For TMV and CMV virus testing, thirty primary shoots were selected from tuberous root samples. The test results are summarized in Table 2.

Table 2. Detection of TMV and CMV virus on primary shoots of RG19.

No.	Sample ID	TMV Virus			CMV Virus		
		Color	OD value	Result	Color	OD value	Result
1	PS 1	Nil	$0.050^{a} \pm 0.001$	-	Nil	$0.049^{a} \pm 0.002$	-
2	PS 2	Nil	$0.054^{a} \pm 0.005$	-	Nil	$0.053^{a} \pm 0.004$	-
3	PS 3	Nil	$0.052^{a} \pm 0.002$	-	Nil	$0.051^{a} \pm 0.003$	-
4	PS 4	Nil	$0.048^{a} \pm 0.002$	-	Nil	$0.048^{a} \pm 0.001$	-
5	PS 5	Nil	$0.054^{a} \pm 0.005$	-	Nil	$0.052^{a} \pm 0.004$	-
6	PS 6	Nil	$0.060^{a} \pm 0.007$	-	Nil	$0.059^{a} \pm 0.007$	-
7	PS 7	Nil	$0.060^{a} \pm 0.006$	-	Nil	$0.059^{a} \pm 0.007$	-
8	PS 8	Nil	$0.060^{a} \pm 0.002$	-	Nil	$0.060^{a} \pm 0.003$	-

9	PS 9	Nil	$0.055^{a} \pm 0.003$	-	Nil	$0.054^{a} \pm 0.002$	-
10	PS 10	Nil	$0.062^{a} \pm 0.005$	-	Nil	$0.059^{a} \pm 0.002$	-
11	PS 11	Nil	$0.060^{a} \pm 0.005$	-	Nil	$0.057^{a} \pm 0.002$	-
12	PS 12	Nil	$0.055^{a} \pm 0.005$	-	Nil	$0.050^{a} \pm 0.005$	-
13	PS 13	Nil	$0.061^{a} \pm 0.014$	-	Nil	$0.055^{a} \pm 0.007$	-
14	PS 14	Nil	$0.072^{a} \pm 0.012$	-	Nil	$0.063^{a} \pm 0.009$	-
15	PS 15	Nil	$0.071^{a} \pm 0.011$	-	Nil	$0.063^{a} \pm 0.012$	-
16	PS 16	Nil	$0.070^{a} \pm 0.010$	-	Nil	$0.064^{a} \pm 0.006$	-
17	PS 17	Nil	$0.058^{a} \pm 0.001$	-	Nil	$0.058^{a} \pm 0.001$	-
18	PS 18	Nil	$0.063^{a} \pm 0.005$	-	Nil	$0.060^{a} \pm 0.005$	-
19	PS 19	Nil	$0.056^{a} \pm 0.002$	-	Nil	$0.055^{a} \pm 0.001$	-
20	PS 20	Nil	$0.055^{a} \pm 0.002$	-	Nil	$0.053^{a} \pm 0.003$	-
21	PS 21	Nil	$0.070^{a} \pm 0.003$	-	Nil	$0.065^{a} \pm 0.005$	-
22	PS 22	Nil	$0.062^{a} \pm 0.002$	-	Nil	$0.072^{a} \pm 0.010$	-
23	PS 23	Nil	$0.062^{a} \pm 0.002$	-	Nil	$0.064^{a} \pm 0.003$	-
24	PS 24	Nil	$0.057^{a} \pm 0.001$	-	Nil	$0.056^{a} \pm 0.002$	-
25	PS 25	Nil	$0.065^{a} \pm 0.005$	-	Nil	$0.064^{a} \pm 0.004$	-
26	PS 26	Nil	$0.061^{a} \pm 0.002$	-	Nil	$0.060^{a} \pm 0.002$	-
27	PS 27	Nil	$0.058^{a} \pm 0.005$	-	Nil	$0.055^{a} \pm 0.003$	-
28	PS 28	Nil	$0.060^{a} \pm 0.005$	-	Nil	$0.060^{a} \pm 0.004$	-
29	PS 29	Nil	$0.065^{a} \pm 0.004$	-	Nil	$0.065^{a} \pm 0.002$	-
30	PS 30	Nil	$0.065^{a} \pm 0.004$	-	Nil	$0.063^{a} \pm 0.004$	-
31	PC (+)	Yellow	$1.755^{b} \pm 0.124$	+	Yellow	$1.849^{b} \pm 0.128$	+
32	NC (-)	Nil	$0.082^{a} \pm 0.019$	-	Nil	$0.068^{a} \pm 0.009$	-
$LSD_{0.5}$			*0.037*			*0.038*	

Note: positive (+), negative (-), negative control (NC-), positive control (PC+), primary shoot (PS). Different letters (a, b) in the same column represent significant differences $p < 0.05$.

Table 2 shows that all thirty primary shoot samples were negative for two types of TMV and CMV viruses. The experimental wells and the negative control samples showed colorless results. However, the positive control samples showed positive results in yellow. In TMV virus detection, the OD value of thirty samples ranged from 0.048 to 0.072. The negative and positive control values were 0.082 and 1.755, respectively. Similarly, in CMV virus tests, the OD value of thirty samples ranged from 0.048 - 0.072, while the positive control value was high at 1.849, which is significantly twenty-five times higher than negative reactions (0.068). Thus, the *in vitro* primary shoot samples from the roots of RG19 were determined to be uncontaminated by TMV and CMV viruses. As a result, these samples were used in the next steps for bulk multiplication.

3.3. Detection of TMV and CMV virus on *in vitro* seedlings RG19

The primary shoots of RG19 continued to be transplanted to the bud propagation medium to multiply the number of shoots rapidly. After five times multiplication, selected shoots that met the standards for transplanting were transferred to the rooting medium to create complete *in vitro* seedlings with complete roots, stems, and leaves. Thirty *in vitro* seedlings from different culture flasks were selected to detect TMV and CMV virus. The detection results are summarized in Table 3.

https://doi.org/10.52111/qnjs.2024.18106

Table 3. Detection of TMV and CMV viruses on RG19 in *in vitro* seedlings.

No.	Sample ID	TMV virus			CMV virus		
		Color	OD value	Result	Color	OD value	Result
1	IS 1	Nil	$0.051^{a} \pm 0.002$	-	Nil	$0.051^{a} \pm 0.006$	-
2	IS 2	Nil	$0.049^{a} \pm 0.004$	-	Nil	$0.054^{a} \pm 0.003$	-
3	IS 3	Nil	$0.045^{a} \pm 0.002$	-	Nil	$0.049^{a} \pm 0.003$	-
4	IS 4	Nil	$0.048^{a} \pm 0.002$	-	Nil	$0.051^{a} \pm 0.001$	-
5	IS 5	Nil	$0.051^{a} \pm 0.006$	-	Nil	$0.056^{a} \pm 0.004$	-
6	IS 6	Nil	$0.052^{a} \pm 0.002$	-	Nil	$0.059^{a} \pm 0.003$	-
7	IS 7	Nil	$0.050^{a} \pm 0.002$	-	Nil	$0.057^{a} \pm 0.003$	-
8	IS 8	Nil	$0.053^{a} \pm 0.003$	-	Nil	$0.056^{a} \pm 0.002$	-
9	IS 9	Nil	$0.058^{a} \pm 0.003$	-	Nil	$0.059^{a} \pm 0.004$	-
10	IS 10	Nil	$0.049^{a} \pm 0.004$	-	Nil	$0.050^{a} \pm 0.019$	-
11	IS 11	Nil	$0.056^{a} \pm 0.008$	-	Nil	$0.058^{a} \pm 0.011$	-
12	IS 12	Nil	$0.054^{a} \pm 0.007$	-	Nil	$0.060^{a} \pm 0.009$	-
13	IS 13	Nil	$0.060^{a} \pm 0.014$	-	Nil	$0.056^{a} \pm 0.003$	-
14	IS14	Nil	$0.054^{a} \pm 0.004$	-	Nil	$0.062^{a} \pm 0.006$	-
15	IS 15	Nil	$0.055^{a} \pm 0.005$	-	Nil	$0.055^{a} \pm 0.003$	-
16	IS 16	Nil	$0.054^{a} \pm 0.002$	-	Nil	$0.058^{a} \pm 0.002$	-
17	IS 17	Nil	$0.055^{a} \pm 0.006$	-	Nil	$0.056^{a} \pm 0.005$	-
18	IS 18	Nil	$0.052^{a} \pm 0.005$	-	Nil	$0.049^{a} \pm 0.004$	-
19	IS 19	Nil	$0.057^{a} \pm 0.010$	-	Nil	$0.054^{a} \pm 0.005$	-
20	IS 20	Nil	$0.056^{a} \pm 0.009$	-	Nil	$0.057^{a} \pm 0.007$	-
21	IS 21	Nil	$0.063^{a} \pm 0.014$	-	Nil	$0.060^{a} \pm 0.005$	-
22	IS 22	Nil	$0.055^{a} \pm 0.001$	-	Nil	$0.061^{a} \pm 0.001$	-
23	IS 23	Nil	$0.056^{a} \pm 0.002$	-	Nil	$0.056^{a} \pm 0.004$	-
24	IS 24	Nil	$0.053^{a} \pm 0.003$	-	Nil	$0.061^{a} \pm 0.002$	-
25	IS 25	Nil	$0.059^{a} \pm 0.002$	-	Nil	$0.061^{a} \pm 0.002$	-
26	IS 26	Nil	$0.050^{a} \pm 0.003$	-	Nil	$0.055^{a} \pm 0.004$	-
27	IS 27	Nil	$0.056^{a} \pm 0.002$	-	Nil	$0.058^{a} \pm 0.005$	-
28	IS 28	Nil	$0.054^{a} \pm 0.002$	-	Nil	$0.060^{a} \pm 0.004$	-
29	IS 29	Nil	$0.054^{a} \pm 0.003$	-	Nil	$0.059^{a} \pm 0.005$	-
30	IS 30	Nil	$0.054^{a} \pm 0.005$	-	Nil	$0.058^{a} \pm 0.001$	-
31	PC (+)	Yellow	$2.020^{b} \pm 0.085$	+	Yellow	$1.901^{b} \pm 0.036$	+
32	NC (-)	Nil	$0.051^{a} \pm 0.002$	-	Nil	$0.053^{a} \pm 0.002$	-
$LSD_{0.5}$			*0.026*			*0.014*	

Note: positive (+), negative h (-), negative control (NC-), positive control (PC+), In vitro seedlings (IS)
Different letters (a, b) in the same column represent significant differences $p < 0.05$.

Table 3 data shows that all thirty *in vitro* seedlings of RG19 and NC samples were negative for two types of TMV and CMV viruses, while PC samples tested with yellow color. In the TMV test, the OD value of thirty samples ranges from 0.045 - 0.063; the negative control was 0.051; the positive control was 2.020, which is significantly thirty-two times higher than the negative reactions. For the CMV test, the OD value of thirty samples ranges from 0.049 - 0.062. With the same pattern, the negative control was 0.053; the positive control was 1.901, which is significantly thirty times higher than the negative reactions. Thus, none of the thirty *in vitro* seedling samples were infected with TMV or CMV viruses.

3.4. Discussion

According to Wang *et al*.[4] and Teng *et al*.,[5] RG plants infected with TMV and CMV often lead to sprouting degradation, causing smaller tuber diameter and reducing the yield and quality of tubers. Similarly, Teng *et al*.,[5] Matsumoto *et al*.,[6] and Zhang *et al*.[7] found some strains of TMV and CMV viruses in RG when cultivated in China and Japan. Of which, the research by Matsumoto *et al*.[6] showed that the TMV virus appeared on RG cultivars with a high rate of plants infected in the first year (27%). This infection rate increased to 31% and 63% in the second and third years. These infected plants also caused a decrease in verbascoside content, which was only recorded at 0.021% and 0.016% in the first year and the 3rd year, respectively. Therefore, it is necessary to select a variety of RG that are not infected with TMV or CMV for cultivation. Teng *et al*.[5] used genetic engineering to create two varieties of RG, LBA1, and LBA2, that were resistant to infection by TMV and CMV viruses.

R. glutinosa plants infected with the TMV and the CMV often have symptoms of leaf mosaic (mosaic pattern of light and dark green), yellow spots on the leaves, stunning symptoms, and necrotic spots.[4,7,8,10] When choosing mother plants during breeding, these are easy-to-identify characteristics to eliminate plants infected with TMV and CMV. In addition, breeding the plant micropropagation system is an ideal solution to the problems caused by diseases. Tissue culture helps eliminate diseases caused by viruses. Plant cell and tissue culture are important in manipulating plants for improved crop varieties. The plant regeneration system is essential to micropropagation approaches leading to plant improvement in *R. glutinosa***.** Plant tissues of *R. glutinosa* will provide a source of disease-free seedlings.

Viruses can also be eliminated by *in vitro* propagation. Before propagation, testing for TMV and CMV viruses on the mother plants, which provide propagation material, is essential to eliminate pathogens from the initial sampling stage. The test results of the stem, tuberous roots, and *in vitro* RG19 seedlings collected from Phu Tho, Vinh Phuc, and Tuyen Quang showed that the samples were not infected with two types of TMV and CMV viruses. These *in vitro* seedlings are the starting material for the propagation of disease-free plants, which contributes to providing a source of good-quality seedlings for cultivation.

4. CONCLUSION

Samples from stems and roots of RG19 grown in the three provinces of Phu Tho, Vinh Phuc, and Tuyen Quang used as materials for *in vitro* culture were not infected with TMV and CMV viruses. Thirty *in vitro* primary shoot samples and thirty complete *in vitro* seedling samples were not infected with two types of TMV and CMV viruses. The test results of the ELISA technique were all negative.

REFERENCES

1. I. M. Chung, J. J. Kim, J. D . Lim, C. Y. Yu, S. H. Kim, S. J . Hahn. Comparison of resveratrol, SOD activity, phenolic compounds and free amino acid in rehmannia glutinosa under temperature and water stress, *Environmental and Experimental Botany*, **2006**, *56,* 44-53.

https://doi.org/10.52111/qnjs.2024.18106

2. R. X. Zhang, M. X. Li, Z. P. Jia. Rehmannia glutinosa: a review of botanicals, chemistry, and pharmacology, *Journal of Ethnopharmacology*, **2008**, *117,* 199-214.

3. H. Zhao, J. Tan, C. H. Qi. Photosynthesis of rehmannia glutinosa subjected to drought stress is enhanced by choline chloride through alleviating lipid peroxidation and increasing proline accumulation, *Plant Growth Regulation*, **2007**, *51,* 255-262.

4. M. Wang, I. F. Lin, L. Q. Huang, Y. F. Chen, Z. G. Wu, G. F. Li, E. S. Weim, R. X. Fang. TMV and CMV widely infect cultivated rehmannia glutinosa Libosch, *Acta Phytopathological Sinica*, **2006**, *36*(2)*,* 189-192.

5. Z. Teng, Y. Shen, J. Li, Z. Lin, M. Chen, M. Wang, M. Li, H. Dong, L. Huang. Construction and quality analysis of transgenic rehmannia glutinosa containing TMV and CMV coat protein, *Molecules*, **2016**, *21,* 1134-1145.

6. M. Matsumoto, Y. Shoyama, I. Nishioka, H. Iwai, S. Wakimoto. Identification of viruses infected in rehmannia glutinosa Libosch var purpurea Makino and effect of virus infection on root yield and iridoid glycoside contents, *Plant Cell Reports*, **1989**, *7,* 636-638.

7. Z. Zhang, L. Zhang, Q. Qiao, Y. Wang, X. Jin. Identification of viral pathogens of rehmannia glutinosa disease in Henan province, *Acta Phytopathologica Sinica*, **2004**, *34*(5)*,* 395-399.

8. J. Liao, C. Hu, J. Kao, T. Deng. Identification of tobacco mosaic virus infecting rehmannia glutinosa, *Plant Pathology Bulletin,* **2007**, *16*, 61-69.

9. J Chen, C. Feng, X. Guo, Y. Zhou, T. Gu, X. Zhuang, L. Cheng, K. Zhang. Development of polyclonal antibodies based serological methods for detection of the rehmannia mosaic virus in field plants, *Frontiers in Sustainable Food System*, **2022**, *6,* 1013470.

10. T. P. Wardani, S. Hartono, S. Sulandari, S. Somowiyarjo. Double infections of rehmannia mosaic virus and potato virus Y on tobacco plants in central Java and special region of Yogyakarta, *Jurnal Perlindungan Tanaman Indonesia*, **2021**, *25*(2)*,* 133-140.

TẠP CHÍ KHOA HỌC
TRƯỜNG ĐẠI HỌC QUY NHƠN

Tổng hợp polyvinyl alcohol/liginin hydrogel và khảo sát khả năng hấp phụ methylene blue

Bùi Thị Thảo Nguyên*, Huỳnh Quang Phú, Phan Quốc Huy

Đại học Bách Khoa - Đại học Quốc gia Thành phố Hồ Chí Minh, Việt Nam

Ngày nhận bài: 11/09/2023; Ngày sửa bài: 19/01/2024;
Ngày nhận đăng: 30/01/2024; Ngày xuất bản: 28/02/2024

TÓM TẮT

Trong nghiên cứu này, hydrogel từ polyvinyl alcohol và lignin đã được tổng hợp. Glyoxal được sử dụng làm chất liên kết chéo với vai trò hình thành liên kết giữa các phân tử polyvinyl alcohol và lignin. Khả năng hấp phụ của hydrogel đối với methylene blue (MB) đã được nghiên cứu với các nồng độ ban đầu của dung dịch methylen blue (MB). Nghiên cứu đường đẳng nhiệt hấp phụ được thực hiện ở nhiệt độ 31^{o}C và pH 7 với mô hình Langmuir và Freundlich. Các hệ số tương quan (R^2) của đồ thị cho thấy số liệu thực nghiệm phù hợp với mô hình Langmuir. Điều này chứng tỏ rằng MB được hấp phụ trên hydrogel theo cơ chế hấp phụ đơn lớp. Hiệu suất hấp phụ MB lớn hơn 88%. Ngoài ra, các đặc tính của hydrogel PVA/lignin đã được nghiên cứu bằng một số phương pháp phân tích, bao gồm quang phổ hồng ngoại biến đổi Fourier (FTIR), phương pháp nhiễu xạ tia X (XRD) và phương pháp quang phổ nhìn thấy UV (UV-Vis).

Từ khóa: *Hấp phụ, methylene blue, polyvinyl alcohol, lignin, hydrogel.*

*Tác giả liên hệ chính.
Email: btnguyen@hcmut.edu.vn

QUY NHON UNIVERSITY
JOURNAL OF SCIENCE

Preparation of poly vinyl alcohol/lignin hydrogels and investigation of the adsorption for methylene blue

Bui Thi Thao Nguyen*, Huynh Quang Phu, Phan Quoc Huy

Ho Chi Minh City University of Technology - Vietnam National University Ho Chi Minh City, Vietnam

Received: 11/09/2023; Revised: 19/01/2024;
Accepted: 30/01/2024; Published: 28/02/2024

ABSTRACT

In this study, hydrogels from polyvinyl alcohol and lignin were synthesized. Glyoxal was used as crosslinking agent with the role of forming bonds between polyvinyl alcohol and lignin molecules. The adsorption capacity of the hydrogels for methylene blue (MB) was investigated with the various initial concentrations of methylene blue (MB) solution. The study of adsorption isotherm was conducted at 31^{o}C and pH 7 with Langmuir and Freundlich models. The correlation coefficients (R^2) of the graphs showed that the experimental data fitted Langmuir model. This proved that MB adsorbed on the hydrogel by mono-layer adsorption mechanism. MB adsorption effiency was over 88%. In addition, the properties of PVA/lignin hydrogels were studied by several analytical methods, including Fourier-transform infrared spectroscopy (FTIR), X-ray diffraction method (XRD) and UV–visible spectrophotometry (UV-Vis).

Keywords: *Adsorption, methylene blue, polyvinyl alcohol, lignin, hydrogel.*

1. INTRODUCTION

Environmental pollution becomes a serious issue not only for Vietnam but also for the whole world. Along with the rapid development of industry, the water environment is being seriously affected. The lack of overall planning in the operation of factories, hospitals, and industrial parks in Vietnam has led to the discharge of untreated wastewater into the environment. Wastewater from industries, especially the textile dyeing, often contains high alkalinity and dangerous organic content, negatively affecting drainage systems and water environment.[1-6] The presence of colorants in wastewater also creates a serious problem, affecting the ecological process and landscapes. A typical dye waste is methylene blue, which is widely used in the textile, paper dyeing, plastic and rubber dyeing, and cosmetics industries. Methylene blue (MB) is an organic dye that has a negative impact on the water environment. About 10-15% of MB dyes from the textile industry are discharged into the environment each year. Wastewater from the dye industry has a high alkalinity (pH 8 - 11) and contains a significant amount of organic matter (COD 620 - 4585 mg/L). This pollutes water, reduces dissolved oxygen in water, and negatively affects the life of aquatic organisms. Prolonged exposure to MB can cause vomiting, increased heart rate, shock, cyanosis, and jaundice.[7-9] Dyes in wastewater, including MB dye, inhibit the penetration of sunlight into

*Corresponding author.
Email: btnguyen@hcmut.edu.vn

https://doi.org/10.52111/qnjs.2024.18107

water and affect the photosynthesis of aquatic species. In addition, MB is considered toxic and potentially carcinogenic to humans.

In order to eliminate wastewater pollutants, hydrogel has been researched and developed as a potential adsorbent material. Hydrogel is a polymer with a 3D network structure, which has an outstanding water absorption capacity. The kinetic adsorption and chemical properties of hydrogel also allow it to adapt to different environmental conditions. Therefore, hydrogel can be used in many fields, including adsorption of pollutants, drug delivery, and water purification.[10,11]

Although various methods have been applied to treat dye-containing wastewater, such as microbial treatment, coagulation, oxidation-reduction, membrane filtration technology, and a combination of other methods, they may encounter complex barriers and be economically inefficient. Meanwhile, the adsorption method is still widely used as an economical solution to treat wastewater due to its simplicity, high efficiency, flexibility, and compatibility with most current wastewater treatment processes.[12-14]

The issue of environmental pollution and the attraction of impressive potential of hydrogel materials lead to the application of hydrogel in water pollution treatment. Especially those hydrogels with biodegradable components such as polyvinyl alcohol (PVA), a non-toxic polymer, and lignin, a natural biomass substance, are familiar and popular.[15-17]

In this work, the hydrogel adsorbents from polyvinyl alcohol and lignin were synthesized. The glyoxal as a crosslinker for the hydrogels was utilized to create three-dimensional network for the hydrogel, which made hydrogel not soluble in the water. The outstanding property is that the preparation of the hydrogel was facile and simple by moulding at 70 ^{o}C. The raw materials are environmentally friendly. The adsorption capacity of these prepared hydrogels for MB was studied by Langmuir and Freundlich adsorption isotherms. The characterization of the hydrogel was investigated by FTIR, SEM, and UV-Vis.

2. MATERIALS AND METHODS

2.1. Materials

PVA (average M_W = 205 000 g/mol, 98-99% hydrolyzed) was supplied by Sigma Aldrich (Germany). Glyoxal and lignin (average M_W = 15000 g/mol) were purchased from Wako Chemical Industries (Japan). All other chemicals were obtained from Guangdong Guanghua Sci-Tech Company (China).

2.2. Synthesis of PVA/lignin hydrogel

Firstly, PVA was slowly added to the flask containing hot water, then the PVA particles would dissolve in the water to form the solution by stirring steadily at 90 ^{o}C for 60 minutes. After that, glyoxal was poured into the solution, and dispersed in the solution for 15 minutes to obtain a homogenous solution. Next, lignin was placed into the solution under stirring for 30 minutes. Then, the mixture was poured into a prepared mold which would be put into the oven at 70 ^{o}C for about 90 minutes in order to create the hydrogel samples.[18]

2.3. Adsorption isotherms

The adsorption equilibrium experiments were carried out with the initial concentrations (C_o) of MB solutions, ranging from 10 to 50 mg/L. The hydrogel samples were soaked into MB solutions, until the solution reached equilibrium concentrations at 31 ^{o}C, pH 7. The equilibrium concentrations (C) were determined by the relationship between the absorbance and the colored solutions. The absorbance of MB solution was tested by UV-Vis spectrophotometer.

The adsorption capacity q (mg/g) and removal efficiency E% were calculated by the equations below:[19]

$$\mathbf{q} = \frac{(\mathbf{C_0} - \mathbf{C}).\mathbf{V}}{\mathbf{m}} \quad (1)$$

$$\mathbf{E} = \frac{\mathbf{C_0} - \mathbf{C}}{\mathbf{C_0}} \mathbf{x\ 100\%} \quad (2)$$

https://doi.org/10.52111/qnjs.2024.18107

Where C_o and C (mg/L) were the initial and equilibrium concentration of the MB solution, respectively. V (L) and m (g) were the volume of the MB solution and the weight of the hydrogel, respectively.

Langmuir (3) and Freundlich isotherm (4) models were used to study the adsorption. The Langmuir isotherm model described the adsorption behavior relating to monolayer adsorption on the surface of the adsorbent while the Freundlich isotherm model reflected multilayers adsorption:[20,21]

$$\frac{C}{q} = \frac{C}{q_\infty} + \frac{1}{bq_\infty}$$

$$\ln q = \frac{1}{n}\ln C + \ln K \quad (4)$$

Where q_∞ (mg/g) was the maximum adsorption capacity, b (L/m.g) was a Langmuir constant presented for the adsorption energy, K (mg/g) was a Freundlich constant associated with the adsorption capacity of the adsorbent, and 1/n was the Freundlich coefficient relative heterogeneity.

The dimensionless equilibrium parameter, R_L, showing the chemical affinity between the absorbent and the absorbate, was calculated as follows:[20]

$$R_L = \frac{1}{1+bC_0} \quad (5)$$

The favorable values of R_L were less than 1.

2.4. Analytical methods

The characterization of hydrogel was studied by Frontier FT-IR/NIR instrument model at Institute of Applied Materials Science, Ho Chi Minh City, Vietnam with the scan rate and speed being 4000 – 4500 cm^{-1} and 0.2 mm/s, respectively and SEM system at Research Laboratories of Saigon Hi-tech Park, Ho Chi Minh City, Vietnam. Crystal phases of the hydrogel samples were investigated with the X-ray diffraction method (XRD) with Cu-Kα radiation (λ=1.54184 Å). The MB solution was examined its absorbance by UV/UV-NIR Horiba Dual-FL at Ho Chi Minh City University of Technology - Vietnam National University Ho Chi Minh City.

3. RESULTS AND DISCUSSION

3.1 Analysis of crystal structure by X-ray diffraction method

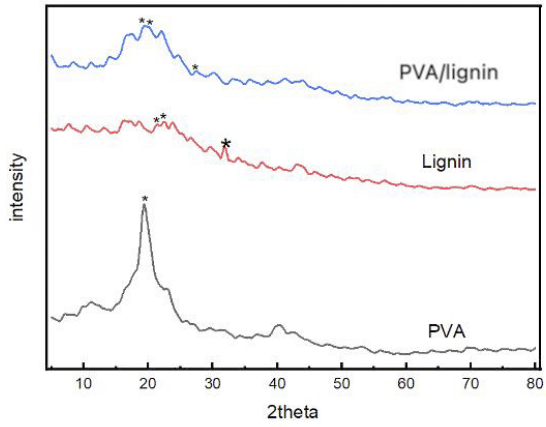

Figure 1. XRD spectrum of lignin and sample.

In this study, the XRD spectra of PVA, lignin, and PVA/lignin composite hydrogel were measured by an X-ray diffraction spectrometer with a scan range from 5° to 80°. From Figure 1, it could be seen that PVA had a main peak around the 2θ angle of 20°, which was a high and narrow signal peak, indicating a specific crystal structure. This characterized the semi-crystallinity structure of PVA polymer. Lignin had a very light XRD spectrum with a few small peaks, indicating that lignin has an amorphous structure.

The PVA/lignin composite with glyoxal agent had some weak and unclear peaks at the positions which was similar to pure PVA. This indicated the formation of cross-linkages between PVA by glyoxal, which made the changes in the structure of PVA network. Therefore, crystal parts of the PVA were disordered and became amorphous parts.

3.2. Analysis of the specific functional groups by FT-IR spectra

In the FTIR infrared spectrum of PVA in Figure 2, the broad peak at 3267 cm^{-1} corresponded to the stretching vibration of the OH group in PVA, indicating the presence of alcohol groups in the polymer. The peak at 2939 cm^{-1} was the symmetric stretching vibration CH groups in PVA. The peaks appearing at 1430 cm^{-1} reflected CH_2. The sharp peak at 1707 cm^{-1} represented

https://doi.org/10.52111/qnjs.2024.18107

the C=O stretching vibration in the amorphous region of PVA and attributed to carbonyl functional groups from residual acetate radicals after PVA synthesis from polyvinyl acetate hydrolysis. The peak at 1089 cm^{-1} was the C-O stretching vibration in PVA.[6]

The FTIR spectrum of lignin in Figure 2 showed greater complexity in its structure, with a peak at 1595 cm^{-1}, indicating the presence of hydroxycinnamic esters in the lignin sample. The peak at 1361 cm^{-1} associated with the syringyl molecular structure of lignin, manifested through C-O stretching during contraction. The peak at 1267 cm^{-1} corresponded to the contraction of the guaiacyl ring, accompanied by C=O stretching. The peak at 1209 cm^{-1} reflected the vibration of C-O-C bonds in ether and ester compounds, or phenolic hydroxyls. The frequency band at 1130 cm^{-1} related to the in-plane deformation vibration of C-H in syringyl aromatic ring groups. Finally, the peak at 1035 cm^{-1} originated from the in-plane deformation of C-H in aromatic rings and C-O bending in primary alcohol catalysis, belonging to the guaiacyl type. The peak at 3453 cm^{-1} presented the vibration of the hydroxyl group.[22]

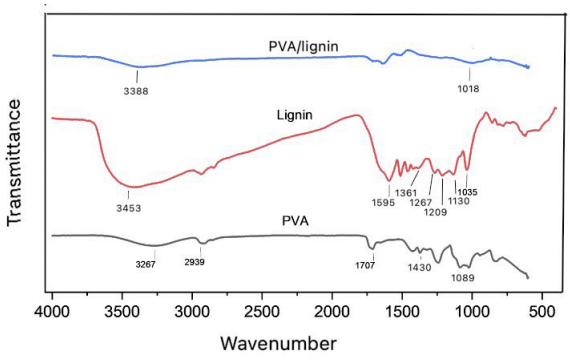

Figure 2. FTIR spectrum of PVA, lignin and PVA/lignin sample.

In the FTIR spectrum of the PVA/lignin in Figure 2, the weak spectra signal at wave numbers 1018 cm^{-1} was asymmetric stretching of the C-O groups in lignin structure. The broad peak at 3388 cm^{-1} reflected the vibration of the hydroxyl group. The shift of the -OH functional group from the 3267 cm^{-1} region in the PVA spectrum and 3453 cm^{-1} peak in lignin spectrum to the field region of 3388 cm^{-1} in the PVA/lignin sample occured in the hydrogel.[23] This result revealed that the cross-linkages which was created by the reaction between hydroxyl groups of PVA with glyoxal (Figure 3) led to the change of the wave number at -OH vibration in the PVA/lignin sample.[24] Moreover, the hydrogen linkage was formed between -OH groups between PVA and lignin.[25,26]

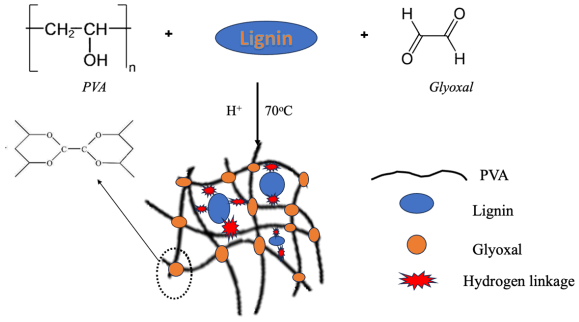

Figure 3. The chemical linkage between PVA, lignin and glyoxal.[25,26]

3.3. Morphology of PVA/lignin hydrogel by SEM image

The SEM image (Figure 4) showed that the surface hydrogel was rough with uneven distribution of PVA and lignin molecules. It also had many pores and holes which illustrated 3D network structure of the hydrogel. The walls between pores was thin and smooth. The hydrogel had continuous structure with various pore, which proved that the hydrogel had high crosslinking density.

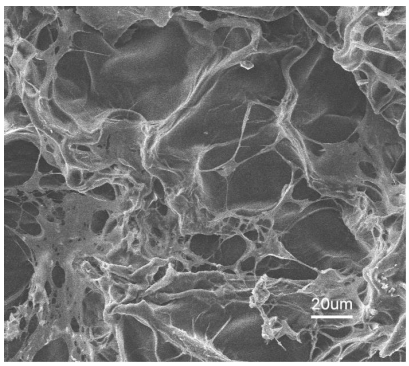

Figure 4. SEM image of PVA/lignin hydrogel.

3.4. Investigation of adsorption capacity for methylene blue

The adsorption capacity and removal efficiency of the PVA/lignin hydrogel were investigated at 31 °C, pH 7, shown in Table 1 and Figure 5.

Table 1. The adsorption capacity of PVA/lignin hydrogel.

C_0 (mg/L)	C (mg/L)	q (mg/g)	E%
10	0.57	9.43	94.32
20	1.17	18.83	94.16
30	2.14	27.86	92.86
40	4.19	35.81	89.53
50	5.92	44.08	88.16

From Table 1 and Figure 5, the adsorption capacity for MB of PVA/lignin hydrogel increased linearly with the equilibrium concentration of MB solution. When equilibrium concentrations were from 0.57 (mg/L) to 5.92 (mg/L), which was the results of the adsorption process with initial concentrations from 10 to 50 mg/L, the amount of MB inserting into the hydrogel increased from 9.43 (mg/g) to 44.08 (mg/g) and the removal efficiency ranged from 88.16% to 94.32%. These data presented that the MB adsorption depended on the moving process of MB from the initial solution to the hydrogels. With increasing concentrations of MB solution, the amount of MB adsorbing on the hydrogel increased to equilibrium. The removal efficiency obtained over 88% and the highest value about 94%. MB was also used as an organic dye in some adsorption experiments by various adsorbents. Chitosan-based composite hydrogel adsorbed MB at adsorption efficiency above 85%.[27] Hydrogels loaded with Huangshui polysaccharides, polyvinyl alcohol, and sodium carboxyl methyl cellulose had MB adsorption ability of 71.07 mg/g.[28] Cellulose based hydrogel showed MB removal capacity up to 83%.[29] Compared to the previous research, the PVA/lignin hydrogel had outstanding removal efficiency over 88.16%.

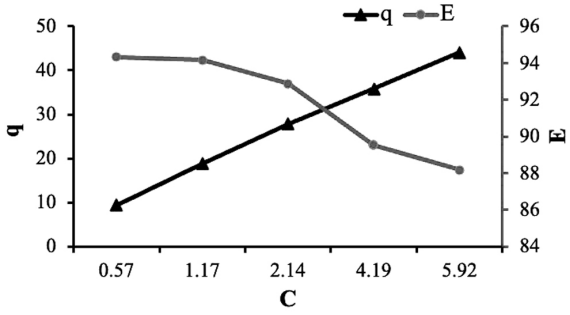

Figure 5. The effect of concentrations on the adsorption amount and removal efficiency.

3.5. Study of adsorption isotherms

The equilibrium adsorption had been studied by isotherm models, Langmuir and Freundlich models. The relationship between q and C according to Langmuir model was presented in the Figure 6a. The relationship between lnq and lnC according to Freundlich model was expressed in Figure 6b.

The maximum amount of MB moleculars adsorbing on the hydrogel could be drawn from Langmuir model, which was about 60 (mg/g). From the correlation coeficients (R^2) in the line graphs (Figures 6a and 6b), it could be seen that the Langmuir curve fitted the experimental parameters. The correlation coefficients (R^2) of the linear form for Langmuir isotherm model were 0.9951 which was much closer to 1.0 than that of Freundlich models. These data revealed that Langmuir model described properly the MB adsorption of PVA/lignin hydrogel adsorbents and affirmed that adsorption occured by the monolayer adsorption on the surface of the hydrogel.

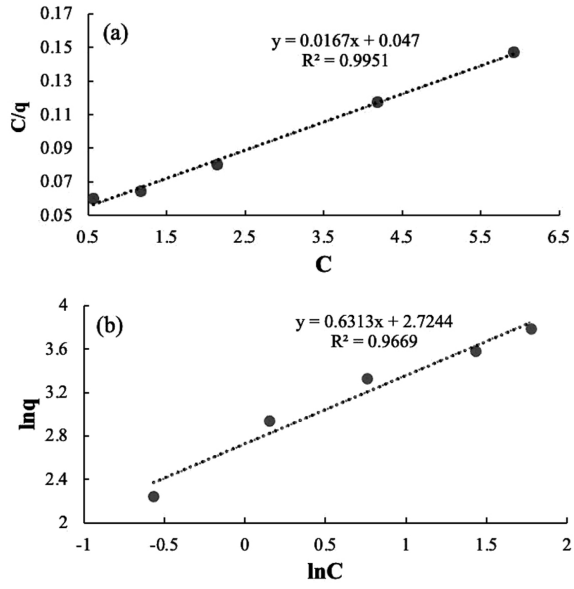

Figure 6. Adsorption isotherms of MB on the hydrogel, Langmuir model (a) and Freundlich model (b).

R_L parameter which discovered the affinity of adsorption on hydrogel, following Langmuir model, could be calculated from the equation (5), which was from 0.05 to 0.2. These values of R_L were smaller than 1, so this is favorable. The

https://doi.org/10.52111/qnjs.2024.18107

results showed the good affinity between MB moleculars and the PVA/lignin hydrogel.

4. CONCLUSION

In this study, the hydrogels based on PVA and lignin were successfully synthesized by using glyoxal crosslinker. The adsorption process was conducted by batch experimental procedure at 31 ^{o}C, pH 7. The maximum adsorption capacity was about 60 mg/g. The experimental data agreed with Langmuir isotherm model, showed that MB adsorbed by monolayer coverages on the hydrogel surfaces. The affinity parameter was lower than 1, indicating good affinity between MB adsorbents and the hydrogel. Moreover, removal efficiency was higher than 88%. Consequently, the hydrogels can be applied for the removal of methylene blue from aqueous solution.

REFERENCES

1. G. Zhao, T. Sun, D. Wang, S. Chen, Y. Ding, Y. Li, G. Shi, H. Sun, S. Wu, Y. Li, C. Wu, Y. Li, Z. Yu, Z. Chen. Treated wastewater and weak removal mechanisms enhance nitrate pollution in metropolitan rivers, *Environmental Research*, **2023**, *231*, 116182.
2. S. Pal, S. Debanshi. Exploring the effect of wastewater pollution susceptibility towards wetland provisioning services, *Ecohydrology & Hydrobiology*, **2023**, *23*(1), 162-176.
3. F. Kazembeigi, S. Bayad, A. Yousefi Nasab, M. Doraghi, I. Parseh. Techno-environmental study on the consequences of carwash wastewater and its management methods, *Heliyon*, **2023**, 19764.
4. P. Chowdhary, A. Raj, R. N. Bharagava. Environmental pollution and health hazards from distillery wastewater and treatment approaches to combat the environmental threats: a review, *Chemosphere*, **2018**, *194*, 229-246.
5. F. B. Elehinafe, O. Agboola, A. D. Vershima, G. O. Bamigboye. Insights on the advanced separation processes in water pollution analyses and wastewater treatment – a review, *South African Journal of Chemical Engineering*, **2022**, *42*, 188-200.
6. C. Y. Lai, Y. M. Sun, Y. L. Liu. Water-soluble ozonated lignin as a hydrophilic modifier for poly(vinyl alcohol) membranes for pervaporation desalination, *Journal of Membrane Science*, **2023**, *685*, 121959.
7. R. Sivakumar, N. Y. Lee. Adsorptive removal of organic pollutant methylene blue using polysaccharide-based composite hydrogels, *Chemosphere*, **2022**, *286*, 131890.
8. E. U. Mughal, A. Javaid, M. Imran, M. A. S. Abourehab, E. B. Elkaeed, N. Naeem, A. Y. A. Alzahrani, A. Sadiq, S. F. Kainat. Complexes of terpyridine scaffold as efficient photocatalysts for the degradation of methylene blue pollutant in wastewater effluents, *Inorganica Chimica Acta*, **2023**, *546*, 121329.
9. S. S. Vedula, G. D. Yadav. Wastewater treatment containing methylene blue dye as pollutant using adsorption by chitosan lignin membrane: development of membrane, characterization and kinetics of adsorption, *Journal of the Indian Chemical Society*, **2022**, *99*(1), 100263.
10. A. A. Hamid, J. Alam, A. K. Shukla, F. A. A. Ali, M. Alhoshan. Sustainable removal of phenol from wastewater using a biopolymer hydrogel adsorbent comprising crosslinked chitosan and κ-carrageenan, *International Journal of Biological Macromolecules*, **2023**, *251*, 126340.
11. S. Ahmad, M. S. Tanweer, T. A. Mir, M. Alam, S. Ikram, J. N. Sheikh. Antimicrobial gum based hydrogels as adsorbents for the removal of organic and inorganic pollutants, *Journal of Water Process Engineering*, **2023**, *51*, 103377.
12. L. Sellaoui, F. Abdulaziz, S. Chebaane, L. Manai, A. Azhary, A. H. Alsehli, M. M. Alsowayigh, A. Piscitelli, A. Erto. Adsorption of pharmaceutical pollutants on activated carbon: physicochemical assessment of the adsorption mechanism via advanced modelling, *Journal of Molecular Liquids*, **2023**, *389*, 122929.
13. X. Huang, W. Mu, and C. Chang. CTAB intercalation into two-dimensional transition-metal carbides: enhancing adsorption performance of Cr(VI), *Journal of Alloys and Compounds*, **2023**, *968*, 172012.

14. X. Cheng, Y. Cheng, C. Wang, B. Hu, J. Wang. Calculation methods on methane adsorption phase density in coal: a critical review and new insights, *Chemical Engineering Journal*, **2023**, *472*, 144778.

15. Z. Chen, J. Luo, Y. Hu, Y. Fu, J. Meng, S. Luo, L. Wang, Y. Zhang, J. Zhou, M. Zhang, H. Qin. Fabrication of lignin reinforced hybrid hydrogels with antimicrobial and self-adhesion for strain sensors, *International Journal of Biological Macromolecules*, **2022**, *222*, 487-496.

16. K. Ingtipi, B. J. Choudhury, V. S. Moholkar. Ultrasound assisted lignin-decorated MWCNT doped flexible PVA–chitosan composite hydrogel, *Materials Today Communications*, **2023**, *35*, 105676.

17. L. Wu, S. Huang, J. Zheng, Z. Qiu, X. Lin, Y. Qin. Synthesis and characterization of biomass lignin-based PVA super-absorbent hydrogel, *International Journal of Biological Macromolecules*, **2019**, *140*, 538-545.

18. K. Enoch, R. C. S, A. A. Somasundaram. Improved mechanical properties of chitosan/ PVA hydrogel – a detailed rheological study, *Surfaces and Interfaces*, **2023**, *41*, 103178.

19. D. C. Quispe, C. A. L. Samanez, Y. C. Quispe, A. M. S. Reynoso, B. S. R. Pacheco, M. M. Z. Puma, G. J. A. López, A. Z. Puma, K. C. Quispe, H. A. Flores. Multimetal removal in aqueous medium using a potato starch/nopal mucilage copolymer: a study of adsorption kinetics and isotherms, *Results in Engineering*, **2023**, *18*, 101164.

20. B. Wu, X. Chen, D. Hou. Modeling of monolayer water adsorption on surface of cement minerals by molecule simulation and adsorption isotherm, *Materials Today Communications*, **2023**, *36*, 106646.

21. O. M. Adedeji, K. Jahan. Removal of pollutants from aqueous product of co-hydrothermal liquefaction: adsorption and isotherm studies, *Chemosphere*, **2023**, *321*, 138165.

22. D. D. Edmundson, R. R. Gustafson, A. B. Dichiara. Sonochemical synthesis of lignin nanoparticles and their applications in poly (vinyl) alcohol composites, *International Journal of Biological Macromolecules*, **2024**, *254*, 127487.

23. T. Liu, Y. Yang, L. Yan, B. Lin, L. Dai, Z. Huang, C. Si. Custom-designed polyphenol lignin for the enhancement of poly(vinyl alcohol)-based wood adhesive, *International Journal of Biological Macromolecules*, **2024**, *258*, 129132.

24. D. Panigrahi, S. Kumar, A. Dhar. Modulating chain conformations of polyvinyl alcohol through low cost and nontoxic glyoxal crosslinker: application in high performance organic transistors, *Organic Electronics*, **2019**, *65*, 193-200.

25. M. Li, Q. Tu, X. Long, Q. Zhang, H. Jiang, C. Chen, S. Wang, D. Min. Flexible conductive hydrogel fabricated with polyvinyl alcohol, carboxymethyl chitosan, cellulose nanofibrils, and lignin-based carbon applied as strain and pressure sensor, *International Journal of Biological Macromolecules*, **2021**, *166*, 1526-1534.

26. H. Bian, L. Jiao, R. Wang, X. Wang, W. Zhu, H. Dai. Lignin nanoparticles as nano-spacers for tuning the viscoelasticity of cellulose nanofibril reinforced polyvinyl alcohol-borax hydrogel, *European Polymer Journal*, **2018**, *107*, 267-274.

27. X. Wan, Z. Rong, K. Zhu, Y. Wu. Chitosan-based dual network composite hydrogel for efficient adsorption of methylene blue dye, *International Journal of Biological Macromolecules*, **2022**, *222*, 725-735.

28. Z. Wu, Q. Liao, P. Chen, D. Zhao, J. Huo, M. An, Y. Li, J. Wu, Z. Xu, B. Sun, M. Huang. Synthesis, characterization, and methylene blue adsorption of multiple-responsive hydrogels loaded with Huangshui polysaccharides, polyvinyl alcohol, and sodium carboxyl methyl cellulose, *International Journal of Biological Macromolecules*, **2022**, *216*, 157-171.

29. Y. E. Bouazzaoui, A. Habsaoui, M. E. Touhami. Hydrogel synthesis using extracted cellulose from Opuntia Ficus indica seeds and its application in methylene blue dye removal, *Chemical Data Collections*, **2022**, *41*, 100918.

https://doi.org/10.52111/qnjs.2024.18107

TẠP CHÍ KHOA HỌC
TRƯỜNG ĐẠI HỌC QUY NHƠN

Tăng cường khả năng bắt giữ khí SO_2 của $M_2(BDC)_2TED$ (M = Mg, V, Co, or Ni) bằng nghiên cứu tính toán

Nguyễn Quang Vinh[1], Nguyễn Trương Mỹ Duyên[2], Nguyễn Lê Bảo Trân[1], Nguyễn Văn Nghĩa[1], Lê Thị Thảo Viễn[1], Huỳnh Thị Minh Thành[1], Nguyễn Thị Xuân Huynh[1,*]

[1]Khoa Khoa học Tự nhiên, Trường Đại học Quy Nhơn, Việt Nam
[2]Trung tâm Khám phá khoa học và Đổi mới sáng tạo, Việt Nam

Ngày nhận bài: 02/12/2023; Ngày sửa bài: 03/02/2024;
Ngày nhận đăng: 05/02/2024; Ngày xuất bản: 28/02/2024

TÓM TẮT

Cùng với việc phát triển các nguồn năng lượng sạch bền vững thì bảo vệ môi trường là vấn đề rất cấp thiết vì ô nhiễm không khí. Trong đó, SO_2 ảnh hưởng nghiêm trọng đến sức khỏe con người. Do đó, việc loại bỏ SO_2 làm sạch môi trường vô cùng cấp bách. Đã có rất nhiều công nghệ được đề xuất để giải quyết vấn đề này nhưng chưa thực sự hiệu quả. Sự nổi lên của vật liệu xốp có bề mặt riêng và tính xốp cực lớn đã thu hút nghiên cứu bắt giữ SO_2. Trong đó, vật liệu khung hữu cơ kim loại rất được quan tâm trong hấp phụ, tách lọc và một số ứng dụng tiềm năng khác. Trong nghiên cứu này, nhóm $M_2(BDC)_2TED$ (M = Mg, V, Co, Ni) được chọn để nghiên cứu khả năng bắt giữ SO_2 bằng phương pháp mô phỏng tại 298 K và áp suất đến 2,5 bar. Kết quả chỉ ra lượng SO_2 hấp phụ trong $M_2(BDC)_2(TED)$ (or M-MOF) theo thứ tự: Co < Ni < V < Mg. Tại 298 K và 2,5 bar, lượng hấp phụ SO_2 lớn nhất với 16 mmol/g cho Mg-MOF và 13 – 14 mmol/g cho các M-MOF còn lại. Nghiên cứu cũng làm sáng tỏ các yếu tố làm tăng cường hấp phụ SO_2 trong M-MOF gồm nhiệt hấp phụ, diện tích bề mặt riêng (SSA) và thể tích rỗng (V_p). Kết quả cho thấy khả năng bắt giữ SO_2 tăng gần tuyến tính theo SSA và V_p. Hơn nữa, bản chất tương tác giữa các DOS của SO_2 với $M_2(BDC)_2(TED)$ cũng được làm sáng tỏ. Các DOS của SO_2 chủ yếu tương tác với quỹ đạo *p* của C và O trong M-MOF ở dưới mức Fermi.

Từ khóa: MOFs *$M_2(BDC)_2TED$, bắt giữ SO_2, hấp phụ SO_2, diện tích bề mặt riêng, thể tích rỗng.*

**Tác giả liên hệ chính.*
Email: nguyenthixuanhuynh@qnu.edu.vn

QUY NHON UNIVERSITY
JOURNAL OF SCIENCE

Computational study on enhancing SO_2 capture capacity of $M_2(BDC)_2TED$ (M = Mg, V, Co, or Ni)

Nguyen Quang Vinh[1], Nguyen Truong My Duyen[2], Nguyen Le Bao Tran[1], Nguyen Van Nghia[1], Le Thi Thao Vien[1], Huynh Thi Minh Thanh[1], Nguyen Thi Xuan Huynh[1,*]

[1]Faculty of Natural Sciences, Quy Nhon University, Vietnam
[2]Explora Science Quy Nhon, Vietnam

Received: 02/12/2023; Revised: 03/02/2024;
Accepted: 05/02/2024; Published: 28/02/2024

ABSTRACT

Along with finding and developing sustainable clean energy sources, environmental protection is highly urgent because the air is increasingly polluted by more and more toxic gases. In particular, the presence of toxic gas SO_2 seriously affects human health. Therefore, removing toxic SO_2 gas to clean the living environment is extremely urgent. Many technologies have been suggested to solve this, but they have not been effective yet. In recent years, the emergence of porous materials with ultra-large specific surface areas and ultra-high porosity has attracted the attention of scientists in SO_2 capture. Among porous materials, metal-organic frameworks are intensely interested in adsorption, separation, and other potential applications. Herein, we select the porous materials $M_2(BDC)_2TED$ (M = Mg, V, Co, Ni) to study the SO_2 capture using simulation approaches. The research was performed at room temperature 298 K and pressure under 2.5 bar. Our results show that the order of metals gradually increasing the SO_2 adsorption uptake in $M_2(BDC)_2(TED)$ is Co < Ni < V < Mg. Specifically, at 298 K and 2.5 bar, the amount of SO_2 adsorption is about 16 mmol/g for Mg-MOF, and about 13 – 14 mol/g for the M-MOF (M = V, Ni, Co). The study also elucidated the influencing factors that enhance SO_2 adsorption in $M_2(BDC)_2TED$, including adsorption isosteric heat, specific surface area, and pore volume. Noticeably, the specific surface areas and pore volumes of M-MOFs almost linearly enhance the SO_2 capture capability at room temperature and low pressure. Furthermore, we also elucidate the orbital interaction nature between SO_2 and $M_2(BDC)_2(TED)$ MOFs in detail. Therein, the DOS peaks of the SO_2 adsorbate mainly interact with the adsorbents' C and O p orbitals below the Fermi level.

Keywords: *$M_2(BDC)_2TED$ MOFs, SO_2 capture, SO_2 adsorption, specific surface area, pore volume.*

1. INTRODUCTION

Sulfur dioxide (SO_2) is a colorless, non-flammable, and common pollutant in industrial production as well as daily life. Exposure to SO_2 may irritate the nose, throat, and eyes. Besides, SO_2 is a corrosive gas with high solubility (120 g/L) in water and can combine with water and air to form sulfuric acid, the main component of acid rain.[1,2,3] Despite the low SO_2 content in the air, it is classified as a toxic gas and one of the six most common environmental pollutants by the US Environmental Protection Organization.[4] Notably, significant amount of sulfur oxides (SO_x), especially SO_2, is released into the environment after the combustion of petroleum-based fuels

**Corresponding author.*
Email: nguyenthixuanhuynh@qnu.edu.vn

https://doi.org/10.52111/qnjs.2024.18108

in internal combustion engines utilized in motorized vehicles.[3] Therefore, removing or reducing the quantities of SO_2 in the atmosphere is exceptionally urgent. In technologies, SO_2 capture based on the adsorption mechanism has been remarkable.[5] Metal-organic frameworks (MOFs) among porous materials are an exciting alternative for SO_2 capture due to outstanding structural properties such as ultrahigh surface area, high porosity, and controllable structural characteristics.[2,4] Therefore, SO_2 capture in nano-porous materials has attracted scientific interest. Many MOFs and other porous candidates have been studied and highly appreciated for SO_2 adsorption. Fu and co-workers showed that functionalized covalent triazine framework (CTF–CSU41) achieved the highest uptake of SO_2 with a maximum capacity of 6.7 mmol/g (*i.e.*, 42.9 wt.%) at (298 K, 0.15 bar).[3,6] For MOFs, MOF-177 exhibited the highest SO_2 uptake with 25.7 mmol/g at (293 K, 1 bar). Some other MOFs also showed high SO_2 capture capacity, ranging from 4.8 to 17.3 mmol/g.[3] Besides many other MOFs, $M_2(BDC)_2(TED)$ or $M(BDC)(TED)_{0.5}$ materials have been attractive for applications in capturing toxic gases (CO_2, SO_2, CH_4, NH_3, H_2S, NO_x, …).[4] In this research, we use simulations to find optimum $M_2(BDC)_2(TED)$ MOFs for SO_2 capture, where M is magnesium (Mg), vanadium (V), cobalt (Co) or nickel (Ni); BDC = 1,4-Benzenedicarboxylate; TED = Triethylen-diamine or DABCO: 1.4-Diazabicyclo [2.2.2] octane.[7]

2. COMPUTATIONAL METHODS

The research approach combines density functional theory (DFT) calculations and grand canonical Monte Carlo (GCMC) simulations. Firstly, we used DFT calculations to optimize the geometries of $M_2(BDC)_2(TED)$ MOFs, namely M-MOFs. Secondly, GCMC simulations were used to obtain the isotherms and isosteric heat of SO_2 adsorption as well as calculate the structural characteristics of the M-MOFs.

To optimize the unit cell, extract partial atomic charges of the M-MOFs, search stable or favourite adsorption sites and DOS/PDOS, we utilized the Vienna ab initio simulation package (VASP)[8,9] for the van der Waals dispersion-corrected density functional theory (vdW-DF).[10,11] The plane-wave basis set with the cut-off energy of 700 eV for the plane-wave basis set.[12,13] We performed the surface Brillouin-zone integrations using the Monkhorst and Pack *k*-point sampling technique with the 3×3×3 mesh grid and the Gamma point at the center.[14] The Methfessel-Paxton smearing of order 1 was used for the ions and geometry relaxation, and atomic charge calculation with the smearing width sigma of 0.1 eV.[15]

GCMC simulations using the RASPA code were selected to study the gravimetric uptakes of SO_2 in the M-MOFs.[16] These simulations were performed in constant volume, temperature, and chemical potential at room temperature (298 K) and pressures up to 2.5 bar. The number of 300000 MC steps were simulated for the random insertion, deletion, translation, and rotation of SO_2 molecules in the simulation box, repeated 3×3×3 times of the primary unit cell along the *a*, *b*, and *c* lengths.

The interactions between atoms of SO_2 gas and the MOFs were described by (*i*) the Coulombic or electrostatic interactions with its cut-off radius of 13 Å, and (*ii*) the van der Waals interactions with the simple Lennard-Jones (LJ) model with the LJ cut-off radius of 20 Å.[17,18] The cut-off radius and other parameters were carefully checked before performing the GCMC simulation. The partial charges of atoms of the M-MOFs were extracted from the density-derived electrostatic and chemical (DDEC6 atomic charges method, listed in Table 1, with the symbols for the atoms shown in Figure 1.[19–22] The qualities of the LJ potential well depth and diameter were determined by the Lorentz–Berthelot combining rules, one of the most common types of mixing rules for unlike atoms.[23,24] The parameters for σ_i and ε_i (*i* refers to the atoms like Fe, H, C, O in the M-MOFs or S, O in SO_2) were selected from the generic

https://doi.org/10.52111/qnjs.2024.18108

force fields for MOFs in the RASPA software package.[16,25]

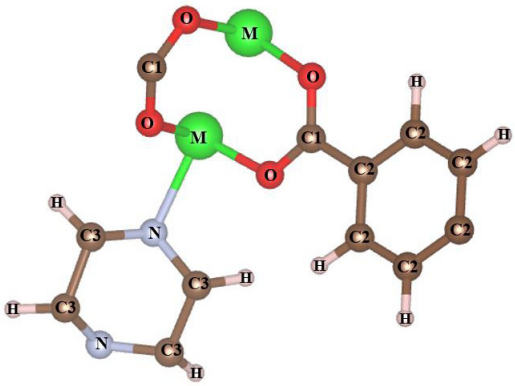

Figure 1. The symbol for atomic types with different charges of M-MOFs.

Table 1. The LJ (ε, σ) and charge parameters (q) for atomic types of M-MOFs and SO_2.

M-MOFs	Atomic types	LJ parameters		q (e)
		ε/kg (K)	σ (Å)	
M = Mg	C1	47.856	3.472	0.739
	C2			-0.073
	C3			0.011
	H	7.648	2.846	0.088
	N	38.949	3.262	-0.362
	O	48.158	3.033	-0.721
	Mg	**55.857**	**2.691**	**1.385**
M = V	C1	47.856	3.472	0.627
	C2			-0.073
	C3			-0.012
	H	7.648	2.846	0.076
	N	38.949	3.262	-0.174
	O	48.158	3.033	-0.574
	V	**8.051**	**2.801**	**0.926**
M = Co	C1	47.856	3.472	0.613
	C2			-0.071
	C3			-0.025
	H	7.648	2.846	0.076
	N	38.949	3.262	-0.099
	O	48.158	3.033	-0.491
	Co	**7.045**	**2.558**	**0.573**
M = Ni	C1	47.856	3.472	0.636
	C2			-0.071
	C3			-0.025
	H	7.648	2.846	0.079
	N	38.949	3.262	-0.118
	O	48.158	3.033	-0.539
	Ni	**7.548**	**2.524**	**0.660**
SO_2[25,26]	O	58.725	3.198	-0.201
	S	189.353	3.410	0.402

In this work, to search the stable or favorite adsorption sites of SO_2 gas in $M_2(BDC)_2(TED)$, we calculated the adsorption energy of SO_2 gas in the $M_2(BDC)_2TED$ series by the expression $\Delta E = E_{(M\text{-}MOF+SO_2)} - (E_{M\text{-}MOF} + E_{SO_2})$. Where $E_{(M\text{-}MOF+SO_2)}$, $E_{M\text{-}MOF}$, and E_{SO_2} are the total energies of the [M - MOF + SO_2] system, the pristine $M_2(BDC)_2TED$ MOF, and the isolated SO_2 molecule, respectively.

3. RESULTS AND DISCUSSION

3.1. Optimization of the unit cell of $M_2(BDC)_2(TED)$

First, we constructed a unit cell based on experimental and computational works for $Ni_2(BDC)_2(TED)$ (BDC = Benzene dicarboxylate, and TED = Triethylenediamine) (Figure 2).[7,27] We optimized all ions and the size of the unit cells. Then, we replaced Ni with other bivalent metals such as Mg, V, and Co, which often appear in MOFs and greatly influence gas adsorption. The results obtained for the unit cells are listed in Table 2 and compared with the experimental data for M = Ni,[28] showing that these optimal results show reliability with 1.61%, 1.57%, and 4.81% for a (or b), c lengths, and the cell volume. The unit cell volume ($V_{M\text{-}MOF}$) of the M-MOFs also does not change much, and they are in slightly increasing order: $V_{Co\text{-}MOF} < V_{V\text{-}MOF} \approx V_{Ni\text{-}MOF} < V_{Mg\text{-}MOF}$.

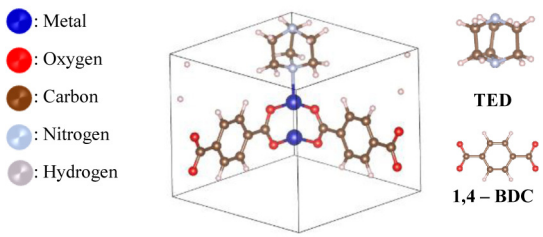

Figure 2. A primary unit cell of M-MOFs (M = Mg, V, Co or Ni).

https://doi.org/10.52111/qnjs.2024.18108

Table 2. The optimized parameters of the unit cell of the $M_2(BDC)_2TED$ structures, compared with other works.

$M_2(BDC)_2TED$	Lattice constant (Å)		Volume of unit cell (Å³)
	a = *b*	*c*	
M = Mg	10.98	9.39	1130
M = V	10.96	9.37	1125
M = Co	10.90	9.31	1113
M = Ni	10.97	9.38	1128
M = Ni (exp. data)[28]	11.15	9.53	1185
Error compared exp. data (%)	1.61	1.57	4.81

3.2. The SO_2 capture capability of $M_2(BDC)_2TED$ MOFs

The SO_2 adsorption isotherms are shown in Figure 3 for both excess and absolute uptakes at pressures up to 2.5 bar. The results show these two uptakes are nearly similar for SO_2 on the M-MOFs (M = Mg, V, Co, or Ni) at low pressure under 2.5 bar. The adsorption uptakes for all metals are listed in Table 3. Our data are also compared to other ones. Compared to MOF-177, the best SO_2 capture to date, M-MOFs strongly adsorb SO_2 at low pressure below 0.5 bar.[1] On the contrary, above 0.5 bar, MOF-177 shows an outstanding uptake compared to our M-MOFs and other MOFs.[1]

The adsorption tendency in Mg-MOF is more substantial than in Ni-MOF, which is consistent with the experimental data of Kui Tan et al. at the same temperature and pressure conditions (0.11 bar, 298 K),[7] and and V. B. López-Cervantes et al (Table 3).[29,30]

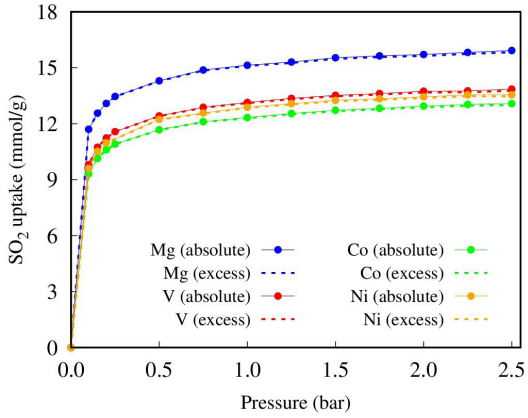

Figure 3. Absolute and excess isotherms of SO_2 on $M_2(BDC)_2(TED)$ at 298 K, where dashed lines and solid lines refer to absolute and excess uptakes.

Table 3. Absolute and excess SO_2 uptakes on $M_2(BDC)_2(TED)$ at 298 K.

M-MOFs	SO_2 uptakes (mmol/g)		
	0.1 bar	1 bar	2.5 bar
M = Mg	11.69	15.13	15.92
M = V	9.80	13.13	13.85
M = Co	9.31	12.32	13.07
M = Ni	9.59	12.88	13.54
M = Ni[17]			13.6 (50 bar)
M = Mg[7]	6.44 (0.11 bar)	8.60 (1.02 bar)	
M = Ni[7]	4.54 (0.11 bar)	9.97 (1.13 bar)	
Mg(II)-MOF[29]		19.5	
Ni(II)-MOF[30]		12.5	
MOF-177[1,29]	1.3	25.7 (maximum, 293 K, 0.97 bar)	-

In this work, we study the adsorption capacity of M-MOFs for SO_2 up to a pressure of 2.5 bar because researching at high pressures is unnecessary, and the results achieved only change a little.[17] The results show that Mg-MOF has the strongest adsorption of SO_2, followed by V-MOF, Ni-MOF, and Co-MOF. Here, Mg-MOF adsorbs superiorly compared to the remaining M-MOFs (M = V, Ni, Co). At 2.5 bar and 298 K, the best uptakes reach for Mg-MOF with n_{exc}=15.82mmol/g,n_{abs}=15.92mmol/g, followedby V-MOF (n_{exc} = 13.77 mmol/g, n_{abs} = 13.85 mmol/g), Ni-MOF (n_{exc} = 13.46 mmol/g, n_{abs} = 13.54 mmol/g), and Co-MOF (n_{exc} = 13.00 mmol/g, n_{abs} = 13.08 mmol/g).

3.3. Effect of structural characteristics and isostericheat on the SO_2 adsorption of $M_2(BDC)_2(TED)$

To explain the reason Mg increases the ability to capture SO_2 based on the adsorption mechanism compared to other metals, we analyze the factors that have a substantial impact on the gas adsorption of MOFs, which are the structural characteristics (specific surface area and pore volume) and adsorption isosteric heat.

Isosteric heat of adsorption, Q_{st}, is an essential factor required to describe the thermal

performance of adsorptive systems.[31] The Q_{st} of SO_2 for the M-MOF series calculated in low pressures under 1.0 kPa are presented in Figure 4. The results show that Q_{st} tends to increase as pressure increases. However, the values change little in the low-pressure region. At higher pressures, the Q_{st} value of SO_2 for M-MOFs is most significant for Mg-MOF, rising from 42.03 kJ/mol to 47.97 kJ/mol. Meanwhile, other M-MOFs increase slightly with pressure. Specifically, uptakes of SO_2 in V-MOF: 40.61 – 44.73 kJ/mol, Co-MOF: 40.93 – 45.37 kJ/mol, and Ni-MOF: 40.78 – 44.94 kJ/mol.

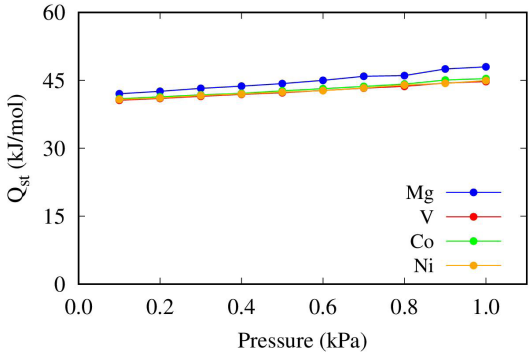

Figure 4. Isosteric heats of SO_2 adsorption for M-MOFs vs the pressure.

The Q_{st} value of SO_2 adsorption is in the order V-MOF ≈ Ni-MOF ≈ Co-MOF < Mg-MOF, exhibiting that SO_2 adsorption on $Mg_2(BDC)_2(TED)$ is the most noticeable as analyzed above. Moreover, we also research the influence of specific surface area (SSA) and pore volume (V_p) on the adsorptive ability of SO_2 on the M-MOFs. The SSA values are smaller than many other MOFs, but the pore volume is relatively large, as detailed in Table 4. The SSA and pore volume of the M-MOFs are in increasing order Co < Ni < V < Mg. This tendency is consistent with H. Xiang's work for $M(BDC)(TED)_{0.5}$ with M is Ni and Co.[32]

Table 4. The specific surface area and the pore volume of $M_2(BDC)_2(TED)$, compared to another work.

M-MOFs	This work		H. Xiang[32]	
	SSA (m^2/g)	V_p (cm^3/g)	SSA (m^2/g)	V_p (cm^3/g)
M = Mg	1930.95	0.87	-	-
M = V	1727.18	0.78	-	-
M = Co	1627.58	0.74	1708	0.619
M = Ni	1686.09	0.76	1905	0.757

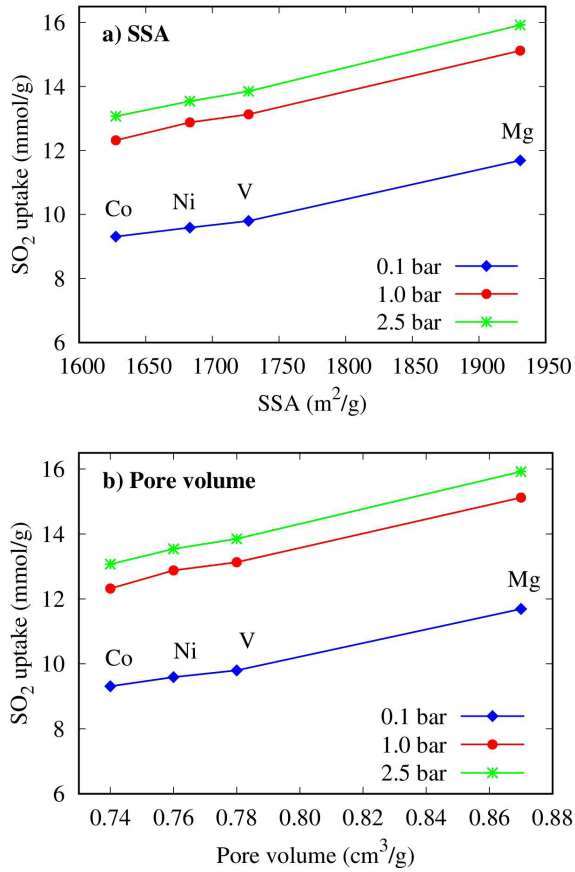

Figure 5. The correlation between the uptakes and (a) the specific surface area (SSA), (b) pore volume (Vp) of $M_2(BDC)_2(TED)$ at 298 K.

The results in Figure 5 express that the amounts of SO_2 adsorption increase almost entirely linearly with SSA and V_p. Among them, the M-MOF with M = Mg is outstanding, which explains the most excellent SO_2 adsorption into $Mg_2(BDC)_2(TED)$. Therefore, these two structural characteristics (V_p and SSA) have a powerful impact on the ability to capture SO_2 on MOFs at room temperature.

3.4. Nature of interaction between SO_2 and $M_2(BDC)_2(TED)$ at the electronic orbital level

GCMC simulation results give us quantitative numbers, results that can be compared with experiments and evaluate the relative adsorption strength of the M-MOFs by changing their metals. Therefore, to clarify the nature of the interaction between SO_2 and M-MOFs, we perform further calculations on the electronic structure through DFT calculations.

https://doi.org/10.52111/qnjs.2024.18108

We indicate the preferential SO_2 adsorption in M-MOFs (M = Mg, V, Co, Ni). In this work, the effect of metals on SO_2 adsorption on the M-MOF is of interest; Therefore, we only search for stable SO_2 adsorption sites near the metal of the MOF. Therefore, we only search for stable SO_2 adsorption sites near the metal of the MOF by evaluating adsorption energies. The values of SO_2 adsorption energies on the M-MOFs are shown in Table 5 and Figure 6. Noting that the more negative ΔE, the more stable the adsorption.

Among the selected metals in this research, vanadium (V) indicates the most considerable SO_2 adsorption with the most negative energy value ΔE = -0,62 eV); the remaining metals show the values of ΔE close to each other, in the range of -0.40 to -0.43 eV. Table 5 also shows that the distance between SO_2 and the metal of all M-MOFs has very little difference except V, which has shorter SO_2-V distance. Although V increases the superior adsorption energy compared to other metals, Mg still gives the most substantial SO_2 adsorption on the $Mg_2(BDC)_2(TED)$. These results exhibit a significant and decisive influence on structural characteristic quantities such as SSA and V_p.

Table 5. Adsorption energy (ΔE) and the distance between the nearest atoms of SO_2 and the M-MOF ($d_{SO_2\text{-}MOF}$).

M-MOF	Adsorption energy, ΔE		($d_{SO_2\text{-}MOF}$)
	(eV)	(kJ/mol)	(Å)
M = Mg	-0.41	-40.21	3.47
M = V	-0.62	-59.91	3.36
M = Co	-0.40	-38.85	3.44
M = Ni	-0.41	-40.45	3.50

To provide further insights into the interaction nature between SO_2 (adsorbate) and M-MOFs (adsorbent), we calculated and analyzed the modification of the total electronic density of states (DOS) and orbital-projected density of states (PDOS) between SO_2 and M-MOFs (M = Mg, V, Co, Ni) for the above favorable SO_2 adsorption systems. First, we analyzed the DOS peaks of isolated SO_2, including $1\sigma^*$, $2\sigma/1\pi/3\sigma$ *2n, 3n, 4n*, and $1\pi^*$ (Figure 7).[27] The results revealed that, after the adsorption of SO_2 on M-MOFs, the adsorbate's DOS peaks shift to the left side of the Fermi level with substantial expansion of the DOS ($2\sigma/1\pi/3\sigma$ and $4n$). There, the total peaks of the SO_2 on M-MOFs with M = Co, Ni, V much stronger shift than those of M = Mg (Figure 7). Notably, V-MOF also causes all DOS peaks of SO_2 to split except the $3n$ peak, which explains the most favorite adsorption of SO_2 in V-MOF compared to the remaining MOFs.

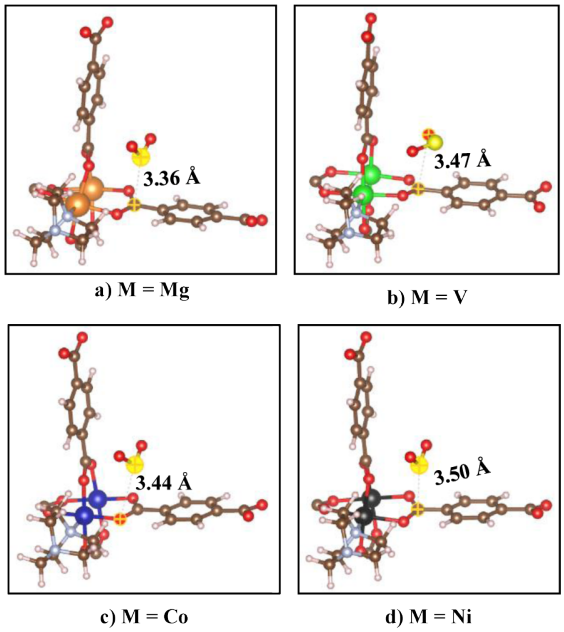

Figure 6. The favorable SO_2 adsorption configurations on $M_2(BDC)_2(TED)$: a) M = Mg, b) M = V, c) M = Co, and d) M = Ni.

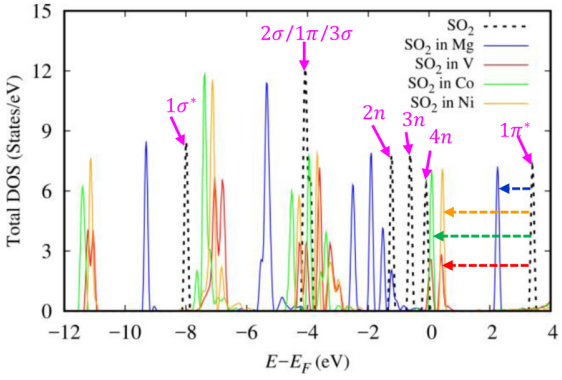

Figure 7. Total DOS of the adsorbed SO_2 in M-MOFs (M = Mg, V, Co or Ni) compared to the isolated SO_2 (black dash line). The Fermi level was set to 0 eV.

Next, the modification of the DOS of the SO_2 molecule and the M-MOF's atoms (C, O, N, and M) was considered (Figure 8). Here, we ignored the weak interaction between H atoms of the MOFs and SO_2. The results indicate that the overlap between the DOS peaks of SO_2 molecule with the majority of C and O *p* orbitals (Figure 8) and a small fraction of M *d* orbitals in M-MOFs (Figure 9) enhances the interaction between the adsorbate and adsorbent. In particular, for $V_2(BDC)_2(TED)$, substantial overlap occurs between SO_2 $1\pi^*$ peak and the M *d* (mainly d_{xz}, d_{yz}, and d_{xy}) orbitals at about 0 eV (Fermi level) compared to other metals. This resonance can explain the most preferred adsorption of SO_2 in V-MOF. In contrast to other metals, Mg shows that the interaction occurs between the C and especially O *p* states of the Mg-MOF with SO_2 $2\sigma/1\pi/3\sigma$ state and N *p* orbitals with SO_2 $2n$ state. Note that we have analyzed the PDOS between SO_2 and the atoms of M-MOFs in detail and discussed the results obtained here despite ignoring some figures.

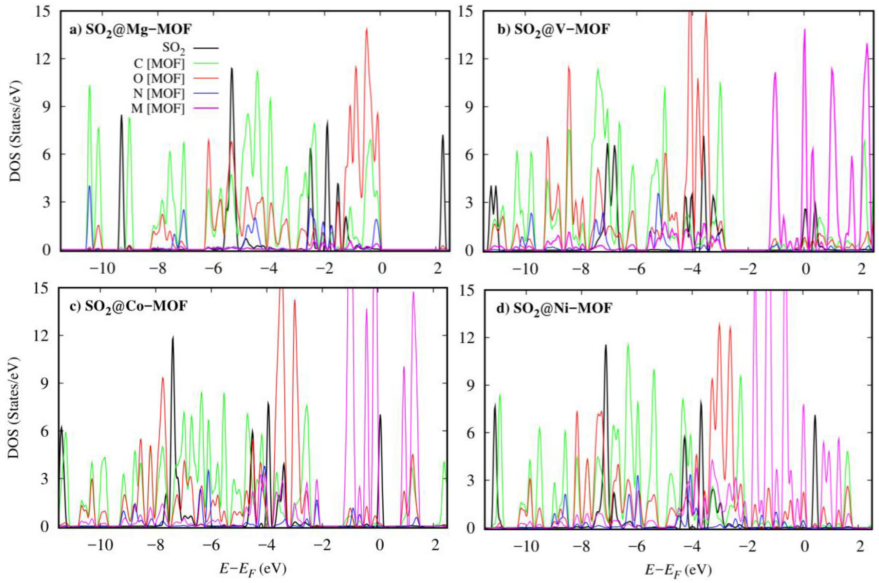

Figure 8. The overlap between DOS of the SO_2 and that of O, N, and M atoms of M-MOFs, where the Fermi level was set to 0 eV: a) SO_2@Mg-MOF, b) SO_2@V-MOF, c) SO_2@Co-MOF, and d) SO_2@Ni-MOF.

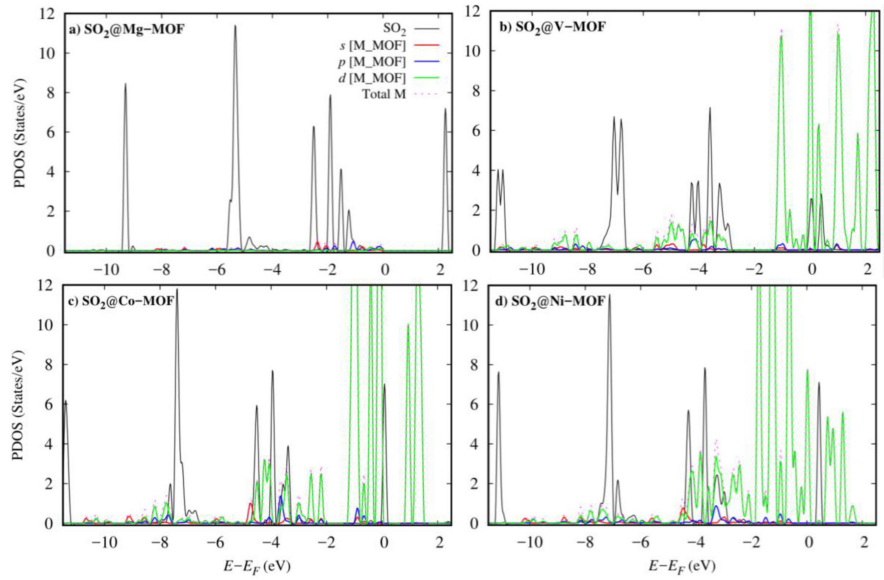

Figure 9. The orbital-projected DOS of the SO_2 with the states (*s*, *p*, *d*) of M atoms of M-MOFs, where the Fermi level was set to 0 eV: a) SO_2@Mg-MOF, b) SO_2@V-MOF, c) SO_2@Co-MOF, and d) SO_2@Ni-MOF.

https://doi.org/10.52111/qnjs.2024.18108

4. CONCLUSION

After optimizing the structure for Ni(BDC)(TED), we replaced the metal to obtain optimized geometries for M(BDC)(TED), with M being Mg, V, and Co by calculations based on vdW-DF. Unit cell volumes are in ascending order of Co < V ≈ Ni < Mg.

The order of metals increasing the SO_2 adsorption uptakes on $M_2(BDC)_2(TED)$ is Co < Ni < V < Mg. At 298 K and 2.5 bar, SO_2 uptakes are about 16 mmol/g for Mg-MOF (n_{exc} = 15.82 mmol/g, n_{abs} = 15.92 mmol/g) and about 13 – 14 mol/g for the M-MOF (M = V, Ni, Co).

Our work also elucidates the factors that enhance the amounts of SO_2 adsorption in $M_2(BDC)_2TED$, including the adsorption isosteric heat, specific surface area, and pore volume. Remarkably, the specific surface areas and pore volumes of M-MOFs almost linearly enhance the SO_2 capture at room temperature and low pressure.

Moreover, the physical insights at electronic orbitals illustrated that the SO_2@ $M_2(BDC)_2(TED)$ interactions are contributed by the C and O *p* orbitals (more predominant) and the metal *d* orbitals (weaker). Therein, the most stable SO_2 adsorption configuration is in $V_2(BDC)_2(TED)$ by the more significant overlap between the V *d* states and the SO_2 orbitals. For SO_2@$Mg_2(BDC)_2(TED)$, the dominant interactions occur between O *p* and C *p* states with $2\sigma/1\pi/3\sigma$ and N *p* with $2n$ of SO_2, respectively.

Acknowledgments

This work was financially supported by the Ministry of Education and Training of Vietnam under the grant number B2022-DQN-05. We also acknowledge supporting the computer time and software granted by the Lab of Computational Chemistry and Modelling (LCCM), Faculty of Natural Sciences, Quy Nhon University, Quy Nhon, Vietnam.

REFERENCES

1. C. Janiak. Metal-organic frameworks with potential application for SO_2 separation and fluegas desulfurization, *ACS Applied Materials & Interfaces*, **2019**, *11*, 17350−17358.
2. E. M. Ahumada, M. L. D. Ramírez, M. D. J. V. Hernández, V. Jancik, I. A. Ibarra. Capture of toxic gases in MOFs: SO_2, H_2S, NH_3 and NO_x, *Chemical Science,* **2021**, *12*, 6772–6799.
3. C. G. Livas, D. Raptis, E. Tylianakis, G. E. Froudakis. Multiscale theoretical study of sulfur dioxide (SO_2) adsorption in metal-organic frameworks, *Molecules*, **2023**, *28*(7), 3122.
4. T. T. T. Huong, P. N. Thanh, N. T. X. Huynh, D. N. Son. Metal – organic frameworks: state-of-the-art material for gas capture and storage, *VNU Journal of Science: Mathematics - Physics*, **2016**, *32*, 67–85.
5. E. M. Ahumada, A. L. Olvera, V. Jancik, J. E. S. Bautista, E. G. Zamora, V. Martis, D. R. Williams, I. A. Ibarra. MOF materials for thecapture of highly toxic H_2S and SO_2, *Organometallics*, **2020**, *39*, 883–915.
6. Y. Fu, Z. Wang, S. Li, X. He, C. Pan, J. Yan, G. Yu. Functionalized covalent triazine frameworks for effective CO_2 and SO_2 removal, *ACS Applied Materials & Interfaces*, **2018**, *10*, 36002–36009.
7. K. Tan, P. Canepa, Q. Gong, J. Liu, D. H. Johnson, A. Dyevoich, P. K. Thallapally, T. Thonhauser, J. Li, Y. J. Chabal. Mechanism of preferential adsorption of SO_2 into two microporous paddle wheel frameworks $M(BDC)(TED)_{0.5}$, *Chemistry of Materials,* **2013**, *25*, 4653–4662.
8. G. Kresse, J. Furthmüller. Efficient iterative schemes for ab initio total-energy calculations using a plane-wave basis set, *Physical Review B*, **1996**, *54*, 11169–11186.
9. G. Kresse, J. Furthmüller. Efficiency of ab-initio total energy calculations for metals and semiconductors using a plane-wave basis set, *Computational Materials Science*, **1996**, *6*, 15–50.
10. J. P. Perdew, J. Chevary, S. Vosko, K. Jackson, M. Pederson, D. Singh, C. Fiolhais. Atoms, molecules, solids, and surfaces: applications of the generalized gradient approximation for exchange and correlation, *Physical Review B*, **1992**, *46*, 6671–6687.

11. J. P. Perdew, K. Burke, M. Ernzerhof. Generalized gradient approximation made simple, *Physical Review Letters*, **1996**, *77*, 3865–3868.

12. P. E. Blöchl. Projector augmented-wave method, *Physical Review B*, **1994**, *50*, 17953–17979.

13. G. Kresse, D. Joubert. From ultrasoft pseudopotentials to the projector augmented-wave method, *Physical Review B*, **1999**, *59*, 1758–1775.

14. J. D. Pack, H. J. Monkhorst. Special points for Brillouin-zone integrations, *Physical Review B*, **1976**, *13*, 5188–5192.

15. M. Methfessel, A. T. Paxton. High-precision sampling for Brillouin-zone integration in metals, *Physical Review B*, **1989**, *40*, 3616–3621.

16. D. Dubbeldam, S. Calero, D. E. Ellis, R. Q. Snurr. RASPA: molecular simulation software for adsorption and diffusion in flexible nanoporous materials, *Molecular Simulation*, **2016**, *42*, 81–101.

17. N. T. X. Huynh, B. T. Duyen, P. T. Tram, T. T. D. Thanh, N. T. M. Duyen. Research on the capture of flue gases of the metal-organic framework $Ni(BDC)(TED)_{0.5}$ by the classical simulation method, *Quy Nhon University Journal of Science*, **2021**, *15*(5), 5–12.

18. N. T. X. Huynh, T. T. Nam, D. N. Son. Evaluation of H_2 and CO_2 adsorption into MIL-88A-Fe by Grand canonical Monte Carlo simulation, *Quy Nhon University Journal of Science*, **2021**, *15*(1), 5–12.

19. T. A. Manz, N. G. Limas. Introducing DDEC6 atomic population analysis: part 1. Charge partitioning theory and methodology, *RSC Advances*, **2016**, *6*, 47771–47801.

20. N. G. Limas, T. A. Manz. Introducing DDEC6 atomic population analysis: part 2. Computed results for a wide range of periodic and nonperiodic materials, *RSC Advances,* **2016**, *6*, 45727–45747.

21. T. A. Manz. Introducing DDEC6 atomic population analysis: part 3. Comprehensive method to compute bond orders, *RSC Advances*, **2017**, *7*, 45552–45581.

22. N. G. Limas, T. A. Manz. Introducing DDEC6 atomic population analysis: part 4. Efficient parallel computation of net atomic charges, atomic spin moments, bond orders, and more, *RSC Advances*, **2018**, *8*, 2678–2707.

23. H. A. Lorentz. Ueber die anwendung des satzes vom virial in der kinetischen theorie der gase, *Annalen der Physik*, **1881**, *248*, 127–136.

24. D. Berthelot. Sur le mélange des gaz, *Comptes Rendus Chimie*, **1898**, *126*, 1703–1855.

25. D. Dubbeldam, K. S. Walton, T. J. H. Vlugt, S. Calero. Design, parameterization, and implementation of stomic force fields for adsorption in nanoporous materials, *Advanced Theory and Simulations,* **2019**, *2*, 1900135.

26. I. M. Martos, A. M. Calvo, J. J. G. Sevillano, M. Haranczyk, M. Doblare, J. B. Parra, C. O. Ania, S. Calero. Zeolite screening for the separation of gas mixtures containing SO_2, CO_2 and CO, *Physical Chemistry Chemical Physics*, **2014**, *16*, 19884–19893.

27. D. N. Son, T. T. Thuy Huong, V. Chihaia. Simultaneous adsorption of SO_2 and CO_2 in an Ni(BDC)(TED)0.5 metal-organic framework, *RSC Advances*, **2018**, *8*, 38648–38655.

28. K. Tan, N. Nijem, P. Canepa, Q. Gong, J. Li, T. Thonhauser, Y. J. Chabal. Stability and hydrolyzation of metal organic frameworks with paddle-wheel SBUs upon hydration, *Chemistry of Materials*, **2012**, *24*, 3153–3167.

29. M. A. Eva, D. W. Kim, W. Mohammad, C. M. Paulina, A. L. Olvera, D. R. Williams, V. Martis, H. A. L. García, S. L. Morales, D. S. Ibarra, G. Maurin, A. I. Ilich, C. S. Hong. Capture and detection of SO_2 by a chemically stable Mg(II)-MOF, *Journal of Materials Chemistry A*, **2022**, *10*, 18636–18643.

30. V. B. L. Cervantes, D. W. Kim, J. L. Obeso, E. M. Ahumada, Y. A. A. Sánchez, E. S. González, C. Leyva, C. S. Hong, I. A. Ibarra, D. S. Ibarra. Detection of SO_2 using a chemically stable Ni(II)-MOF, *Nanoscale*, **2023**, *15*, 12471–12475.

31. I. E. Menshchikov, A. V. Shkolin, E. M. Strizhenov, E. V. Khozina, S. S. Chugaev, A. A. Shiryaev, A. A. Fomkin, A. A. Zherdev. Thermodynamic behaviors of adsorbed methane storage systems based on nanoporous carbon adsorbents prepared from coconut shells, *Nanomaterials*, **2020**, *10*, 1–26.

32. H. Xiang, A. Ameen, P. Gorgojo, F. R. Siperstein, S. M. Holmes, X. Fan. Selective adsorption of ethane over ethylene on $M(BDC)(TED)_{0.5}$ (M = Co, Cu, Ni, Zn) metal-organic frameworks (MOFs), *Microporous and Mesoporous Materials*, **2020**, *292*, 109724.

https://doi.org/10.52111/qnjs.2024.18108

TẠP CHÍ KHOA HỌC
TRƯỜNG ĐẠI HỌC QUY NHƠN

Sản xuất các axít béo thiết yếu không bão hòa đa chuỗi dài bởi sinh trưởng quang tự dưỡng, hợp dưỡng và dị dưỡng ở các vi sinh vật quang hợp và không quang hợp: tổng quan

Phan Minh Tâm[1], Trần Nguyên Vũ[2,*]

[1]Khoa Khoa học Sinh học, Trường Đại học Nông Lâm Thành phố Hồ Chí Minh, Việt Nam
[2]Khoa Sinh học – Công nghệ Sinh học, Trường Đại học Khoa học Tự nhiên Thành phố Hồ Chí Minh, Việt Nam

Ngày nhận bài: 25/08/2023; Ngày sửa bài: 05/12/2023;
Ngày nhận đăng: 16/02/2024; Ngày xuất bản: 28/02/2024

TÓM TẮT

Một số vi sinh vật quang hợp và không quang hợp như vi tảo, sinh vật nguyên sinh hoặc nấm, được biết đến như là nguồn sản xuất tự nhiên của các axit béo không bão hòa đa chuỗi dài (LC-PUFA). Trong đó, một số loài được biết đến như là những sinh vật dị dưỡng bắt buộc, hợp dưỡng hoặc quang tự dưỡng bắt buộc. Tuy nhiên, ngày càng có nhiều loài vi tảo, trước đây được biết là sinh vật quang tự dưỡng bắt buộc, nhưng nay được xác định là sinh vật hợp dưỡng hoặc dị dưỡng. Các con đường sinh tổng hợp và điều kiện nuôi cấy của các vi sinh vật này được so sánh để làm nổi bật các yếu tố ảnh hưởng đến quá trình sản xuất và phân phối LC-PUFA trong tế bào. Sản xuất LC-PUFA đã được cải thiện bằng cách lựa chọn quy trình nuôi cấy và chủng vi sinh vật. Các phân tích về sản lượng chuyển đổi và năng suất của LC-PUFA trong nuôi cấy quang tự dưỡng, hợp dưỡng và dị dưỡng làm sáng tỏ hiệu suất sản xuất LC-PUFA bởi các sinh vật quang hợp và không quang hợp.

Từ khóa: *Vi tảo, axit béo không bão hòa đa (PUFA), sinh trưởng quang tự dưỡng, sinh trưởng hợp dưỡng, sinh trưởng dị dưỡng.*

**Tác giả liên hệ chính.*
Email: tnvu@hcmus.edu.vn

QUY NHON UNIVERSITY
JOURNAL OF SCIENCE

Photo-autotrophic, mixotrophic and heterotrophic production of essential long chain polyunsaturated fatty acids in photosynthetic and non-photosynthetic microorganisms: a review

Tam Minh Phan[1], Nguyen Vu Tran[2,*]

[1]Faculty of Biological Sciences, Nong Lam University Ho Chi Minh City, Vietnam
[2]Faculty of Biology - Biotechnology, Ho Chi Minh City University of Science, Vietnam

Received: 25/08/2023; Revised: 05/12/2023;
Accepted: 16/02/2024; Published: 28/02/2024

ABSTRACT

Some photosynthetic and non-photosynthetic microorganisms such as microalgae, stramenopiles or fungi, are known as natural producers of long chain polyunsaturated fatty acids (LC-PUFAs). Among those, some species are known as obligate heterotrophs, mixotrophs or obligate phototrophs. However, more and more microalgal species, previously reported as obligate photo-autotrophs, are now identified as mixotrophs or heterotrophs. The biosynthetic pathways and cultivation conditions of these microorganisms are compared to highlight the factors influencing production and distribution of LC-PUFAs in the cells. LC-PUFA production has been improved by the choice of cultivation processes and microorganism strains. Analyses of the conversion yields and productivities of LC-PUFAs in photo-autotrophic, mixotrophic and heterotrophic cultivation elucidate the performance of LC-PUFA production by photosynthetic and non-photosynthetic organisms.

Keywords: *Microalgae, polyunsaturated fatty acid (PUFA), photoautotrophic growth, mixotrophic growth, heterotrophic growth.*

Abbreviations: LC-PUFAs: long chain polyunsaturated fatty acids; GLA: gamma-linolenic acid; ARA: arachidonic acid; EPA: eicosapentaenoic acid; DHA: docosahexaenoic acid; H: heterotrophic growth; M: mixotrophic growth; P: photoautotrophic growth; DO: dissolved oxygen; PKS: polyketide synthase; ROS: reactive oxygen species; TAG: triacylglycerol; MAG: monoacylglycerol; PC: phosphatidylcholine; PE: phosphatidylethanolamine; MGDG: monogalactosyldiacylglycerol; DPG: diphosphatidylglycerol; SQ: sulfoquinovosyldiglyceride; mg/L/d: milligram.liter^{-1}.day^{-1}.

1. INTRODUCTION

During last decades, there was growing interest in supplying unsaturated lipids to animal and human.[1] Indeed, some particular unsaturated lipids have been shown to benefit to animal and human health.[2-4] These lipids are provided either by food intake or by extracts e.g. fish oils, olive oils, soybean oils, canola oils, flaxseed oils.[5] These sources are dependent on seasonal variations or the availability of natural resources. Moreover, fish oils are dependent on risks of contamination by xenobiotics[6,7] and of unpleasant smell and taste. Therefore, these drawbacks were the reason why relatively recent bioprocesses for production by microorganisms in bioreactors have been developed.[8,9] One of

**Corresponding author.*
Email: tnvu@hcmus.edu.vn

https://doi.org/10.52111/qnjs.2024.18109

the first industrial applications was the DHA production by a microalga *Crypthecodinium cohnii*.[10] Other photosynthetic and non-photosynthetic microorganisms were also found to produce unsaturated lipids.[11,12]

The unsaturated lipids having 18 carbons or more in length with two or more double bonds were characterized as LC-PUFAs. Gamma-linolenic acid (GLA), arachidonic acid (ARA), eicosahexaenoic acid (EPA) and docosahexaenoic acid (DHA) are the essential LC-PUFAs which have been found in different sources as plant, fish, egg… In recent years, these essential LC-PUFAs have been produced by microorganisms.[1] These microorgnisms include some microalgae, lower fungi, and bacteria which were grown in photoautotrophic, mixotrophic or heterotrophic condition (aerobic or anaerobic condition). These conditions also affect LC-PUFA content in the cells.[13] LC-PUFAs produced by microorganisms were naturally esterified as glycolipids, phospholipids, and neutral lipids which were constituted of membrane compositions.

Oxygen plays an important role for most life on the earth because all higher organisms are aerobioses. Oxygen is indispensable for aerobioses. In cells, oxygen can transform into more reactive forms, Reactive Oxygen Species (ROS) which are toxic to cells. Under oxidative stresses, cells have to maintain the balance of the production between ROS and antioxidant enzymes. However, when the generation of ROS overtakes antioxidant enzymes, the damage of lipids, proteins and nucleic acids occurs.[14] Besides the effects of cell component damage, oxygen also participates in biosynthesis and metabolism of cell compositions. During biosynthesis of LC-PUFAs, oxygen plays a role as an electron acceptor in reduction of fatty acids to form the double bonds.

In cultivation, some factors were useful for overproduction of LC-PUFAs such as temperature, pH, salinity, light,[15,16] oxygen tension.[17] Besides the environmental factors, nutritional factors also affect LC-PUFA biosynthesis. Organisms used in culture can be photoautotrophs, mixotrophs or heterotrophs. Photoautotrophs are organisms that obtain energy from light and carbon source from CO_2 to synthesize organic compounds in the cells while mixotrophs can use energy from light and carbon sources from organic compounds.[18] Heterotrophs obtain energy and carbon sources from organic compounds.

For improvement of LC-PUFA production, many different types of bioreactors were used from pilot to industrial scales.[9,19,20] Depending on the value of the desired products, photosynthetic production can be carried out in open systems and closed systems (photobioreactor).[16] For heterotrophic culture, the classical enclosed bioreactors were used. Industrial reactors and data are available for some photoautotrophic and heterotrophic processes but a lesser point for mixotrophic process.

The objective of this review is to compare the performance of LC-PUFA production by photosynthetic and non-photosynthetic microorganisms.

2. MICROBIAL SOURCES OF LC-PUFA

LC-PUFAs are produced by various microorganisms, from prokaryotes to eukaryotes. They could be also classified either as non-photosynthetic microorganisms or photosynthetic microorganisms (Table 1).

Non-photosynthetic LC-PUFA producers constitute a large group of microorganisms that obtain energy and carbon from organic compounds. This group includes bacteria, fungi, fungus-like microorganisms and some microalgae. Some bacteria have been shown to produce EPA[21] or DHA.[22] These bacteria are *Shewanella*[22-25] and *Moritella*.[26] Some fungi can produce GLA, ARA or EPA. GLA-producing fungi include genera *Mortierella*.[27-29] *Cunninghamella*,[1,30-32] *Pythium*[33] and *Mucor*.[1,34,35] ARA-producing fungi include genera *Mortierella*[36,37] and *Pythium*.[38] These fungal genera are also able to produce EPA.[39-41] Other groups include fungus-like microorganisms,

known as Stramenopiles, characterized as particularly marine stramenopilan protists belonging to the class Labyrinthulomycetes. They differ from fungi in composition of their cell walls (absence of chitin) and rhizoids.[42] Stramenopiles produce high levels of DHA up to 65.9% of total fatty acids.[43] The genera *Thraustochytrium*,[44-47] *Schizochytrium*[48-50] and *Aurantiochytrium*[51,52] are representatives for DHA production. Finally, the microalga *Crypthecodinium* is included in the non-photosynthetic microorganisms, as it is an obligate heterotroph. This microalga can produce high amounts of DHA up to 63.2% of total fatty acids.[53]

Photosynthetic microorganisms are the microorganisms for which energy is provided by light and carbon either by inorganic carbon (photoautotrophy) or by organic carbon sources (mixotrophy). This group includes cyanobacteria and microalgae. Some of them can grow mixotrophically and/or heterotrophically.[54-57] Cyanobacterium *Spirulina* only biosynthesizes GLA while some other microalgae can biosynthesize ARA, EPA or DHA. Not all cyanobacteria or microalgae species can produce LC-PUFAs, only certain cyanobacteria or microalgae can biosynthesize these LC-PUFAs. Microalgae can produce ARA such as *Porphyridium*,[58] *Parietochloris*,[59-61] *Euglena*[62] and *Galdieria*.[63] Microalgae produce EPA such as *Monodus,*[64-66] *Porphyridium*,[58,67] *Phaeodactylum*,[68,69] *Nannochloropsis*,[70-72] *Navicula*,[73,74] *Nitzschia*,[75-78] *Skeletonema*.[79] Some microalgae such as *Rhodomonas,*[80] *Isochrysis*[81] or *Pavlova*[82] contain both EPA and DHA in their cells. *Porphyridium* produces both ARA and EPA.[58] *Nannochloropsis*,[72] *Nitzschia laevis*[13] can produce EPA in 3 modes of nutrition. *Spirulina* can also grow and produce GLA in 3 modes of nutrition.[57,83]

Table 1. Distribution of LC-PUFAs in microorganisms.

Microorganisms		Strains (*)	GLA	ARA	EPA	DHA
Non-photosynthetic	Bacteria	*Shewanella oneidensis* ATCC 700550[23]			+	
		Shewanella putrefaciens MAC1[24]			+	
		Shewanella baltica[25]			+	
		Shewanella morhuae[25]			+	
		Moritella marina ATCC 15381[26]				+
	Fungi	*Mucor circinelloides*[1]	+			
		Mucor mucedo[1]	+			
		Mucor rouxii[34]	+			
		Mucor inaquisporus[35]	+			
		Cunninghamella elegans CCF1318[1]	+			
		Cunninghamella echinulata CCRC 31840[30]	+			
		Pythium debaryanam[33]	+			
		Pythium ultimum[38]		+	+	
		Pythium irregulare[84]			+	
		Mortierella elongata NRRL 5513[41]			+	
		Mortierella isabellina[29]	+			
		Mortierella ramanniana MM15-1[28]	+			
		Mortierella alpina ATCC 16266[37]		+		
		M. alpina ATCC 32222[40]			+	

https://doi.org/10.52111/qnjs.2024.18109

	Fungus-like protists	*Thraustochytrium aureum* ATCC 34304[44]				+
		Thraustochytrium roseum ATCC 28210[47]				+
		Schizochytrium mangrovei FB3[85]				+
		Schizochytrium limacinum SR21[49]				+
		Aurantiochytrium mangrovei MP2[51]				+
		Aurantiochytrium limacinum mh0186[52]				+
	Microalgae	*C. cohnii* ATCC 30772[86-88]				+
Photosynthetic	Cyanobacteria	*Spirulina platensis* UTEX 1928[57]	+			
	Microalgae	*Porphyridium cruentum* SAG 1380-1a[58]		+	+	
		Parietochloris incisa[59-61]		+		
		Skeletonema costatum[79]			+	
		Monodus subterraneus Petersen UTEX 151[66]			+	
		Nitzschia laevis[75]			+	
		Nannochloropsis sp.[72]			+	
		Navicula saprophila[73,74]			+	
		Phaeodactylum tricornutum UTEX 640[68]			+	
		Glaucocystis nostochinearum[62]			+	
		Cyanophora paradoxa[62]			+	
		Euglena gracilis[62]		+	+	
		Galdieria sp. USBA-GBX-832[63]		+	+	
		Rhodomonas salina[80]			+	+
		Pavlova lutheri SMBA 60[82]			+	+
		Isochrysis galbana UTEX LB 987[81]			+	+

(*) Representative strains associated with applied biotechnological studies.

3. OXYGEN AND LC-PUFA BIOSYNTHESIS

There are two different biosynthetic pathways of LC-PUFAs in microorganisms: anaerobic and aerobic pathways (Figure 1).[89] This classification is based on the oxygen dependence of PUFA biosynthesis reactions.

The term "anaerobic pathway" does not mean that the pathway only occurs in anaerobic condition. It can operate in the presence of oxygen but oxygen was not used for formation of double bonds. The formation of double bonds in this pathway is carried out by a dehydration to

remove a water molecule from hydroxyacyl-acyl carrier protein (ACP).

The anaerobic pathway was found in some non-photosynthetic microorganisms such as some bacteria and fungus-like microorganisms. LC-PUFA biosynthesis in some bacteria is generally carried out by PKS-like system.[90] To date, intermediates of this pathway have not yet been determined in detail. Some fungus-like microorganisms such as *Thraustochytrium* and *Schizochytrium* carried out two pathways for LC-PUFA biosynthesis: Polyketide Synthase (PKS) anaerobic pathway and aerobic pathway.[91] Results of studies in *C. cohnii* indicated that DHA biosynthesis by this microalga was not catalyzed by the desaturases and elongases in aerobic pathway[92] but would be made by anaerobic PKS pathway.[93]

In aerobic pathway, molecular oxygen is required in biosynthesis of unsaturated fatty acids. It acts as an electron acceptor for double bond formation in the unsaturated fatty acids. This process is catalyzed by the desaturase enzymes which remove two H atoms from saturated or unsaturated fatty acids to form double bonds in these fatty acids. These two H atoms combine with the O atom of O_2 to form H_2O. The other O atom is reduced by cytochrome b_5.[94-96]

The aerobic pathway occurs in microorganisms such as cyanobacteria, fungi and microalgae. Desaturases use molecular oxygen to form double bonds for unsaturated fatty acids production. This biosynthetic pathway has been studied in photosynthetic microorganisms by using ^{14}C labelled intermediates. In the red microalga *P. cruentum*, it was shown that externally supplied unsaturated fatty acids were assimilated in mixotrophic cultures. Two routes of EPA biosynthesis from linoleic acid (C18:2, n-6) precursors have been suggested: one route along n-6 pathway and another along n-3 pathway.[97] In diatom *P. tricornutum*, four routes of EPA biosynthesis were revealed by use the radiolabeled intermediates. Two routes pass along n-3 pathway, one route pass along n-6 pathway and other route pass along both n-3 and n-6 fatty acids as intermediates.[98] In *Parietochloris incisa*, ARA biosynthesis is carried out in cytoplasm and in chloroplast.[99] In *Pavlova* and *Isochrysis*, DHA was synthesized by aerobic pathway. Gene *IgASE1* which encoded an elongating enzyme in aerobic pathway was identified in *I. galbana* and expressed in yeast.[100] In addition, the genes *pavELO* (*Pavlova*), which catalysed conversion of EPA into DPA and *IgD4* (*Isochrysis*) catalysed conversion of DPA into DHA, were also identified and transformed into yeast cells. The yeast cells were cultured with exogenously supplied EPA and they can synthesize DHA from EPA.[101] Many desaturase and elongase genes in *M. alpina* have been isolated and characterized.[102] This indicated that PUFA biosynthesis in this fungus is carried out by aerobic pathway. Other proof showed that when using SAN 9785, the inhibitor of desaturases, GLA content in the cells of *Spirulina* was significantly influenced.[67]

Using intermediates of the biosynthetic pathways seems to increase the content of LC-PUFAs. The ARA content of *Porphyridium* was 23.2% of total fatty acids after addition of linoleate to the culture medium compared with 16.8% in the control.[97] Similarly, GLA content was 36.0% of total fatty acids when *Spirulina* was grown with linoleate, against 20.4% in the control.[103] In the culture of *Mortierella* for EPA production, linseed oil contains α-linolenic acid (precursor for EPA biosynthesis) as a major fatty acid (58%) was supplemented in the medium, resulted in an increase of EPA content.[40]

https://doi.org/10.52111/qnjs.2024.18109

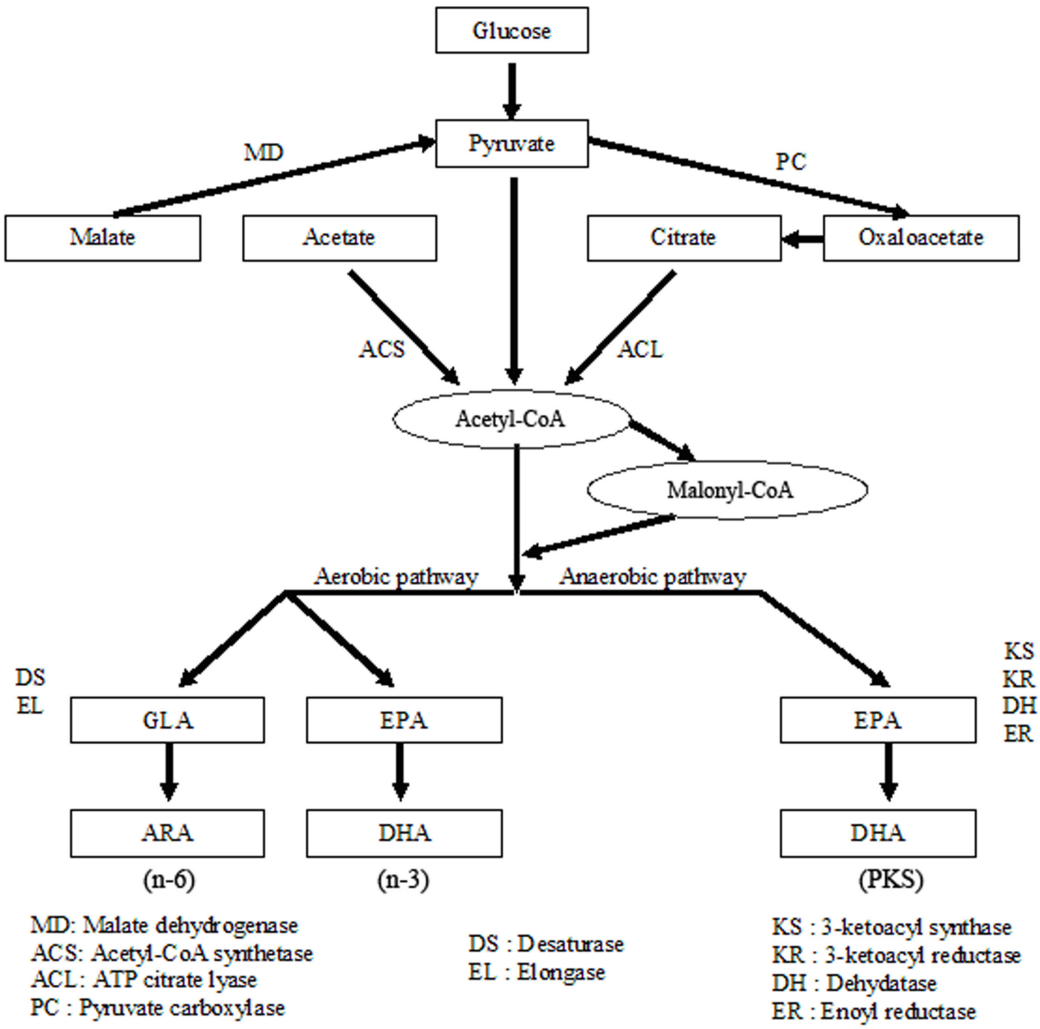

Figure 1. Pathway of LC-PUFA biosynthesis.

4. FACTORS AFFECTING LC-PUFA PRODUCTION

4.1. Nutritional factors

4.1.1. Carbon sources

Carbon constitutes from 49 to 57% of biomass and about 80% of the LC-PUFAs, provided either by inorganic forms such as CO_2 or HCO_3^- for carbon skeletons in photoautotrophic growth or by organic forms as energy sources and carbon skeletons in mixotrophic or heterotrophic growth.

Glucose is the most commonly used carbon source for heterotrophic growth of microorganisms. However, the suitable carbon sources for growth and LC-PUFA production would be different among microorganisms. Starch and maltose were the suitable carbon sources for DHA production by *T. aureum* ATCC 34304.[44] Starch was also the preferred carbon source for GLA production by *C. echinulata* CCRC 31840[30] or for ARA production by *M. alpina* ATCC 32222,[28] whereas glucose was optimal for DHA production by *Thraustochytrium* sp. KK17-3.[104] Glucose was also the suitable carbon source for growth and EPA production by *P. irregulare* ATCC 10951[39] or for GLA production by *Mucor hiemalis* M4.[105] Glucose and starch were suitable carbon sources for ARA production by *Mortierella alliacea* YN-15.[106] Although ARA yield was highest with glycerol, ARA content in lipids was quite low. Thus, glucose was the best choice for ARA production by *M. alpina* ATCC

16266.[37] In *M. alpina* CBS 528.72, glucose gave the optimal growth and total lipid content but rhamnose gave a higher ARA content in total fatty acids.[107] The complexe sources as rice bran, wheat bran, peanut meal, sweet potato, linseed oil, soybean oil,… were also investigated for ARA production by *M. alpina* ATCC 32222.[28] Marine microalga *C. cohnii* could utilize acetic acid,[108] ethanol,[87] carob pulp[109] for DHA production.

Some microalgae as *N. laevis* UTEX 2047 could mixotrophically grow with glucose[13] or *Nannochloropsis* sp. could utilize glucose or ethanol[72] for EPA production. *P. tricornutum* UTEX-640 could also grow and produce EPA in mixotrophic conditions with various carbon sources. Glycerol was found as the most suitable carbon source for growth and EPA production by this microalga.[55,56] *Navicula saprophila* could grow with acetate in mixotrophic condition.[73,74]

In the photoautotrophic culture of *P. tricornutum* UTEX 640, the different concentrations of CO_2 were examined for growth and EPA production. The optimal biomass and EPA yield were 2.5 g/L and 87.5 mg/L, respectively, obtained at 1% CO_2.[68] In the 4-day cultivation of *Nannochloropsis* sp., 2% CO_2 was supplied 12 h prior to the end of the exponential growth gave the highest EPA yield and productivity which were 340 µg/L and 126 µg/L/d, respectively. This productivity was twice as high as that in ambient air.[110] The elevation of CO_2 concentration (350 to 2800 µL/L CO_2) in photoautotrophic culture resulted in an increase of EPA content (21.9% to 25.3% of total fatty acids) in *Nannochloropsis* sp.[111] *M. subterraneus* UTEX 151 was cultured at two different concentrations of CO_2 (1% and 5%). EPA content in total fatty acids obtained at 1% CO_2 was higher than that obtained at 5% CO_2.[64]

4.1.2. Nitrogen sources - nitrogen starvation

Nitrogen constitutes from 8 to 12% of biomass. LC-PUFA producing microorganisms can grow on organic or inorganic nitrogen sources. *T. aureum* ATCC 34304 could utilize organic nitrogen sources as tryptone, peptone, malt extract, yeast extract and sodium glutamate. Cells were grown with yeast extract gave 5.0 g/L biomass and 247.7 mg/L DHA yield while those were 3.8 g/L (biomass) and 269.6 mg/L (highest DHA yield) with sodium glutamate.[44] Tryptone was the most suitable for DHA production by *Thraustochytrium* sp. KK17-3 with 232.8 mg/L DHA.[104] *M. alpina* LPM 301 was grown in the medium with urea or potassium nitrate as nitrogen sources for ARA production. ARA yield was 4.5 g/L after 189 h of cultivation with potassium nitrate and 4.2 g/L after 210 h with urea.[112] Some other strains of *Mortierella* fungi have been studied with the inorganic and organic nitrogen sources. Yeast extract was found as the best nitrogen source for growth and ARA production by *M. alpina*.[113] Furthermore, combination of soluble starch 120% and the mixture (2:1, wt/wt) of KNO_3 and yeast extract were the best nitrogen sources for ARA production by *M. alpina* ATCC 32222.[28] Ammonium hydroxide was used in the culture of *M. alpina* DSA-12 as the nitrogen source and pH control.[114] Ammonium nitrate was found as suitable nitrogen source for GLA production by *C. echinulata*.[30] *N. laevis* UTEX 2047 was heterotrophically cultivated with glucose. Nitrate, ammonium and urea were investigated for growth and EPA production. Biomass and EPA yield were over 4 g/L and 90 mg/L, respectively, obtained with nitrate or urea but only 1.24 g/L biomass and 21.58 mg/L EPA with ammonium.[76] Combination by the ratio 32:1 of glucose and mixture (1:2.6:1.3) of nitrate, tryptone and yeast extract was optimal for EPA production by *N. laevis* UTEX 2047.[78]

Mixotrophic cultivation was carried out with *P. tricornutum* UTEX 640 in the presence of glycerol with urea or nitrate. The best results were 1.52 g/L/d biomass and 43.13 mg/L/d EPA obtained with 0.01 M urea in fed-batch.[56]

In the photoautotrophic cultivation of *P. tricornutum* UTEX 640, urea was the optimal nitrogen source for EPA production.[68] Nitrate,

https://doi.org/10.52111/qnjs.2024.18109

nitrite and urea were utilized in the culture of *I. galbana*. DHA content in total fatty acids was highest (14.13%) obtained with urea at early stationary phase.[115] $(NH_4)_2HPO_4$ was the suitable source of nitrogen for growth and GLA production by *S. platensis*.[116]

I. galbana CCAP 927/1 was cultivated in nitrate starvation, DHA content in total fatty acids increased from 1.19 to 4.52% from 2nd day to 5th day of cultivation.[117] Nitrogen starvation induced an increase in ARA content over 60% of total fatty acids in *P. incisa*.[60]

4.1.3. Phosphorus sources - phosphorus starvation

Phosphorus participates in the energy transfer within cells and constitutes about 5-6% of phospholipids.

In fungus *P. irregulare* ATCC 10951, optimal EPA production (about 31 mg/L) was obtained at 0-3 mM phosphate. The increase of phosphate concentrations (6 – 24 mM) resulted in a decrease of EPA yield.[39]

Effects of phosphate (0.05 - 0.5 g/L) were also examined on the growth and EPA production by *P. tricornutum* UTEX 640. Little change in biomass was observed in this range of phosphate concentrations but EPA yield was higher at phosphate levels of 0.1 – 0.5 g/L.[68]

Phosphorus starvation was studied by 7-day cultivation of *P. tricornutum* in the phosphorus-deficient medium (no phosphate was added). A comparative control was made in parallel with 6.9 mg/L NaH_2PO_4. Results indicated that EPA content in total fatty acids decreased from 26.8% to 6.9% in the condition of phosphorus deficiency.[118] Other study showed that EPA content decreased from 28.2 to 15.5% mol of fatty acids when decreasing phosphate concentration (K_2HPO_4) from 175 to 0 µM in the 4-day cultivation of *M. subterraneus*.[119]

4.1.4. Silicate

Silicate is an essential nutrient for diatom growth because cells need silicate to form their frustules. *N. laevis* UTEX 2047 was heterotrophically grown with glucose and silicate. The highest EPA yield (131 mg/L) was obtained at 20 g/L glucose and 32 mg/L silicate while the highest EPA productivity was 15.1 mg/L/d at 20 g/L glucose and 64 mg/L silicate.[75]

In photoautotrophic conditions, the range of silicate from 8.8 – 176 µM has been examined for EPA production in the culture of *Nitzschia inconspicua*. Results showed that there was not significantly change in EPA content (about 4.0% of total fatty acids) and EPA yield (about 0.2 mg/L).[120] Similarly, the photoautotrophic growth of *P. tricornutum* was not significantly different in the levels of 0 to 50 mg/L silicate. Increase of silicate levels from 50 to 500 mg/L resulted in reducing growth (2.6 to 1.8 g/L biomass) and EPA content (72.5 to 35.0 mg/L EPA).[68]

4.2. Environmental factors

4.2.1. Temperature

Optimal temperature for growth is often different from optimal temperature for LC-PUFA accumulation. The increase of LC-PUFA contents at low temperature is attributed to the cells maintaining fluidity of membranes by biosynthesizing more LC-PUFAs.

Effect of temperature on production of ARA and EPA was studied in *P. ultimum*. The optimal temperature for ARA and EPA production was 25 °C.[38] This temperature was also found as the most suitable temperature for ARA accumulation in *M. alpina*[107] and *T. roseum* ATCC 28210 for DHA production.[45] Highest DHA content in total fatty acids was found when *S. limacinum* OUC88 was cultured at 16 – 23 °C.[121] In *Aurantiochytrium* sp. strain mh0186, cells grew well at 15 – 30 °C, but weakly at 10 °C. The amount of DHA in total fatty acids was highest at 10 °C. The DHA yield was similar at 15 – 30 °C and was significantly higher than those at 10 and 35 °C.[122] Similarly, *Shewanella* was cultivated at 10, 15 and 25 °C. The cells accumulate with the highest concentration of EPA (6.3% of total lipids) at 10 °C. At 25 °C,

EPA concentration in dry weight is lower (1.5% of total lipids).[25] *Galdieria* cells accumulate higher concentrations of PUFAs at 25 °C when compare to 45 °C.[63]

A range of temperature from 10 to 30 °C was investigated in the culture of *P. tricornutum* 2038. Growth was inhibited at 30 °C, slow at 25 °C and optimal at 20 °C. EPA content in dry weight was highest at 10 °C.[123] However, optimal temperature for biomass and EPA production by *P. tricornutum* UTEX 640 was found at 21.5 – 23 °C in the study of Yongmanitchai and Ward (1991).[68] The effect of temperature on GLA content was also studied in *S. platensis* UTEX 1928. The suitable temperature for GLA accumulation was from 25 to 33 °C.[124] The optimal EPA production was obtained at 8 °C in the culture of *Porphyridium purpureum* 1380-1b.[125]

4.2.2. pH

Generally, heterotrophic cultures were related to acid pH conditions. pH in the range of 5.5 – 6.5 was suitable for biomass and ARA production by *M. alpina*. Maximal ARA content in total fatty acids was obtained at initial pH 6.5.[107] ARA yield was highest at initial pH 6.0.[126] Initial pH 6 was also favourable for DHA production by *Thraustochytrium*.[44,45] Optimal growth and EPA production were obtained at initial pH 6 – 7 in culture of *P. irregulare*.[39] The highest DHA content in total fatty acids was 56.8% at initial pH 7.2 in *C. cohnii* ATCC 30556.[127]

In *R. salina*, the concentrations of EPA and DHA accumulated in dry weight when cultivated at pH 8.5 are 0.8% and 0.3%, respectively, compare to 0.6% and 0.2% at pH 7.[80]

Yongmanitchai and Ward have found the maximal EPA yield (93.1 mg/L) at initial pH 7.6 in the photoautotrophic culture of *P. tricornutum* UTEX 640.[68] The range of pH from 5.0 to 8.5 was tested for EPA production in *P. purpureum* 1380-1b. The highest EPA yield (1.79 mg/L) was obtained at pH 7.6.[125]

4.2.3. Salinity

Some studies relating to effects of salinity on growth and LC-PUFA production have been investigated. A wide tolerance to salinity was found in *S. limacinum* when this fungus-like microorganism was cultured in the salinity range from 0% to 200% that of seawater. In the optimal range of salinity for growth (50 – 200% of seawater), there was little change in dry cell weight. Although this strain could grow at 0% of salinity, the growth was lower than those at the optimal range of salinity.[49] *Thraustochytrium* sp. showed a slight resistance to high salinity, up to 200% that of seawater. The optimal salinity for growth and DHA production was 75% that of seawater.[104] Sea salt from 2 – 50 g/L was also examined for growth and DHA production by *Thraustochytrium* sp. The highest biomass (24.7 g/L) and DHA yield (4.6 g/L) were obtained at 2 g/L NaCl.[46] The optimal concentration of NaCl for DHA production by *C. cohnii* ATCC 30556 was 9 g/L.[128]

In *P. lutheri* SMBA 60, NaCl concentrations from 5 to 45 g/L were examined for EPA and DHA production. The highest EPA (about 4.7 mg/L) and DHA yield (about 2.6 mg/L) were obtained at 5 – 15 g/L NaCl.[129] *P. tricornutum* UTEX 640 gave the highest EPA yield at 0 – 10 g/L NaCl.[68] *Spirulina* was cultivated in the range 0 – 3.5 g/L NaCl, GLA content increased as NaCl level was raised to 0.6 g/L and then it decreased. GLA yield was highest (27 µg/mL) at 0.2 g/L NaCl concentration.[130]

4.2.4. Light

Light also stimulates the growth and DHA production in *T. aureum*. Biomass and DHA yield in light exposed cultures were 70.4 g/L and 269.6 mg/L, respectively, higher than those in dark cultures.[44] After that, some cultivations of *Thraustochytrium* for DHA production were carried out under light by other authors.[45,131]

Light affects growth and fatty acid composition of microorganisms, especially the photosynthetic ones. *P. lutheri* SMBA 60 was

https://doi.org/10.52111/qnjs.2024.18109

grown in semi-continuous cultures at the different light intensities 9, 19 and 30 W/m^2. The highest EPA and DHA productivities were obtained at 19 W/m^2.[132] Effects of intensities and photoperiods on fatty acid production by *I. galbana* have also been studied.[133] Percentage of EPA in total fatty acids and in dry weight were 35.7% and 4.4%, respectively when *M. subterraneus* was grown at 90 µmol photon/m^2/s, which was higher than those at 170 µmol photon/m^2/s.[64] GLA content in total fatty acids of *S. platensis* increased from 31.1 to 36.0% when increased the light intensity from 860 to 1400 µmol photon/m^2/s.[124]

4.2.5. Culture age

Effect of culture age on ARA production by *M. alpina* I_{49}-N_{18} was investigated. ARA yield increased and was maximal at the 6th day, and then decreased.[113] The GLA yield was also maximal after 5 – 6 days in the culture of *C. echinulata* CCRC 31840.[30]

In photoautotrophic culture of *Pavlova viridis*, EPA and DHA content in late exponential phase (4 days) were 22.1 and 3.5 mg/g biomass, respectively, and decreased in linear phase (7 days) and stationary phase (13 days).[134]

4.2.6. Dissolved oxygen

Oxygen constitutes from 27 to 32% of biomass and about 10% of the LC-PUFAs. The levels of DO affected growth and LC-PUFA production in heterotrophic culture of various microorganisms. *C. cohnii* gave higher DHA yield when cultured at DO of 10 – 50% of air saturation level.[17] In *S. limacinum* SR21, the culture was carried out in two stages, the first stage for biomass production where concentration of dissolved oxygen at 50% whereas at 10% for DHA production in the second stage.[49] DHA content of total fatty acids was 30.6% and 40% at 40% DO and 5% DO, respectively.[135] *Mucor rouxii* ATCC 24905 was shifted from anaerobic to aerobic conditions resulted in an increase of biomass and fatty acid content. Oxygen induced the expression of Δ^9-, Δ^{12}- and Δ^6- desaturase genes resulted in an increase of unsaturated fatty acids.[136]

5. DISTRIBUTION OF LC-PUFAS IN LIPID CLASSES

Distribution of LC-PUFAs in lipid classes is various among microorganisms. The nutritional and environmental factors affect the distribution of LC-PUFAs in the cells. Information on LC-PUFA localization in the lipid classes is determinant for the purification process.

In *C. echinulata* ATHUM 4411, GLA distribution depended on developmental stages. GLA content in PC remained over 20% of total fatty acids in mid exponential, late exponential and stationary phase whereas that was changed in other lipid classes. ARA content in dry weight increased in non-polar lipids but decreased in polar lipids through growth phases.[32] The distribution of LC-PUFAs in lipid classes in *M. alpina* SC9 was influenced by salinity. TAG was the dominant lipid class of the cells (261.16 mg/g) which contained the highest proportion of ARA (30.29% of total fatty acids). When the cells were cultured at 20 g/L NaCl, TAG content increased 296.55 mg/g but ARA content decreased 21.24%.[137] In *N. laevis* UTEX 2047, neutral lipids (78.6%) were the major component of the total lipids, in which TAG was the predominant component (87.9%) of neutral lipids. EPA was present 37.44% in TAG, 22.49% in MAG and 15.91% in PC.[138] EPA content increased in polar lipids but decreased in neutral lipids at 10 – 30 g/L NaCl.[139] When increasing the temperature from 15 to 23 °C, EPA content slightly decreased in TAG but increased in glycolipids. EPA content in phospholipids at 19 °C was higher than that at 15 °C and 23 °C.[140] In *S. mangrovei* FB3, TAG was the predominant component with 97.2% of neutral lipids. Neutral lipids constitute 95.9% of total lipids. PC was the major polar lipids which accounted for 47.78% of phospholipids. DHA was found as the main polyunsaturated fatty acid since it was 29.74% in TAG and 39.61% in PC.[85] PC in *C. cohnii* was the major component (63.6%) of polar lipids in which 57.2% were DHA.[141] However, it was stated that DHA accumulated predominantly in *C. cohnii* cells as TAG, the neutral lipid fraction.[10]

N. saprophila was mixotrophically grown with acetate in which PC was the major component (55.7% of lipids) and EPA was concentrated 28.2% in PC whereas PC was only 47.9% of lipids and EPA was 19.0% of PC in photoautotrophic culture.[74]

In the photoautotrophic culture of *P incisa*, TAG was the dominant lipid with 42.9% of fatty acids in the logarithmic phase and 77% in the stationary phase. ARA was mainly present in TAG with 43% in logarithmic phase and 47% in stationary phase.[59] Under nitrogen starvation, neutral lipids and ARA content in neutral lipids were 86.8% and 63.7% of total fatty acids compared to 62.1% and 50.8% in the control, respectively.[60] In *P. lutheri*, TAG was the major component of nonpolar lipids and MGDG was the main component of polar lipids. EPA was present 45% in MGDG and 33% in TAG. DHA was distributed 27% in TAG, 22% in DPG and 21% in betaine lipids.[82] Light affected distribution of EPA in lipid classes. Under low light intensity (9 W/m^2), EPA accumulated in polar lipids was higher than that in non-polar lipids whereas it was conversely when cultured at 19 and 30 W/m^2. At these conditions of light, DHA content in non-polar lipids was higher than that in polar lipids. When increasing light intensity from 9 to 30 W/m^2, EPA and DHA contents in polar lipids decreased while EPA and DHA contents in non-polar lipids at 19 W/m^2 were higher than those at 9 and 30 W/m^2.[132] Galactolipid fraction contained 92% GLA in *S. platensis* 2340.[142] Nitrogen starvation affected distribution of ARA and EPA in *P. cruentum*. ARA content in total fatty acids increased from 19.9% to 30.7% in the neutral lipids and from 46.3% to 61.2% in PC whereas EPA decreased from 43.2% to 16.9% in MGDG, 29.4% to 8.6% in SQ and 17.4% to 2.9% in PC.[58]

Formation of lipid bodies was revealed by using fluorescent staining of endoplasmic reticulum (ER). Lipid bodies surrounded ER in oleaginous fungus *M. ramanniana* IFO 8187.[143] The same result was observed in *S. limacinum* SR21. The lipid bodies often contact with ER in all stages of the cells.[144]

In the photosynthetic microorganisms, the lipid body formation occurred in the inner thylakoid spaces of the chloroplast structure in *Isochrysis*[145] or *M. subterraneus* UTEX 151.[65]

Table 2. Distribution of LC-PUFAs in lipid classes.

Microorganisms	Modes of nutrition	LC-PUFAs	LC-PUFAs (mg/g dry weight)	
			Polar lipids	Non polar lipids
Cunninghamella echinulate ATHUM 4411[32] (a)	H	GLA	0.93	7.04
M. alpina SC9[137] (b)	H	ARA	1.22	84.95
N. laevis UTEX 2047[139] (c)	H	EPA	9.81	61.19
N. laevis UTEX 2047[138]	H	EPA	5.87	9.11
S. mangrovei FB3[85]	H	DHA	9.00	193.17
P. lutheri SMBA 60[82]	P	EPA	8.41*	4.95*
P. lutheri SMBA 60[82]	P	DHA	6.39*	2.26*
P. lutheri SMBA 60[132] (d)	P	EPA	526.94*	170.77*
P. lutheri SMBA 60[132] (d)	P	DHA	69.77*	177.99*

*Unit: mg/g ash free dry weight (AFDW); (a) late exponential phase; (b) 0 % NaCl; (c) 10 g/L NaCl; (d) 9 W/m^2

https://doi.org/10.52111/qnjs.2024.18109

6. LC-PUFA YIELD AND PRODUCTIVITY OF PHOTOSYNTHETIC AND NON-PHOTOSYNTHETIC MICROORGANISMS

Non-photosynthetic microorganisms only grow and produce LC-PUFAs in heterotrophic condition while photosynthetic microorganisms can grow and produce LC-PUFAs in photoautotrophic, mixotrophic and heterotrophic conditions (Table 4). The LC-PUFA producers for high productivity have been selected to compare the performance of their production (Table 3).

Table 3. Comparison of LC-PUFA yield and productivity of selected microorganisms.

LC-PUFAs	Microorganisms	Modes of nutrition	Biomass (g/L)	LC-PUFA yield (g/L)	LC-PUFA productivity (mg/L/d)
GLA	*M. rouxii* CBS 416.77[35]	H	24.0	0.532	336.0
	C. echinulata CCRC 31840[31]	H	38.1	1.349	269.8
	M. ramanniana CBS 112.08[27]	H	12.0	0.451	112.8
	S. platensis M2[28]	P	-	-	26.4
ARA	*M. alpina* DSA-12[114]	H	72.5	18.800	1504.0
	M. alpina ME-1[146]	H	39.8	19.020	3396.4
	P. incisa comb. nov[147]	P	21.0	2.667	70.2
EPA	*M. alpina* 20-17[148]	H	24.5	1.350	103.8
	N. laevis UTEX 2047[77]	H	-	-	174.6
	P. irregulare[84]	H	14.22	0.176	-
	P. tricornutum UTEX 640[56]	M	15.4	0.436	43.1
	P. tricornutum UTEX 640[149]	M	-	-	56.0
	P. tricornutum UTEX 640[69]	P	1.7	0.083	25.1
	M. subterraneus UTEX 151[66]	P	-	-	58.9
DHA	*C. cohnii* ATCC 30772[87]	H	109	11.700	1276.4
	S. limacinum ATCC 1381[48]	H	48.1	13.300	3325.0
	Schizochytrium[135]	H	178	33.286	16560.0
	I. galbana UTEX LB 2307[150]	P	-	-	4.3

6.1. Heterotrophic production

Until now, numerous data of heterotrophic LC-PUFA production by non-photosynthetic microorganisms have been published.

For GLA production, fungi were found as producers in high GLA productivity. *M. rouxii* CBS 416.77 was cultivated with glucose and Difco yeast extract. Biomass and GLA productivity were 24 g/L and 336 mg/L/d, respectively.[35]

Higashiyama *et al*. has compared productivity of ARA production by *Mortierella*, in which strain *M. alpina* 1S-4 gave high ARA productivity (1300 mg/L/d).[36] However, Hwang *et al.* cultivated *M. alpina* DSA-12 in fed-batch by using NH_4OH as a nitrogen source and pH control which obtained 1504 mg/L/d ARA, higher than former productivity in the culture of Higashiyama *et al*.[114] *M. alpina* ME-1 was a UV-mutant of ATCC 16266 gave 19020 mg/L ARA at 5.6 days which was highest found in the reports.[146]

EPA production has been reviewed by Bajpai and Bajpai.[15] High EPA yield and productivity were 1350 mg/L and 103.8 mg/L/d in the culture of *M. alpina* 20-17.[148] *N. laevis* UTEX 2047 was grown in perfusion culture with cell bleeding. EPA productivity obtained in this cultivation (174.6 mg/L/d) was highest EPA productivity found.[77]

Stramenopiles were utilized as DHA producing microorganisms. DHA yield and productivity have been compared among various strains. *S. limacinum* SR21 gave the highest DHA yield and productivity with 13300 mg/L and 138 mg/L/h DHA.[151,152] The other strain of *Schizochytrium* which has been studied by Bailey *et al*. produced a very high concentration of DHA 23.45 g/L in 42 h.[135] *C. cohnii* was also a DHA producing microalga. The parameters of culture and DHA production were collected in the review of Mendes *et al*.[10] The fed-batch cultivation on ethanol produced 11700 mg/L DHA in 220 h was the highest productivity in this microalga.[87]

6.2. Mixotrophic production

Mixotrophic production was found in photoautotrophic microorganisms which have growth capacity with organic compounds under light. Up to now, most of LC-PUFA producing microorganisms in mixotrophic condition were EPA producing microalgae and GLA producing cyanobacteria (Table 4). *P. tricornutum* UTEX-640 was cultivated with carbon sources to evaluate growth and EPA production. Glycerol was found as the most suitable source of carbon.[56,69] Fed-batch culture with 0.1 M concentration of glycerol and the successive additions of ammonium chloride gave 16.2 g/L biomass concentration, 61.5 mg/L/h biomass productivity and 33.5 mg/L/d EPA productivity. This EPA productivity was 10-fold greater than the maximum productivity obtained in the photoautotrophic control culture.[55] Additionally, fed-batch with glycerol and urea gave 43.13 mg/L/d EPA productivity which was 13-fold higher than the maximum EPA productivity obtained in photoautotrophic culture of the control.[56] Other result of *P. tricornutum* UTEX-640 indicated that EPA productivity (56 mg/L/d) in mixotrophic culture (with glycerol) was approximately 3-fold higher than that in photoautotrophic culture.[149] *N. saprophila* was mixotrophically cultivated with acetate. EPA content obtained in this condition was 19.2 mg/g biomass that was higher than those obtained in photoautotrophic and heterotrophic conditions.[73] EPA content in biomass was 34.6 mg/g when *N. saprophila* was cultured with 2 mM acetate and 2% CO_2.[74] Performance of EPA production in three nutritional modes was compared in the culture of *N. laevis* UTEX 2047. Growth and EPA production were highest in mixotrophic culture. EPA yield and productivity were 52.32 mg/L and 10.46 mg/L/d, respectively.[13] *Nannochloropsis* sp. also showed that they can grow and produce EPA in 3 nutritional modes. Glucose and ethanol were utilized as carbon sources for EPA production which gave 23.4 mg/L and 23.0 mg/L EPA, respectively, in mixotrophic cultivation after 8 days.[72] An increase of EPA yield up to 56 mg/L was obtained in 10 days of fed-batch culture with an addition of glucose and nitrate.[152] *S. platensis* KCTC AG20590 was mixotrophically cultivated with the long or short chain carbon sources. Results indicated that GLA content increased when compared with the control.[83]

Table 4. Comparison of LC-PUFA productivity between the nutritional modes.

Strains	LC-PUFAs	LC-PUFA productivity (mg/L/d)		
		PA	M	H
Nannochloropsis sp.[72]	EPA	3.13	3.34	1.44
N. laevis UTEX 2047[13]	EPA	3.39	10.46	6.37
P. tricornutum UTEX-640[56]	EPA	3.35	43.13	-
P. tricornutum UTEX-640[149]	EPA	18.0	56.0	-
N. saprophila[74]	EPA	4.93	14.8	-
S. platensis KCTC AG20590[83]	GLA	0.43	1.70	-

6.3. Photoautotrophic production

Photoautotrophic production was only found in photosynthetic microorganisms. Table 5 presented performance of essential LC-PUFAs from photosynthetic microorganisms.

GLA productivity was 26.4 mg/L/d obtained from *S. platensis* M2 in outdoor culture.[66]

Parietochloris[147] and *Porphyridium*[153] were ARA-producing microalgae. EPA productivity was 70.2 mg/L/d and 6.5 mg/L/d, respectively.

For EPA production, *Phaeodactylum* was known as photoautotrophic EPA producer. Meiser *et al*. cultivated *P. tricornutum* UTEX 640 under continuous light in batch culture.[154] Maximal EPA productivity 118 mg/L/d were obtained. *Nannochloropsis* sp. was cultivated in flat plate reactor under 1000 µmol photon/m^2/s gave 127.9 mg/L/d EPA.[71]

Until now, *Rhodomonas, Pavlova* and *Isochrysis* were found as photosynthetic microalgae produced DHA. However, productivity of DHA production by these microalgae was less than that by non-photosynthetic microorganisms (Table 3). The highest DHA productivity was 4.3 mg/L/d, obtained when cultured *I. galbana* in optical fiber photobioreactor.[150]

Table 5. LC-PUFA productivity of photoautotrophic production.

LC-PUFAs	Strains	LC-PUFA productivity (mg/L/d)
GLA	*S. platensis* M2[66]	26.4
	S. platensis KCTC AG20590[83]	0.4
ARA	*P. incisa* comb. nov[147]	70.2
	P. cruentum IAM R-3[153]	6.5
EPA	*S. putrefaciens* MAC1[24]	58.3
	P. cruentum IAM R-3[153]	3.6
	M. subterraneus UTEX 151[154]	56.0
	M. subterraneus UTEX 151[64]	25.7
	M. subterraneus UTEX 151[66]	58.9
	P. tricornutum UTEX 640[68]	19.0
	P. tricornutum UTEX 640[69]	25.1
	P. tricornutum UTEX 640[154]	50.0
	P. tricornutum UTEX 640[155]	13.0
	P. tricornutum UTEX 640[156]	118.0
	P. tricornutum UTEX 640[157]	47.8
	P. tricomutum TFX-1[158]	6.0
	Nannochloropsis sp.[70]	32.0
	Nannochloropsis sp.[71]	127.9
	Nannochloropsis sp. PP983[111]	1.2
	P. lutheri SMBA 60[160]	0.5
	P. lutheri SMBA 60[132]	1.3
	I. galbana Parke[160]	4.8
	I. galbana[161]	15.3
	I. galbana[162]	7.2
DHA	*P. lutheri* SMBA 60[159]	0.2
	P. lutheri SMBA 60[132]	0.7
	I. galbana UTEX LB 2307[151]	4.3
	I. galbana CCMP 1324[163]	0.6
	I. galbana CCAP 927/1[164]	0.2
	I. galbana[162]	3.1

7. YIELD CONVERSION OF LC-PUFA PRODUCTION

Conversion yield is calculated on the ratio of production to substrate. It permits to evaluate productivity economically. Table 6 showed conversion yield of biomass and LC-PUFAs in some LC-PUFA producers.

Table 6. Biomass and LC-PUFAs conversion yield of microorganisms.

Microorganisms	Substrate (S)	$Y_{X/S}$ (g. g^{-1})	LC-PUFAs	$Y_{LC\text{-}PUFA/S}$ (mg. g^{-1})	Modes of nutrition
M. circinelloides CBS 203.28[34]	Acetic acid	0.30	GLA	10.00	H
C. cohnii ATCC 30772[108]	Acetic acid	0.12	DHA	30.00	H
M. isabellina ATHUM 2935[35]	Glucose	0.50	GLA	7.70	H
M. alpina DSA-12[114]	Glucose	0.44	ARA	95.40	H
Schizochytrium G13/2S[165]	Glucose	0.39	DHA	64.02	H
Aurantiochytrium limacinum mh0186[52]	Glucose	0.38	DHA	71.67	H
Thraustochytrid G13[166]	Glucose	0.46	DHA	56.25	H
C. cohnii ATCC 30556[128]	Glucose	0.50	DHA	38.59	H
C. cohnii ATCC 30772[86]	Glucose	0.37	DHA	21.27	H
Nannochloropsis sp.[72]	Glucose	0.20	EPA	8.75	M
N. laevis UTEX 2047[13]	Glucose	0.42	EPA	10.46	M

X: biomass; Y: conversion yield

8. IMPROVEMENT FOR LC-PUFA PRODUCTION

Microalgae cultivation in large volume increases the productivity of biomass and LC-PUFAs. Nowadays, a lot of photobioreactors were invented for microalgae culture.

Cultivation of non-photosynthetic microorganisms was carried out in the closed and sterile systems with the sources of organic carbon. Because of heterotrophic culture, light was not necessary in this system. Source of carbon is usually one of the factors influencing production. Thus, fed-batch or continuous culture were often used to improve LC-PUFA production.

Conversely, light was necessary in cultivation of photosynthetic microorganisms.[167] Thus, bioreactors can be designed to obtain light effectively. By using a new type of enclosed photobioreactor in which light was efficiently distributed by light diffusing optical fibers, DHA from *Isochrysis* was obtained 4.3 mg/L/d (Table 3), twofold greater than that obtained using flat glass bottles.[150] *Nannochloropsis* sp. was cultured in a flat plate reactor with a narrow (1 – 2 cm) light path and rigorous stirring exposed to high photon flux densities (1000-3000 µmol photons/m^2/s). Biomass and EPA yield were obtained 40.6 g/L and 2302 mg/L, respectively.[71]

Culture in two stages of temperature is a strategy for improvement of LC-PUFA production: the first stage for biomass production and the second for LC-PUFA production. In the second stage, temperature was usually decreased to produce more LC-PUFAs.

In *P. irregulare* ATCC 10951, cells were initially grown at 25 °C for 1, 2 or 3 days and then shifted to 12 °C for 6, 8, 9 days. The best combination was 2 days at 25 °C, followed by 6 days at 12 °C, which gave 93.1 µg/ml EPA.[39] *M. alpina* ATCC 32222 was cultured for 8 days at 25 °C gave a high biomass (52.4 g/L)

https://doi.org/10.52111/qnjs.2024.18109

and ARA yield (9.1 g/L). Then, the culture was incubated at 15 °C. The maximal ARA content was obtained (11.1 g/L) in 11 days of fermentation.[168] An increase in cellular DHA content by 19.9% and productivity by 6.5% was observed when the temperature in the culture of *C. cohnii* ATCC 30556 was shifted from 25 °C for 2 days to 15 °C for 1 day compared with that maintained at 25 °C for 3 days.[126] A shift of temperature from 30 °C for 32 h to 20 °C for 12 h in the culture of *Schizochytrium* sp. HX-308 resulted in an increase of DHA content which is present 6.05% in dry cell weight and 51.98% in total fatty acids.[169] In *C. cohnii* CCMP 316, n-dodecane was added in the culture as an oxygen vector. The DHA content in total fatty acids, the DHA content in biomass and DHA yield increased by 16, 39 and 22%, respectively, at 0.5% n-dodecane.[53]

The increase of DHA content (15.7 to 17.8 mg/g biomass) was also found when *I. galbana* LB 2307 was shifted from 24 °C to 17 °C for 24 h.[150] In the culture of *P. tricornutum* 2038, cells were cultivated at 25 °C and then shifted to 20, 15, 10 °C. An increase of EPA content per dry mass was observed after 12 h, 24 h and 48 h at 10 °C, 15 °C and 20 °C, respectively. The highest EPA yield was 6.6 mg/L when temperature was shifted from 25 °C to 10 °C for 12 h, which raised by 120% compared with the control.[123] After decantation, biomass of *S. costatum* was obtained and incubated at 15 °C for 15 h, resulted in an increase in EPA content from 11 mg/g to 19 mg/g of dry weight.[79]

9. CONCLUSION

The limitation of essential LC-PUFA sources originating from animals and plants has promoted the research on other sources. Microorganisms were found as potential sources for LC-PUFA production because they could grow fast on culture media and contain high LC-PUFA content in their cells. Besides heterotrophically LC-PUFA producing microorganisms, many microalgae have been discovered as LC-PUFA producers. Among these microalgae, some strains could produce LC-PUFAs in 2 or 3 modes of nutrition. Among nutritional modes, heterotrophy was found as a mode of high productivity production. However, mixotrophy has also potential for improvement of LC-PUFA productivity in photosynthetic microorganisms. Further researches need to focus on new microalgal strains to diversify LC-PUFA sources.

REFERENCES

1. O. P. Ward, A. Singh. Omega-3/6 fatty acids: alternative sources of productions, *Process Biochemistry*, **2005**, *40*, 3267-3652.
2. C. H. Ruxton, S. C. Reed, M. J. Simpson, K. J. Millington. The health benefits of omega-3 polyunsaturated fatty acids: a review of the evidence, *Journal of Human Nutrition and Dietetics*, **2004**, *17*, 449-459.
3. A. Molfino, M. I. Amabile, M. Monti, S. Arcieri, F. F. Rossi, M. Muscaritoli. The role of docosahexaenoic acid (DHA) in the control of obesity and metabolic derangements in breast cancer, *International Journal of Molecular Science*, **2016**, *17,* 505.
4. K. Christina, F. Maria, S. Anastasis, P. Ioannis. DHA/EPA (Omega-3) and LA/GLA (Omega-6) as bioactive molecules in neurodegenerative diseases, *International Journal of Molecular Sciences*, **2023**, *24*, 10717.
5. W. S. Harris. Fish oil supplementation: evidence for health benefits, *Cleveland Clinic Journal of Medicine*, **2004**, *71*, 209-221.
6. U. Varanasi, J. E. Stein. Disposition of xenobiotic chemicals and metabolites in marine organisms, *Environmental Health Perspectives*, **1991**, *90*, 93-100.
7. J. S. Christiansen, R. A. Dalmo, K. Ingebrigtsen. Xenobiotic excretion in fish with aglomerular kidneys, *Marine Ecology Progress Series*, **1996**, *136*, 303-304.
8. N. T. Eriksen. The technology of microalgal culturing. *Biotechnology Letters*, **2008**, *30*, 1525-1536.

9. C. U. Ugwu, H. Aoyagi, H. Uchiyama. Photobioreactors for mass cultivation of algae, *Bioresource Technology*, **2008**, *99*, 4021-4028.

10. A. Mendes, A. Reis, R. Vasconcelos, P. Guerra, T. L. D. Silva. Crypthecodinium cohnii with emphasis on DHA production: a review, *Journal of Applied Phycology*, **2009**, *21*, 199-214.

11. W. R. Barclay, K. M. Meager, J. R. Abril. Heterotrophic production of long-chain omega-3 fatty acids utilizing algae and algae-like microorganisms, *Journal of Applied Phycology*, **1994**, *6*, 123-129.

12. I. K. Goldberg, U. Iskandarov, Z. Cohen. LC-PUFA from photosynthetic microalgae: occurrence, biosynthesis, and prospects in biotechnology, *Applied Microbiology and Biotechnology*, **2011**, *91*, 905-915.

13. Z. Y. Wen, F. Chen. Production potential of eicosapentaenoic acid by the diatom nitzschia laevis, *Biotechnology Letters*, **2000**, *22*, 727-733.

14. U. Bandyopadhyay, D. Das, R. K. Banerjee. Reactive oxygen species: oxidative damage and pathogenesis, *Current Science*, **1999**, *77*, 658-666.

15. P. Bajpai, P. K. Bajpai. Eicosapentaenoic acid (EPA) production from microorganisms: a review, *Journal of Biotechnology*, **1993**, *30*, 161-183.

16. Z. Y. Wen, F. Chen. Heterotrophic production of eicosapentaenoic acid by microalgae, *Biotechnology Advances*, **2003**, *21*, 273-294.

17. D. J. Kyle, S. E. Reeb, V. J. Sicotte. Production of docosahexaenoic acid by dinoflagellates, United States Patent, US 5407957, 1995.

18. A. L. Reysenbach, S. L. Cady. Microbiology of ancient and modern hydrothermal systems, *Trends in Microbiology*, **2001**, *9*, 79-86.

19. L. Xu, P. J. Weathers, X. R. Xiong, C. Z. Liu. Microalgal bioreactors: challenges and opportunities, *Engineering in Life Sciences*, **2009**, *9*, 178-189.

20. B. Wang, C. Q. Lan, M. Horsman. Closed photobioreactors for production of microalgal biomasses, *Biotechnology Advances*, **2012**, *30*, 904-912.

21. D. S. Nichols, J. L. Brown, P. D. Nichols, T. A. McMeekin. Production of eicosapentaenoic acid and arachidonic acids by an antarctic bacterium: response to growth temperature, *FEMS Microbiology Letters*, **1997**, *152*, 349-354.

22. K. Watanabe, C. Ishikawa, I. Ohtsuka, M. Kamata, M. Tomita, K. Yazawa, H. Muramatsu. Lipid and fatty acid compositions of a novel docosahexaenoic acid-producing marine bacteria, *Lipids*, **1997**, *32*, 975-978.

23. Y. S. Jeong, S. K. Song, S. J. Lee, B. K. Hur. The growth and EPA synthesis of shewanella oneidensis MR-1 and expectation of EPA biosynthetic pathway, *Biotechnology and Bioprocess Engineering*, **2006**, *11*, 127-133.

24. N. Houshang, G. Mansel. Production of EPA by shewanella putrefaciens MAC1 in selected culture media, *Journal of Food Science and Technology*, **2008**, *5*, 75-81.

25. E. D. Frank, E. M. Joseph, J. J. Brittany, S. Sydney, P. L. James, J. D. Kellen, P. R. Michael, B. M. James. The microbiota of freshwater fish and freshwater niches contain omega-3 fatty acid-producing shewanella species, *Applied and Environmental Microbiology,* **2016**, *82,* 218-231.

26. N. Morita, M. Tanaka, H. Okuyama. Biosynthesis of fatty acids in the docosahexaenoic acid-producing bacterium moritella marina strain MP-1, *Biochemical Society Transactions*, **2000**, *28*, 943-945.

27. A. M. Lindberg, G. Molin. Effect of temperature and glucose supply on the production of polyunsaturated fatty acids by the fungus mortierella alpina CBS 343.66 in fermentor cultures, *Applied Microbiology and Biotechnology*, **1993**, *39*, 450-455.

28. O. Hiruta, Y. Kamisaka, T. Yokochi, T. Futamura, H. Takebe, A. Satoh, T. Nakahara, O. Suzuk. Gamma-linoleic acid production by a low temperature-resistant mutant of mortierella ramanniana, *Journal of Fermentation and Bioengineering*, **1996**, *82,* 119-123.

29. M. Xian, J. Nie, Q. Meng, J. Liu, C. Zhou, Y. Kang, K. Zhen. Production of γ-linolenic acid by disrupted mycelia of mortierella isabellina,

Letters in Applied Microbiology, **2003**, *36*, 182-185.

30. H. C. Chen, C. C. Chang. Production of γ-linolenic acid by the fungus cunninghamella echinulata CCRC 31840, *Biotechnology Progress*, **1996**, *12*, 338-341.

31. H. C. Chen, T. M. Liu. Inoculum effects on the production of γ-linolenic acid by the shake culture of cunninghamella echinulata CCRC 31840, *Enzyme and Microbial Technology*, **1997**, *21*, 137-142.

32. H. Gema, A. Kavadia, D. Dimou, V. Tsagou, M. Komaitis, G. Aggelis. Production of γ-linolenic acid by cunninghamella echinulata cultivated on glucose and orange peel, *Applied Microbiology and Biotechnology*, **2002**, *58*, 303-307.

33. K. C. Naveena, Ramalingappa. Production of polyunsaturated fatty acids (PUFAs) from microbes and their secondary metabolites, *International Journal of Current Microbiology Applied Sciences*, **2018**, *7*, 2680-2689.

34. A. M. Lindberg, L. Hansson. Production of γ-linolenic acid by the fungus mucor rouxii on cheap nitrogen and carbon sources, *Applied Microbiology and Biotechnology*, **1991**, *36*, 26-28.

35. E. V. Emelyanova. Lipid and γ-linolenic acid production by mucor inaquisporus, *Process Biochemistry*, **1997**, *32*, 173-177.

36. P. K. Bajpai, P. Bajpai, O. P. Ward. Arachidonic acid production by fungi, *Applied and Environmental Microbiology*, **1991**, *57*, 1255-1258.

37. K. Higashiyama, S. Fujikawa, E. Y. Park, S. Shimizu. Production of arachidonic acid by mortierella fungi, *Biotechnology and Bioprocess Engineering*, **2002**, *7*, 252-262.

38. S. R. Gandhi, J. D. Weete. Production of the polyunsaturated fatty acids arachidonic acid and eicosapentaenoic acid by the fungus pythiumultimum, *Journal of General Microbiology*, **1991**, *137*, 1825-1830.

39. E. E. Stinson, R. Kwoczak, M. J. Kurantz. Effect of cultural conditions on production of eicosapentaenoic acid by pythium irregulare, *Journal of Industrial Microbiology*, **1991**, *8*, 171-178.

40. P. Bajpai, P. K. Bajpai, O. P. Ward. Eicosapentaenoic acid (EPA) production by mortierella alpina ATCC 32222, *Applied Biochemistry and Biotechnology*, **1991**, *31*, 267-272.

41. P. K. Bajpai, P. Bajpai, O. P. Ward. Optimisation of culture conditions for production of eicosapentaenoic acid by mortierella elongata NRRL 5513, *Journal of Industrial Microbiology*, **1992**, *9*, 11-18.

42. L. Bongiorni, R. Jain, S. Raghukumar, R. Aggarwal. Thraustochytrium gaertnerium sp. nov.: a new thraustochytrid stramenopilan protist from mangroves of Goa, India, *Protistología*, **2005**, *156*, 303-315.

43. A. Singh, S. Wilson, O. P. Ward. Docosahexaenoic acid (DHA) production by thraustochytrium sp. ATCC 20892, *World Journal of Microbiology and Biotechnology*, **1996**, *12*, 76-81.

44. P. K. Bajpai, P. Bajpai, O. P. Ward. Optimization of production of docosahexaenoic acid (DHA) by thraustochytrium aureum ATCC 34304, *Journal of the American Oil Chemists' Society*, **1991**, *68*, 509-514.

45. Z. Y. Li, O. P. Ward. Production of docosahexaenoic acid by thraustochytrium roseum, *Journal of Industrial Microbiology*, **1994**, *13*, 238-241.

46. A. Singh, O. P. Ward. Production of high yields of docosahexaenoic acid by thraustochytrium roseum ATCC 28210, *Journal of Industrial Microbiology*, **1996**, *16*, 370-373.

47. A. M. Burja, H. Radianingtyas, A. Windust, C. J. Barrow. Isolation and characterization of polyunsaturated fatty acid producing thraustochytrium species: screening of strains and optimization of omega-3 production, *Applied Microbiology and Biotechnology*, **2006**, *72*, 1161-1169.

48. T. Yaguchi, S. Tanaka, T. Yokochi, T. Nakahara, T. Higashihara. Production of high yields of docosahexaenoic acid by schizochytrium sp. strain SR21, *Journal of the American Oil Chemists' Society*, **1997**, *74*, 1431-1434.

49. T. Yokochi, D. Honda, T. Higashihara, T. Nakahara. Optimization of docosahexaenoic

acid production by schizochytrium limacinum SR21, *Applied Microbiology and Biotechnology*, **1998**, *49*, 72-76.

50. Z. Chi, Y. Liu, C. Frear, S. Chen. Study of a two-stage growth of DHA-producing marine algae schizochytrium limacinum SR21 with shifting dissolved oxygen level, *Journal of Applied Phycology*, **2009**, *81*, 1141-1148.

51. M. K. M. Wong, C. M. K. Tsui, D. W. T. Au, L. L. P. Vrijmoed. Docosahexaenoic acid production and ultrastructure of the thraustochytrid aurantiochytrium mangrovei MP2 under high glucose concentrations, *Mycoscience*, **2008**, *49*, 266-270.

52. N. Nagano, Y. Taoka, D. Honda, M. Hayashi. Optimization of culture conditions for growth and docosahexaenoic acid production by a marine thraustochytrid, aurantiochytrium limacinum mh0186, *Journal of Oleo Science*, **2009**, *58*, 623-628.

53. T. L. D. Silva, A. Reis. The use of multiparameter flow cytometry to study the impact of n-dodecane additions to marine dinoflagellate microalga crypthecodinium cohnii batch fermentations and DHA production, *Journal of Industrial Microbiology and Biotechnology*, **2008**, *35*, 875-887.

54. C. K. Tan, M. Johns. Screening of diatoms for heterotrophic eicosapentaenoic acid production, *Journal of Applied Phycology*, **1996**, *8*, 59-64.

55. M. C. C. García, J. M. F. Sevilla, F. G. A. Fernández, E. M. Grima, F. G. Camacho. Mixotrophic growth of phaeodactylum tricornutum on glycerol: growth rate and fatty acid profile, *Journal of Applied Phycology*, **2000**, *12*, 239-248.

56. M. C. C. García, A. S. Mirón, J. M. F. Sevilla, E. M. Grima, F. G. Camacho. Mixotrophic growth of the microalga phaeodactylum tricornutum, influence of different nitrogen and organic carbon sources on productivity and biomass composition, *Process Biochemistry*, **2005**, *40*, 297-305.

57. M. Mühling, A. Belay, A. B. Whitton. Variation in fatty acid composition of arthrospira (spirulina) strains, *Journal of Applied Phycology*, **2005**, *17*, 137-146.

58. Z. Cohen. The production potential of eicosapentaenoic and arachidonic acids by the red alga porphyridium cruentum, *Journal of the American Oil Chemists' Society*, **1990**, *67*, 916-920.

59. C. Bigogno, I. K. Goldberg, S. Boussiba, A. Vonshak, Z. Cohen. Lipid and fatty acid composition of the green oleaginous alga parietochloris incisa, the richest plant source of arachidonic acid, *Phytochemistry*, **2002**, *60*, 497-503.

60. I. K. Goldberg, C. Bigogno, P. Shrestha, Z. Cohen. Nitrogen starvation induces the accumulation of arachidonic acid in the freshwater green alga parietochloris incisa (trebouxiophyceae), *Journal of Phycology*, **2002**, *38*, 991-994.

61. A. E. Solovchenko, I. K. Goldberg, S. D. Cohen, Z. Cohen, M. N. Merzlyak. Effects of light intensity and nitrogen starvation on growth, total fatty acids and arachidonic acid in the green microalga parietochloris incisa, *Journal of Applied Phycology*, **2008**, *20*, 245-251.

62. V. L. Angélica, A. Felipe, N. Karla. Microalgae, a potential natural functional food source – a review, *Polish Journal of Food and Nutrition Sciences*, **2017**, *67*, 251–263.

63. G. López, C. Yate, F. A. Ramos, M. P. Cala, S. Restrepo, S. Baena. Production of polyunsaturated fatty acids and lipids from autotrophic, mixotrophic and heterotrophic cultivation of galdieria sp. strain USBA- GBX-832, *Scientific Reports*, **2019**, *9*, 10791.

64. Z. Cohen. Production potential of eicosapentaenoic acid by monodus subterraneus, *Journal of the American Oil Chemists' Society*, **1994**, *71*, 941-945.

65. H. Qiang, H. Zhengyu, Z. Cohen, A. Richmond. Enhancement of eicosapentaenoic acid (EPA) and γ-linolenic acid (GLA) production by manipulating algal density of outdoor cultures of monodus subterraneus (eustigmatophyta) and spirulina platensis (Cyanobacteria), *European Journal of Phycology*, **1997**, *32*, 81-86.

66. C. P. Liu, L. P. Lin. Morphology and eicosapentaenoic acid production by monodus subterraneus UTEX 151, *Micron*, **2005**, *36*, 545-550.

https://doi.org/10.52111/qnjs.2024.18109

67. Z. Cohen, S. Didi, Y. M. Heimer. Overproduction of γ-linolenic and eicosapentaenoic acids by algae, *Plant Physiology*, **1992**, *98*, 569-572.

68. W. Yongmanitchai, O. P. Ward. Growth of and omega-3 fatty acid production by phaeodactylum tricornutum under different culture conditions, *Applied Microbiology and Biotechnology*, **1991**, *57*, 419-425.

69. W. Yongmanitchai, O. P. Ward. Growth and eicosapentaenoic acid production by phaeodactylum tricornutum in batch and continuous culture systems, *Journal of the American Oil Chemists' Society*, **1992**, *69*, 584-590.

70. G. C. Zittelli, F. Lavista, A. Bastianini, L. Rodolfi, M. Vincenzini, M. R. Tredici. Production of eicosapentaenoic acid by nannochloropsis sp. cultures in outdoor tubular photobioreactors, *Journal of Biotechnology*, **1999**, *70*, 299-312.

71. N. Zou, C. Zhang, Z. Cohen, A. Richmond. Production of cell mass and eicosapentaenoic acid (EPA) in ultrahigh cell density cultures of nannochloropsis sp. (Eustigmatophyceae), *European Journal of Phycology*, **2000**, *35*, 127-133.

72. F. Xu, W. Cong, Z. L. Cai, Ouyang. Effects of organic carbon sources on cell growth and eicosapentaenoic acid content of nannochloropsis sp. *Journal of Applied Phycology*, **2004**, *16*, 499-503.

73. M. Kitano, R. Matsukawa, I. Karube. Changes in eicosapentaenoic acid content of navicula saprophila, rhodomonas salina and nitzschia sp. under mixotrophic conditions, *Journal of Applied Phycology*, **1997**, *9*, 559-563.

74. M. Kitano, R. Matsukawa, I. Karube. Enhanced eicosapentaenoic acid production by navicula saprophila, *Journal of Applied Phycology*, **1998**, *10*, 101-105.

75. Z. Y. Wen, F. Chen. Heterotrophic production of eicosapentaenoic acid by the diatom nitzschia laevis: effects of silicate and glucose, *Journal of Industrial Microbiology and Biotechnology*, **2000**, *25*, 218-224.

76. Z. Y. Wen, F. Chen. Optimization of nitrogen sources for heterotrophic production of eicosapentaenoic acid by the diatom nitzschia laevis, *Enzyme and Microbial Technology*, **2001**, *29*, 341-347.

77. Z. Y. Wen, F. Chen. A perfusion-cell bleeding culture strategy for enhancing the productivity of eicosapentaenoic acid by nitzschia laevis, *Applied Microbiology and Biotechnology*, **2001**, *57*, 316-322.

78. Z. Y. Wen, Y. Jiang, F. Chen. High cell density culture of the diatom nitzschia laevis for eicosapentaenoic acid production: fed-batch development, *Process Biochemistry*, **2002**, *37*, 1447-1453.

79. A. Blanchemain, D. Grizeau. Increased production of eicosapentaenoic acid by skeletonema costatum cells after decantation at low temperature, *Biotechnology Techniques*, **1999**, *13*, 497-501.

80. L. Christos, W. Eric, M. Tanja, C. Bert, R. Johan, V. R. Sandra, B. Leen, V. H. Jasper, R. T. Klaas. Effect of pH on rhodomonas salina growth, biochemical composition, and taste, produced in semi-large scale under sunlight conditions, *Journal of Applied Phycology,* **2022**, *34*, 1215–1226.

81. R. Vazhappilly, F. Chen. Eicosapentaenoic acid and docosahexaenoic acid production potential of microalgae and their heterotrophic growth, *Journal of the American Oil Chemists' Society*, **1998**, *75*, 393-397.

82. L. A. Meireles, A. C. Guedes, F. X. Malcata. Lipid class composition of the microalga pavlova lutheri: eicosapentaenoic and docosahexaenoic acids, *Journal of Agricultural and Food Chemistry*, **2003**, *51*, 2237-2241.

83. E. K. Kim, G. G. Choi, H. S. Kim, C. Y. Ahn, H. M. Oh. Increasing γ-linolenic acid content in spirulina platensis using fatty acid supplement and light-dark illumination, *Journal of Applied Phycology*, **2012**, *24*, 743-750.

84. L. R. Giovanni, L. L. Antonio, M. G. Beatriz, V. Vito, R. Raffaele, S. Raffaele, M. Paolo. New Biotechnological production of EPA by pythium irregulare using alternative sustainable media obtained from food industry by-products and waste, S*ustainability*, **2023**, *15*, 1147-1162.

85. K. W. Fan, Y. Jiang, Y. W. Faan, F. Chen. Lipid characterization of mangrove thraustochytrid - schizochytrium mangrovei, *Journal of Agricultural and Food Chemistry*, **2007**, *55*, 2906-2910.

86. M. E. D. Swaaf, T. C. D. Rijk, G. Eggink, L. Sijtsma. Optimisation of docosahexaenoic acid production in batch cultivations by crypthecodinium cohnii, *Journal of Biotechnology*, **1999**, *70*, 185-192.

87. M. E. D. Swaaf, J. T. Pronk, L. Sijtsma. Fed-batch cultivation of the docosahexaenoic-acid-producing marine alga crypthecodinium cohnii on ethanol, *Applied Microbiology and Biotechnology*, **2003**, *61*, 40-43.

88. A. Chalimaa, A. Hatzidakia, A. Karnaouri, E. Topakas. Integration of a dark fermentation effluent in a microalgal-based biorefinery for the production of high-added value omega-3 fatty acids, *Applied Energy*, **2019**, *152*, 102-109.

89. X. Qiu. Biosynthesis of docosahexaenoic acid (DHA, 22:6-4, 7, 10, 13, 16, 19): two distinct pathways, *Prostaglandins Leukotrienes and Essential Fatty Acids*, **2003**, *68*, 181-186.

90. J. G. Metz, P. Roessler, D. Facciotti, C. Levering, F. Dittrich, M. Lassner, R. Valentine, K. Lardizabal, F. Domergue, A. Yamada. Production of polyunsaturated fatty acids by polyketide synthase in both prokaryotes and eukaryotes, *Science*, **2001**, *293*, 290-293.

91. J. C. Lippmeier, K. S. Crawford, C. B. Owen, A. Rivas, J. G. Metz, K. E. Apt. Characterization of both polyunsaturated fatty acid biosynthetic pathways in schizochytrium sp, *Lipids*, **2009**, *44*, 621-630.

92. M. E. D. Swaaf, T. C. D. Rijk, P. V. D. Meer, G. Eggink, L. Sijtsma. Analysis of docosahexaenoic acid biosynthesis in crypthecodinium cohnii by ^{13}C labelling and desaturase inhibitor experiments, *Journal of Biotechnology*, **2003**, *103*, 21-29.

93. C. Ratledge. Fatty acid biosynthesis in microorganisms being used for single cell oil production, *Biochimie*, **2004**, *86*, 807-815.

94. J. G. Jaworski. Biosynthesis of monoenoic and polyenoic fatty acids. *The biochemistry of plants*, Academic Press, Orlando, 1987.

95. B. Behrouzian, P. H. Buist. Mechanism of fatty acid desaturation: a bioorganic perspective, *Prostaglandins, Leukotrienes and Essential Fatty Acids*, **2003**, *68*, 107–112.

96. D. U. Antonio. Biosynthesis of polyunsaturated fatty acids in lower eukaryotes, *Life*, **2006**, *58*, 563–571.

97. D. Shiran, I. Khozin, Y. M. Heimer, Z. Cohen. Biosynthesis of eicosapentaenoic acid in the microalga porphyridium cruentum: the use of externally spplied fatty acids, *Lipids*, **1996**, *31*, 1277-1282.

98. T. Arao, M. Yamada. Biosynthesis of polyunsaturated fatty acids in the marine diatom, *Phaeodactylum Tricornutum*, *Phytochemistry*, **1994**, *35*, 1177-1181.

99. C. Bigogno, I. K. Goldberg, D. Adlerstein, Z. Cohen. Biosynthesis of arachidonic acid in the oleaginous microalga parietochloris incisa (chlorophyceae): radiolabeling studies, *Lipids*, **2002**, *37*, 209-216.

100. B. Qi, F. Beaudoin, T. Fraser, A. K. Stobart, J. A. Napier, C. M. Lazaru. Identification of a cDNA encoding a novel C18-Δ^9 polyunsaturated fatty acid-specific elongating activity from the docosahexaenoic acid (DHA)-producing microalga isochrysis galbana, *FEBS Letters*, **2002**, *510*, 159-165.

101. S. L. Pereira, A. E. Leonard, Y. S. Huang, L. T. Chuang, P. Mukerji. Identification of two novel microalgal enzymes involved in the conversion of the ω3-fatty acid, eicosapentaenoic acid, into docosahexaenoic acid, *Biochemical Journal,* **2004**, *384*, 357-366.

102. E. Sakuradani, A. Ando, J. Ogawa, S. Shimizu. Improved production of various polyunsaturated fatty acids through filamentous fungus mortierella alpina breeding, *Applied Microbiology and Biotechnology*, **2009**, *84*, 1-10.

103. Q. K. Pham, H. D. Chastel. Method for mixotrophic culture of spirulinas for producing a biomass rich in omega-6 polyunsaturated fatty acids and/or in sulpholipids, United States Patent, US 0017558, 2003.

104. J. Huang, T. Akia, K. Hachida, T. Yokochi, S. Kawamoto, S. Shigeta, K. Ono, O. Suzuki.

https://doi.org/10.52111/qnjs.2024.18109

Profile of polyunsaturated fatty acids produced by thraustochytrium sp. KK17-3, *Journal of the American Oil Chemists' Society*, **2001**, *78*, 605-610.

105. S. M. T. Tornisielo, J. M. Vieira, M. Cecília, V. S. Carneiro, J. S. Govone. Fatty acid production by four strains of mucor hiemalis grown in plant oil and soluble carbohydrates, *African Journal of Biotechnology*, **2008**, *6*, 1840-1847.

106. T. Aki, Y. Nagahata, K. Ishihara, Y. Tanaka, T. Morinaga, K. Higashiyama, K. Akimoto, S. Fujikawa, S. Kawamoto, S. Shigeta, K. Ono, O. Suzuki. Production of arachidonic acid by filamentous fungus, mortierella alliacea strain YN-15, *Journal of the American Oil Chemists' Society*, **2001**, *78*, 599-604.

107. A. Nisha, G. Venkateswaran. Effect of culture variables on mycelial arachidonic acid production by mortierella alpine, *Food and Bioprocess Technology*, **2008**, *4*, 232-240.

108. C. Ratledge, K. Kanagachandran, A. J. Anderson, D. J. Grantham, J. C. Stephenson. Production of docosahexaenoic acid by crypthecodinium cohnii grown in a pH-auxostat culture with acetic acid as principal carbon source, *Lipids*, **2001**, *36*, 1241-1246.

109. A. Mendes, P. Guerra, V. Madeira, F. Ruano, T. L. Silva, A. Reis. Study of docosahexaenoic acid production by the heterotrophic microalga crypthecodinium cohnii CCMP 316 using carob pulp as a promising carbon source, *World Journal of Microbiology and Biotechnology*, **2007**, *23*, 1209-1215.

110. H. Hoshida, T. Ohira, A. Minematsu, R. Akada, Y. Nishizawa. Accumulation of eicosapentaenoic acid in nannochloropsis sp. in response to elevated CO_2 concentrations, *Journal of Applied Phycology*, **2005**, *17*, 29-34.

111. H. Hu, K. Gao. Response of growth and fatty acid compositions of nannochloropsis sp. to environmental factors under elevated CO_2 concentration, *Biotechnology Letters*, **2006**, *28*, 987-992.

112. V. K. Eroshin, A. D. Satroutdinov, E. G. Dedyukhina, T. I. Chistyakova. Arachidonic acid production by mortierella alpina with growth-coupled lipid synthesis, *Process Biochemistry*, **2000**, *35*, 1171-1175.

113. C. Yuan, J. Wang, Y. Shang, G. Gong, J. Yao, Z. Yu. Production of arachidonic acid by mortierella alpina I_{49}-N_{18}, *Food Technology and Biotechnology*, **2002**, *40*, 311-315.

114. B. H. Hwang, J. W. Kim, C. Y. Park, C. S. Park, Y. S. Kim, Y. W. Ryu. High-level production of arachidonic acid by fed-batch culture of mortierella alpina using NH_4OH as a nitrogen source and pH control, *Biotechnology Letters*, **2005**, *27*, 731-735.

115. J. P. Fidalgo, A. Cid, E. Torres, A. Sukenik, C. Herrero. Effects of nitrogen source and growth phase on proximate biochemical composition, lipid classes and fatty acid profile of the marine microalga isochrysis galbana, *Aquaculture*, **1998**, *166*, 105-116.

116. B. K. De, S. Chaudhury, D. K. Bhattacharyya. Effect of nitrogen sources on γ-linolenic acid accumulation in spirulina platensis, *Journal of the American Oil Chemists' Society*, **1999**, *76*, 153-156.

117. K. J. Flynn, J. L. Garrido, M. Zapata, H. Opik, C. R. Hipkin. Changes in fatty acids, amino acids and carbon/nitrogen biomass during nitrogen starvation of ammonium and nitrate grown isochrysis galbana, *Journal of Applied Phycology*, **1992**, *4*, 95-104.

118. R. Siron, G. Giusti, B. Berland. Changes in the fatty acid composition of phaeodactylum tricornutum and dunaliella tertiolecta during growth and under phosphorus deficiency, *Marine Ecology Progress Series*, **1989**, *55*, 95-100.

119. I. K. Goldberg, Z. Cohen. The effect of phosphate starvation on the lipid and fatty acid composition of the freshwater eustigmatophyte monodus subterraneus, *Phytochemistry*, **2006**, *67*, 696-701.

120. W. L. Chu, S. M. Phang, S. H. Goh. Environmental effects on growth and biochemical composition of nitzschia inconspicua grunow, *Journal of Applied Phycology*, **1996**, *8*, 389-396.

121. L. Zhu, X. Zhang, L. Ji, X. Song, C. Kuang. Changes of lipid content and fatty acid composition of schizochytrium limacinum in

response to different temperatures and salinities, *Process Biochemistry*, **2007**, *42*, 210-214.

122. Y. Taoka, N. Nagano, Y. Okita, H. Izumida, S. Sugimoto, M. Hayashi. Influences of culture temperature on the growth, lipid content and fatty acid composition of aurantiochytrium sp. strain mh0186, *Marine Biotechnology*, **2009**, *11*, 368-374.

123. H. Jiang, K. Gao. Effects of lowering temperature during culture on the production of polyunsaturated fatty acids in the marine diatom phaeodactylum tricornutum (bacillariophyceae), *Journal of Phycology*, **2004**, *40*, 651-654.

124. M. A. Tedesco, E. O. Duerr. Light, temperature and nitrogen starvation effects on the total lipid and fatty acid content and composition of spirulina platensis UTEX 1928, *Journal of Applied Phycology*, **1989**, *1*, 201-209.

125. A. M. Nuutila, A. M. Aura, M. Kiesvaara, V. Kauppinen. The effect of salinity, nitrate concentration, pH and temperature on eicosapentaenoic acid (EPA) production by the red unicellular alga porphyridium purpureum, *Journal of Biotechnology*, **1997**, *55*, 55-63.

126. P. K. Bajpai, P. Bajpai, O. P. Ward. Production of arachidonic acid by mortierella alpina ATCC 32222, *Journal of Industrial Microbiology*, **1991**, *8*, 179-186.

127. Y. Jiang, F. Chen. Effects of medium glucose concentration and pH on docosahexaenoic acid content of heterotrophic crypthecodinium cohnii, *Process Biochemistry*, **2000**, *35*, 1205-1209.

128. Y. Jiang, F. Chen, S. Z. Liang. Production potential of docosahexaenoic acid by the heterotrophic marine dinoflagellate crypthecodinium cohnii, *Process Biochemistry*, **1999**, *34*, 633-637.

129. A. P. Carvalho, I. Pontes, H. Gaspar, F. X. Malcata. Metabolic relationships between macro - and micronutrients, and the eicosapentaenoic acid and docosahexaenoic acid contents of pavlova lutheri, *Enzyme and Microbial Technology*, **2006**, *38*, 358-366.

130. G. Mahajan, M. Kamat. γ-Linolenic acid production from spirulina platensis, *Applied Microbiology and Biotechnology*, **1995**, *43*, 466-469.

131. J. D. Weete, H. Kim, S. R. Gandhi, Y. Wang, R. Dute. Lipids and ultrastructure of thraustochytrium sp. ATCC 26185, *Lipids*, **1997**, *32*, 839-845.

132. A. C. Guedes, L. A. Meireles, H. M. Amaro, F. X. Malcata. Changes in lipid class and fatty acid composition of cultures of pavlova lutheri, in response to light intensity, *Journal of the American Oil Chemists' Society*, **2010**, *87*, 791-801.

133. I. Tzovenis, N. D. Pauw, P. Sorgeloos. Optimisation of T-ISO biomass production rich in essential fatty acids II, effect of different light regimes on the production of fatty acids, *Aquaculture*, **2003**, *216*, 223-242.

134. Z. Xu, X. Yan, L. Pei, Q. Luo, J. Xu. Changes in fatty acids and sterols during batch growth of pavlova viridis in photobioreactor, *Journal of Applied Phycology*, **2008**, *20*, 237-243.

135. R. B. Bailey, D. DiMasi, J. M. Hansen, P. J. Mirrasoul, C. M. Ruecker, G. T. Veeder, T. Kaneko, W. R. Barclay. Enhanced production of lipids containing polyenoic fatty acid by very high density cultures of eukaryotic microbes in fermenters, United States Patent, US 8216812B2, 2006.

136. R. Ruenwai, S. Cheevadhanarak, S. Rachdawong, M. Tanticharoen, K. Laoteng. Oxygen-induced expression of Δ^6-, Δ^9- and Δ^{12}-desaturase genes modulates fatty acid composition in mucor rouxii, *Applied Microbiology and Biotechnology*, **2010**, *86*, 327-334.

137. S. Y. Ho, F. Chen. Lipid characterization of mortierella alpina grown at different NaCl concentrations, *Journal of Agricultural and Food Chemistry*, **2008**, *56*, 7903-7909.

138. G. Q. Chen, Y. Jiang, F. Chen. Fatty acid and lipid class composition of the eicosapentaenoic acid-producing microalga nitzschia laevis, *Food Chemistry*, **2007**, *104*, 1580-1585.

139. G. Q. Chen, Y. Jiang, F. Chen. Salt-induced alterations in lipid composition of diatom nitzschia laevis (bacillariophyceae) under heterotrophic culture condition, *Journal of Phycology*, **2008**, *44*, 1309-1314.

https://doi.org/10.52111/qnjs.2024.18109

140. G. Q. Chen, Y. Jiang, F. Chen. Variation of lipid class composition in nitzschia laevis as a response to growth temperature change, *Food Chemistry*, **2008**, *109*, 88-94.

141. R. J. Henderson, J. W. Leftley, J. R. Sargent. Lipid composition and biosynthesis in the marine dinoflagellate crypthecodinium cohnii, *Phytochemistry*, **1988**, *27*, 1679-1683.

142. Z. Cohen, M. Reungjitchachawali, W. Siangdung, M. Tanticharoen. Production and partial purification of γ-linolenic acid and some pigments from spirulina platensis, *Journal of Applied Phycology*, **1993**, *5*, 109-115.

143. Y. Kamisaka, N. Noda, T. Sakai, K. Kawasaki. Lipid bodies and lipid body formation in an oleaginous fungus, mortierella ramanniana var. angulispora, *Biochimica et Biophysica Acta*, **1999**, *1438*, 185-198.

144. E. Morita, Y. Kumon, T. Nakahara, S. Kagiwada, T. Noguchi. Docosahexaenoic acid production and lipid-body formation in schizochytrium limacinum SR21, *Marine Biotechnology*, **2006**, *38*, 319-327.

145. C. P. Liu, L. P. Lin. Ultrastructural study and lipid formation of isochrysis sp. CCMP1324, *Botanical Bulletin of Academia Sinica*, **2001**, *42*, 207-214.

146. M. J. Jin, H. Huang, A. H. Xiao, Z. Gao, X. Liu, C. Peng. Enhancing arachidonic acid production by nortierella alpina ME-1 using improved mycelium aging technology, *Bioprocess Biosyst Eng*, **2009**, *32*, 117-122.

147. Z. C. Wu, Z. Cohen, I. K. Goldberg, A. Richmond. Characterization of growth and arachidonic acid production of parietochloris incisa comb. nov (trebouxiophyceae, chlorophyta), *Journal of Applied Phycology*, **2002**, *14*, 453-460.

148. S. Shimizu, H. Kawashima, Y. Shinmen, K. Akimoti, H. Yamada. Microbial conversion of an oil containing γ-linolenic acid to an oil containing eicosapentaenoic acid, *Journal of the American Oil Chemists' Society*, **1989**, *66*, 342-347.

149. J. M. F. Sevilla, M. C. C. García, A. S. Mirón, E. H. Belarbi, F G. Camacho, E. M. Grima. Pilot-plant-scale outdoor mixotrophic cultures of phaeodactylum tricornutum using glycerol in vertical bubble column and airlift photobioreactors: studies in fed-batch mode, *Biotechnology Progress*, **2004**, *20*, 728-736.

150. J. G. Burgess, K. Iwamoto, Y. Miura, H. Takano, T. Matsunaga. An optical fibre photobioreactor for enhanced production of the marine unicellular alga isochrysis aft. galbana T-Iso (UTEX LB 2307) rich in docosahexaenoic acid, *Applied Microbiology and Biotechnology*, **1993**, *39*, 456-459.

151. T. E. Lewis, P. D. Nichols, T. A. McMeekin. The biotechnological potential of thraustochytrids, *Marine Biotechnology*, **1999**, *1*, 580-587.

152. F. Xu, Z. L. Cai, W. Cong, F. Ouyang. Growth and fatty acid composition of nannochloropsis sp. grown mixotrophically in fed-batch culture, *Biotechnology Letters*, **2004**, *26*, 1319-1322.

153. M. Akimoto, A. Shirai, K. Ohtaguchi, K. Koide. Carbon dioxide fixation and polyunsaturated fatty acid production by the red alga porphyridium cruentum, *Applied Biochemistry and Biotechnology*, **1998**, *73*, 269-278.

154. F. G. A. Fernández, F. G. Camacho, J. A. S. Pérez, J. M. F. Sevilla, E. M. Grima. Modeling of eicosapentaenoic acid (EPA) production from phaeodactylum tricornutum cultures in tubular photobioreactors, effects of dilution rate, tube diameter and solar irradiance, *Biotechnology & Bioengineering*, **2000**, *68*, 173-183.

155. E. M. Grima, J. A. S. Pérez, F. G. Camacho, J. U. Cardona, J. M. F. Sevilla, F. G. A. Fernández. Biomass and eicosapentaenoic acid productivities from an outdoor batch culture of phaeodactylum tricornutum UTEX 640 in an airlift tubular photobioreactor, *Applied Microbiology and Biotechnology*, **1995**, *42*, 658-663.

156. A. Meiser, U. S. Staiger, W. Trosch. Optimization of eicosapentaenoic acid production by phaeodactylum tricornutum in the flat panel airlift (FPA) reactor, *Journal of Applied Phycology*, **2004**, *16*, 215-225.

157. E. M. Grima, F. G. G. Camacho, J. A. S. Pérez, J. U. Cardona, F. G. A. Fernández, J. M. F. Sevilla. Outdoor chemostat culture of phaeodactylum tricornutum UTEX 640 in a tubular photobioreactor for the production of eicosapentaenoic acid, *Biotechnology and Applied Biochemistry*, **1994**, *20*, 279-290.

158. A. Reis, L. Gouveia, V. Veloso, H. L. Fernandes, J. A. Empis, J. M. Novais. Eicosapentaenoic acid-rich biomass production by the microalga phaeodactylum tricornutum in a continuous-flow reactor, *Bioresource Technology*, **1996**, *55*, 83-88.

159. A. P. Carvalho, F. X. Malcata. Effect of culture media on production of polyunsaturated fatty acids by pavlova lutheri, *Cryptogamie Algologie*, **2000**, *21*, 59-71.

160. E. M. Grima, J. A. S. Pérez, J. L. G. Sánchez, F. G. Camacho, D. L. Alonso. EPA from isochrysis galbana, growth conditions and productivity, *Process Biochemistry*, **1992**, *27*, 299-305.

161. E. M. Grima, J. A. S. Pérez, F. G. Camacho, J. M. F. Sevilla, F. G. A. Fernández. Effect of growth rate on the eicosapentaenoic acid and docosahexaenoic acid content of isochrysis galbana in chemostat culture, *Applied Microbiology and Biotechnology*, **1994**, *41*, 23-27.

162. E. M. Grima, J. A. S. Pérez, F. G. Camacho, J. L. G. Sánchez, D. L. Alonso. N-3 PUFA productivity in chemostat cultures of microalgae, *Applied Microbiology and Biotechnology*, **1993**, *38*, 599-605.

163. Y. H. Lin, F. L. Chang, C. Y. J. Y. Tsao, Leu. Influence of growth phase and nutrient source on fatty acid composition of isochrysis galbana CCMP 1324 in a batch photoreactor, *Biochemical Engineering Journal*, **2007**, *37*, 166-176.

164. L. Poisson, F. Ergan. Docosahexaenoic acid ethyl esters from isochrysis galbana, *Journal of Biotechnology*, **2001**, *91*, 75-81.

165. E. Ganuza, M. S. Izquierdo. Lipid accumulation in schizochytrium G13/2S produced in continuous culture, *Applied Microbiology and Biotechnology*, **2007**, *76*, 985-990.

166. R. D. Bowles, A. E. Hunt, G. B. Bremer, M. G. Duchars, R. A. Eaton. Long-chain n-3 polyunsaturated fatty acid production by members of the marine protistan group the thraustochytrids: screening of isolates and optimisation of docosahexaenoic acid production, *Journal of Biotechnology*, **1999**, *70*, 193-202.

167. A. P. Carvalho, S. O. Silva, J. M. Baptista, F. X. Malcata. Light requirements in microalgal photobioreactors: an overview of biophotonic aspects, *Applied Microbiology and Biotechnology*, **2011**, *89*, 1275-1288.

168. A. Singh, O. P. Ward. Production of high yields of arachidonic acid in a fed-batch system by mortierella alpina ATCC 32222, *Applied Microbiology and Biotechnology*, **1997**, *48*, 1-5.

169. Y. Zeng, X. J. Ji, M. Lian, L. J. Ren, L. J. Jin, P. K. Ouyang, H. Huang. Development of a temperature shift strategy for efficient docosahexaenoic acid production by a marine fungoid protist, schizochytrium sp. HX-308, *Applied Biochemistry and Biotechnology*, **2011**, *164*, 249-255.

https://doi.org/10.52111/qnjs.2024.18109

TẠP CHÍ KHOA HỌC
TRƯỜNG ĐẠI HỌC QUY NHƠN
TẬP 18, SỐ 1, THÁNG 02 - 2024
ISSN: 1859-0357 E-ISSN: 2815-6242

MỤC LỤC